universität wien

MASTERARBEIT / MASTER'S THESIS

Titel der Masterarbeit / Title of the Master's Thesis

"Down-regulation of Bromodomain PHD finger Transcription Factor (*BPTF*) in tumour cells and its influence on NK cell activity"

verfasst von / submitted by

Viola Hedrich, BSc

angestrebter akademischer Grad / in partial fulfilment of the requirements for the degree of

Master of Science (MSc)

Wien, 2019/ Vienna 2019

Studienkennzahl lt. Studienblatt / degree programme code as it appears on the student record sheet:	A 066 834
Studienrichtung lt. Studienblatt / degree programme as it appears on the student record sheet:	Masterstudium Molekulare Biologie
Betreut von / Supervisor:	Doz. Dr. Wolfgang Sommergruber

Acknowledgements

Mein Dank gilt allen, die mich dabei unterstützt haben mein Masterpraktikum zu absolvieren und meine Masterarbeit zu verfassen.

Besonders bedanken muss ich mich dabei bei meiner Betreuer Wolfgang Sommergruber. Durch sein Wissen und seine Hilfsbereitschaft, hat er mich immer unterstützt und es geschafft mich mit seiner Begeisterung für Wissenschaft anzustecken. Weiters gilt mein Dank dem gesamten“ WoSo“ Lab. Ohne Annika Osswald, die mich mit ihrer freundlichen und genauen Art, in diverse Labortechniken und wichtige biologische Themen eingeschult hat, hätte ich die benötigten Laborskills sicher nicht so gut erlernen können. Nathalie und Herwig standen mir zur Seite, wenn ich sie gebraucht habe und hatten beide immer (mindestens) einen passenden Witz parat, der einem Laborfrischling wie mir immer wieder neuen Mut und Trost gespendet hat.

Meine Familie stand immer hinter mir, obwohl sie zu diesem Zeitpunkt selbst einige Tiefen durchstehen musste. Besonders froh bin ich, dass mein Freund Konstantin so viel Verständnis hatte und immer für mich da war (nicht nur um mich zu später Stunde noch zum nächsten amerikanischen Schnellimbiss für ein „rettendes“ Abendessen zu chauffieren) ☺

Thanks to all of you!

Declaration

I declare that I have written this Master thesis independently and that I have not used any additional sources than the mention citations.

I endeavoured to descry all holders of image rights and to obtain their consent for using their images in this Master thesis. If any copyright infringements are detected, please contact me.

Viola Hedrich Mödling, April 2019

Deklaration

Hiermit erkläre ich, dass ich diese Masterarbeit eigenständig verfasst habe und keine zusätzlichen Quelle - zu den genannten - genutzt habe. Ich habe mich bemüht, sämtliche Inhaber der Bildrechte ausfindig zu machen und ihre Zustimmung zur Verwendung der Bilder in dieser Arbeit eingeholt. Sollte dennoch eine Urheberrechtsverletzung bekannt werden, ersuche ich um Meldung bei mir.

Viola Hedrich Mödling, April 2019

Content

1. Abstract

The tumour microenvironment (TME) influences the way tumour cells (TCs) migrate, proliferate and how they "immunologically behave". To elucidate the underlying molecular mechanisms of the cross-talk between TCs and cells of the TME with a particular focus on immune cells, we made use of our novel 3D models consisting of TCs (non-small cell lung cancer (NSCLC)-derived cell lines NCI-H157 and NCI-H1437), stroma cells (fibroblasts) and immune cells (focus on donor-derived primary NK cells; PNKs) embedded in a Matrigel/collagen matrix. Emerging evidence indicates that particularly epigenetic events in TCs influence their immunological behaviour. Understanding the underlying biological mechanisms may lead to identification of novel therapeutic targets inside TCs that increase their immunogenicity. Modulating those regulators would allow restoring the intrinsic immune response towards neoplasms without interfering with or specifically targeting immune cell functions. One of those potential novel epigenetic targets is the bromodomain PHD finger transcription factor (*BPTF*), a reader of the histone code and an essential subunit of the nucleosomal remodeling factor (NURF). In the course of my Master thesis I studied both, the effect of genetic and pharmacologic inhibition of *BPTF* on the activation of PNKs. For this, we applied BI90, a potent and specific proprietary inhibitor of the bromodomain (BRD) of *BPTF*. Treating respective mono-cultures with BI90 did not generate any adverse effect *per se.* Thus, BI90 could be applied for pharmacological *BPTF* inhibition in simple spheroid (floater) and complex 3D embedded co-cultures. In all 3D models killing of TCs by activated PNKs was significantly increased upon BI90 treatment accompanied by an increase in *GZMB* and *IFNG* levels in the supernatant of the respective 3D cultures. Interestingly, the rate of infiltration and activation of PNKs was lower in 3D embedded models, clearly supporting our previous finding that the cross-talk between TCs and stromal cells (FBs) induces a strong immunosuppressive environment. As pharmacologic inhibition of *BPTF* most likely modulate only a very focused set of genes in TCs, we next performed genetic perturbation experiments by either knocking down (KD via siRNA) or knocking out (KO via CRISPR/Cas9) *BPTF* in TCs. Importantly, NCI-H1437 *BPTF* KO cells (pools) and NCI-H157 *BPTF* KD cells were again significantly better killed in co-cultures with PNKs compared to the nontarget control group. According to the location of sgRNAs used, domain specific effects in depletion assays were observed. Strongest effects were observed targeting the N-terminal

domain, while those recognizing more C-terminal domains (PHD-finger, BRD) showed weaker or no effects. In order to gain a more detailed biological understanding, *BPTF* KO single cell clone cultures were isolated and gene expression profiling of five different *BPTF* KO single cell clones was performed. Similarly, a detailed time-resolved transcriptional analysis of the BI90-treated cultures was performed. According to a recent publication by Mayes and colleagues, heparanase (*HSPE*) might be the reason for the executed immunosuppressive effect by TCs via *BPTF*. *HSPE* cleaves heparan sulfates, known co-ligands of PNKs natural cytotoxicity receptor. In contrast, we found that *HPSE* transcript abundance stayed unaffected both in BI90-treated as well as in *BPTF* KD or KO cultures. However, we found many genes affected (down-regulated) by *BPTF* KO which are mainly involved in cell cycle regulation. Interestingly, it is known that inhibitors targeting cell cycle regulators, not only arrest cells but also increase their immunogenicity. Comparison of transcripts being up- or down-regulated in at least three out of five *BPTF* KO single cell clones with the those of BI90-treated tumour cells revealed only an overlap of six down-regulated (*CLSPN*, *RARRES1*, *KNTC1*, *KIF11*, *KIAA0101* and *XRCC2*) and two up-regulated genes (*IFIH1* and *GMFG*). In particular, *IFIH1*, also known as *MDA5* (Melanoma Differentiation-Associated protein 5) might substantially contribute to the immunogenic visibility of TCs. *IFIH1* is part of the RIG-I-like receptor (RLR) family and functions as a pattern recognition receptor (recognizing dsRNA) that is a sensor for viral infection. It is known that cancer cells can mimic a viral infection to activate RNA sensing pattern recognition receptors and interferon response pathways subsequently stimulating cytotoxic immune cells including NK cells. Consequently, TCs get killed via induced cell lysis and apoptosis. Therefore, impaired NURF function – due to *BPTF* KO/inhibition - may induce cellular stress and expression of endogenous retroviral dsRNA leading to an increase in immunogenicity and triggering an *IFIH1*-dependet type 1 interferon response. Clearly, further studies are needed to proof this hypothesis. However, despite many open questions in the context of the underlying molecular mechanisms of *BPTF*-mediated immune escape, we showed that *BPTF* can be regarded as a highly promising target in the immunological approach of combating human cancer.

2. Zusammenfassung

Das “tumour microenvironment” (TME) beeinflusst unter anderem wie Tumorzellen wachsen, migrieren bzw. „immunologische verhalten“. Mittels moderner 3D *in vitro* Modellen, versuchen wir den „Cross-talk“ zwischen Tumorzellen und TME – mit speziellem Augenmerk auf Immunzellen – besser zu verstehen. Unsere Modelle bestehen aus von Nicht-kleinzelligem Lungenkarzinom (NSCLC) abgeleiteten Zelllinien (NCI-H157 bzw. NCI-H1437), Bindegewebszellen (Fibroblasten) und Immunzellen (primäre humane Natürliche Killerzellen; PNKs) eingebettet in eine Matrigel/Kollagen Matrix. Neusten Erkenntnissen zufolge dürfte das immunologische Verhalten von Tumorzellen vor allem durch den epigenetischen Status der Tumorzellen beeinflusst werden. Das Erforschen und Verstehen der zugrundeliegenden molekularen Mechanismen führt hoffentlich zur Identifikation von neuen therapeutischen Targets innerhalb der Tumorzellen. Dadurch könnte die Immunogenität der Tumorzellen erhöht werden und die intrinsische Immunantwort gegen Tumore indirekt - ohne die Funktion der Immunzellen zu modulieren - reaktiviert werden.

Der Bromodomain PHD finger Transkriptionsfaktor (*BPTF*) ist ein solches potenzielles neues therapeutisches Target. *BPTF* ist ein „Reader“ des Histoncodes und eine essentielle Untereinheit des Nucleosomal Remodelling Faktors (NURF). Im Zuge meiner Masterarbeit habe ich sowohl die Effekte von pharmakologischer als auch genetischer *BPTF* Inhibition auf PNK Aktivität untersucht. Für pharmakologische Inhibition wurde BI90 - ein selektiver und potenter Inhibitor der *BPTF* Bromodomäne (BRD) – genutzt. Die Behandlung der einzelnen Monokulturen mit BI90 zeigte keine ungewünschten Nebeneffekte, weshalb BI90 zur pharmakologischen *BPTF* Inhibition genutzt werden konnte. Sowohl in simplen 3D Floater als auch in komplexen eingebetteten Co-Kulturen war die PNK-abhängige Tumorzellzytotoxizität signifikant erhöht im Vergleich zu den Kontrollen. Passend dazu detektierten wir erhöhte *GZMB* und *IFNG* Werte im Überstand von BI90 behandelten Co-Kulturen. In den eingebetteten Modellen waren die gemessenen Effekte schwächer. Dies stimmt mit vorausgegangen Untersuchungen überein, dass der Cross-talk zwischen Tumorzellen und Fibroblasten immunsuppressiv wirkt.

Im nächsten Schritt analysierten wir die Effekte von genetischer *BPTF* Depletion. Sowohl Knock Down (KD via siRNAs) als auch Knock Out (KO via CRISPR/Cas9) wurde durchgeführt.

NCI-H1437 *BPTF* KO cells (pools) / NCI-H157 *BPTF* KD wurden im Vergleich zur Nontarget Kontrolle signifikant besser durch PNKs abgetötet. Abhängig von der jeweiligen sgRNA-Bindungsstelle, wurden Domäne-spezifische Effekte auf die Tumorzellen Viabilität *per se* identifiziert. Die stärksten Ergebnisse lieferten jene sgRNAs, welche in der N-terminale Domäne binden. Schwächere bzw. keine Effekte zeigten jene, welche mehr C-terminale Domänen (PHD2, BRD) erkannten.

Um ein besseres biologisches Verständnis zu erlangen, wurden *BPTF* KO Einzelzellkulturen generiert und Genexpressionsprofiling durchgeführt. Ergänzend wurde eine detaillierte Transkriptionsanalyse (mit mehreren Zeitpunkten) von BI90-behandelten Tumorzellen erstellt. Laut aktueller Literatur scheint Heparanase (*HPSE*) eine Rolle in der *BPTF*-abhängigen Immunsuppression zu spielen. *HPSE* schneidet Heparansulfate, Ko-Liganden für PNKs aktivierende Natürliche Zytotoxizitätsrezeptoren. Im Unterschied dazu konnten wir keine Deregulation der *HPSE* feststellen – weder in den *BPTF* KO Proben, noch in den BI90-behandelten. Viele der von uns als dereguliert identifizierten Gene (verringerte Expression), sind mit Zellzyklusregulation assoziiert. Es wurde gezeigt, dass Inhibitoren von Zellzyklusregulatoren, nicht nur die Zellen arretieren, sondern auch immunogener machen. Der Vergleich zwischen Genen dereguliert in *BPTF* KO Einzelzellkulturen (mindestens in 3/5) und BI90-behandelten Tumorzellen zeigte nur geringe Übereinstimmung. Sechs Gene sind in beiden Experimenten hinunterreguliert (*CLSPN*, *RARRES1*, *KNTC1*, *KIF11*, *KIAA0101* and *XRCC2*) und zwei hochreguliert (*IFIH1* und *GMFG*). *IFIH1*, gehörend zur RIG-I-like receptor (RLR) Familie, ist ein Pattern Recognition Rezeptor (PRP). Es erkennt das Vorhandensein von dsRNA – ein Zeichen für virale Infektion - innerhalb der Zelle. Tumorzellen haben die Fähigkeit virale Infektionen zu imitieren, um eine Immunantwort, durch Aktivierung von Interferon Pathways, auszulösen. Die Konsequenz ist Tumorzelllyse und Apoptose. *BPTF* KO/Inhibition hat beeinträchtigte NURF Funktionalität zur Folge und löst dadurch möglicherweise zellulären Stress aus. Als Antwort auf diesen kann es zur Expression von endogener retroviraler dsRNA kommen. Das Vorhandensein der dsRNA ihrerseits kann *IFIH1*-abhängige Type 1 Interferon Antwort auslösen. Um diese Hypothese zu untermauern und um den molekularen Mechanismus des *BPTF*-abhängigen Immuneescapes besser zu verstehen, sind weitere Analysen dringend notwendig. Trotz aller noch offenen Fragen,

haben wir gezeigt, dass *BPTF* als vielversprechendes Target zur Erhöhung der Tumorzell-immunogenität im Kampf gegen Krebserkrankungen angesehen werden kann.

3. Introduction

Cancer progression and therapy failure are not only dependent on tumour cells but also on the surrounding stroma. The chronic host response caused by presence of malignancies leads to transformation of a healthy microenvironment into a so-called tumour microenvironment (TME) also referred to as tumour stroma. As a consequence tumours cannot be seen as an independent, autonomous system [1]. Interactions between cancer cell and surrounding non-malignant cells are crucial for cancer growth, progression and therapy failure. This cross-talk favors neo-angiogenesis, epithelial-mesenchymal transition (EMT), modulation of patient's immune response towards neoplasms to name but a few [2]. The TME's composition and behaviour such as oxygen supply or extracellular matrix tension have a huge impact on the behaviour of malignant cells. Therefore, understanding the crosstalk between malignant cell and cells present in the TME is a major goal of cancer research.

3.1. Tumour Microenvironment (TME)

The TME is composed of an extracellular matrix (ECM) and various types of healthy, genetically stable cell types including fibroblasts, pericytes, endothelial and immune cells (e.g.: mast cells, dendritic cells, lymphocytes) (**Figure 1**) [2, 3]. Additional cells (of various kinds) promoting tumour growth are actively recruited into the TME triggered by secretion of paracrine signals (cytokines, growth factors) from malignant and non-malignant cells [4]. The most important components of the TME are described below.

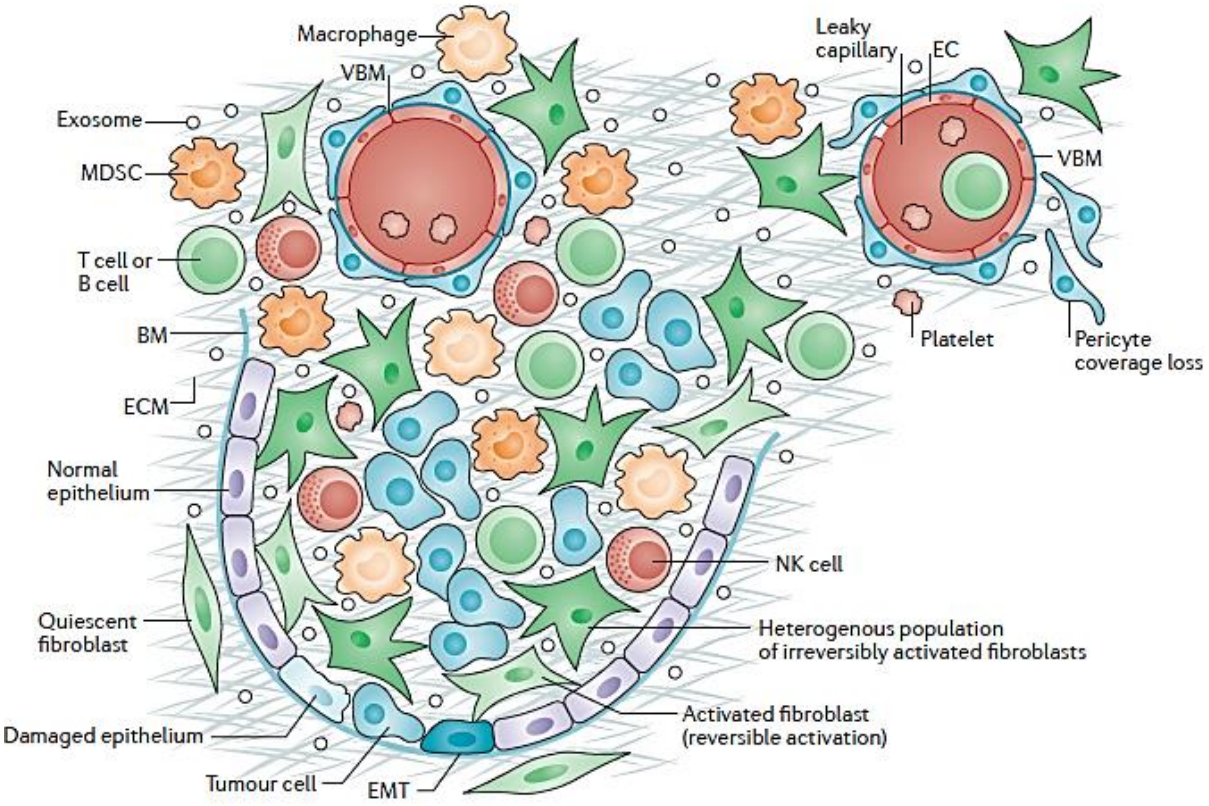

Figure 1: Cellular composition of the tumour microenvironment (TEM).

(BM, basement membrane; EC, endothelial cell; ECM, extracellular matrix; EMT, epithelial to mesenchymal transition; MDSC, myeloid-derived suppressor cell; NK, natural killer; BM, basement membrane; VBM, vascular basement membrane)

Modified from: Kalluri, 2016 [1]

3.1.1. Extracellular Matrix (ECM)

ECM is a scaffold found in all organs and tissues in the human body. It is comprised of water, polysaccharides and proteins secreted by cells present in this microenvironment. Fibroblasts (FBs) are the main source of ECM proteins. The major components are fibrous proteins and proteoglycans (PGs). The fibrous proteins include collagen (up to 30%), fibronectin, laminins and elastin to name but a few. The networks formed by these proteins influence cell adhesion, migration and tissue development. PGs (e.g. hyaluronic acid) form a hydrated gel which fills empty spaces inside protein networks. The main functions of PGs are hydration, buffering and force resistance. ECM has the ability to bind growth factors (GFs) and provides

ligands for cell surface receptors like integrins or discoidin domain receptors. Those interactions cause receptor activation, subsequent signal transduction and may alter gene expression. Each tissue has its own unique ECM composition adapted to the function. Variation is performed by post-translational protein modification or by remodeling. FBs secrete enzymes for ECM remodeling like matrix metalloproteinases (MMPs). Specialization comes along with specific biochemical and biomechanical processes unique for the present organ. In order to maintain tissue homeostasis secretion and remodeling are highly regulated processes [5, 6].

Tumours are frequently surrounded by a more rigid TME [7]. It is caused by reorganization of ECM by cancer cells and fibroblasts. Both decompose the ECM by increased secretion of MMPs. Thereby bound growth factors (GFs) like vascular-endothelial growth factor (VEGF) are released. VEGF as an example can trigger neo-angiogenesis [5, 8]. The stiffness of the TME can even alter drug responses by the mechanogenetic feedback cells receive from the culture substrate [9].

3.1.2. Tumour Cells

Tumour cells derive from healthy genetically stable cells via dynamic changes in the genome caused by mutation and by epigenetic alterations. These mutations typically involve oncogenes and tumour suppressor genes. Mutations in oncogenes lead to gain of function, while tumour suppressor gene mutation causes loss of function in corresponding gene products [8]. One mutation alone does not lead to formation of cancer. It is rather a multistep process involving many alterations to transform a healthy cell into a malignant one involving different stages of pre-malignancies. Thus explaining why numbers of diagnosed cases increase with aging [8].

3.1.2.1. Epithelial Mesenchymal Transition (EMT)

The term epithelial mesenchymal transition describes a biological process that allows differentiated epithelial cells to change their phenotype to a mesenchymal one. It comes along with profound changes in their behaviour. Epithelial cells are polar and form tight layers. They are connected to each other via tight junctions and interact with the basement membrane via their basal surface. Their apical surfaces interact with the environment and

have specialized functions depending on the present organ. Thus, epithelial cells are part of a tight network and cannot leave those structures [10, 11] In contrast mesenchymal cells exhibit enhanced migratory phenotypes, invasiveness, increased ECM production and increased resistance to apoptosis [12]. Via certain biological mechanisms cells have the ability to shift their phenotype from an epithelial to a mesenchymal one. Malignant cells undergone EMT bear stem cell like properties and a fibroblastoid shape. Additionally, they are migratory and invasive. Thus, those cells are able to metastasize, which indicates poor prognosis for patients [13]. Recently, EMT has been proposed as the ultimate survival mechanism of cancer cells [14].

EMT is induced in the presence of certain growth factors (GFs) including transforming growth factor β1 (*TGFB1*/TGFβ1), hepatocyte growth factor (*HGF*) or platelet-derived growth factor (PDGF). Exposure of epithelial cells to those GFs lead to downstream activation of transcription factors (TFs) like zinc-finger protein SNAIL (*SNAI1*) and SLUG (*SNAI2*), basic helix-loop-helix protein *TWIST*, homeobox protein Goosecoid (*GSC*) to name but a few. It is thought that each of those transcription factors is sufficient to trigger EMT in a specific way. In addition to the presence of specific TFs certain microRNAs belonging to miR-200 family are down-regulated. However, the detailed underlying mechanisms remain unclear [13].

Induction of EMT leads to changes in gene expression in involved cells (**Figure 2**). Typical epithelial markers like E-cadherin, laminin-1, desmoplaktin and the tight junction protein zonula occludens-1 (*TJP1*/*ZO-1*) are exchanged by expression of proteins correlating with a mesenchymal phenotype and behaviour such as N-cadherine, β-catenin, α-smooth muscle actin (α-SMA), fibronectin and vimentin [12]. The change from E- to N-cadherin expression during EMT is also known as the cadherin switch [15].

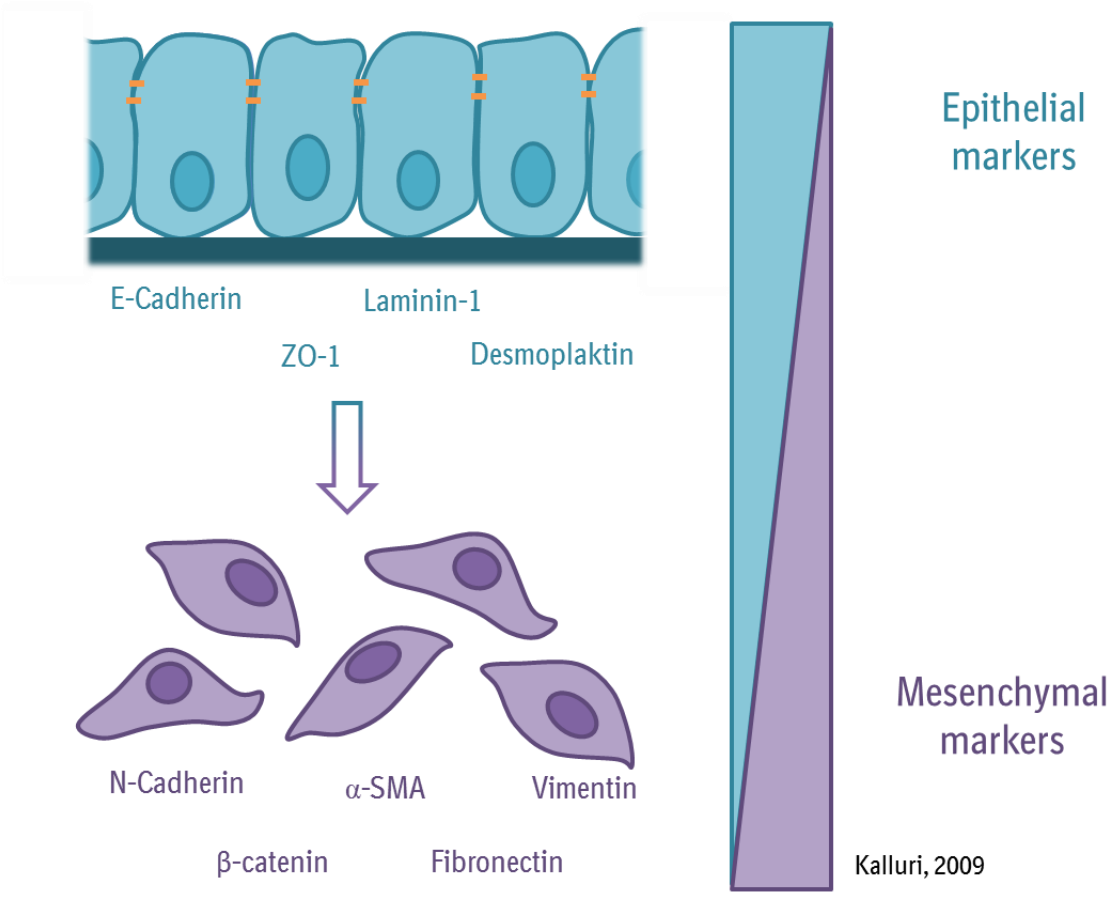

Figure 2: Expression of markers changing during epithelial mesenchymal transition (EMT).

Epithelial cells form layers due to interactions via tight junctions (orange) and with basement membrane (dark blue). Typical epithelial markers include: E-cadherin, laminin-1, desmoplaktin and the tight junction protein zonula occludens-1 (*TJP1*/ZO-1).
These markers are lost during EMT while others are gained like N-cadherine, β-catenin, α-SMA, fibronectin or vimentin.

Figure drawn by author based on Kalluri and Weinberg, 2009 [12]

Taube *et al*. calculated an "EMT score" for human cancer cell lines, depending on their expression profile of epithelial and mesenchymal markers [13]. Rudisch and colleagues made use of this EMT-score to correlate various non-small cell lung cancer (NSCLC) cell lines with their invasive behaviour [16], two of them have been used in the course of this Master Thesis representing an invasive (NCI-H157) and a non-invasive (NCI-H1437) cellular model (**Figure 3**) [13, 16].

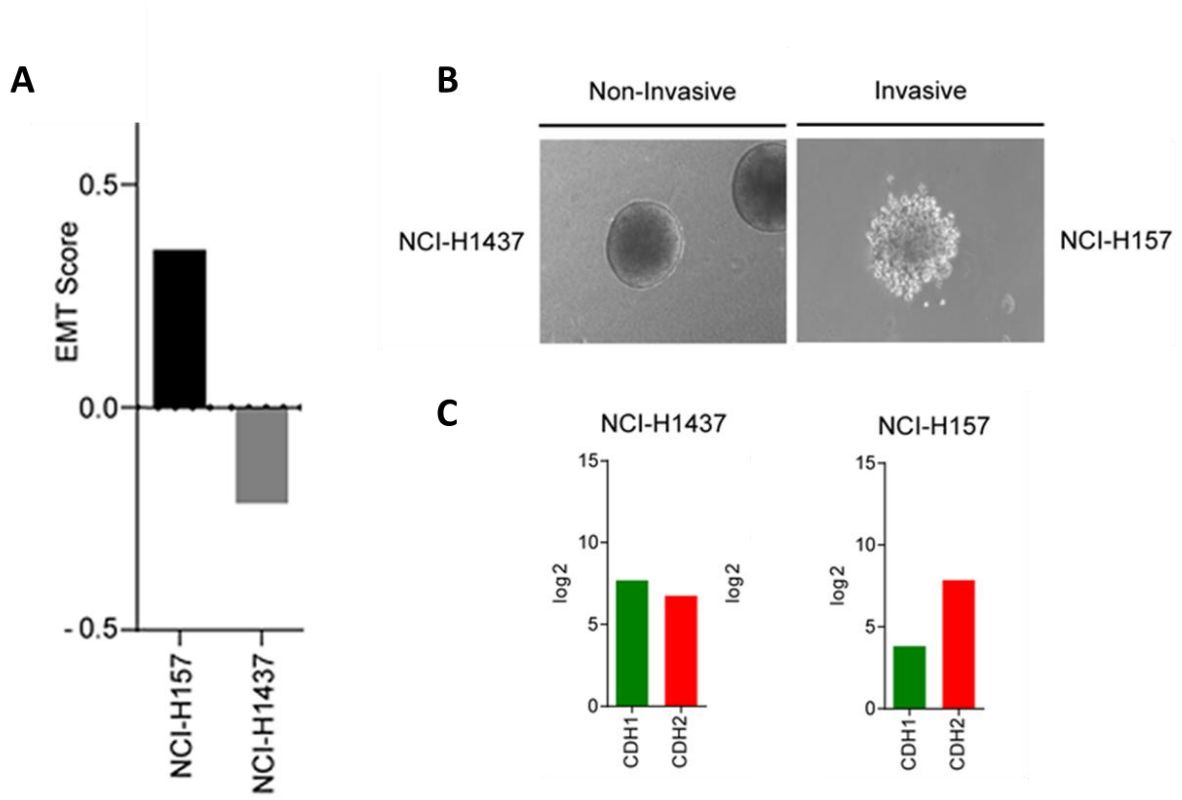

Figure 3: EMT score of NCI-H1437 and NCI-H157 (A), their three-dimensional growth behaviour in collagen I after 72 hours (B) and expression levels of E-cadherin (*CDH1*) and N-cadherin (*CDH2*) (C).

Modified from Rudisch *et al.* 2015 [16]

3.1.3. Fibroblasts

3.1.3.1. Fibroblasts in Healthy Tissues

Fibroblasts (FBs) were first described in the 19th century and later on defined as cells capable of collagen production. They are part of the connective tissue with a likely mesenchymal lineage origin. FBs are embedded in the ECM lacking a connection to the basement membrane. Under normal, healthy conditions FBs have an insignificant metabolic and transcriptomic activity referred to as resting or quiescent [1].

FBs have a major impact on production of ECM metabolites including growth factors, substrates and MMPs to name but a few. In the last years FBs have gained centre stage, as they are thought to play a crucial role in cancer growth, invasion and metastasis [17].

Further they are thought to be able to modulate the immune cells by altering bioavailability of inflammatory metabolites like tryptophan and arginine [18].

FBs are able to survive extreme stress which would be lethal for other cell types. This may be explained by presence of (normally silent) intrinsic survival programmes and by their cellular plasticity. They are part of the general host response to tissue damage e.g. caused by mechanical trauma, radiation, extreme temperature, toxins or pathogens [1]. During wound healing resting FBs become activated and start proliferating. The underlying mechanisms need to be elucidated. However, it seems as if there are (at least) two ways to activate them: a reversible and an irreversible one [1]. The switch from an activated state back to the resting one seems to be determined by epigenetic regulation (**Figure 4**).

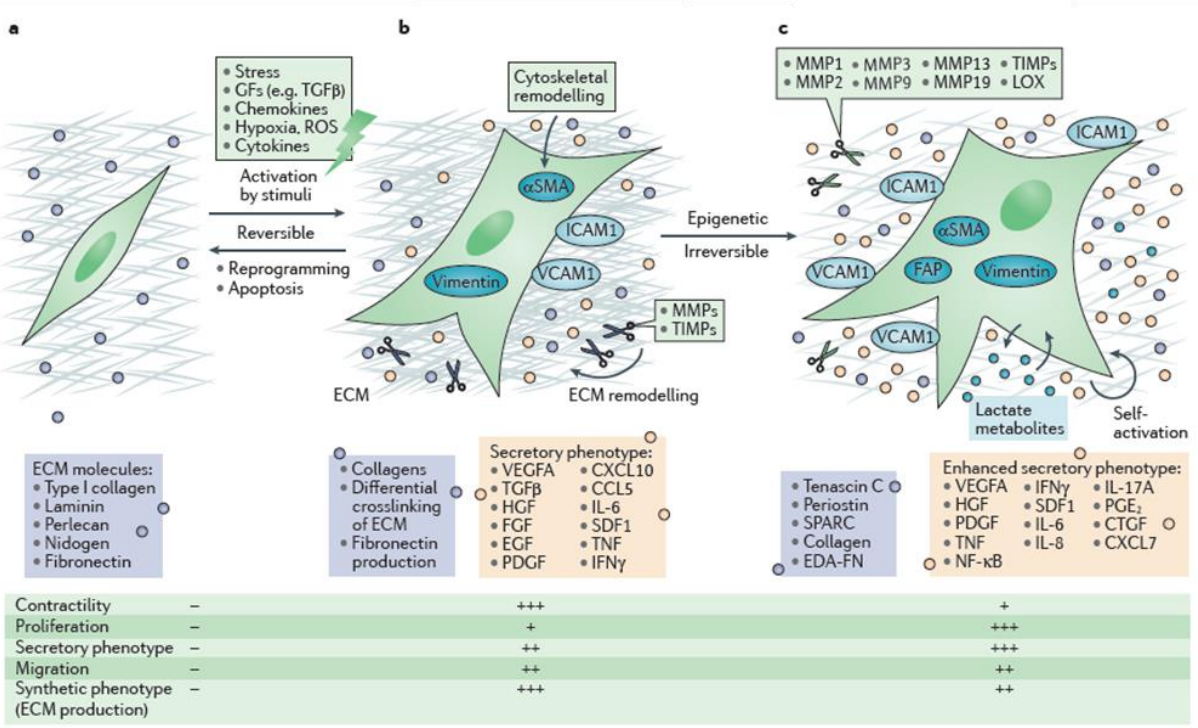

Figure 4: Different states of FBs: Resting (A), reversible (B) and irreversible activated FBs (C).

Resting FBs are activated by the presence of stimuli indicating tissue injury (e.g. cytokines like interleukin 6 (IL-6); growth factors like transforming growth factor beta (TGFβ), platelet derived growth factor PDGF) and become activated normal fibroblasts. Activation comes with changes in shape: Resting FBs have a spindle like shape, while reversible activated FBs bear a stellar form. Anyhow, activation cannot only be monitored by changes in shape, but also by alterations in gene expression. For instance, expression of α smooth muscle actin (αSMA) and vimentin is acquired. They gain the ability to remodel and rearrange the cytoskeleton and the ECM. Reversible, activated FBs proliferate and are contractile.

(CCL5, C-C motif chemokine ligand 5 (also known as RANTES); CTGF, connective tissue growth factor; CXCL, C-X-C motif chemokine ligand; EDA-FN, extradomain A-fibronectin; EGF, epidermal growth factor; FAP, fibroblast activation protein; FGF, fibroblast growth factor; GFs, growth factors; HGF, hepatocyte growth factor; ICAM1, intercellular adhesion molecule 1; IFNγ, interferon-γ; IL, interleukin; LOX, lysyl oxidase; MMP, matrix metalloproteinase; NF-κB, nuclear factor-κB; PDGF, platelet-derived growth factor; PGE2, prostaglandin E2; ROS, reactive oxygen species; SDF1, stromal cell-derived factor 1; TGFβ, transforming growth factor-β; TIMPs, tissue inhibitors of metalloproteinases; TNF, tumour necrosis factor; VEGFA, vascular endothelial growth factor A; VCAM1, vascular adhesion molecule 1.)

Modified from: Kalluri R., 2016 [1]

If a cell is damaged, it starts to secret damage and repair signals in order to restore tissue homeostasis. Wound healing - as an answer to acute injury - typically leads to the

recruitment of immune cells, endothelial cells (to promote angiogenesis) and additional FBs to depose and remodel the ECM. It is suggested that reversibility of FB activation is guaranteed by programmed cell death or reprogramming after completing the wound healing process. The majority of reversible activated FBs seem to undergo apoptosis, while only few recess to the resting ground state [1].

3.1.3.2. Fibroblasts and Cancer

The occurrence and accumulation of malignant cells is a long-lasting signal for starting and maintaining wound healing-like response [19]. It is possible that reversible activated FBs gain additional properties such as a further increased secretory phenotype, an ECM remodelling potential, robust autocrine activation, immunomodulatory signalling functions and an enhanced proliferation rate. Acquisition of additional functions seems to be driven by long-lasting or permanent injury stimuli [20], as caused by cancer lesions: Activated FBs exhibiting the above described characteristics are termed cancer-associated fibroblasts (CAFs) [17]. These changes seem to be partly triggered by epigenetic mechanisms, leading to increased activity of anti-apoptotic and pro-proliferative pathways. Furthermore, it is thought that cancer cells directly recruit activated FBs by secretion of growth factors (GFs) like TGFβ, PDGF (platelet-derived growth factor) and FGF2 (fibroblast growth factor 2). *PDGF* secretion positively influences the proliferation of FBs and therefore seems to be crucial for transformation of normal activated fibroblasts (NAFs) into CAFs [21-23]. Proliferation and invasion of CAFs seem to be dependent on the presence of TGFβ in the tumour stroma, too. Unfortunately, a detailed understanding of the underlying mechanisms is still missing. It leads to the formation of a tumour promoting stroma correlating with bad prognosis for patients [1].

In vitro analysis has shown that tumour cells have the ability to reprogram FBs gene expression within a few hours to days thereby altering fibroblasts secretome [16, 24-27]. It indicates that reprogramming of normal FBs into CAFs can be a fast process and independent from fibroblasts origin. However, the epithelial-mesenchymal transition (EMT) status of co-cultivated tumour cell lines has a strong impact on this process [16]. Tumour cells and reprogrammed FBs together may be sufficient to alter activity of additional present cell types, in particular cells of the immune system [28].

3.1.4. Natural Killer (NK) Cells

NK cells are innate lymphoid cells developing in the bone narrow. Between 5 and 20% of all peripheral blood lymphocytes are NK cells. They are phenotypically defined by the expression of CD56 and CD16 as well as lack of CD3. Depending on expression levels of CD56 NK cells are divided in $CD56^{bright}$ and $CD56^{dim}$ subpopulations [29]. Impaired NK cell functions increase the risk of developing cancer. Presence of inactive NK cells corresponds with bad prognosis for affected patients [29].

Due to their ability to recognise and eliminate pathogens, infected or transformed cells without prior sensitization, NK cells are crucial for immunosurveillance [30, 31]. They are constantly in a "primed-state" as they store granules filled with granzymes or perforin in their cytoplasm (**Figure 6**). NK cells express various different activating and inhibiting receptors on their surface. As a consequence, they have the ability to work via several modes of action in parallel [32, 33].

3.1.4.1. NK Cell Education - From Missing "Self" Hypothesis to Self-tolerance Models

Missing self-hypothesis was first described in the 1980ies as an important mechanism allowing NK cells to distinguish healthy cells from infected or transformed ones by expression levels of major histocompatibility (MHC) class I [34]. Normal healthy cells used MHC class I to present peptides derived from proteasomal degraded cytosolic proteins. Peptides and MHC proteins are coupled in the endoplasmatic reticulum (ER) and transferred to the cell membrane. T cells recognise those as "self" proteins and do not attack healthy cells expressing MHC I proteins. Infected or malignant cells express peptides derived from pathogenic or e.g. nuclear and/or mutated proteins. By presenting "non-self" peptides (peptides that are normally not presented by healthy cells) by MHC class I, T cells have the ability to recognise damaged or infected cells and induce an adaptive immune response [35]. To circumvent T cell- mediated killing pathogens and tumour cells can prevent MHC class I expression in general. Thus, T cell activity is prevented. Lack of MHC class I expression causes NK cell activation and cell lysis (**Figure 5**). However, today it is clear that missing self-hypothesis is incomplete and only lack of MHC class I is not sufficient to trigger target cell lysis by NK cells [32, 36].

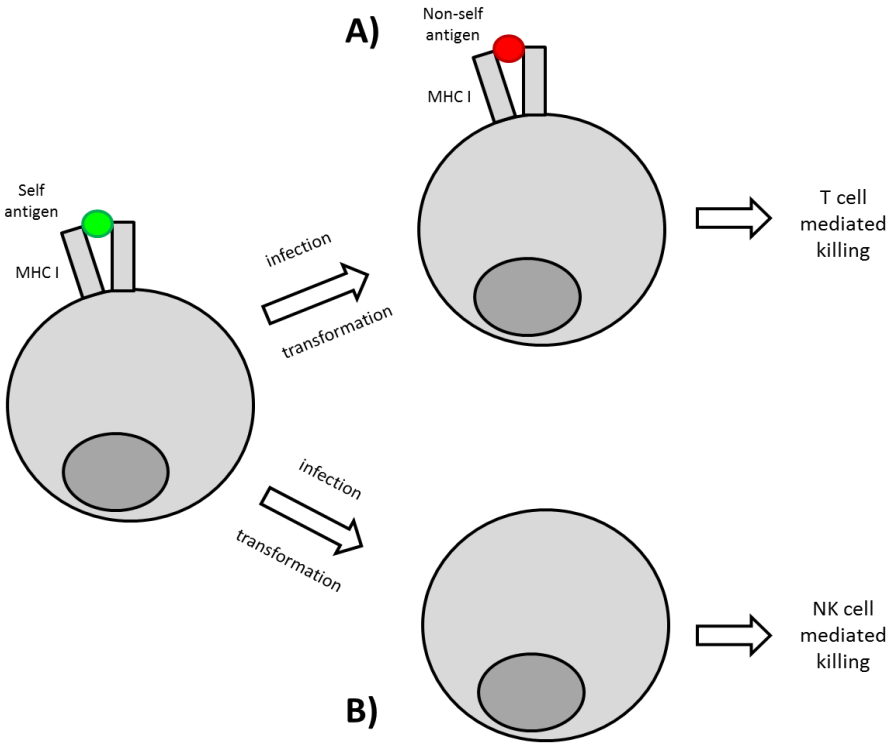

Figure 5: Schematic presentation of incomplete missing „self“ hypothesis.

Healthy cell expresses a self-antigen (green) via MHC class I. Due to transformation or infection A) a non-self-antigen is expressed leading to T cell recognition and killing or B) to loss of MHC class I expression. It prevents T cell recognition and cytotoxicity, however, causes NK cell activation and killing.

It was shown that mice completely lacking MHC Ia due to mutations in e.g. β 2-microtubulin possess normal amounts of NK cells. However, those NK cells have a high self-tolerance towards surrounding cells missing MHC Ia. This increased tolerance is also referred to as hypo-responsiveness [33]. Additionally, evidence was brought up that even NK cells completely lacking inhibiting receptor expression exist. B6 mice are known to encode for three different functional inhibiting receptors (Ly49I, Ly49C [37] and NKG2A [38]) [33]. Therefore, NK cells in this mouse model can express between zero and three different inhibiting receptors. About 85 % will express at least one of the three, indicating that residual 15 % of total NK cell population should completely lack NK cell inhibiting receptor expression. Analysis of this small subpopulation exhibited that these NK cells show a mature phenotype and normal expression levels of activating receptors [33]. Like NK cells derived from MHC class Ia deficient mice, NK cells lacking inhibiting receptor expression show higher

self-tolerance and eradicate tumour cells less effective than NK cell populations expressing inhibiting receptors. Thus inhibiting receptor missing NK cells seem to be in a hypo-responsive state [33, 39]. In order to explain those findings different models were discussed to explain NK cell education mechanisms leading to altered responsiveness. They all have in common that MHC class I molecules are crucial for NK cell education. However, different modes of interaction are discussed [33].

3.1.4.1.1. "Disarming" Model

It postulates that NK cells are by default highly responsive. Surrounding cells express normal levels of NK cell activating receptor ligands and low levels of NK cell inhibitory receptor ligands. Therefore, signalling triggered by activating receptors constantly overrules signalling of inhibiting receptors. This persistent stimulus shifts NK cells towards a hypo-responsive state to prevent constitutive NK cell activation and target cell lysis [33].

3.1.4.1.2. "Arming" Model

Under default conditions NK cells are in a hypo-responsive state. To increase their responsiveness, interactions with NK cell activating receptor ligands are necessary. Hypo-responsive NK cells are often considered as immature. However, with regard to their surface marker expression, no correlation was seen [33, 40]. They do show typical NK cell surface marker expression [39]. Additionally it is possible to shift responsive (mature) NK cells into a hypo-responsive state [33].

3.1.4.1.3. Tuning Model

Responsiveness of NK cells depend on their expression levels of activating and inhibiting receptors. Additionally, NK cell receptor's affinity towards MHC class I molecules and MHC class I expression levels of surrounding target cells are important. As a consequence, each NK cell obtains individual stimulation from their surface receptors. Activating and inhibiting interactions cause both downstream signalling inside NK cells, leading to individual net stimulations. High net stimulation shifts NK cells towards hypo-responsiveness while low or no net stimulation causes high responsiveness [33].

3.1.4.2. Natural Killer Cell Inhibiting Receptors (NKIRs)

Healthy cells express human leukocyte antigen class 1 (HLA-1). HLA-1 serves as a ligand for killer cell lectin-like receptors (KLRs) and inhibitory killer cell immunoglobulin-like receptors

(KIRs). Those interactions cause downstream signalling inside NK cells via immunoreceptor tyrosine-based inhibitory motifs (ITIMs). It results in prevention of NK cell activation. The most prominent one is NKG2A [41, 42].

3.1.4.3. Natural Killer Cell Activating Receptors (NKARs)

NK cell activating receptors is an umbrella term for a verity of different receptors. The majority is not NK cell specific but expressed by other immune cells (mainly T-cells) as well [43]. If a target cell is infected, faces cellular stress or is transformed, it starts up-regulating activating receptor ligands or reduces inhibitory ligand expression. The signalling inside NK cells is shifted towards activation. It results in target cell clearance by secretion of perforins, interferon γ (*IFNG*) and granzymes or by directly interacting with target cells. Thereby extrinsic apoptosis pathways are triggered inside target cells. Depending on the activated receptor different signalling cascades are stimulated [43]. One distinguishes between immunoreceptor tyrosine-based activation motifs (ITAM)-dependent and ITAM-independent signalling cascades upon NKAR activation [44, 45]. Involved signalling cascades partially influence the outcome - at least in murine systems: ITAM-dependent pathways have the ability to cause both main functions – cytotoxicity and cytokine secretion, while ITAM-independent ones may only cause cytotoxicity [42, 46].

3.1.4.3.1. Natural Cytotoxicity Receptors (NCRs)

Natural cytotoxicity receptors are one NK cell specific class of NKARs [42]. The human genome encodes for three different NCRs (i) NKp46 (*NCR1*), (ii) NKp44 (*NCR2*) and (iii) NKp30 (*NCR3*), while the murine one only encodes one: NCR1 which is the homologue of NKp46 [47, 48]. NKp44 is only expressed upon activation of circulating NK cells, while expression is *constant* in some subtypes of organ-specific NK cells [42].

Natural cytotoxicity receptors are essential for recognition and clearance of transformed or virally infected cells [49]. Interaction of NCRs and their ligands leads to a strong NK cell activation and cytotoxicity [50]. The more NCR subtypes are involved, the stronger the response is [42]. All three induce signalling pathways via ITAMs. As a consequence, NCR activation can cause both cytotoxicity and cytokine production [42, 46]. Even though the three receptors belong to one family they do have specialised functions. NKp46 for example is thought to play a major role in controlling metastasis [42]. However as only few NCR

ligands are elucidated, receiving a more detailed understanding of the similarities and differences between the three receptors is difficult.

One known co-ligand of all three NCRs is the family of heparan sulfate gylcoproteins (HSPGs). HSPGs are glycoproteins found on mammalian cells surface or in the ECM [51]. Each natural cytotoxicity receptor recognises different epitopes of heparan sulfate (HS) on HSPGs. However, the underlying mode of interaction is the same in all three cases: NCRs possess a positively charged binding pocket which allows interactions with negatively charged HSPGs. The ligand themselves on tumour cells remain unclear so far [42].

3.1.4.4. Balance Between Activating and Inhibiting Signals Regulates NK Cell Activity

Whether NK cells attack target cells or not depend on the present cross-talk between them. NK cell's cytotoxic potential is regulated by activating and inhibiting receptors expressed on their surface (**Figure 6**) [31]. Target cells express corresponding ligands. Due to this interaction downstream signalling is activated in NK cells. Target cell's destiny is depending on which signal cascade in NK cells overrules the other one [29, 41, 42, 52]. Additionally, NK cells bear regulatory functions. By secretion of cytokines they have the ability to regulate functions of other immune cells. It is known that NK cells modulate dendritic cell's function and thereby trigger an adaptive immune response [29]. It was shown that NK cells themselves have a kind of memory as well [42, 53].

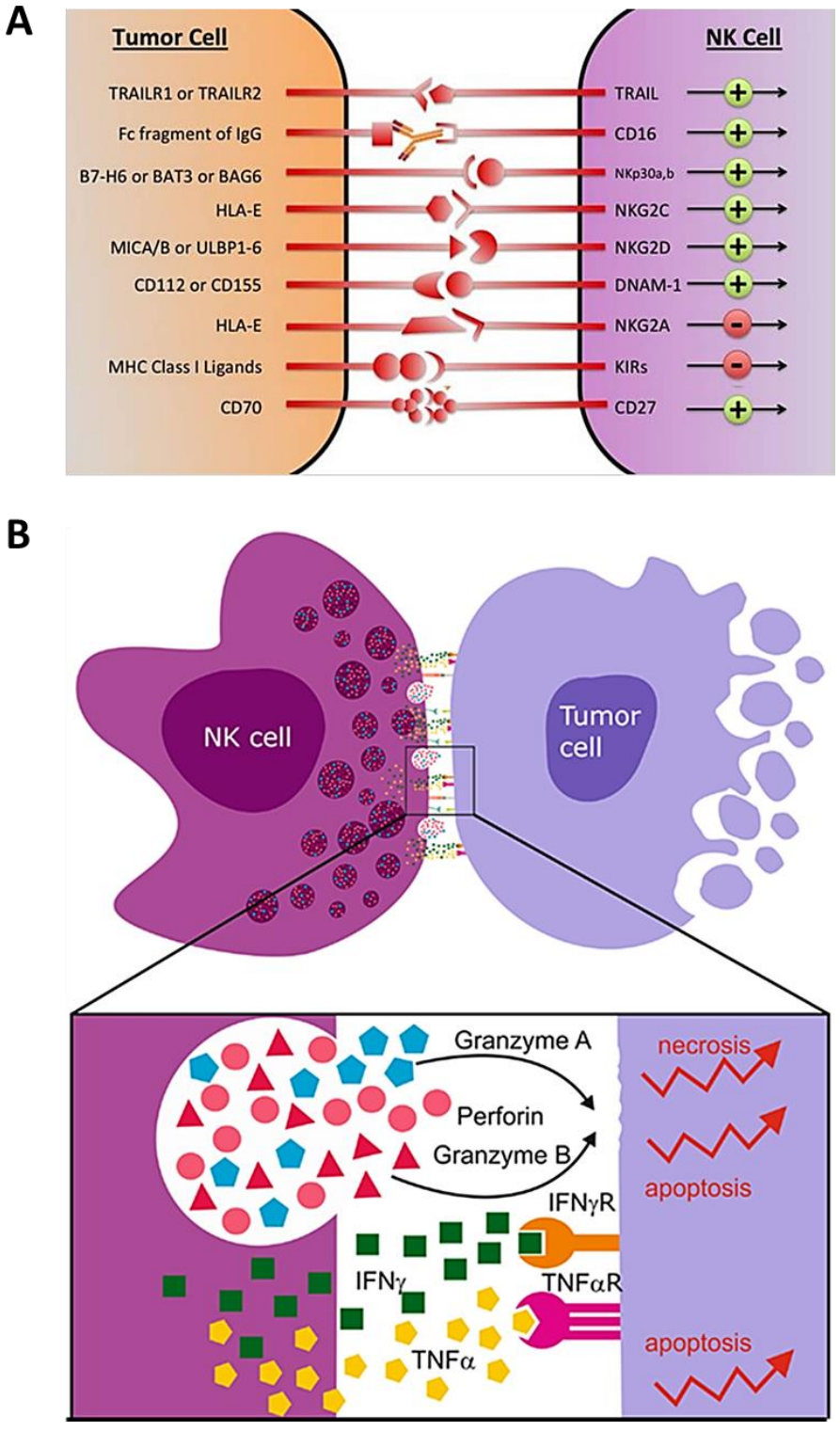

Figure 6: Cell - cell interactions between NK cells and tumour cells (A). Release of cytotoxic and immunostimmulatory molecules by NK cells and their effects on tumour cells (B) .

A) Modified from: Chester *et al.*, 2015 [31]

B) Modified from: Navarro *et al.*, 2015 [30]

3.2. Tumour Escape Mechanisms from Immune Cell-mediated Killing

Due to genetic and epigenetic alterations tumour cells access various possibilities to escape the body's immune response including NK cell-mediated killing (**Figure 7**) [41]. These mechanisms are either directly executed by malignant cells themselves or by reprogrammed genetically stable cells present in the TME [41].

Tumour cells tend to down regulate NKARs ligands and up-regulate NKIRs ligands, thereby favouring an inhibiting signalling inside NK cells [54, 55]. Furthermore, they down regulate surface death receptors like *TNF* receptors including *FAS* [41, 56]. By reducing their expression malignant cells prevent apoptosis triggered by NK cells binding [41]. Cancerous cells are also thought to gain the potential to produce soluble versions of NKARs ligands, thereby redirecting NK cells cytotoxicity [41, 57, 58]. Another important aspect is the altered secretory profile of tumour cells, which dramatically interferes with (immune) cells present in the TME. On the one hand malignant cells secret low levels of immunostimulatory cytokines and chemokines like interleukin 15 (IL15) or type 1 interferons (IFNs) [41, 59, 60]. On the other hand, large amounts of immunosuppressive factors including TGFβ or IL10 are released [41]. Elevated levels of immunosuppressive molecules do not only directly influence NK cells cytotoxic potential negatively, but also recruit additional immune cells like regulatory T cells (T_{regs}). T_{regs} have the potential to further negatively influence NK cell activity [41, 61]. Another cell type that is involved in tumour escape via several mechanisms are platelets [62]. They produce TGFβ [63]. Additionally, they have the ability to physically shelter malignant cells from NK cells binding and produce a pseudo-self-status by transferring MHC class I onto tumour cells [41, 64]. Another molecular feature is hypoxia and/or inflammation of the tumour and its stroma. Hypoxia induced factor 1α (*HIF1A*) alters gene expression leading to development of an even more immunosuppressive status [65]. On top of that hypoxia causes release of exosomes containing TGFβ and induces autophagy in malignant cells. As a consequence, autophagy increases cancer cell´s tolerance towards granzymes secreted by NK cells to trigger lysis of target cells [41].

Studies showed that patients suffering from cancer possess NK cells with reduced expression levels of NKARs in comparison to healthy individuals [41]. This may be explained by the permanently ongoing crosstalk between tumour cells, TME and recruited NK cells.

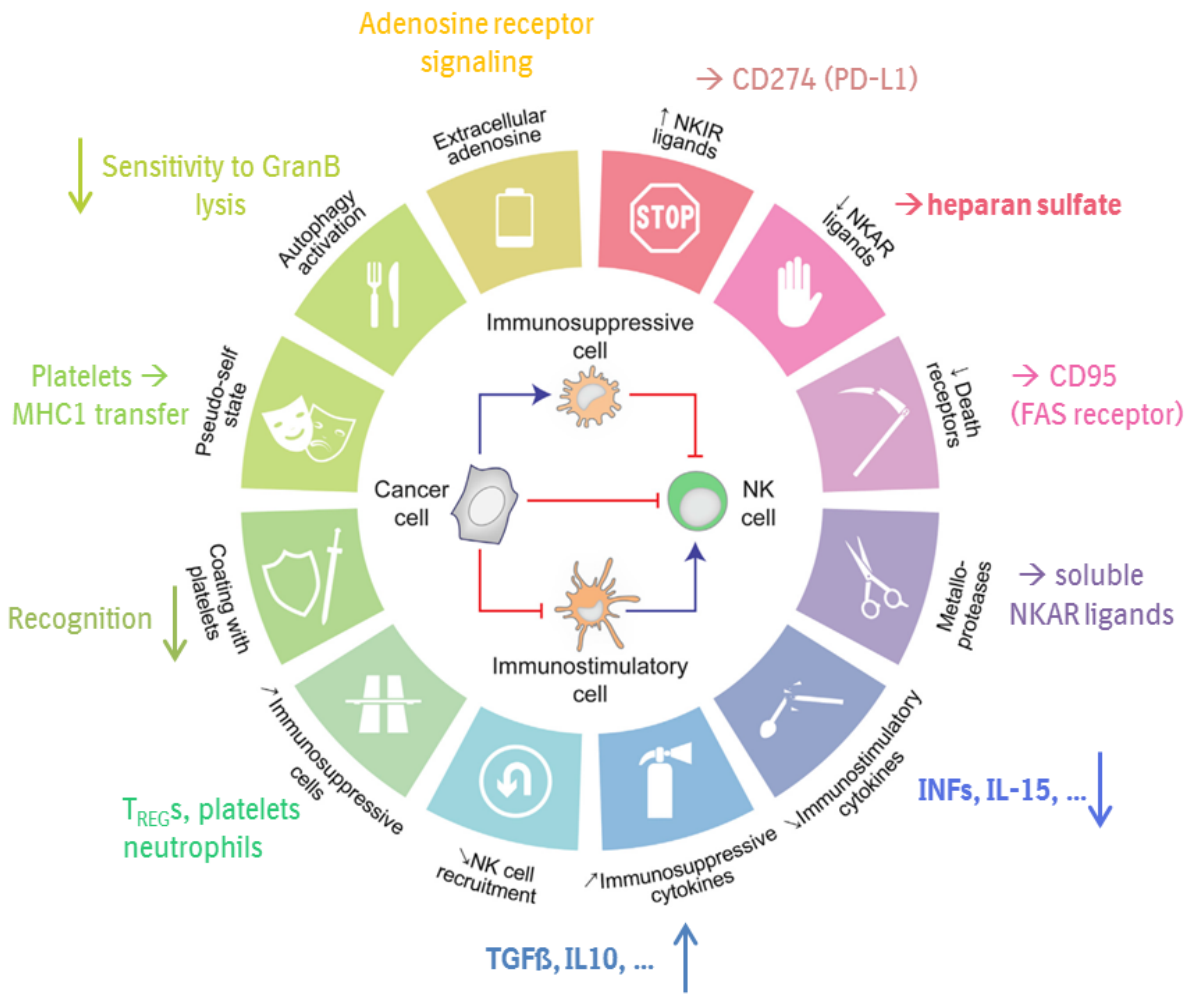

Figure 7: Tumour escape mechanisms from immune cell - mediated killing.

Mechanisms of importance for this thesis are highlighted in bold.

Modified from Lopez-Soto, Gonzalez *et al*. 2017 [41]

3.3. Bromodomain PhD Finger Transcription Factor (*BPTF*) Regulates NK Cell Activating Receptor (Co -) Ligand Expression

3.3.1. Bromodomain PhD Finger Transcription Factor (*BPTF*)

It is the largest subunit of nucleosome remodelling factor (NURF). NURF belongs to the ISWI family of remodelling complexes [66, 67]. NURF's ATPase subunit is *SMARCA1* (SNF2L) [68-70]. Additionally it contains WD-repeat domain proteins (*RBBP7* (retinoblastoma-binding protein p46) / *RBBP4* (retinoblastoma-binding protein p48). They may be involved in targeting NURF to chromatin, as *RBBP4* is known to directly interact with histone 4 (H4)[12] [69].

BPTF is essential for formation of NURF and not present in any other remodelling complex [68]. It is comprised of 810 amino acids leading to a molecular weight of roughly 320kDa[3]. It contains six different domains (**Figure 8**) [66]. The high mobility group box A (HMGA) contains AT-hooks and an acidic part, which is thought to interact with nucleosomes [69]. AT-hooks in general are known to interact with the DNA minor groove, if the sequence is AT-rich [69]. The DDT domain (name by DNA-binding homeobox- containing proteins and the different transcription and chromatin remodelling factors in which it is found) may be necessary for interaction with the ATPase [69] and is claimed to possess DNA-binding properties [71]. So far the disordered glutamate-rich (Q-rich) domain has not been described in more detail [69]. The bormodomain-proximal PHD finger (PHD2) and the bromodomain itself are essential for interacting with modified histones [67, 69].

[1] (https://www.genecards.org/cgi-bin/carddisp. pl?gene =RBBP7
[2] https://www.genecards.org/cgi-bin/carddisp.pl?gene=RBBP4, 31.03.2019
[3] https://www.ncbi.nlm.nih.gov/gene/2186, 03.07.2018

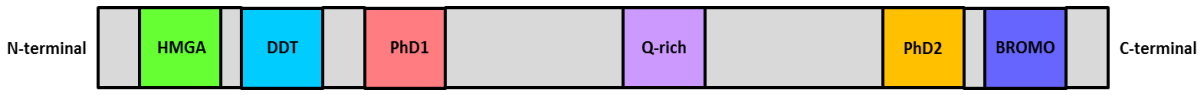

Figure 8: *BPTF* and its domains.

High mobility group box A (HMGA), DNA-binding homeodomain and different transcription factors domain (DDT), plant-homeodomain (PHD) finger domain 1 and 2, Q-rich domain and bromodomain (BROMO)

Figure drawn by author.

BPTF selectively binds histone 3 trimethylated lysins at position 4 (H3K4me3) (**Figure 9**). Trimethylation or lysine 4 of histone 3 in 5' regions of genes is a typical marker for transcriptional activity [66]. Binding is usually enabled by the bromodomain-proximal PHD-finger domain. Due to the chemical and structural properties of the binding pocket only H3K4me3 is bound efficiently. The pocket is divided into two parts: "K4me3-cage" and R2 binding pocket. For optimal fit lysine and arginine need to be separated by one residue (T3 in histone 3). Other methylated lysine residues are directly positioned after an arginine lacking a "spacer" amino acid and therefore do not fit in the divided pocket. "K4me3-cage" is comprised of four amino acids (Y10, Y17, Y23, W32) participating in the interaction with K4me3. For optimal interaction presence of three methyl-groups is necessary [66, 72].

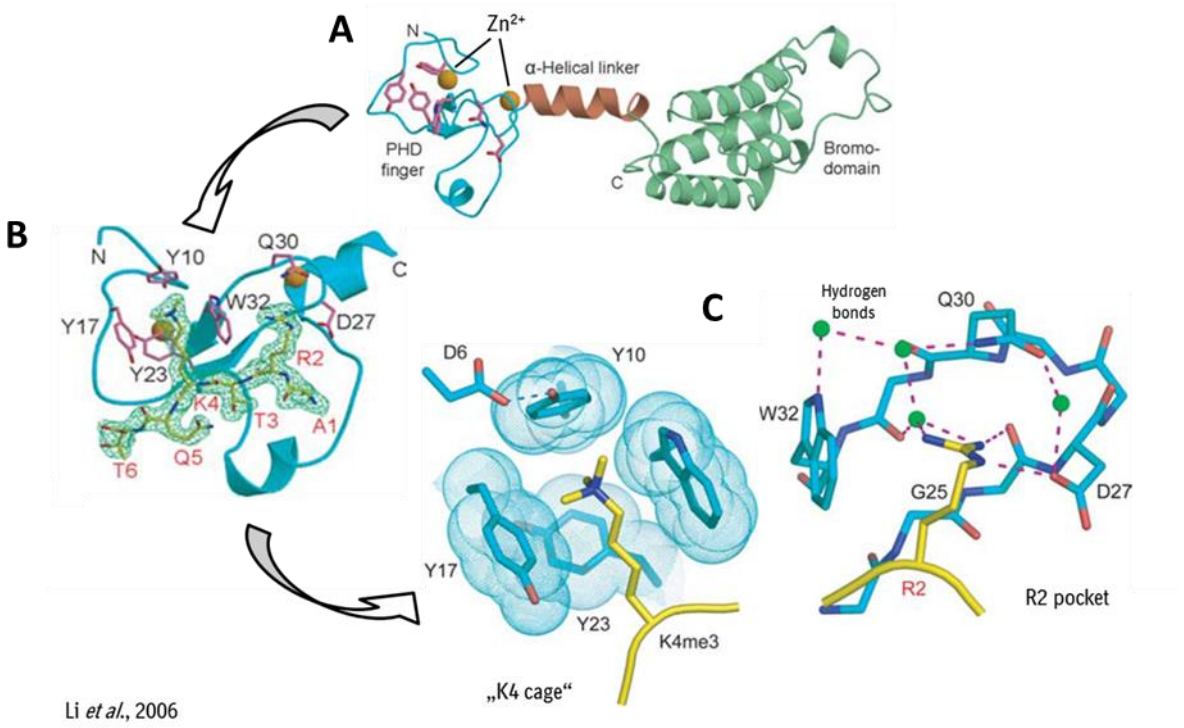

Figure 9: Crystal structure of PhD finger domain 2 (blue), linker (orange) and following bromodomain (green) of *BPTF* (A).

PhD finger domain selectively binds H3K4me3. High specificity is a consequence of the structure of the present binding pocket (B): For optimal fit K and R need to be separated by one „spacer“ (T), as the binding pocket is divided into a „K4 cage“ and R2 pocket (C). Other tri-methylated K-residues in histone 3 are located directly after an R.

Modified from Li *et al*. 2006 [66]

In vitro binding experiments identified interactions between with acetylated H4K12, H4K16 and H4K20 and *BPTF*s bromodomain [67]. Interestingly, if H4K12, H4K16 or H4K20 acetylation is combined with H3K4me3, binding of H4K16ac is favoured. Another observation is that crystal structures of the bromodomain - in complex with either H4K12ac or H4K16ac - revealed different H4K16ac peptide orientations, while the structure of the bromodomain was almost identical in both cases. This was not seen for H3K12ac. Whether or not this is important for H4K16ac selectivity needs to be determined by further analysis. Additional possible mechanisms explaining H4K16ac preference remains to be elucidated [67].

A summary of the interaction of *BPTF*s bromodomain-proximal PHD-finger and the bromodomain with histone tails are shown below (**Figure 10**). For successful targeting of

NURF to chromatin interactions of the PHD finger and the bromodomain with the corresponding histone tails are necessary [67].

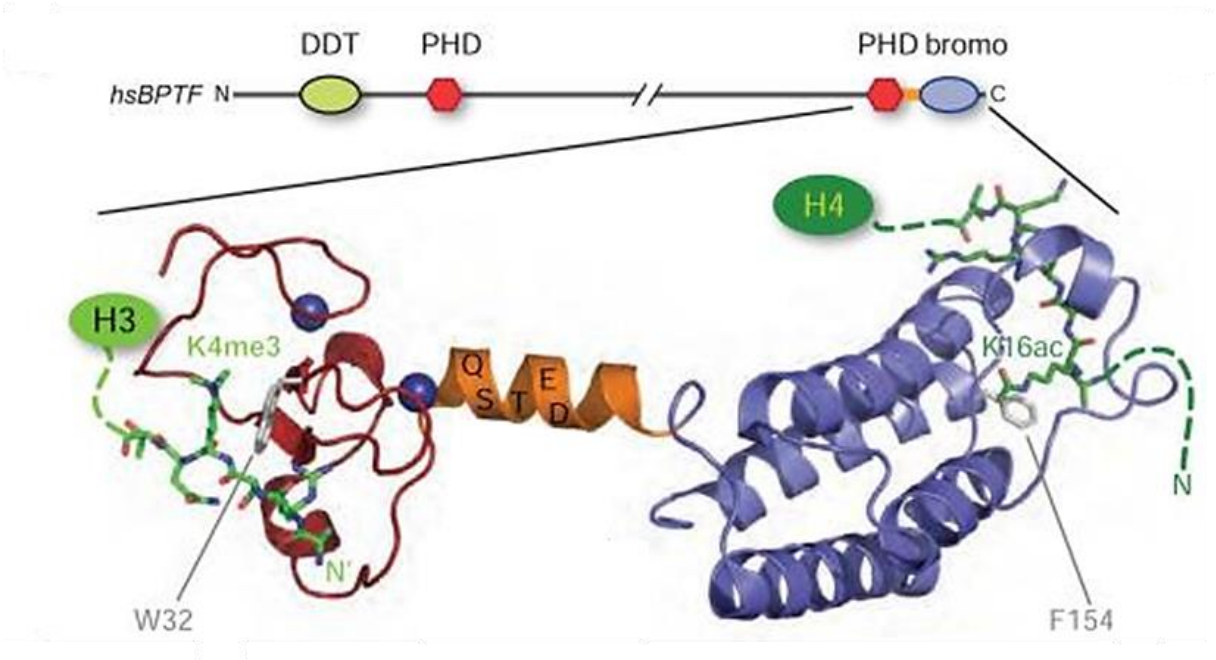

Figure 10: *BPTF*'s PHD-finger domain (red) and bormodomain (purple) interacting with histone tails. The a-helix (orange) represents the linker domain.

Modified from: Ruthenburg *et al.*, 2011 [67]

3.3.2. *BPTF* Knock Down Reduces Tumour Weights in Immunocompetent BALB/c Mice

Mayes and colleagues showed that shRNA-mediated *BPTF* knock down (KD) leads to reduction of tumour weights in a murine immunocompetent BALB/c model (**Figure 11A**) [68]. However, no differences - regarding tumour weights - were observed when the same experiments were redone in immune-deficient NOD/SCID, Ifrg2r$^{-/-}$ (NSG) mice (**Figure 11B**) [68]. These results suggest that reduction is not directly caused by reducing the tumour cell´s viability or proliferation rate due to absence of a functional NURF complex, but by increasing tumour's immunogenicity [68]. It may cause immune cell activation followed by tumour clearance.

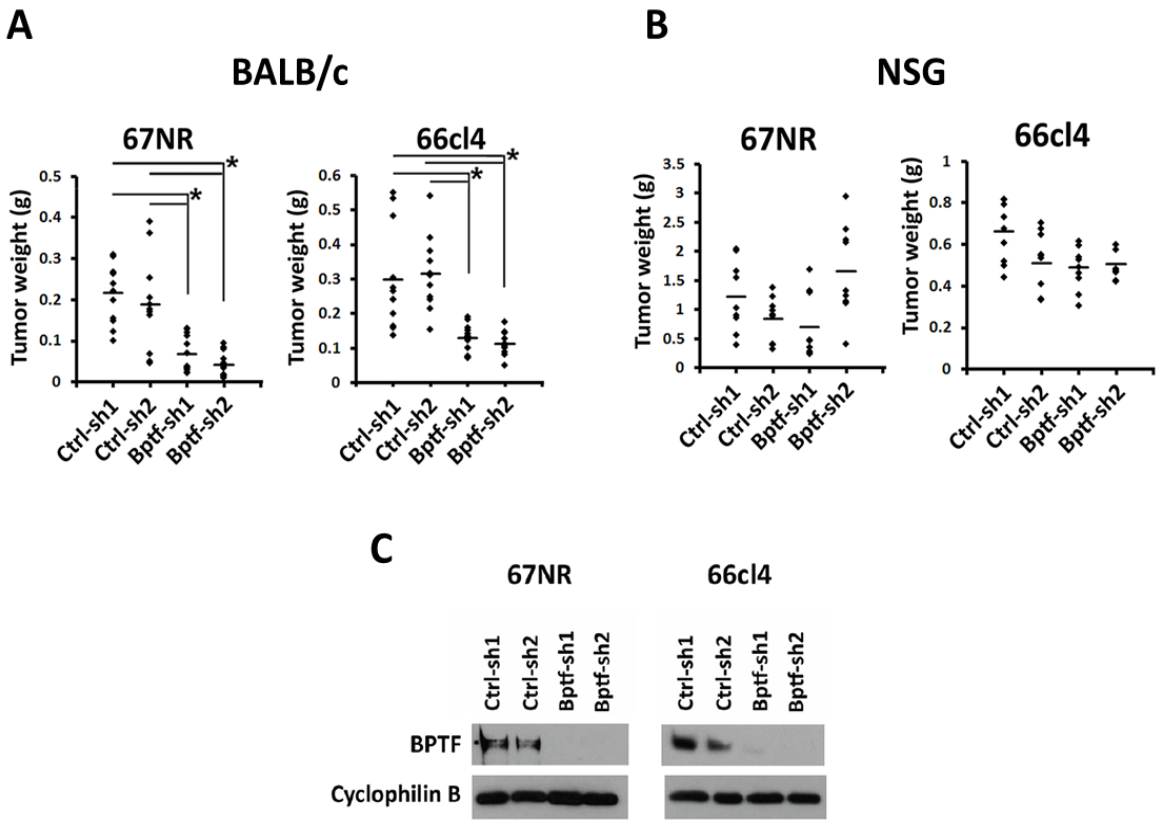

Figure 11: Effects of *BPTF* KD on tumour weight in immunocompetent and immune-deficient mice.

BPTF knock down (KD) reduced tumour weights in (A) immunocompetent BALB/c mice after 3 to 4 weeks, however, lacks a phenotype in (B) immune-deficient NOD/SCID, Ifrg2r-/- (NSG) mice. *BPTF* KD was confirmed by Western blotting (C). 67NR and 66cl4 are two mouse breast cancer cell lines, which were transplanted into the mammary fat pad.

Modified from: Mayes *et al*., 2017 [68]

3.3.3. Possible Mechanisms of *BPTF*-induced Tumour Immune Escape

Above described data suggests that NURF complex is one epigenetic regulator utilized from tumour cells during progression to escape from the immune system. Potentially underlying biological mechanisms are described below.

3.3.3.1. NURF-mediated Heparanase Expression Leads to Reduced NCR-co-ligand Expression – Hypothesis 1

In the presence of *BPTF*, a functional NURF complex is formed. NURF binds regulatory regions of *HPSE* gene. *HPSE* encodes for heparanase, which removes heparan sulfates (HSs)

from heparan sulfate proteoglycans (HSPGs) present on cells surface. NURF may induce heparanase expression, which is subsequently secreted and removes HSs [68]. As discussed above, heparan sulfates are known natural cytotoxicity receptor co-ligands [42]. Thus, NURF activity positively influences tumour immune escape [68].

By knocking down *BPTF*, formation of a functional NURF complex is prevented. As a consequence, *BPTF* cannot bind to regulatory regions of *HPSE*. HSs are present on cells surface and serve as co-ligands for NCRs [42, 68]. However, this particular interaction of tumour cells and NK cells seem to be necessary to push NK cells signalling from "not killing" towards "killing". As a consequence, NK cells become activated and are ready to destroy malignant cells using their cytotoxic repertoire (**Figure 12**).

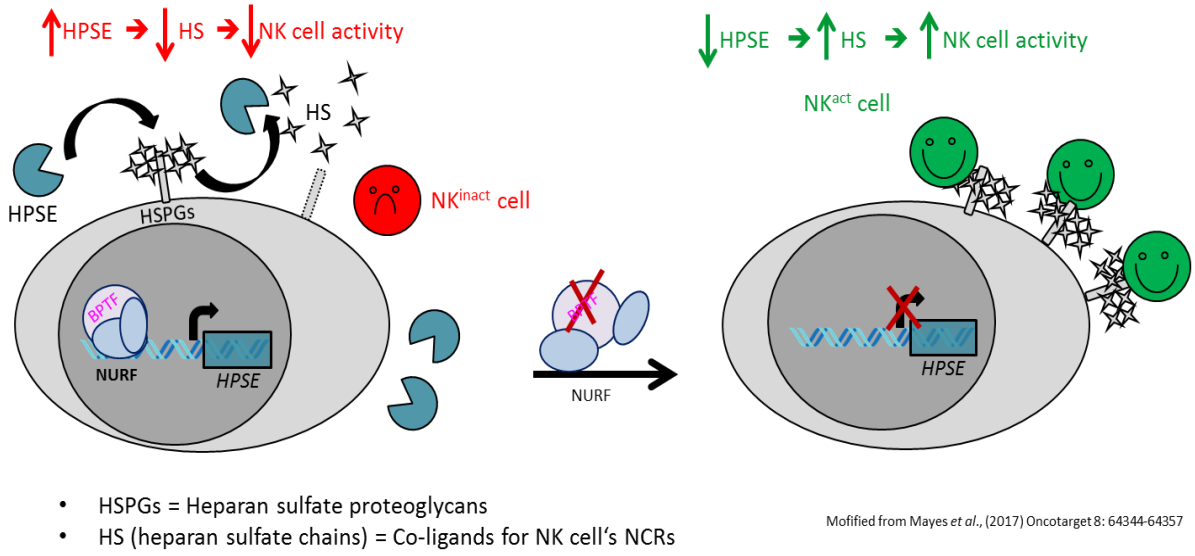

Figure 12: Hypothesis 1 - *BPTF* KD increases the recognition of tumour cells by NK cells.

In presence of *BPTF* NURF is formed. Heparanse expression is triggered by *HPSE* transcription. Heparanase is secreted and removes heparan sulfates from heparan sulfate proteoglycans (HSPGs). NK cell activation depends on the presence of HSs as NCR co-ligands. In their absence NK cells cannot bind and remain inactive.
By knocking down *BPTF* NURF cannot be formed. *HPSE* is not transcribed. Thus, HSs are present at the cell surface and NK cells are able to bind. Binding leads to NK cell activation and subsequently to tumour cell killing.

Figure drawn by author based on Mayes *et al.*, 2017 [68]

3.3.3.2. NURF Expression Indirectly Influences Peptides Presented via MHC Molecules – Hypothesis 2

NURF formation - in the presence of BPTF - prevents expression of *PSMB8*, *PSMB9, TAP1* and *TAP2* (**Figure 13**) [73]. *PSMB8* and *PSMB9* encode for proteasome subunit beta 8 and 9. Both proteins are subunits necessary for generation of the immunoproteasome. Its function is processing of peptides presented via MHC class I[4,5]. Elevated *PSMB8* and *PSMB9* expression leads to higher immunoproteasome activity, which furthermore leads to increased production of antigenic peptides. These peptides are highly affine towards MHC complexes and T cell receptors (TCRs) [73].

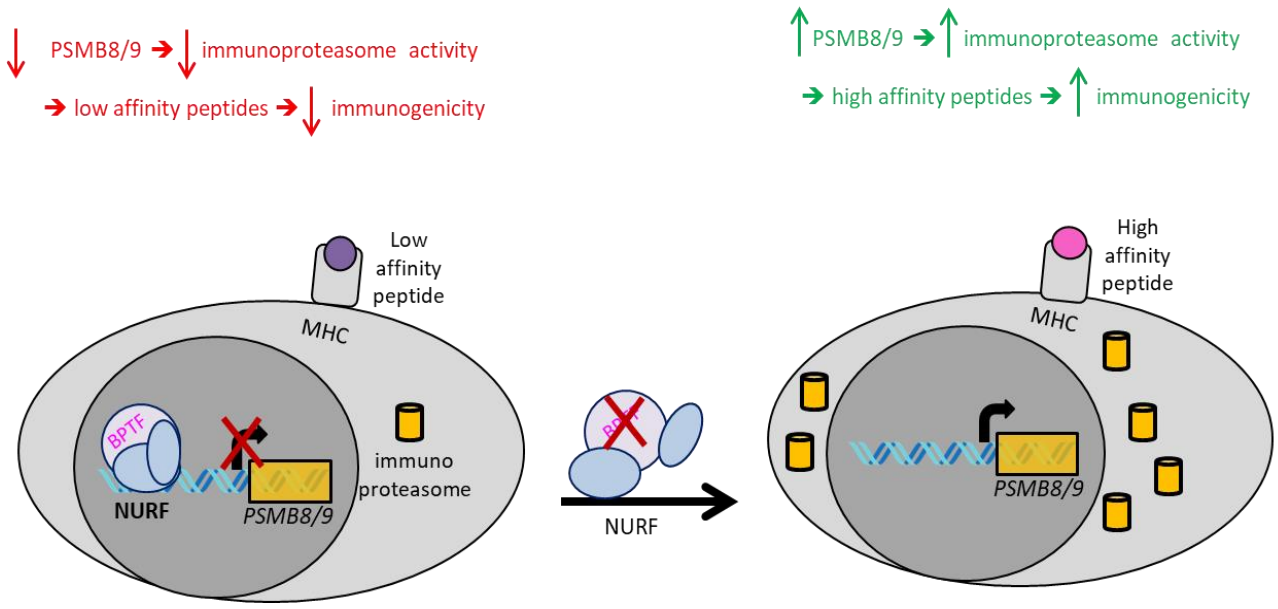

Figure 13: ~~H~~ypothesis 2: NURF (indirectly) regulates peptide presentation via MHC complexes.

Presence of NURF prevents *PSMB8 & PSMB9* expression, which leads to low activity of immunoproteasomes (orange). Due to reduced activity low affinity peptides (purple) are inserted into MHC complexes. Thus the tumour cell´s immunogenicity is reduced.

In absence of NURF *PSMB8 &PSMB9* are expressed, causing an increase in immunoproteasome activity. Thus high affinity peptides (pink) are generated and presented via MHC complexes.

Figure drawn by author based on Mayes *et al.,* 2016 [73]

[4] https://www.ncbi.nlm.nih.gov/gene/5696, 07.08.2018
[5] https://www.ncbi.nlm.nih.gov/gene/5698, 07.08.2018

TAP1 and *TAP2* encode for transporter 1 and 2, ATP binding cassette subfamily B member. These proteins transport degraded cytosolic peptides from the cytosol into the endoplasmatic reticulum (ER)[6,7]. High *TAP1* and *TAP2* expression decides which peptides are imported into the ER. Peptides imported are coupled with MHC complexes inside the endoplasmatic reticulum [73]. Thus, *PSMB*s and TAPs have the ability to alter the immunogenicity of tumour cells. As these genes are negatively regulated by NURF, their inhibition via *BPTF* KD and/or pharmacologic inhibition have the potential to restore immune cells activity towards tumours.

3.3.3.3. Critical Issues Concerning Hypothesis 1 and 2

As only two topic-related publications are released so far, a detailed understanding of the mechanistic network(s) behind is missing. Additionally, heparan sulfates are only co-ligands, while NCR ligands - in this context - remain to be elucidated. As tumour escape mechanisms are complex and *BPTF*/NURF influences expression of various genes, deregulation of *HPSE* expression might be just one deregulated pathway out of many. There might exist additional causative molecular events for elevated tumour killing of *BPTF* KD cells. One event could be the repression of *PBSM8/9* and *TAP1/2* by NURF as their expression levels could be restored by NURF inhibition. So far, there is no evidence that distinct stimulatory molecules are induced or at least be modulated.

3.4. Three-dimensional (3D) *In Vitro* Models – Appropriate Tools to Address Complex Biological Questions

Under standard two-dimensional (2D) culture techniques cells are maintained on plastic surfaces as monolayers making fast analyses possible in a well-established system. Those approaches are easy to handle and results are obtained within short time. It allows treatments 24 hours after seeding, as it is possible to seed a large number of cells [74]. It is frequently used for high throughput screens for small chemical entity testing. However, on the one hand these screens can lead to hits which can't be reproduced *in vivo* and on the

[6] https://www.ncbi.nlm.nih.gov/gene/6890, 07.08.2018
[7] https://www.ncbi. nlm.nih.gov/gene/6891, 07.08.2018

other hand some molecules might not cause an effect in a 2D approach but would do so in a 3D one. Two-dimensional cell culture systems do not mimic the native environment of cancer or normal tissues. Therefore, they do not recapitulate three-dimensional cell morphology [74]. Cells cultivated in 2D bare all the same environmental settings and thus differ significantly from the actual conditions in patients suffering from cancer. No oxygen or nutrient supply gradients are developed. Transcriptomes of two-dimensional versus three-dimensional cultured cells differ [74, 75]. To overcome these limitations novel culture models were developed. Three-dimensional structures can be partially recapitulated by 3D *in vitro* culture systems. Most importantly, cell-cell and – depending on the 3D approach – cell-matrix interactions are present. Nutrient and oxygen gradients towards centres of multicellular tumour spheroids (MCTSs) are developed (**Figure 16**). Due to those differences a variety of different transcriptional programs are activated. Examples are the specific up-regulation of *CYP* (cytochrome P450) enzymes involved in degradation/clearance of many small chemical therapeutics [75], the *MDR* gene [76, 77] involved in resistance or the change in the transcription factor activity [78], to name but a few. For instance, expression of *MDR* proteins is one explanation why potential 2D hits do not cause a response in 3D assays or *in vivo* systems. Another explanation would be that targets of a certain chemical entity might not be expressed under standard two-dimensional cultivation or *vice versa*. In 3D cultures FBs exhibit a characteristic growth phenotype (fibroblastoid) and ECM secretion, which is not found when FBs are cultivated in 2D [74, 79].

3.4.1. Three-dimensional Floater Assay

3D floater assays are the most simple three-dimensional culture method. Tumour cells are seeded in ultra-low attachment plates. Due to special treatments of the plate´s surface, adherence of cells is prevented. Cells remain in suspension and are thereby forced to interact with each other. (Tumour) Cells are incubated until compact multicellular tumour spheroids (MCTSs) are formed. Floater assays can be easily handled and might represent an option to use for high through put screens instead of standard 2D approaches. Responses to treatments can be analyzed through measuring the size and morphology of the spheroids or by immunohistochemical evaluation before and after treatment. Determination of cancer cells viability is another option. However, floater models can also be used to address more complex questions like immune cell mediated tumour cell killing (**Figure 14**) [74, 79].

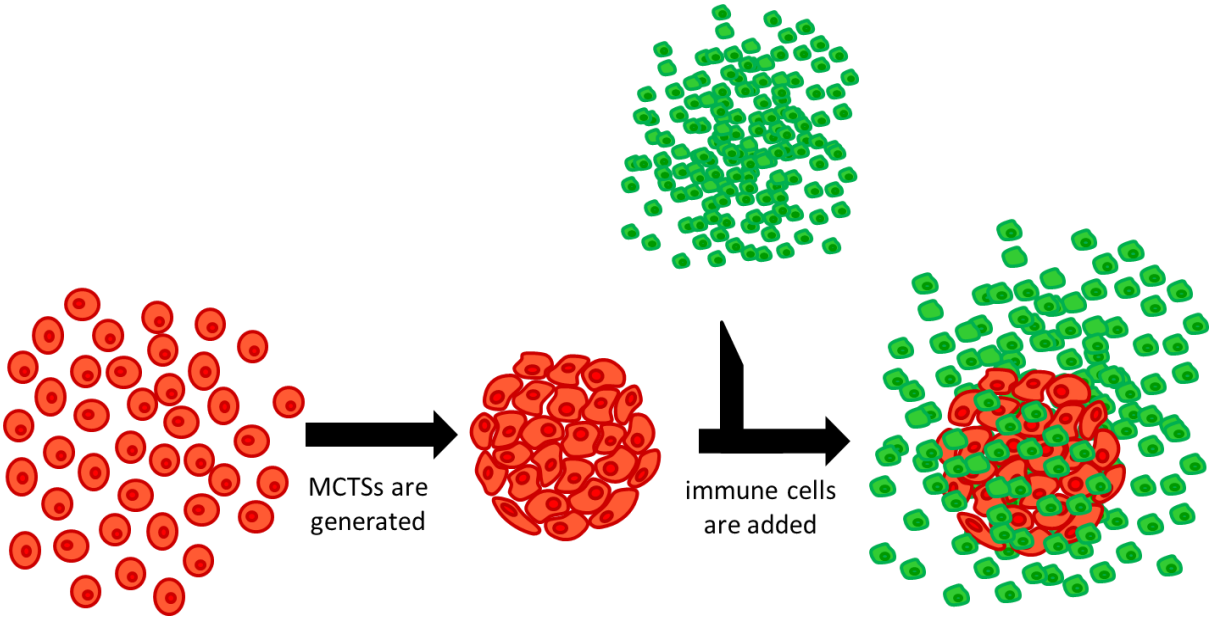

Figure 14: Generation of a 3D floater killing assay.

Tumour cells are seeded as mono-cultures and incubated in a U-shaped low attachment well until compact MCTSs are formed. Immune cells are added to each MCTS. Viability of tumour cells is monitored at least over 10 days.

Figure drawn by author.

3.4.2. Three-dimensional Embedded Assay

Tumour cells are embedded in a matrix. The permanent cell – matrix interaction ("crosstalk") recapitulates more faithfully the *in vivo* situation than any 2D cultivation method on plastic or coated surfaces. Commonly used matrices are Matrigel® or collagen type I. Matrigel® is composed of different ECM proteins including collagen type IV, laminin and perlecan/*HSPG2*. However, it should be kept in mind that the composition differs from batch to batch. For instance, lot variation seen for collagen type I may lead to reduced diversity of containing substances/proteins compared to Matrigel®. Both, Matrigel® and Collagen type I, are fluid, when stored at low temperatures (+4°C), but form a three-dimensional gel, when heated up to 37°C, since the containing proteins form aggregates. Independent of which matrix is used, interaction between cells and ECM strongly influences gene expression. Levels of noncoding microRNAs are increased compared to floater assays and might even reach tissue-like expression levels [80]. Thus, presence of a matrix, particularly in a 3D setting, strongly influences growth of cancerous and non-cancerous cells including cells derived from the

immune system [74, 81-85]. Cultivation on Matrigel® or collagen is also an appropriate alternative if cells do not grow well in suspension. Additionally, those models are well suited for studying cellular invasiveness [85, 86] or to test small chemical entities an *in vivo* like system with defined molecular characteristics [74, 79]. By adding additional cell types like fibroblast, endothelial or immune cells complexity is further increased (**Figure 15**). 3D *in vitro* models allow for studying molecular mechanisms others than tumour, stromal cell and immune cell interactions [74]. Embedded approaches can be analysed via confocal live cell fluorescence microscopy, histological analysis, biochemical examination and functional experiments to name but a few options [74].

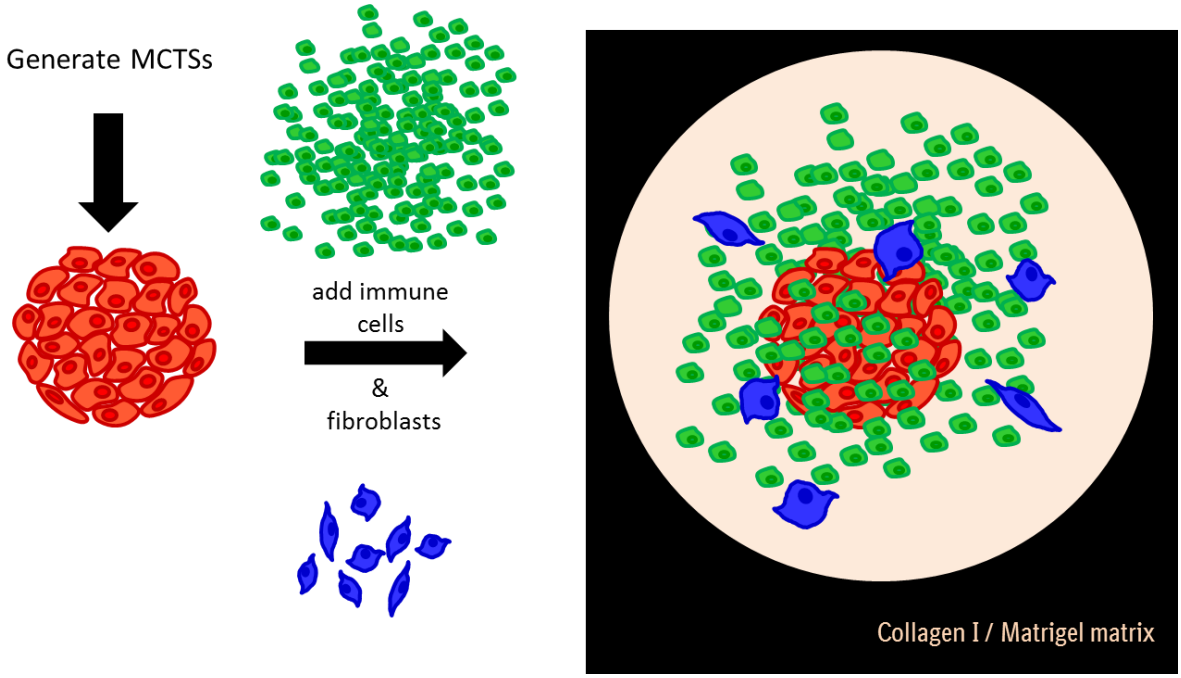

Figure 15: Establishment of 3D embedded culture models.

Tumour cells are seeded as mono-cultures and incubated until compact MCTSs are formed. Immune cells and fibroblasts are re-suspended in a collagen I / Matrigel mixture. Suspension is used to cover MCTSs.

Figure drawn by author.

2D cultures 3D models can be used for drug target identification, validation and small chemical entity testing. In contrast to two-dimensional models and floater assays, genes involved tumour - stroma interaction can be identified in embedded co-culture models [74]

whereas both floater and embedded cultures can be used to identify genes modulating immune response [74, 79].

One limitation of 3D cultures is their size as regions well supplied through diffusion are short. Subsequently, this leads to malnutrition, hypoxia and necrosis in the core of MCTSs with a diameter greater than 200 µm (**Figure 16**). Therefore, to ensure sufficient nutrition and oxygen supply larger aggregates rely on presence of blood vessels. Recently, Wang and colleagues succeeded in a near-physiological microenvironment simulation (including vessel formation) on chip to evaluate drug resistance of different loci in tumour mass [87]. Finally, 3D assays are more time consuming and might cause technical challenges compared to easy to handle but non-physiologic standard 2D culture techniques [74, 79].

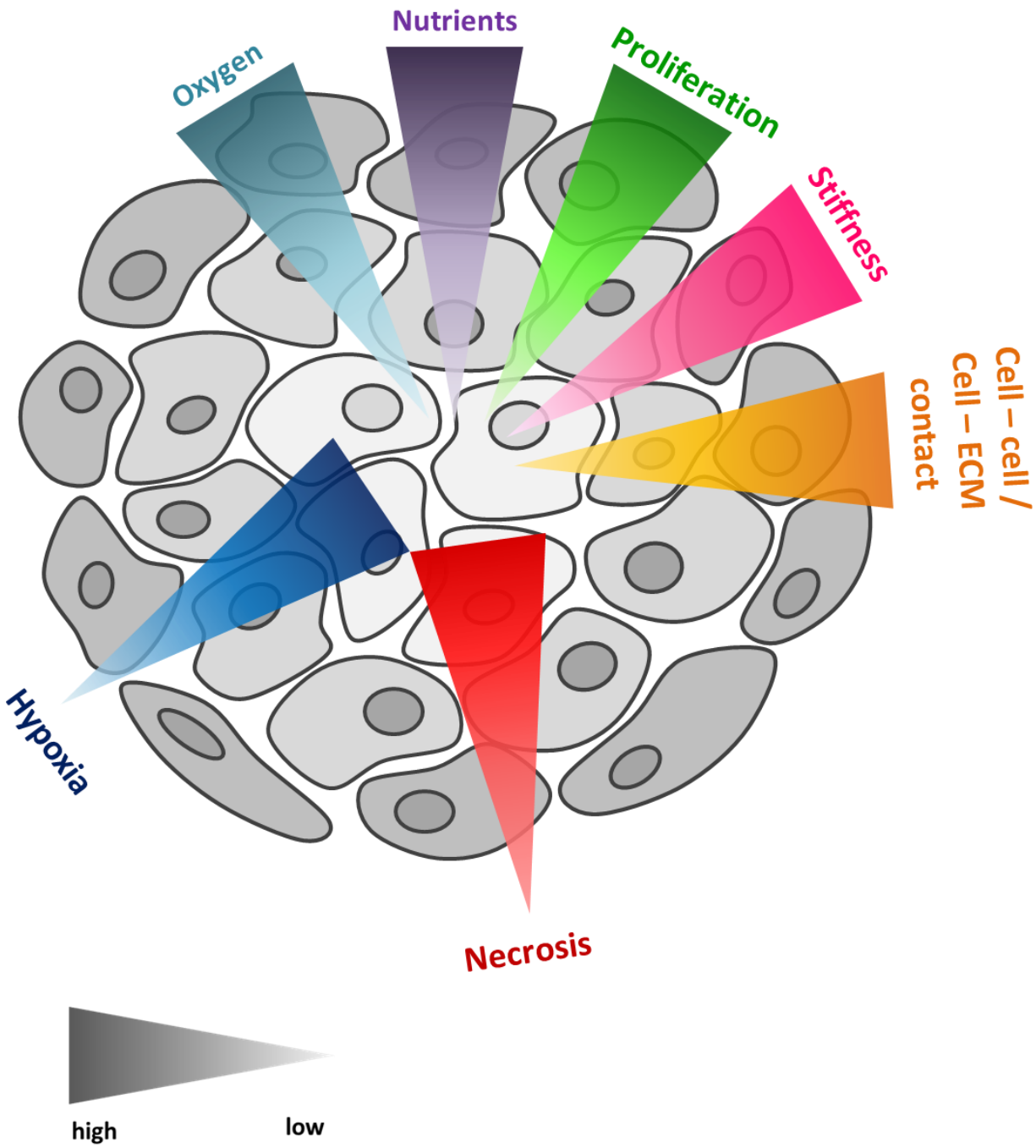

Figure 16: In three-dimensional (3D) *in vitro* cultures various gradients are formed in spheroids reaching a size of 200µm including oxygen and nutrient gradients due to lack of blood vessels.

Figure drawn by author.

3.5. Aim

At present, the underlying molecular mechanisms modulating NK cell activity during tumour infiltration remains one of the major challenges that need to be tackled in the endeavour of fighting cancer. Hereinafter, it was of interest to gain further information on genes being directly or indirectly involved in this process. The main focus was laid on the pharmacologic as well as on the genetic inhibition of *BPTF*, a "**B**romodomain **P**HD Finger **T**ranscription **F**actor, the largest subunit of the NURF (nucleosome remodeling factor) complex that is necessary for the chromatin remodeling required for transcription. This complex catalyzes nucleosome sliding on DNA and interacts with sequence-specific transcription factors and was recently discussed as being potentially involved in T cell and NK cell activation.

To accomplish the objectives, robust complex three-dimensional *in vitro* models will be established, developed and optimized to analyse the molecular requirements of NK cell infiltration into multicellular tumour spheroids derived from non-small cell lung cancer (NSCLC) cell lines. In particular, it will be analysed whether *BPTF* inhibition in tumour cells does influence NK cell mediated cytotoxicity. Furthermore, it will be determined whether the EMT score of used NSCLC cell lines impacts on the outcome. For knock down (KD) of *BPTF* in tumour cells small interfering RNAs (siRNAs) and for knock out (KO) the CRISPR/Cas9-system will be applied. Both the influence of genetic as well as the pharmacologic inhibition on the NK cell infiltration/activation will be analysed in complex 3D models consisting of tumour, stromal (fibroblasts) and immune cells. The availability of a small chemical and specific *BPTF* inhibitor is of great advantage as it will allow comparing effects caused by pharmacological target inhibition with those due to genetic target inhibition. Ultimately, transcription profiling of all different treatment modalities will allow the identification of deregulated genes most likely involved in altering the tumour cell´s immunogenicity. Finally, the identification of those putative target genes will enable the formation of a more detailed hypothesis of how *BPTF* interacts with pathways in the tumour cell being involved in tumour immune escape

4. Material and Methods

4.1. Reagents

4.1.1. Buffers

4.1.1.1. Tris-buffered Saline, 0.1% Tween 20 (TBS-T)

Reagent	Volume [L]	Catalog Number	Company
Tris-buffered saline (TBS)	1	170-6435	Biorad
10% Tween 20	0.1	161-0781	Biorad
H_2O	8.9		
Final volume:	**10**		

4.1.1.2. MOPS ((3-N-morpholino)-propansulfonic acid) Running Buffer

Reagent	Volume [L]	Catalog Number	Company
20X XT MOPS	0.5	161-0788	Biorad
H_2O	9.5		
Final volume:	**10**		

4.1.1.3. HEPEX Lysis Buffer Complete

Reagent	Concentration Stock	Concentration Final	Dilution	Volume [mL]
Hepes pH 7.4	1 M	20 mM	1:50	20
NaCl	5 M	100 mM	1:50	20
EDTA pH 7.4	500 mM	5 mM	1:100	10
Na_3VO_4	200 mM	1 mM	1:200	5
NaF	500 mM	30 mM	1:16,67	60
Glycerol	100 %	5 %	1:20	50
SDS	10 %	0.1 %	1:100	10
Triton X-100	10 %	1 %	1:10	100
β-Glycerophosphate	1 M	1 mM	1:1000	1
DTT	1 M	1 mM	1:1000	1
H_2O				723
Final volume:				**1000**

4.1.2. Fluorophores

Fluorophore	Absorption Maximum	Emission Maximum	Localisation
mKate2[8]	588 nm	633 nm	Nucleus
dTomato[9]	554 nm	581 nm	Cytoplasm

Table 1: Used fluorophores

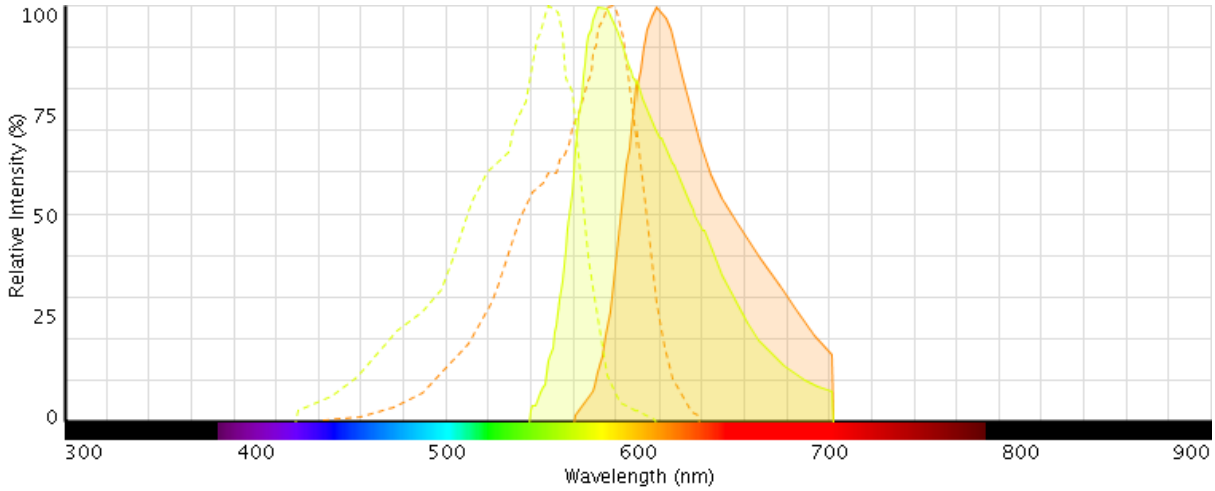

Figure 17: Absorption (dotted lines) and emission spectra (full lines) of dTomato (yellow) and mKate2 (orange).

X-Axis: Wavelength [nm]. Y-Axis: Relative intensity in percentage. Spectra were created using *Fluorescence Spectra Viewer* by *Thermofisher Scientific*.

Fluorescence dye	Absorption Maximum	Emission Maximum	Localization	Binding & Staining Mechanism
Cell Tracer CFSE [10]	494 nm	521nm	Cytoplasm	Cell Tracer CFSE diffuses into cells and binds covalently to intracellular amines. Due to the covalent binding of the fluorophore, it is passed from dividing cells to their daughter cells, allowing analysis over longer time and different generations.
Cell Tracer Blue CMAC (7-amino-4-chloro methylcoumarin)[11]	353 nm	466nm	Cytoplasm	It passes through cell membranes but is immobilised in the cytoplasm. Immobilisation occurs through

[8] Product data sheet IncuCyte NucLight Reagents
[9] http://www.fluorophores.tugraz.at/substance/1088, 12.07.2017
[10] Thermofisher Manual: CellTrace™ Cell Proliferation Kits by Invitrogen
[11] Thermofisher Manual: CellTracker™ Fluorescent Probes by Life Technologies

				a chemical reaction, performed by glutathione transferase catalysing a reaction between the chloromethyl group of the fluorophore and the thiol group of glutathione. It leads to a retained impermanent blue fluorescent dye of cells over three to four generations

Table 2: Used fluorescence dyes

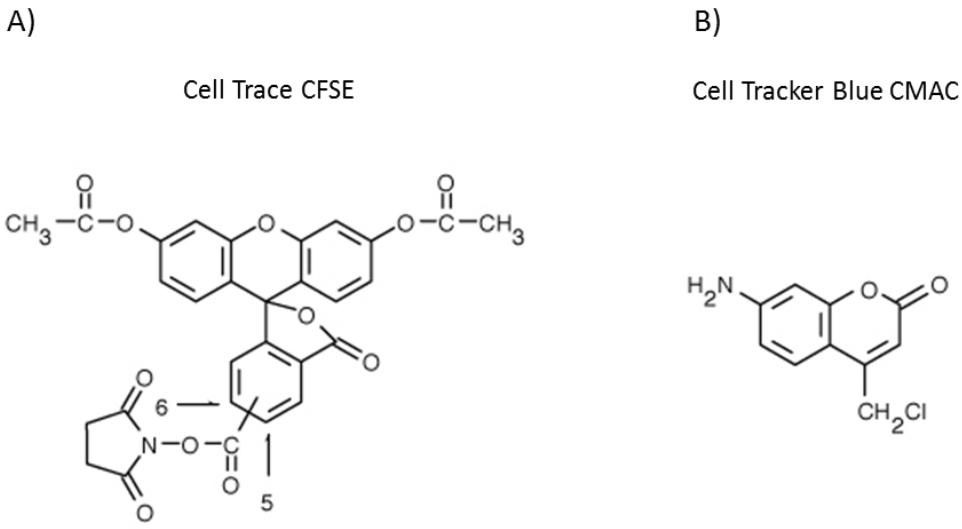

Figure 18:

A) Chemical structure of Cell Tracer CFSE ($C_{29}H_{19}NO_{11}$; 2,5-Pyrrolidinedione, 1-[[[3',6'-bis(acetyloxy)-3-oxospiro[isobenzofuran-1(3H),9'-[9H]xanthen]-5(or-6)-yl]carbonyl]oxy]) © Thermofisher Scientific, https://www.thermofisher.com/order/catalog/product/C34554 (16.07.2017)

B) Chemical structure Cell Tracker Blue CMAC (7-amino-4-chloromethylcoumarin ($C_{10}H_8NO_2Cl$)) © Thermofisher Scientific, https://www.thermofisher.com/order/catalog/product/C2110 (16.07.2017)

4.2. Simple WES Antibodies

Target	Host / Isotype	Class	Dilution	Concentration [mg/mL]	Catalog Number	Company
BPTF	rabbit	polyclonal	WES: 1:25	1 mg/mL	ABE21	EMD Millipore Corp. Merck KGA
Vinculin *	rabbit	monoclonal	1:2000	0.054 mg/mL	ab129002	Abcam

			WES: 1:500			
Goat Anti-Rabbit Secondary HRP Conjugate **	rabbit	----	WES: 1:1	----	042-206	Protein Simple
Goat Anti-Mouse Secondary HRP Conjugate **	mouse	----	WES: 1:1	----	042-205	Protein Simple

Table 3: Used antibodies

*** housekeeping genes; ** secondary antibodies**

4.3. pPCR Primer

Target	Amplicon Length	Catalog Number	Company
BPTF	115	4331182 (HS00925866 m1 BPTF)	Applied Biosystems
BPTF	64	4331182 (HS00189461 m1 BPTF)	Applied Biosystems
HPSE	52	4331182 (Hs00935036 m1)	Applied Biosystems
NDST1	70	4331182 (Hs00155454 m1)	Applied Biosystems

Table 4: Used qPCR primers

4.4. siRNAs

Name	Target	Catalog Number	Company
SMARTpool: ON-TARGETplus *BPTF* siRNA	Human *BPTF*	L-004025-00	Dharmacon
ON-TARGETplus *BPTF* siRNA Targeted Region: Non-Coding, ORF	Human *BPTF*	J-004025-05	Dharmacon
ON-TARGETplus *BPTF* siRNA Targeted Region: Non-Coding, ORF	Human *BPTF*	J-004025-06	Dharmacon
ON-TARGETplus *BPTF* siRNA Targeted Region: Non-Coding, ORF	Human *BPTF*	J-004025-07	Dharmacon
ON-TARGETplus *BPTF* siRNA Targeted Region: Non-Coding, ORF	Human *BPTF*	J-004025-08	Dharmacon

Table 5: Used siRNAs

4.5. Vectors and Plasmids

Name	Company	Catalog Number
pRSF91.dTomato-Blasti-control targets	-----	-----
IncuCyte® NucLight Red Lentivirus Reagent (EF-1 Alpha Promoter, Puromycin selection)	Essen Bioscience	4476

Table 6: Used plasmids and vectors. For plasmid details see supplementary data.

4.6. Cell Culture Media and Supplements

Name	Company	Catalog Number
Roswell Park Memorial Institute 1640 Medium (RPMI 1640)	Gibco	#61870-010
Dulbecco's Modified Eagle Medium (DMEM)	Lonza	#BE-12-604F
Fetal Bovine Serum (FBS/FCS)	GE Healthcare Life Science	#SH30071.03
Sodium Pyruvate	Gibco	#11360-039
MEM Non-essential Aminoacids	Gibco	#11140-035
Penicillin-Streptomycin (Pen/Strep) (10,000 U/mL)	Gibco	#15140148
Blastcidin	Invitrogen	#R210-01
Puromycin	Sigma	#P8833
Fibroblast Basal Medium	PromoCell	#C-23210
Supplement Mix - Fibroblast Growth Medium 3	PromoCell	#C-39345

Table 7: Used cell culture media and added supplements

4.7. Cell Lines:

Name	Organism	Tissue	Histology Type	Medium	Split Ratio	Times / Week
primary NK cells	human	peripheral blood	normal	RPMI1640 + 10 % human serum + 1 % Pen/Strep + 10 ng/mL IL2	-	-
293FT	human	embryonic kidney	normal	DMEM complete + 10 % FCS + 500 µg/mL G418	1: 10	2
Lenti-X™ 293T	human	embryonic kidney	Normal, transformed with adenovirus type 5 DNA, that also expresses the SV40 large T antigen	DMEM complete + 10 % TET approved FCS	$4x10^6$ cells / T175 flask	2
NCI-H1437	human	lung	NSCLC, adenocarcinoma	RPMI1640 + 10 % FCS + 1% Na Pyruvate + 1% NEAA	1:5	2
NCI-H157	human	lung	NSCLC,	RPMI1640 +	1:5	2

			squamous cell carcinoma	10 % FCS + 1 % Na Pyruvate + 1 % NEAA		
NCI-H1437Cas9/Puro	human	lung	NSCLC, adenocarcinoma	RPMI1640 + 10 % FCS + 1 % Na Pyruvate + 1 % NEAA + 1 µg/mL Puromycin	1:5	2
NCI-H157Cas9/Puro	human	lung	NSCLC, squamous cell carcinoma	RPMI1640 + 10 % FCS + 1 % Na Pyruvate + 1 % NEAA + 1 µg/mL Puromycin	1:5	2
NCl-H1437 dTomato	human	lung	NSCLC, adenocarcinoma	RPMI1640 + 10 % FCS + 1 % Na Pyruvate + 1 % NEAA + 60 µg/mL Blasticidin	1:5	2
NCl-H1437 mKate2	human	lung	NSCLC, adenocarcinoma	RPMI1640 + 10 % FCS + 1 % Na Pyruvate + 1 % NEAA + 1 µg/mL Puromycin	1:5	2
NCl-H157 dTomato	human	lung	NSCLC, squamous cell carcinoma	RPMI1640 + 10 % FCS + 1 % Na Pyruvate + 1 % NEAA + 30 µg/mL Blasticidin	1:5	2
NCl-H157 mKate2	human	lung	NSCLC, squamous cell carcinoma	RPMI1640 + 10 % FCS + 1 % Na Pyruvate + 1 % NEAA + 1 µg/mL Puromycin	1:5	2
human dermal fibroblasts (HDF)	human	skin	normal	fibroblast basal medium + supplementary 3	1:3	Only after usage

Table 8: Used cell lines

NCI-H1437 and NCI-H157 were purchased from ATCC (CRL-5872 and CRL-5802), while 293FT were from Invitrogen (R70007) and Lenti-X™ 293T from Clonetech (632180). Neonatal human dermal fibroblasts (HDFs) were from Innoprot (P10857).

All cell lines were maintained in cell culture flasks under standard cell culture conditions (37°C, 5 % CO_2) in adequate culture medium. The used culture medium varied depending on the cell line (see table *cell lines*). In order to generate mKate2 positive cell lines, cells were transduced with IncuCyte® NucLight Red Lentivirus Reagent (#4625, Essen BioScience) according to manufacturer's protocol. For detailed information about the used plasmid see supplementary data (**Figure 56**). A multiplicity of infection (MOI) of three was chosen. In parallel, the required concentration of antibiotics to kill non transfected cells was determined in kill curve experiments (for used antibiotics concentrations see table *cell lines*). Selection was started 72 hours after transfection. The dTomato containing plasmid was electroporated in NCI-H1437 and NCI-H157. For details about the used plasmid see supplementary data (**Figure 57**). To maintain stable expression of red fluorescence proteins, Puromycin or Blasticidin was added to medium. However, during the final assays antibiotics were omitted.

Cells were split twice a week. Split ratios depend on the cell line (see Table 8: Used cell lines). In order to split adherent cells, medium was removed and cells were washed once with PBS (phosphate buffered saline, #1839805, Gibco). After detaching cells with trypsin for 5 minutes, culture medium was added to the cell-trypsin solution. Cell suspensions were transferred into 50mL tubes (#352070, Falcon) and centrifuged (5 minutes, 290 g, room temperature (RT)) using an Eppendorf 5810R refrigerated centrifuge. Supernatants were removed and cell pellets re-suspended in the appropriate volume of fresh media (e.g. 5 mL). Solutions were mixed thoroughly to ensure single cell suspensions. Calculated volumes (e.g. 1 mL) were added to flasks pre-filled with fresh culture media.

For thawing cells, fresh, pre-warmed medium was added into a 50 mL tube (#352070, Falcon). Frozen cell suspensions were pre-warmed in *VWR inculine*. Cell suspensions were transferred into the 50 mL tube containing pre-warmed fresh medium and centrifuged (5 minutes, 290 g, RT). Supernatants were completely removed and pellets re-suspended in

appropriate volumes of fresh media. If necessary, media were exchanged after 24 hours to remove dead cells and remaining freezing media. Antibiotics were added 24 hours after thawing (see Table 8: Used cell lines).

For seeding of distinct numbers of cells, cell viability and density was determined, using *Vi-cell XR cell viability analyser* (Beckman Coulter). It automatically performs cell staining and cell counting by Trypan Blue exclusion method[12]. After counting, necessary volume of cell suspension was added to fresh tubes prefilled with an appropriate volume of fresh medium and seeded into respective plates.

4.8. Presto Blue/Viability Assay

For cell viability analysis, Presto Blue assay was performed at the indicated time point. Each well received 1/10th of total media volume of Presto blue solution, which is based on resazurin. Resazurin is a blue-coloured weakly fluorescing chemical, that can irreversibly reduced to a pink-coloured, highly fluorescent form called resorufin in the presence of $NADH+H^+$ produced by living cells [88, 89]. After addition of Presto Blue, plates were incubate at 37°C until a colour change was observable by the naked eye. Once a pink colour was detected, fluorescence was measured using a fluorescence plate reader.

4.9. Isolation of Peripheral Blood Mononuclear Cells (PBMCs) from Buffy Coats

Buffy coats were obtained from "Red Cross Vienna". They were diluted 1:2 with D-PBS + 2 % FCS. 15 mL lymphoprep (#07811, Stemcell Technologies) was added to 50 mL tubes and overlaid with 30 mL diluted buffy coat. Gradient-centrifugation was performed (15 minutes, 974 g with slow acceleration (3) and without brakes (0)) to separate erythrocytes, blood plasm and PBMCs (interphase). The top layer was discarded and the interphase was carefully transferred into a fresh 15 mL tube using a 1000 µL pipette. PBMCs were washed twice with 15 mL PBS + 2 % FCS (6 minutes, 340 g). To remove residual erythrocytes 5 mL aluminium-chloride-potassium (ACK) lysis buffer (#A1049201, Gibco/Thermofisher Scientific) were

[12] http://www.beckman.com/particle /instruments/cell-sizing-and-processing/vi-cell-xr, 21.06.2017

added for 3-5 minutes. To remove traces of ACK lysis buffer cells were washed with PBS + 2% FCS (6 minutes, 340 g). Cell number was determined and PBMCs were frozen in CryoStor® CS10 (#07930, Stemcell Technologies) (concentration = $1x10^8$ cells/mL) at -80°C.

4.10. Three-Dimensional (3D) Infiltration and Killing Assays

NSCLC cell lines NCI-H157 and NCI-H1437 were grown in 3D to assess primary NK (PNK) cell's infiltration potential into the small tumour spheroids.

NCI-H157mKate2 and NCI-H1437mKate2 were used for killing analysis, while NCI-H157dTomato and NCI-H1437dTomato were used to study NK cell infiltration because dTomato is expressed in the cytoplasm (see Table 1: Used fluorophores & Figure 17) and therefore, the whole multicellular tumour spheroids (MCTSs) appear as large red areas on fluorescence microscopy images. This is essential for the used evaluation algorithm, which allows quantitative analysis of the amount of infiltrated NK cells into MCTSs. Analysis is based on the cell's volume, which is calculated via the size of the green (PNK) and red (tumour cells) dots present in the images. The algorithm compares the volume of green area with the red one. Thereby also NK cell clusters can be integrated into analysis. Additionally, the distance from NK cells (green) towards the mass center of the MCTSs is calculated, as an indication for infiltration. The algorithm was co-developed with the University of Turku and programmed by Hannu-Pekka Schukov, *HiPerSoft Solutions*. In contrast, mKate2 is only expressed in the nuclear (see Table 1: Used fluorophores & Figure 17) and allows a better resolution.

4.10.1. Isolation of Primary NK Cells from PBMCs

PBMCs were thawed and re-suspended in RoboSep Buffer (#20104, Stemcell Technologies; concentration: $5x10^6$ cells/mL). Cell suspension was transferred into a 14 mL round-bottom tube (#14-959-10B, Falcon). NK cells were isolated using *EasySep Human NK Cell Enrichment Kit* (#19055, Stemcell Technologies). The kit was used according to manufactures' instructions: 50 µL of *Human NK cell Enrichment Cocktail* were added per 1 mL cell suspension. The mixture was incubated for 10 minutes. 100 µL magnetic beads per 1 mL cell suspension were added. After incubating for 5 minutes, the lid was removed and the tube

placed into *Big Easy Magnet* (#18001, Stemcell Technologies) for 2.5 minutes. The magnet was lifted and the solution was poured into a new 50 mL tube. After centrifugation (5 minutes, 453 g), NK cells were re-suspended in NK cell medium and cell number was determined.

4.10.2. Pre-stimulation of NK Cells and Pre-treatment of Tumour Cells

All primary NK cells (PNKs) were pre-stimulated with IL2 (10 ng/mL) for three days. To inactivate PNKs transforming growth factor β (TGFβ; 1 ng/mL) was added. For high activation primary NK cells received IL12 (5 ng/mL) and IL18 (50 ng/mL). Tumour cell were treated with BI90 for three days starting 24 hours after seeding. Concentration varied between 2 µM and 0.125 µM. BI90 was diluted to 20X working solutions in D-PBS + 2 % DMSO (#D5879, Sigma-Aldrich). 10 µL medium/well were removed and replaced by 10 µL of working solutions (1:20 dilution). DMSO concentration was kept constant at 0.1 % in all conditions.

72 hours after stimulation or treatment light microscope images were taken using Leica light microscope. Activation can be assumed if PNKs form clusters. Activated PNKs interact with each other leading to cluster formation and produce interferon γ (*IFNG*) inside. Non-activated PNK remain in suspension as single cells and do not produce *IFNG* [90].

4.10.3. Floater Assay

5000 NCI-H1437mKate2 or NCI-H157mKate2 cells were seeded in 200µl medium in 96 well clear black round bottom ultra-low attachment spheroid microplates (#4520, Corning).

Cells were incubated for four days to allow formation of compact MCTSs. Six to ten MCTSs were harvested and pooled. Supernatant was discarded and 300 µL of 1X TrypLE Express Enzyme (#12604013; Gibco/ThermoFisher Scientific) were added. After incubation of 5 – 15 minutes (until MCTSs were dissolved – formation time depends on cell line) 700 µL of tumour cell medium were added, to stop the reaction. Cell number was determined using *Vi-Cell XR Cell Viability Analyser* (Beckman Coulter). Average cell number per spheroid was calculated.

Determination of NK cell number needed:

Number of tumour cells x 3 (Effector : Target ratio) x 4 (Amount of wells / Condition)

Appropriate amount of NK cell solution was transferred into 1.5 mL Eppendorf tubes and centrifuged (5 minutes, 453 g). Supernatants were discarded and pellets re-suspended in 400 µL of tumour cell medium without antibiotics plus necessary cytokines (RPMI1640 + 10% FCS + 1 % Na Pyruvate + 1 % NEAA + IL2 (20 ng/mL) or + IL2 (20 ng/mL), IL12 (10 ng/mL), IL18 (100 ng/mL) or IL2 (20 ng/mL) + TGFβ (2 ng/mL). Compounds were diluted to 20X working solutions. 110 µL medium were removed from each MCTS. 100 µL NK cell solution was added per well. 10 µL of 20X working solution or D-PBS + 2 % DMSO were added. Fluorescence of tumour cells was measured directly afterwards. Fluorescence was measured twice a day (morning and evening) for 7 to 10 days using *Perkin Elmer's Wallac 2100 EnVision™*.

4.10.4. Embedded Assay

5000 NCI-H157mKate2 or 10000 NCI-H1437mKate2 cells were seeded per well in 200 µl medium. For killing analysis 96 well clear black round bottom ultra-low attachment spheroid microplates (#4520, Corning) were used, while for infiltration 96 well clear round bottom ultra-low attachment microplates (#7007, Corning) were used. For details regarding pre-stimulation and pre-treatment see *Pre-stimulation of NK Cells and Pre-treatment of Tumour Cells.* Tumour cells were incubated for four days to allow formation of compact MCTSs. They were embedded in a collagen/Matrigel medium-mixture (20 % - 50 % - 30 %) together with HDF and primary NK cells. Final concentration of collagen (#354236, Corning™) and Matrigel (#356239, Corning) were 3 mg/mL and 8 mg/mL respectively. It is important to prepare the collagen/Matrigel mixture on ice, as they are liquid at +4°C, but form a gel-like scaffold at RT/+37°C.

Before embedding, primary NK cells and HDF were stained. NK cells were stained with *Cell Tracer CFSE* (#C34554, Thermofischer) and HDF with *Cell Tracer Blue CMAC* (#C2110, Thermofisher). For detailed information about the dyes see Table 2 and Figure 17.

NK cells and HDFs were transferred into 1.5 mL Eppendorf tubes and centrifuged (NK cells: 453 g, 5 minutes; HDF: 290 g, 5 minutes). Supernatant was discarded and pellets re-suspended in 1 mL of D-PBS. 1 µL (= 1:1000 dilution) of *Cell Tracer CFSE* or *Cell Tracer Blue* was added and incubated 20 minutes at RT protected from light. Cells were washed once

with 1 mL of D-PBS. Supernatant was removed and cells were re-suspended in collagen/Matrigel-solution (on ice).

170 µL of medium were removed and 70 µL of the collagen/Matrigel/cell solution added per well. Plates were incubated 1.5 hours in an incubator at 37°C. Afterwards 100 µL of RPMI1640 + 10 % FCS without phenol red + Glutamax, NEAA, sodium pyruvate (#12-918F, Lonza) were added on top of the collagen/Matrigel/medium mixture. Interleukins, compounds (or corresponding DMSO control) were added to both collagen/Matrigel/medium mixture and the additional medium on top.

For killing analysis red fluorescence of mKate2 expressing tumour cells were measured every day for one week using *Perkin Elmer's Wallac 2100 EnVision*^{TM}, starting right after adding medium on top of the gel.

Infiltration was analysed using a *LSM700* confocal fluorescence microscope (Zeiss). Images were taken after 24 hours, 48 hours, 72 hours and 96 hours after embedding. Z-stacks and maximum intensity projections were generated. Maximum intensity projections were either evaluated manually (by counting) or by an evaluation algorithm co-developed with the University of Turku.

4.11. siRNA Mediated Knock Down (KD) Studies

5X siRNA Buffer (#B-002000-UB-100, Dharmacon) was diluted in RNase-free water (#129112, Qiagen) to generate a 1X solution. 5 nmol siRNA were re-suspended in 250 µl 1X siRNA buffer to prepare a 20 µM stock. For used siRNAs see Table 5: Used siRNAs.

In order to perform reverse transfection RNAiMAX (transfection reagent) and siRNA master mixes were prepared:

Master Mix 1 (Transfection Reagent)		
	6-well	**96-well**
RNAiMAX / well [µL]	2,5	0,5
OptiMEM / well [µL]	122,5	24,5
number of wells	X	X
RNAiMAX total [µL]	**2,5µL * X**	**0,5µL * X**

Master Mix 2 (siRNA)		
	6-well	**96-well**
dilution factor siRNA stock	400	400
µL total / well	1250	200
µL siRNA stock / well	3,125	0,5
OptiMEM / well [µL]	121,875	24,5
number of wells / siRNA	Y	Y
µL siRNA stock total	**3,125µL * Y**	**0,5 * Y**
OptiMEM total [µL]	**121,875µL * Y**	**24,5µL * Y**

siRNA (final concentration: 50 nM) and RNAiMAX solution (2.5 µL RNAiMAX/6-well) were mixed 1:1 and incubated at room temperature for 20 minutes. 250 µL of transfection mixture were added/well (6-well plates). Afterwards, 1 mL of cell suspension ($0{,}375 \times 10^6$ cells/mL) was added to each well. For 96-well plates volumes were reduced to 50 µL of transfection mixture and 150 µL of cell suspension per well.

Plates were incubated at 37°C, 5 % CO_2. Lysates were prepared after 24 hours, 48 hours, 72 hours and 96 hours post transfection. Plates were washed once with DPBS. 60 µL of HEPEX lysis buffer + 1 % Halt™ protease and phosphatase inhibitor cocktail (#78441, Thermofisher Scientific) were added per well. Plates were incubated 10 minutes on ice before transferring

samples were into tubes. Samples were stored at -20°C until Western blot analysis was performed to determine KD efficiency.

4.12. Clustered Regularly Interspaced Short Palindromic Repeats (CRISPR) Assay

4.12.1. Virus Production

$4x10^6$ HEK293 LentiX cells were seeded per 10 cm dish in 8 ml culture medium. The next day cells were transfected using LentiX packaging single shot (VSV-G) system (#631276, Clonetech): 7 µg plasmid DNA (concentration = 1 µg/µL) were mixed with 593 µL sterile distilled water (#15230147, Gibco). Mixture was added to LentiX packaging single shot vials (one vial/plasmid), vortexed shortly and incubated 10 minutes at RT. Solution was added carefully (dropwise) to 10 cm dishes and incubated under standard cell culture conditions. The day after transfection additional 6 mL medium were added per dish. 24 hours later virus was harvested in 2 mL cryotubes and stored at -80°C.

4.12.2. Transduction

On day one $0.15x10^6$ cells were seeded per 6-well in 2.5 mL medium + 8 µg/mL polybrene (#sc134220, Santa Cruz) without antibiotics. 24 hours later medium was exchanged to medium without polybrene and without antibiotics (1 mL/well). Virus was defrosted and 100 µL or 200 µl or 400 µL virus solution were added per 6-well. On day 3 medium was exchanged again (2.5 mL/well). Cells were detached and washed three times on day 4 and transferred into fresh 6-well plates to reduce present virus amount.

4.12.3. Flow Cytometric Analysis

Starting from day 5 after transduction cells were analyzed by flow cytometry regularly. For this, cells were detached using trypsin. $1/5^{th}$ of the cell suspension was transferred into a 1.5 mL tube and centrifuged. Pellets were re-suspended in 200 µL FACS buffer (D-PBS + 2 % FCS + 0.1 % NaN_3) and transferred into a round bottom 96-well plate (#3799, Corning). Flow cytometric analysis was performed using a FACS Canto II (BD Bioscience).

4.12.4. Fluorescence Activated Cell Sorting

Cells were detached with 2.5 mL accumax solution/T75 flask. In order to remove clumping cells from the solution, cells were filtered through a grid into FACS tubes. Cells were sorted using a FX500 Exchangeable Fluidics Cell Sorter (Sony). Sorted cells were collected in 15 mL tubes, which were coated with a thin layer of FCS. Sample pressure was set between 5 and 7, depending which setting provided the best event rate (~ 5000/second). From each population GFP positive ($0.1x10^6$) and GFP negative ($1x10^6$) cells were sorted. After sorting cells were centrifuged (290 g, 5 minutes). Supernatant was discarded and cells re-suspended in culture medium supplemented with 1 % Pen-Strep. Antibiotics were added to prevent bacterial contamination, as sorting process is not sterile. Depending on number of sorted cells, cells were either seeded in T75 (GFP negative) or T12.5 flasks (GFP positive).

4.13. Interferon γ (*IFNG*) and Granzym B (*GZMB*) Secretion Analysis

QC capture beads for *IFNG* and *GZMB* (kit #90702, Sartorius) were diluted 1:50 together to prepare a working solution. 10 µL of capture beads working solution were transferred into each 384-well using *Thermo Scientific Matrix Equalizer Pipette*. 10 µL of sample were added/well. Sample and capture beads were incubated one hour at RT protected from light. 10 µL of detection reaction were added/well and incubated two hours at RT in darkness. Plates were measured using *Intellicyt iQue Screener* (Sartorius) according to manufacturers' instructions.

4.14. Simple WES

In order to determine protein concentrations Bradford assays were performed: 100 µL of Quick Start™ Bradford 1X Dye Reagent (#5000205, Biorad) were added into 96-wells. 1 µL of either protein sample or protein standard was added. For generation of a standard curve, seven different protein concentrations (between 2000 mg/mL and 125 mg/mL) and a blank were used. Plates were measured at 595 nm using a Spectramax photometer (Molecular

Devices). Sample analysis was performed in triplicates and mean concentration was calculated.

All reagents present in standard pack (#PS-ST03-8A, Protein Simple) were prepared including a 400 mM Dithiothreitol (DTT) solution. A 5X fluorescent master mix was prepared by adding 20 µL of 400 mM DTT solution and 20 µL of 10X sample buffer. Biotinylated ladder stock was diluted in 16 µL distilled water + 2 µL 10X sample buffer and 2 µL of DTT solution.

Protein stocks were diluted in 0.1X sample buffer to receive a 0.2 mg/mL protein solution used for analysis. One part 5X fluorescent master mix was added per sample. Protein solutions and biotinylated ladder were denatured (95°C, 5 minutes) using a PCR thermocycler and stored on ice. Primary antibodies were diluted in Antibody Diluent 2 (dilution depends on used antibodies and varied between 1:25 and 1:500). Chemoluminescence substrates (luminol-S and peroxide) were mixed in equal amounts (200 µL each) and stored on ice.

WES plates were filled with biotinylated ladder, protein samples, WES antibody diluent 2, primary antibody and secondary antibody solutions, luminol-peroixed mixture and wash buffer as indicated in manufacture's protocol. Plates were placed into WES devices and run using Compass software.

4.14.1. Simple WES Quantification

Calculated areas of target proteins and housekeeping proteins were identified. Quotient of target divided by housekeeping protein was calculated and normalised towards used control.

4.15. Expansion of Plasmid DNA

4.15.1. Preparation of Agar Plates

200 mL autoclaved Millipore water were poured into a 500 mL Schott flask. One pack of imMedia™ Growth Medium powder (100 µg/mL ampicillin; #Q60120; Invitrogen) was added. Mixture was heated up in a microwave until whole powder was dissolved. Solution was

cooled down and poured into 10 cm dishes. Dishes were incubated at RT until agars were cooled down. Plates were stored upside down at +4°C until used. Before usage, plates were pre-warmed at 37°C.

4.15.2. Bacterial Transformation

One Shot™ Stbl3™ Chemically Competent *E. coli* (#C737303, Invitrogen) were thawed on ice. 5ng DNA were transferred into a fresh 1.5 mL tube and stored on ice. 50 µL of *E. coli* solution were added/1.5 mL tube (+4°C room with chilled tips). After mixing gently, mixture was incubated 30 minutes on ice. Afterwards tubes were placed into a swimmer in a water bath (42°C) for 45 seconds. Subsequently, tubes were placed on ice for two minutes. 250 µL S.O.C medium (#15544034, Invitrogen) was added/tube. *E. coli* culture was incubated 30 minutes at 37°C and 225 rpm (thermomixer).

100 µL of each *E. coli* solution were dispensed on agar plates and incubated upside down at 37°C over night. Dishes were stored at +4°C from morning to afternoon. Colonies were picked and 100 mL overnight *E. coli* cultures were prepared (37°C and 225 rpm) in Erlenmeyer flasks.

4.15.3. Maxi Preparation

Maxi preps were performed using EndoFree Plasmid Maxi Kits (#12362, Qiagen): 100 mL *E. coli* cultures were transferred into 250 mL tubes (#430776, Corning) and centrifuged 1112 g, 10 minutes. Supernatant was discarded and pellets re-suspended in 10 mL of buffer P1 + RNase A solution + LyseBlue reagent (1:1000). 10 mL of buffer P2 were added. Solution turns consistently blue, if solutions are mixed properly. After incubating for five minutes at room temperature, 10 mL of chilled buffer P3 were added. If all components are mixed properly, solution loses the blue colour and turns clear again. Tubes were incubated 5 minutes on ice. Samples were centrifuged 1112 g, 5 minutes. Supernatant was transferred into QIAfilter maxi cartridges and incubated 10 minutes at room temperature. Lysate was filtered into a fresh 50 mL tube (already containing 2.5 mL buffer ER) by using a plunger. Mixture was vortexed and incubated on ice for 30 minutes. In the meantime, qiagen tips-500 were equilibrated with 10 mL of QBT buffer.

Lysates were transferred on equilibrate tips and filtered through. After washing twice with 30 mL of buffer QC, DNA was eluted in 15 mL of pre-warmed (56°C) buffer QN. 10.5 mL isopropanol were added to precipitate DNA (vortex). Samples were centrifuged 30 minutes at 4°C with 40900 g using an Avanti centrifuge. Supernatant was removed and 5 mL ethanol were added. After centrifuging again (10 minutes, 40900 g) supernatant was removed. To remove residual traces of ethanol samples centrifuged once again (1 minute, 40900 g). Pellets were re-suspended in 200 µL buffer TE and transferred into fresh 1.5 mL tubes. Concentration was determined using a Nanodrop UV/Vis photo spectrometer. Samples were stored at -20 °C until needed.

4.16. Quantitative Polymerase Chain Reaction (qPCR)

4.16.1. RNA Extraction

RNA was extracted by usage of Qiagen's RNeasy Mini Kit (#74104): After removing supernatant, cells were washed once with PBS. 600 µL of buffer RLT + 40 µL 1 M DTT/mL (#43816; Sigma) were added per 6-well to lyse cells. Mixture was transferred onto QIA shredder spin column and centrifuged (18407 g, 2 minutes). 600 µL of 70 % ethanol (RNase-free) were added per sample and mixed thoroughly. 600 µL sample were transferred onto RNeasy spin columns (max. Volume: 700 µL) and centrifuged (18407 g, 15 seconds). Flow through was discarded, residual 600 µL were loaded and procedure was redone. 350 µL buffer RW1 were added to RNeasy spin columns and centrifuged (18407 g, 15 seconds). A DNase digest master mix (#79254, Qiagen) was prepared:

	1 Sample	**X Samples**
µL Dnase 1 stock solution	10	* X
µL buffer RDD	70	* X
µL total	**80**	**10X + 70X**

75 µL of DNase master mix were added per column and incubated 15 minutes at room temperature. 350 µL buffer RW1 were added and centrifuged (14680 g, 15 seconds). After discarding the flow through, 500 µL of buffer RPE were added and centrifuged (14680 g, 2 minutes). Flow through was discarded and RNeasy spin columns placed on a fresh tube. To

remove residual traces of present ethanol samples were centrifuged again (14680 g, 1 min). RNeasy spin columns placed on a fresh 1.5 mL collection tube. 40 µL of pre-warmed (37°C) RNase-free water were added per sample and centrifuged (8000 g, 1 minutes).

RNA concentration and quality were determined using a Nanodrop UV/Vis photo spectrometer. RNA was stored at -80°C.

4.16.2. Generation of Complementary DNA (cDNA)

For cDNA synthesis SuperScript™ VILO™ cDNA Synthesis Kit (#11754050, Invitrogen) was used. A 6X master mix was prepared for each sample:

	1X	**13X**
µl 5X Vilo Rx buffer	4	52
µl 10X Superscript Enzyme Mix	2	26
µl RNA + H2O*	14	182
µl total	**20**	**260**

*1 µg RNA was used per reaction. Therefore, the required volume of RNA solution (for 13 reactions) was mixed with RNase-free water (for 13 reactions) to receive a final volume of 182 µL and stored on ice.

20 µL master mix were added per well of a PCR plate (#951020303, Eppendorf). Plate was sealed with a film and centrifuged (693 g, 3 minutes). cDNA was prepared using a GeneAmp PCR System 9700 device. The following set up was used:

temperature [°C]	**time [minutes]**
25	10
42	60
85	5
4	oo

cDNA was stored at -20°C.

4.16.3. qPCR

qPCR was performed using QuantiTect Multiplex PCR Kit (#204543; Qiagen). For each sample six replicates were used. To compare expression levels of selected target genes, normalisation to expression levels of housekeeping genes is necessary. Therefore, each reaction contains fluorescently labelled primers for 18S rRNA (#4319413E, Thermofisher Scientific; VIC®/MGB labelled)) and a selected target gene (*HPSE*: #Hs00935036_m1,

Thermofisher Scientific; FAM®/MGB labelled; *BPTF*: #Hs00925866-m1 & # Hs00189461-m1, Thermofisher Scientific; FAM®/MGB labelled).

For each sample a 7X master mix was prepared:

	1X	**7X**
µL cDNA-Template	2	14
µL 2X Quanti-Tect	12,5	87,5
µL 20X Primer (target gene)	1,25	8,75
µL 20X Primer (housekeeping gene)	1,25	8,75
µL H_2O	8	56
µL total	**25**	**175**

20 µL of master mix were added per well. Plates were (#4346906, Applied Systems) sealed with an optical film and centrifuged (693 g, 3 minutes). qPCR was prepared using a StepOnePlus real-time PCR system. The following set up was used:

time	**temperature [°C]**	**cycles**
8 min	95	1
45 sec	94	45
45 sec	60	

Data was analysed using *StepOne* software.

4.17. Generation of Venn diagrams

Venn diagrams were generated according to http://bioinformatics.psb.ugent.be. Lists of deregulated genes (fold change (FC) log ≥ 1.8, p-value ≤ 0.01) including heat maps were received from ATLAS Biolabs GmbH Affymetrix Gene Chips (Affymetrix EXP).

4.18. Statistical analysis

Unpaired t–tests were used to compare e.g. viability of treated samples with its corresponding control. T-tests were calculated using *graphpad prism 6*. P-values were also determined by *graphpad prism 6*. To graphically illustrate, symbols (stars) were used: ns (not

significant) for p-values > 0.05, * for $p \leq 0.05$, ** for $p \leq 0.01$, *** for $p \leq 0.001$ and **** for $p \leq 0.0001$.

5. Results

5.1. Basic Considerations on 3D Co-culture Models

Prior to generation of complex three-dimensional (3D) *in vitro* culture models, it is a prerequisite to gain as much as possible of knowledge about the key factors and cellular components driving these models. This includes cell types, chemicals, and cytokines but also comprises their potential influence on each other. The most important molecular parameters and cellular systems, which impact on the behaviour of 3D models, are briefly summarized below. Receiving a basic understanding is obligatory to be able to draw conclusions from future experiments and the generated data sets thereof.

5.1.1. Effect of Dimethyl Sulfoxide (DMSO) on Primary NK Cell (PNKs) Viability and Activity

DMSO is an organic solvent[13]. It is commonly used to dissolve small chemical entities including BI90, a specific PBTF inhibitor. Recently, NK-92, a human NK cell line, was shown to be sensitive to DMSO [91]. As primary NK cells (PNKs) will be exposed to low levels of DMSO in our experimental settings as well, it is essential to know whether presence of DMSO does influence PNKs activity and/or their viability. Secretion of interferon γ (*IFNG*) and granzyme B (*GZMB*) – typically both are produced by activated NK cell – was analyzed in presence and absence of DMSO (**Figure 19**, **Figure 20**) [92].

[13] https://chem.nlm.nih.gov/chemidplus/name/dmso, 13.07.2018

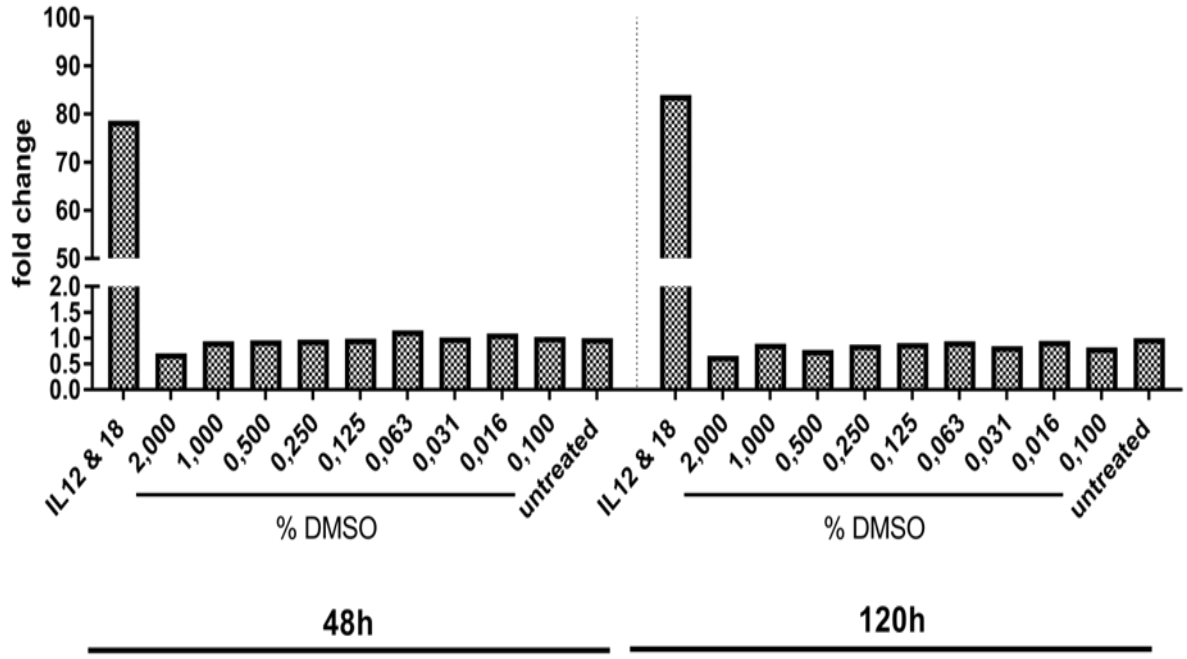

Figure 19: Granzyme B (*GZMB*) secretion by primary NK cells (PNKs)

PNKs were stimulated with either IL2 (10 ng/mL), IL12 (5 ng/mL) and IL18 (50 ng/mL) or IL2 (10 ng/mL) at different DMSO concentrations (2 – 0.016 w/v %).

X-Axis: Different stimulation and treatment modalities. Untreated refers to IL2 stimulation only.

Y-Axis: Fold change of *GZMB* secretion normalized to untreated.

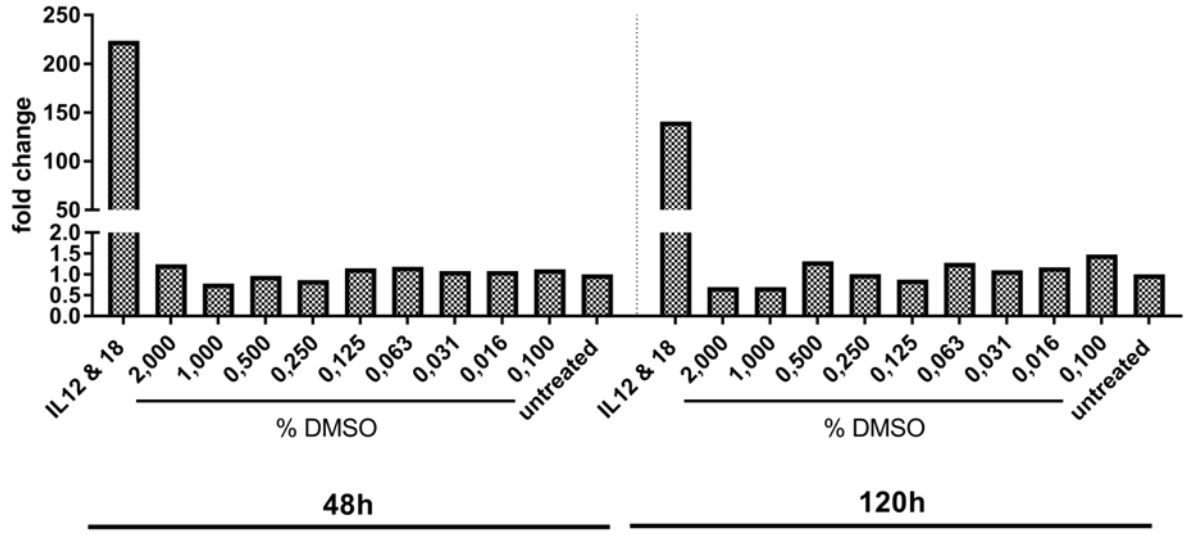

Figure 20: Interferon γ (*IFNG*) secretion by primary NK cells (PNKs).

PNKs were stimulated with either IL2 (10 ng/mL), IL12 (5 ng/mL) and IL18 (50 ng/mL) or IL2 (10 ng/mL) at different concentrations of DMSO (2 – 0.016 w/v %).

X-Axis: Different stimulation and treatment modalities. Untreated refers to IL2 stimulation only.

Y-Axis: Fold change of *IFNG* secretion normalized to untreated.

In the concentration range of 0.016 – 2 w/v %, DMSO does not interfere with human primary NK cell activity, as levels of *GZMB* and *IFNG* were neither increased nor decreased in presence of the organic solvent. Pre-stimulation with IL12 and IL18 causes increased production, indicating that the used PNKs can be activated [92, 93]. However, as it cannot be completely obviated that DMSO interferes with NK cells behaviour in one or another way, the DMSO concentration was kept constant (0.1 %) under all conditions of each experiment.

5.1.2. Optimal Effector to Target (E:T) Ratio

Determination of an optimal E:T ratio is essential. Presence of too many NK cells would lead to complete tumour cell clearance while too few might do not kill efficiently enough or even not all. In both cases the dynamics of the therapeutic window would be distorted. The optimal E:T ratio is key for further studies and assay design and had to be determined/adapted for each of the experimental settings. As exemplified in **Figure 21**, different effector to target ratios were used to identify the most appropriate E:T ratio in the two-dimensional co-cultivation of NCI-H157 or NCI-H1437 with PNKs.

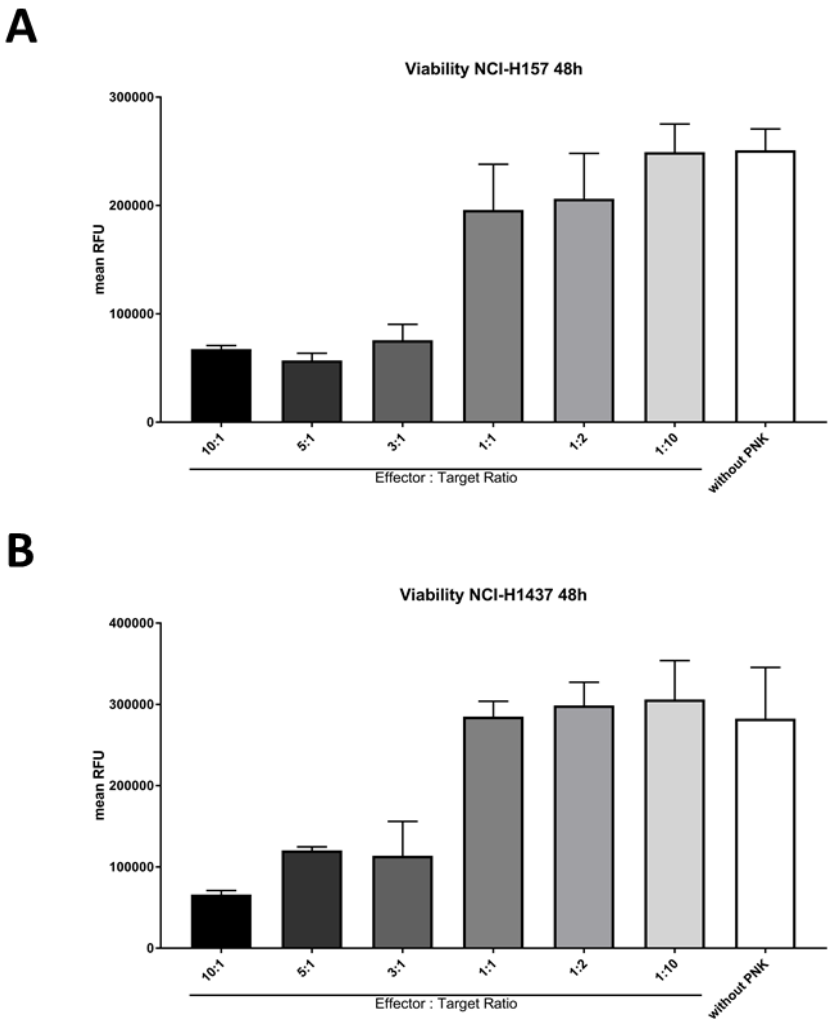

Figure 21: Viability of A) NCI-H157 or B) NCI-H1437 after 48 hours of 2D co-cultivation with primary NK cells (PNKs).

$1x10^4$ tumour cells were seeded in 100 µL medium. After 24 hours between $1x10^3$ (E:T = 1:10) and $1x10^5$ (E:T = 10:1) PNKs were added in 100 µL medium per well. Viability was determined 48 hours after addition of PNKs. 20 µL of Presto Blue solution were added per well. Plates were incubated for three hours and fluorescence intensity was measured using a plate reader (Viktor, Perkin Elmer). Analysis was performed in triplicates for each condition.
X-Axis: Different culture conditions.
Y-Axis: Mean RFU (+STD) indicating tumour cell viability.
Mean RFU: Mean relative fluorescence units.

Small effector to target ratios (1:1, 1:2, 1:10) do not cause strong reduction in tumour cell viability. High E:T ratios (10:1, 5:1) kill tumour cells efficiently. For further studies an E:T ratio of 3:1 was selected as it would allow therapeutic dynamics in both directions. In general, killing effects are thought to be weaker when target cells are grown in 3D as NK cells in 2D

can more efficiently interact with all present tumour cells than this would be the case in a multicellular tumour spheroid (MCTS) 3D setting [74].

5.1.3. Long-term IL12 and IL18 Stimulation Influences PNKs Cytotoxic Potential

Effects on NK cells in long term exposure to interleukins (ILs) and cytokines was determined (**Figure 22**). PNKs had been pre-stimulated with IL2, IL12, IL18 and TGFβ for five days prior to co-cultivation with tumour cells.

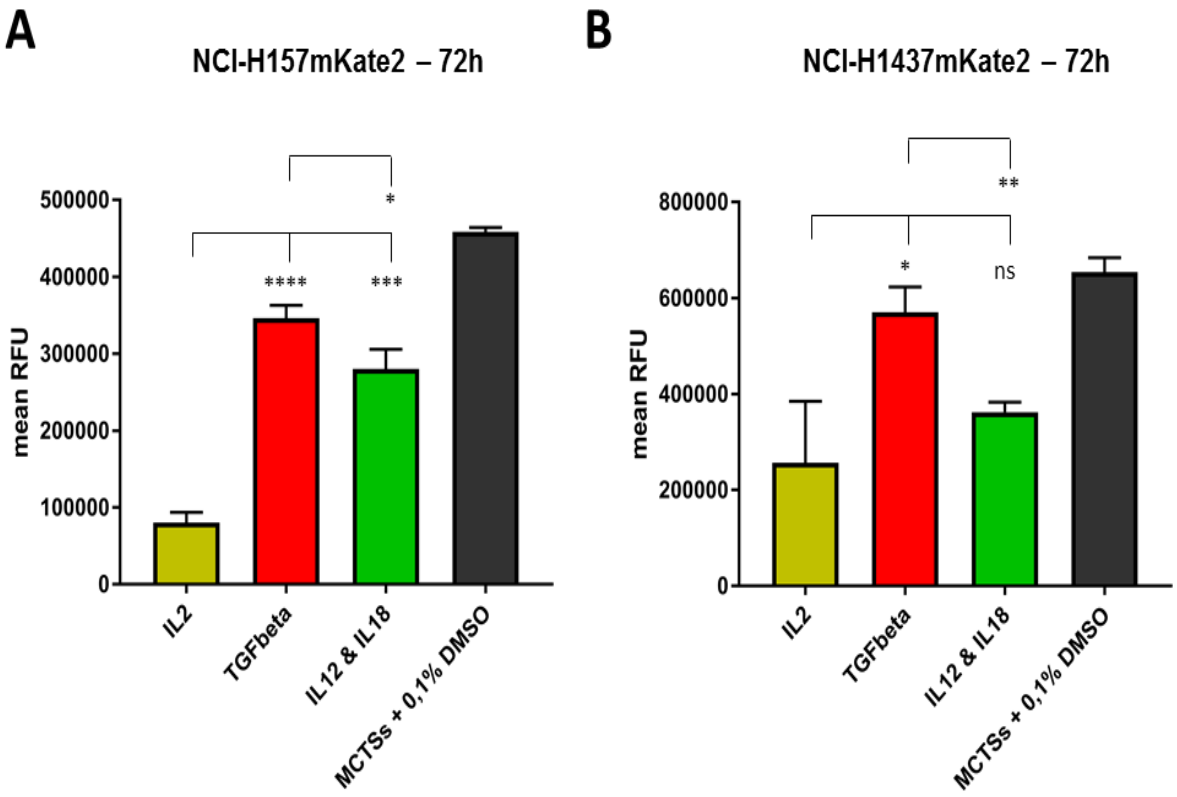

Figure 22: Viability of A) NCI-H157 or B) NCI-H1437 after 72 hours of 2D co-cultivation with PNKs.

PNKs were either pre-simulated with IL2 (10 ng/mL) or TGFβ (1 ng/mL) and IL2 (10 ng/mL) or IL12 (5 ng/mL), IL18 (50 ng/mL) and IL2 (10 ng/mL) for 120 hours. $1x10^4$ tumour cells were seeded. Pre-stimulated PNKs were added (E:T = 3:1) after 24 hours. Interleukins and cytokines were added in the co-culture as well.
Viability was determined by Presto Blue assay 72 hours after adding PNKs. Analysis was performed in triplicates for each condition.
X-Axis: Different culture conditions.
Y-Axis: Mean RFU (+ STD) indicating tumour cell viability.
Mean RFU: Mean relative fluorescence units

In contrast to NCI-H1437, 72 hours pre-stimulation of PNKs with IL12 and IL18 causes significantly less NCI-H157 tumour cell killing compared to IL2 pre-stimulation alone. As NCI-H157 has a high and NCI-H1437 a low EMT score, a much longer co-cultivation of NCI-H1437 might be necessary to detect similar significant differences between IL2 and IL12 & IL18 pre-stimulated co-cultures of PNKs.

5.1.4. Influence of BI90 on Non-small Cell Lung Carcinoma (NSCLC) Cell Lines and Primary NK Cells (PNKs)

BI90 is a proprietary BI bromodomain PHD finger transcription factor (*BPTF*) inhibitor. This small chemical entity binds efficiently to *BPTF´*s bromodomain (BRD). Its K_D for *BPTF* is in the low nM range (2.9 nM). To other BRD-containing proteins BI90 binds less efficiently (to three of them with a 10- to 20-fold higher K_D and to all other BRD-containing proteins with a K_D more than 100-fold higher). Thus, selectivity of BI90 is ensured. However, at first BI90´s direct effects on either tumour or immune cell functions had to be characterized in order to study BI90's potential of modulating tumour cells immunogenicity in three-dimensional models.

5.1.4.1. Viability of Non-small Cell Lung Cancer (NSCLC) Cell Lines in 2D Cultures after BI90 Treatment

Based on knock down (KD) studies it was hypothesized that KD of *BPTF* in target tumour cells may cause a PNK-mediated tumour cell killing *in vivo* [68]. In order to characterize potential off-target effects of BI90 on proliferation/viability of tumour cell mono cultures Presto Blue assays at different time points and BI90 concentrations were performed. By this a direct anti-proliferative effect of BI90 on tumour cells should be ruled out. As clearly shown in **Figure 23**, none of the administered BI90 doses was able to reduce the viability of the four NSCLC cell lines tested.

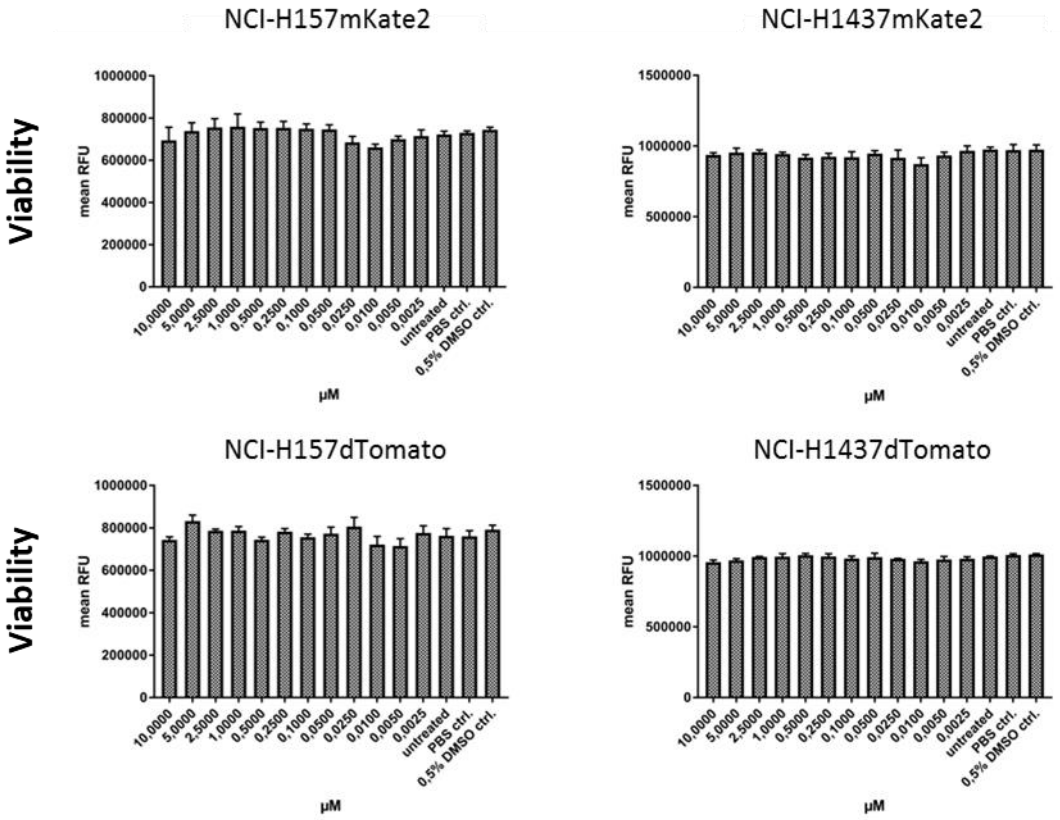

Figure 23: Viability of four different NSCLC cell lines after treatment for 72 hours with BI90.

$5x10^3$ cells each of NCI-H157mKate2, NCI-H157dTomato, NCI-H1437mKate2 and NCI-H1437dTomato were seeded per 96-well in 190 µL medium. 24 hours after seeding, 10 µL of differently concentrated BI90 solutions were added. Final BI90 concentration in the assay varied between 10 µM and 2.5 nM. Controls received either 10 µL of PBS (untreated) or 10 µL of PBS + 10 % DMSO leading to final concentration of 0.5 % DMSO in the assay. Viability was determined 72 hours after adding compound. 20 µL of Presto Blue solution were added per well. Plates were incubated for three hours. Fluorescence intensity was measured using a plate reader (Viktor, Perkin Elmer). Analysis was performed in triplicates for each condition.

X-Axis: Different concentrations of BI90 in µM and controls (untreated, PBS and 0.5 % DMSO control).
Y-Axis: Mean RFU (+ STD) indicating tumour cell viability.
Mean RFU: Mean relative fluorescence units.

5.1.4.2. Multicellular Tumour Spheroid (MCTS) Formation and Growth in the Presence of BI90

As shown in 5.1.4.1 for growth in 2D, likewise growth of NCI-H157 and NCI-H1437 in 3D is not hampered by addition of BI90; neither the formation of MCTS (**Figure 24**) nor the growth/viability in 3D (**Figure 25**).

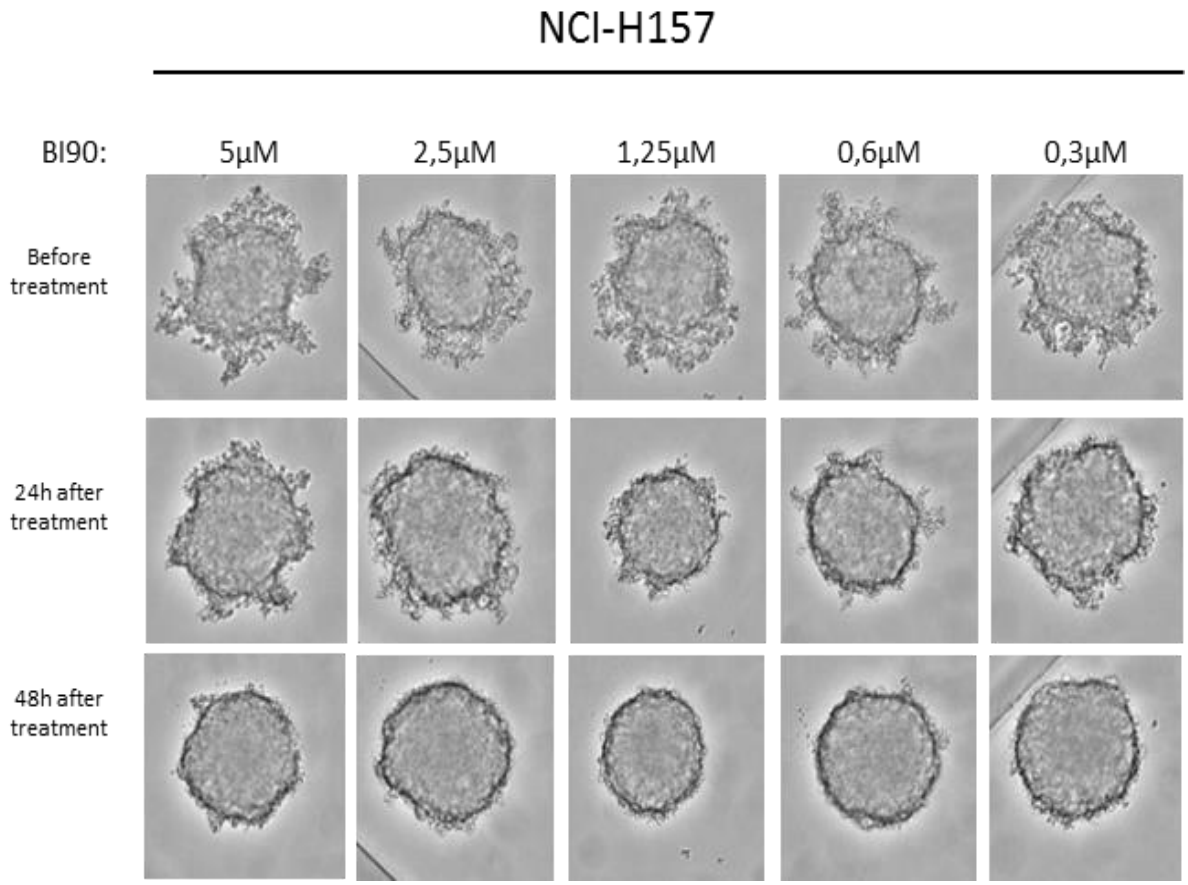

Figure 24: Multicellular tumour spheroid (MCTS) formation in presence of BI90.

NCI-H157 and NCI-H1437 were seeded in ultra-low attachment plates ($5x10^3$ cells in 200 µL of medium per 96-well). Plates were incubated 48 hours before adding 10 µL of differently concentrated BI90-solutions. Concentration series was from 5 µM to 300 nM.
Images were taken before treatment, 24 hours and 48 hours afterwards using Clone Select Imager (CSI).

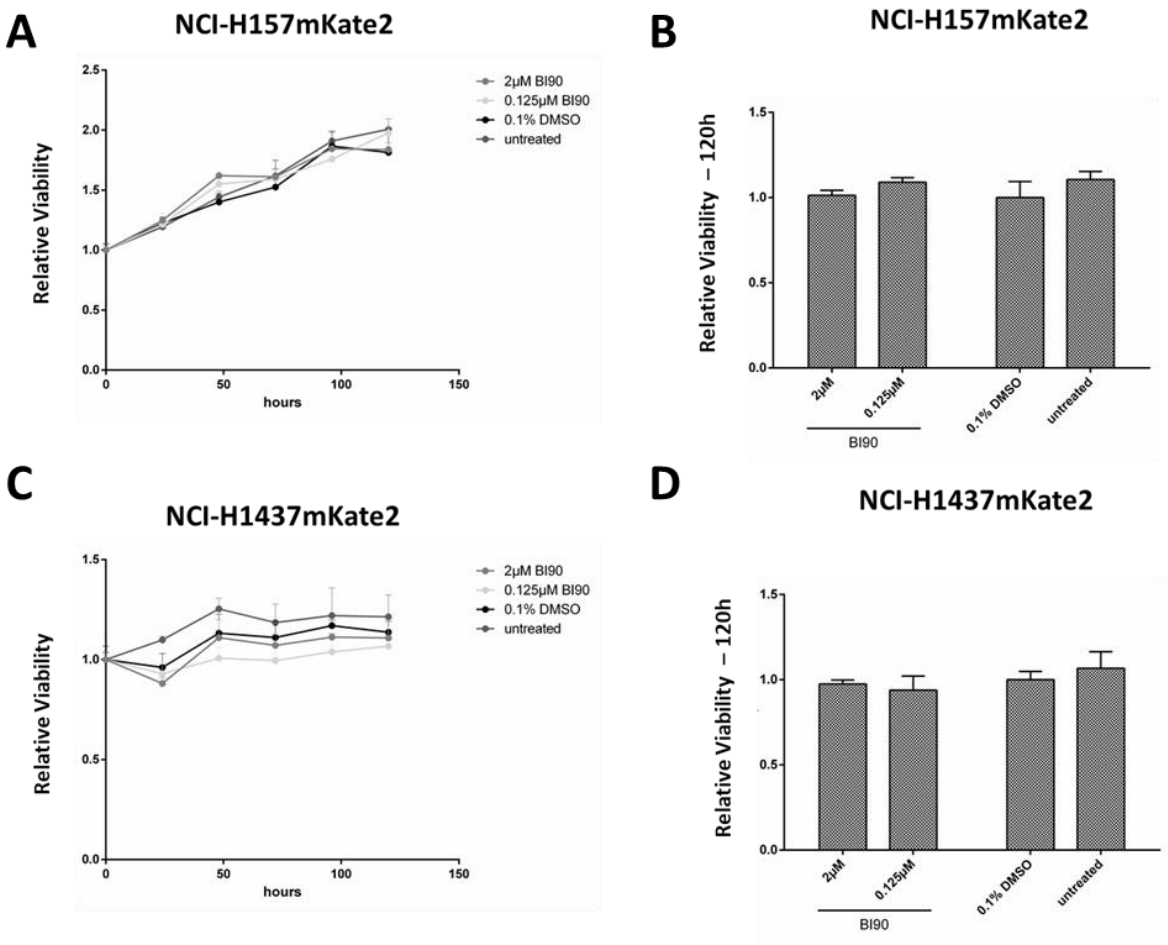

Figure 25: 3D growth potential of NCI-H157mKate2 (A, B) and NCI-H1437mKate2.

NCI-H157mKate2 (A, B) and NCI-H1437mKate2 (C, D) were grown as floater spheroids (mono-culture) in presence of BI90 (2 µM or 0.125 µM), 0.1 % DMSO or were left completely untreated. Growth was monitored over 120 hours (A, C). For better visualization, end points (120 hours) are presented as bar charts (B, D).

$5x10^3$ cells were seeded in 190 µL of medium per 96-well. Plates were incubated 24 hours before adding 10 µL of differently concentrated BI90 solutions or DMSO. Fluorescence (mKate2) was measured starting on day four after seeding, when compact spheroids had been formed. Analysis was performed in triplicates for each condition.

X-Axis: Different culture conditions.
Y-Axis: Relative tumour cell viability. For end point analysis relative viability was normalized to 0.1 % DMSO control.

5.1.4.3. Effect of BI90 Treatment on the Viability and Activity of Primary NK Cells (PNKs)

Next the viability and activity of PNKs after treatment with BI90 was examined (**Figure 26**). Moreover, the influence of BI90 on secretion of *GZMB* and *IFNG* by primary NK cell was examined (**Figure 27**). As tumour cells will be treated with BI90 before co-cultivation with immune cells, PNKs will be exposed to the drug as well. As an influence of BI90 on the activity of PNKs could not be ruled out *a priori*, secretion of *GZMB* and *IFNG* levels were determined at three time points.

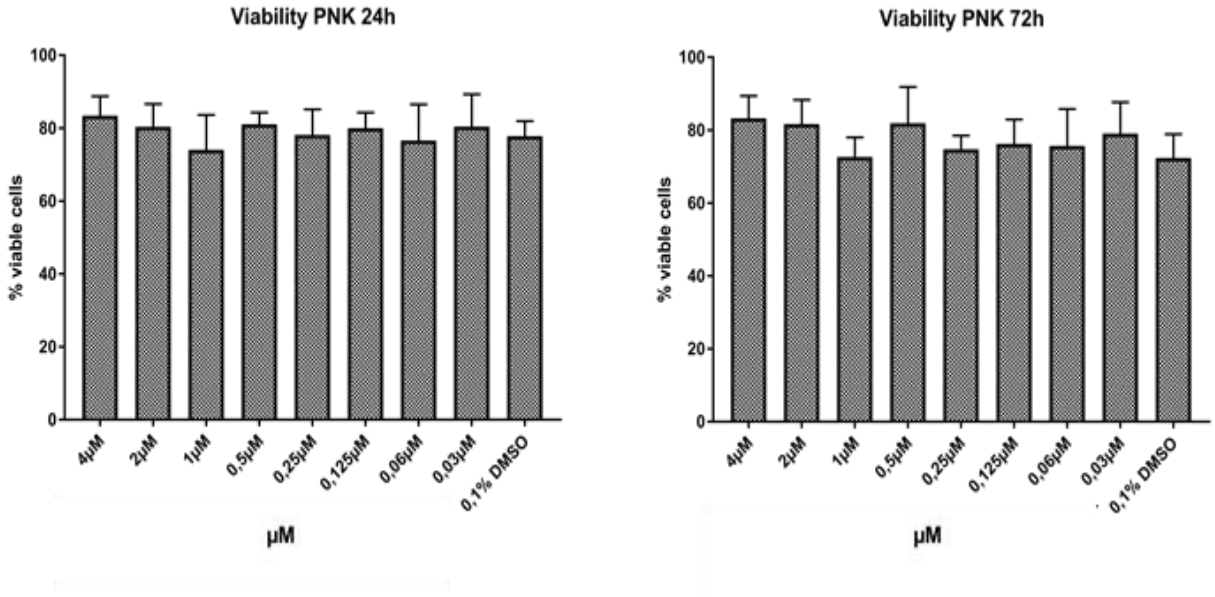

Figure 26: Viability of PNKs from two different donors after treatment with BI90.

PNKs were isolated from PBMCs using NK cells enrichment kit (see 4.9.1.). $4x10^5$ PNKs per donor were seeded in 1.9 mL medium/well into a 12-well plate. Either 100 µL of differently concentrated BI90-solution or PBS + 2 % DMSO were added. BI90 concentration series was from 4 µM to 300 nM. Final DMSO concentration was 0.1 %. Viability was determined 24 and 72 hours after addition of BI90. Viability was measured using automatic Trypan Blue Dye Exclusion method (Vi-CELL XR).
Analysis was performed in technical triplicates for each condition. For analysis, results from both Donors were combined.
X-Axis: Different concentrations of BI90 in µM and 0.1 % DMSO control.
Y-Axis: Percentage of viable cells.

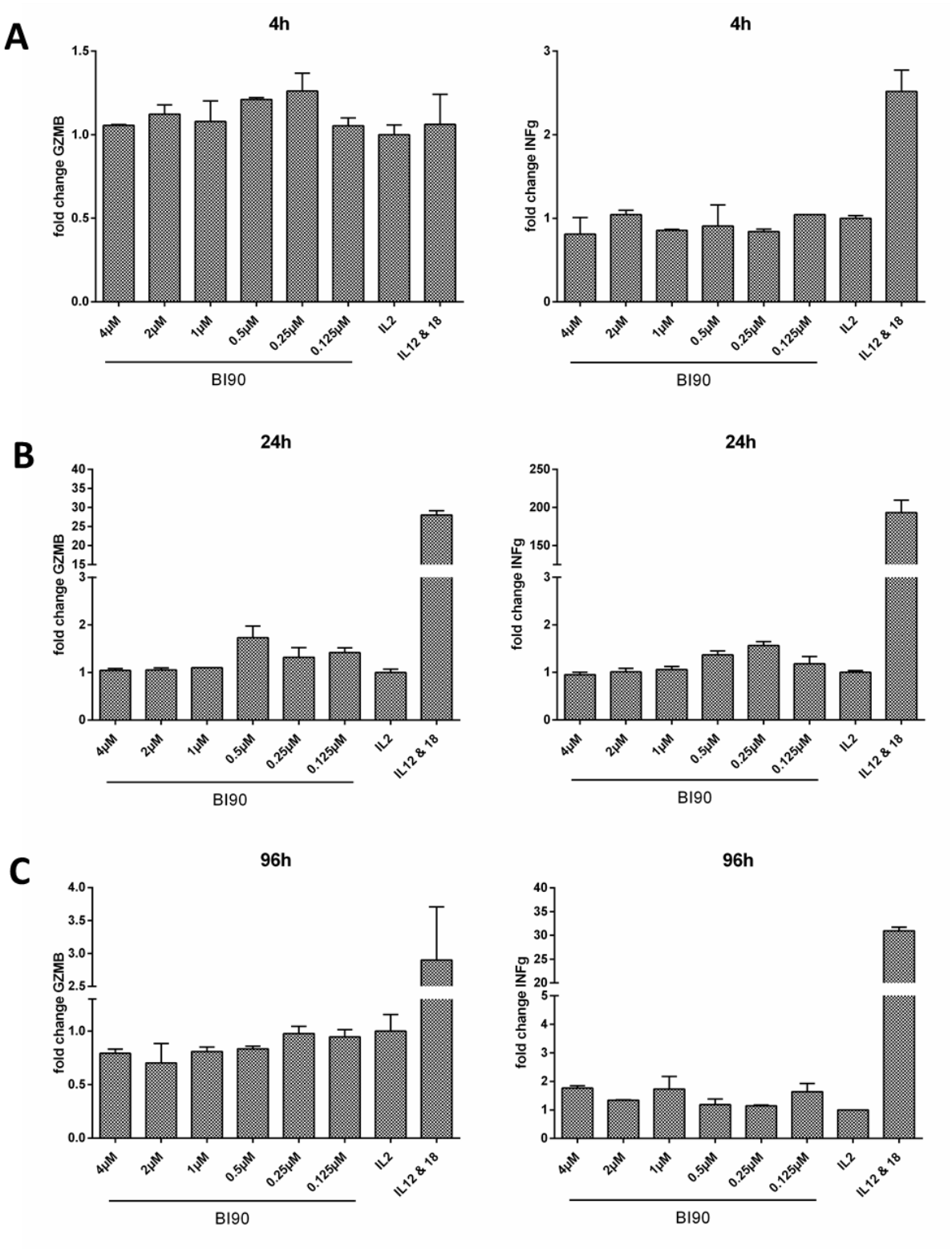

Figure 27: Secreted levels of Granzyme B (*GZMB*) and interferon γ (*INFG*) after 4 hours (A), 24 hours (B) and 96 hours (C) of treatment with BI90.

NK cells stimulation with either IL2 (10 ng/mL) or IL2 (10 ng/mL), IL12 (5 ng/mL) and IL18 (50 ng/mL) or IL2 (10 ng/mL) and different concentrations of BI90 (4 – 0.125 µM). X-Axis: Different stimulation and treatment conditions. Y-Axis: Fold changes normalized to untreated (IL2).

BI90 does neither significantly influence PNK's viability or activity nor the secretion of *GZMB* and *IFNG* in a dose-dependent manner. This holds true independently of the time of co-cultivation. Increased *IFNG* secretion is already detectable after 4 hours after adding IL12 and IL18. At 24 hours *GZMB* and *IFNG* levels reach their maxima but are still elevated after 96 hours in the positive control.

5.2. Three-dimensional (3D) Co-cultivation Studies in the Presence of BI90

5.2.1. Tumour Cell Viability in 3D Floater Cultures

To analyze if BI90 treatment does alter tumour cells´ immunogenicity in 3D co-cultures as well, 3D floater killing assays were performed. Floater assays are the simplest version of 3D models. They are relatively easy in handling and their generation is rather fast compared to other 3D models [74]. Even though they do not recapitulate the *in vivo* situation as good as other 3D culture systems such as matrix-embedded co-culture systems, they nevertheless are suitable for generating a first proof of concept [74]. According to preliminary data, genetic perturbation of *BPTF* prevented NURF formation and subsequently tumour cells became more immunogenic [68, 73]. If this also holds true for a pharmacologic inhibition of *BPTF* by BI90 tumour cell killing was determined in different 3D models. At first, 3D floater co-culture systems of NCI-H1437 or NCI-H157 and PNKs were generated and tumour cells viability was determined in the presence of BI90 (**Figure 28**, **Figure 29**). Supernatants were collected from NCI-H1437 + PNK co-cultures for analysis of *IFNG* and *GZMB* secretion levels (**Figure 30**).

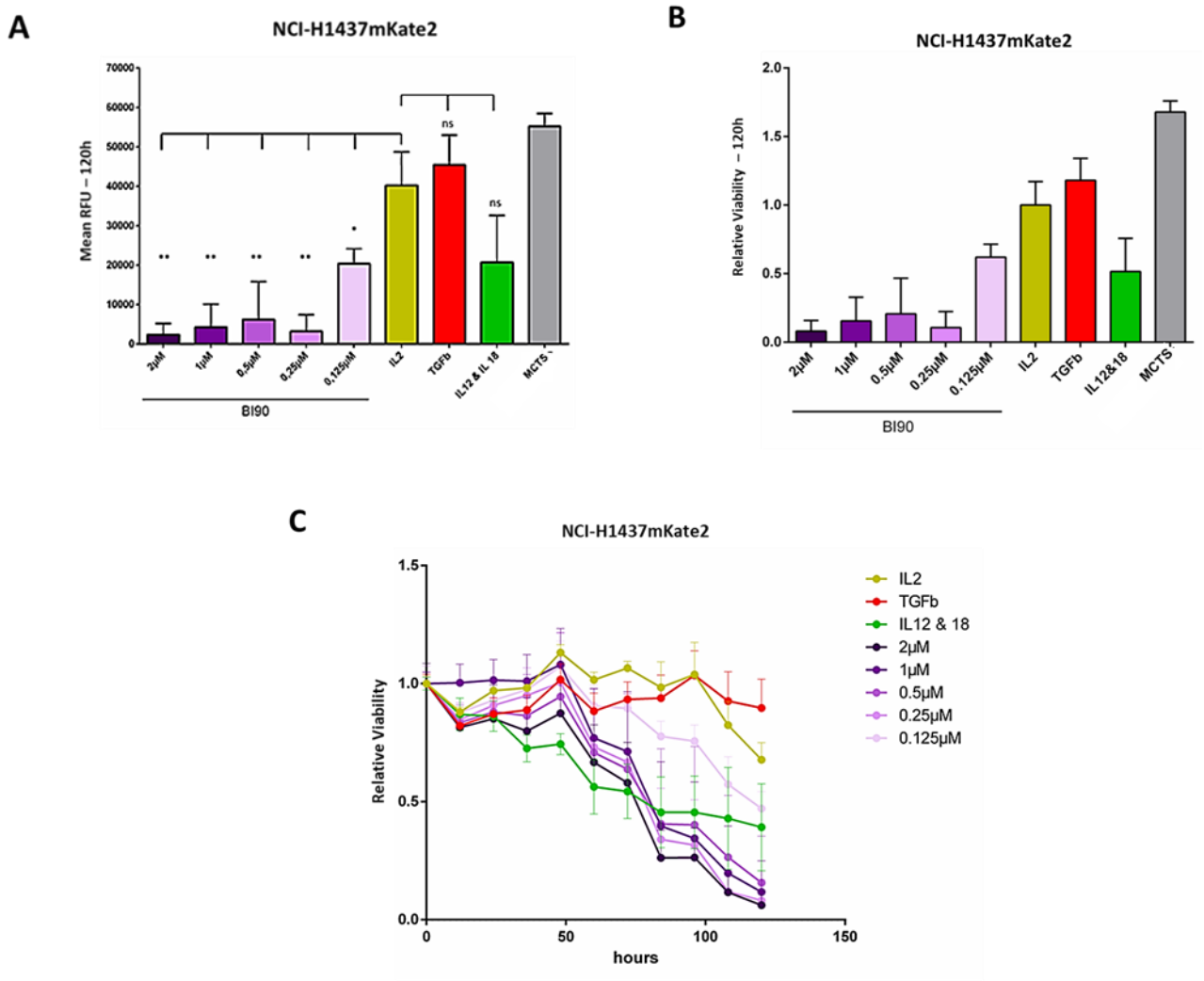

Figure 28: BI90 treatment of 3D co-cultures from NCI-H1437mKate2 floater spheroids and PNKs.

Mean RFU (A) and relative viability (B) compared to IL2 control of MCTSs were determined after 120 hours. (C) Time course of NCI-H1437mKate2 viability after adding PNK.

$5x10^3$ cells were seeded in 190 µL of medium per 96-well. Plates were incubated 24 hours before adding 10 µL 20X of the respective BI90 solutions. Concentration series were from 2 µM to 125 nM. PNKs were isolated from PBMCs and pre-stimulated for 72 hours with either IL2 (10 ng/mL), or TGFb (1 ng/mL) plus IL2 (10 ng/mL) as a negative control. Treatment with IL12 (5 ng/mL) and IL18 (50 ng/mL) and IL2 (10 ng/mL) served as a positive control. After 96 hours six MCTSs were harvested, pooled and dissolved to determine the cell number per MCTS. The E:T ratio was 3:1. Fluorescence of tumour cells determined using Perkin Elmer's EnVision. Analysis was performed in triplicates for each condition.

X-Axis: Different treatment conditions (A, B) or hours (C).
Y-Axis: Mean RFU (+STD) indicating tumour cell viability (A). Relative Viability (B, C).
E:T ratio: Effector (PNKs):Target (tumour cells) ratio; ns: not significant; Mean RFU: Mean relative fluorescence units.
Assay was repeated three times with three different PNK donors. Figure represents one representative example. $p > 0.5$: ns, $p < 0.05$: *, $p < 0.01$: **, $p < 0.001$: ***

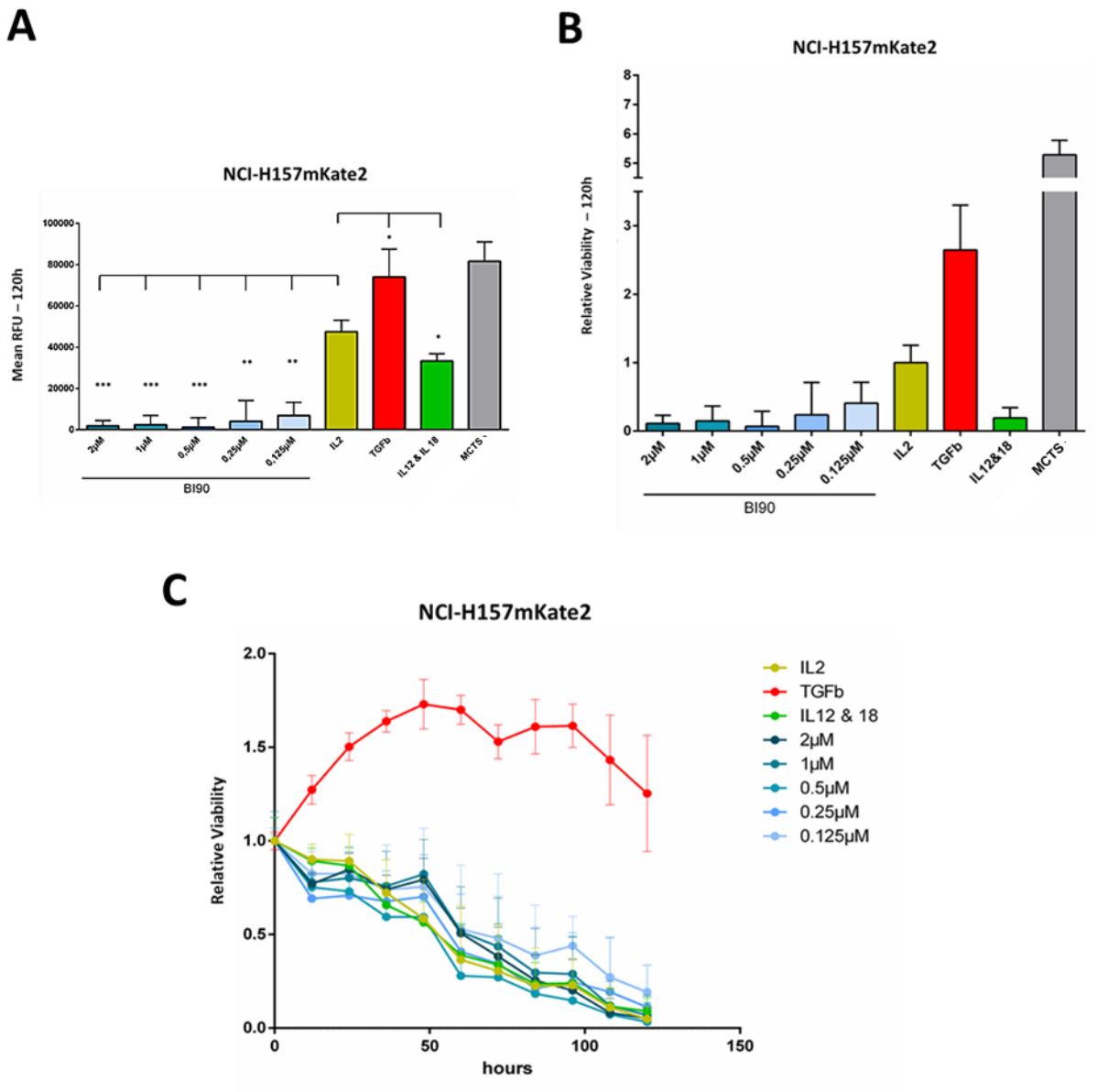

Figure 29: BI90 treatment of 3D co-cultures from NCI-H157mKate2 floater spheroids and PNKs.

Mean RFU (A) and relative viability (B) compared to IL2 control of MCTSs were determined after 120 hours. (C) Time course of NCI-H157mKate2 viability after adding PNKs.
For assay details see Figure 28.

X-Axis: Different treatment conditions (A, B) or hours (C).
Y-Axis: Mean RFU (+STD) indicating tumour cell viability (A). Relative Viability (B, C).
Mean RFU: Mean relative fluorescence units.
$p > 0.5$: ns, $p < 0.05$: *, $p < 0.01$: **, $p < 0.001$: ***

For both cell lines, treatment with BI90 leads to significantly increased tumour cell killing compared to IL2 control. In case of IL2 control MCTSs were pre-treated with 0.1 % of DMSO only. Co-cultivation for five days leads to almost complete NCI-H157 tumour cell clearance even at a low concentration of BI90 (**Figure 29**). In 3D NCI-H1437mKate2 floater co-cultures, reduction in MCTS viability was even higher in BI90 treated spheroids than in the respective positive control (IL12 & IL18) except for the lowest concentration of BI90 (0.125 µM). Positive control (IL12 & IL18) and DMSO & IL2 control exhibited strong reduction in MCTSs viability. As described, stimulation of NK cells with TGFβ reduced PNK's cytotoxic potential [94]. However, significant differences between IL2 and TFGβ stimulation were only observed in NCI-H157, as IL2 stimulation did not induce strong killing of DMSO treated NCI-H1437 MCTSs.

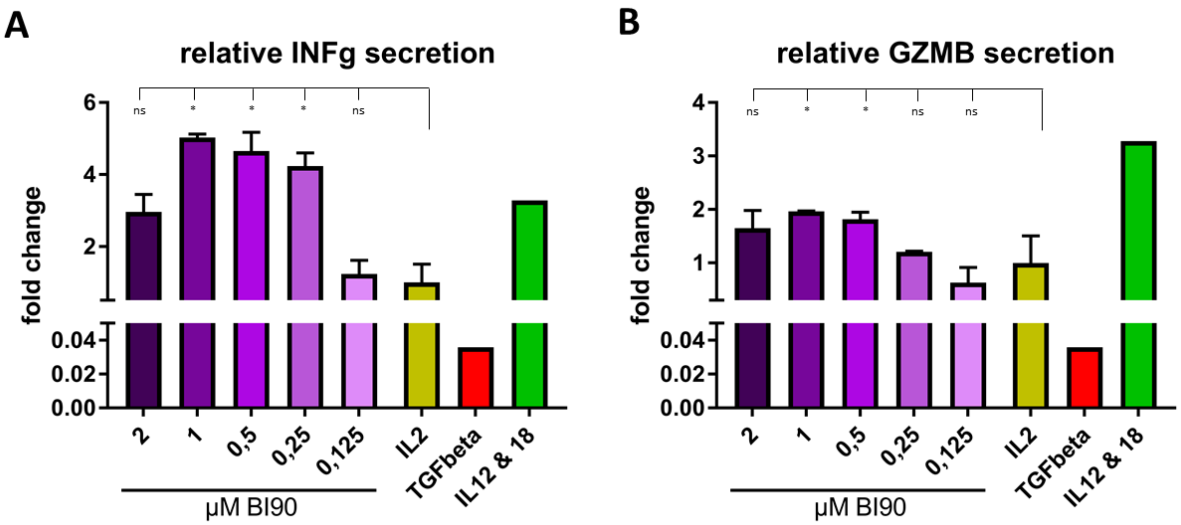

Figure 30: *IFNG* (A) and *GZMB* (B) secretion in 3D floater co-cultures of NCI-H1437mKate2 and PNKs after 72 hours.

For details see Figure 28. For analysis results from two PNK donors were combined.
X-Axis: Different assay conditions.
Y-Axis: Fold change of *IFNG* and *GZMB* normalized to IL2 treatment.
ns: not significant
$p > 0.5$: ns, $p < 0.05$: *

TGFβ reduces *IFNG* and *GZMB* production, while the addition of IL12 & IL18 stimulates the production in comparison with IL2 treatment. An increase in *IFNG* secretion was also

observed in BI90 treated co-cultures. Except for 2 µM a dose dependent production of *IFNG* is observed. The same holds true for secretion of *GZMB*.

5.2.2. Tumour Cell Viability and PNK Infiltration in BI90 Treated 3D Embedded Co-Cultures

Next we analyzed whether BI90 treatment does also lead to an increase in the immunogenicity of NSCLC cells in a more complex *in vivo*-like assay set up (for details see Introduction and Discussion). 3D embedded co-cultures of NCI-H1437 or NCI-H157, HDFs and PNKs were generated. Viability of NCI-H1437mKate2 (**Figure 31**, **Figure 32**) and NCI-H157mKate2 (**Figure 33**) was analysed. In addition, the infiltration of PNKs into MCTS was monitored and quantified. To enable the analysis of active migration, PNKs were stained with Cell Tracer CFSE and HDFs with Cell Tracker Blue. Confocal fluorescence image z-stacks were made 24 hours, 48 hours and 72 hours after embedding. Maximum intensity projections were generated (**Figure 31C**, **Figure 33C**) and infiltration of PNKs into MCTSs was calculated either by counting or using an algorithm co-developed at the University of Turku (**Figure 34**).

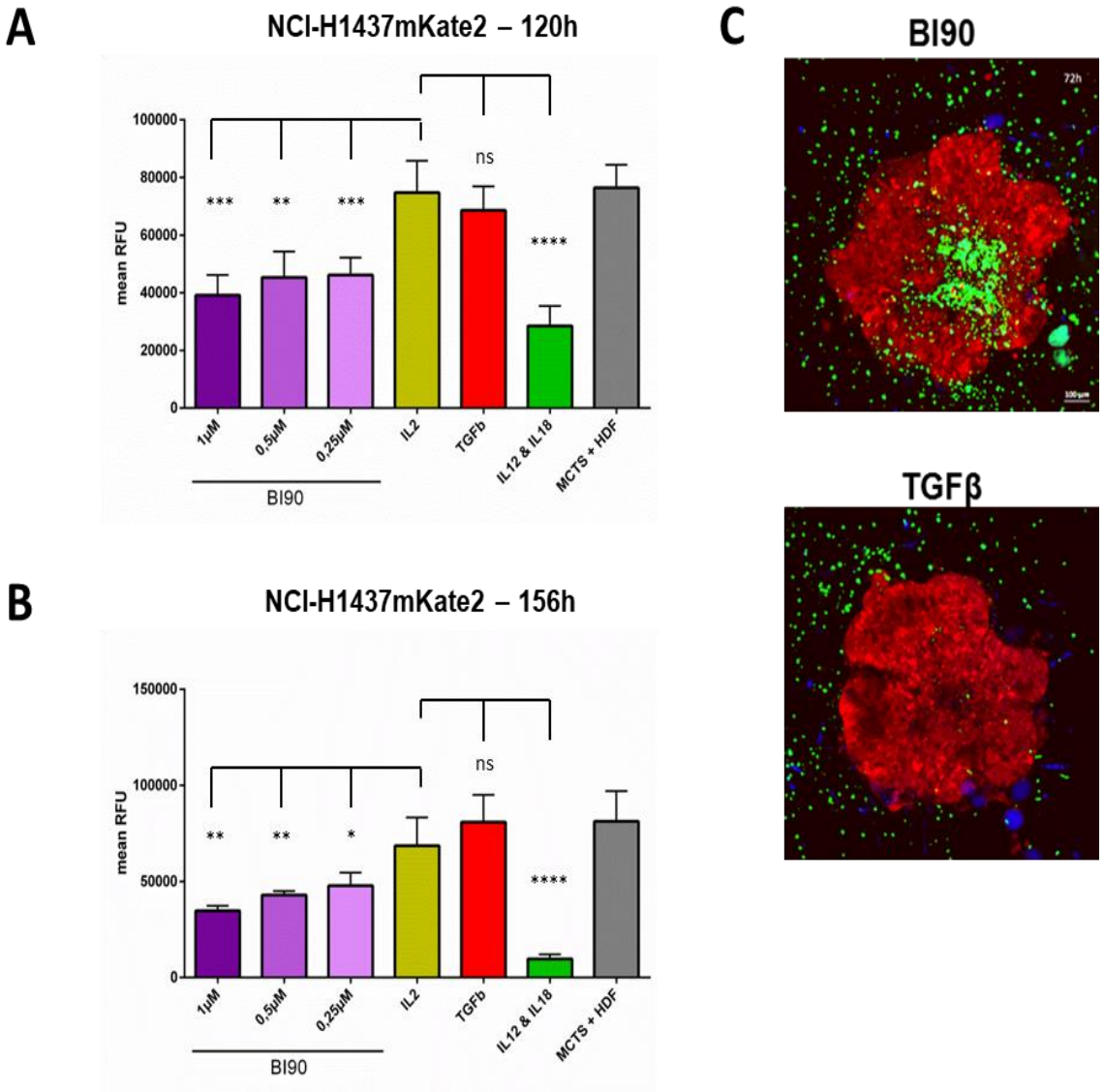

Figure 31: Tumour cell viability (NCI-H1437) in embedded triple cultures treated with BI90.

NCI-H1437mKate2 were grown as spheroids and embedded with PNKs and human dermal fibroblasts (HDFs). Tumor cell viability of MCTS was determined 120 hours (A) and 156 hours (B) after embedding. (C) Maximum intensity projections of z-stacks from triple-culture with PNKs and HDFs. BI90: 1 µM; TGFß: 1 ng/mL; IL2: 10 ng/mL; IL12: 5 ng/mL; IL18: 50 ng/mL. MCTSs: red (mKate2), PNKs: green (CFSE) and HDFs: blue (cell tracer blue).

$1x10^4$ cells were seeded in 190 µL of medium per 96-well. Plates were incubated 24 hours before adding 10 µL of 20X BI90 solutions. Concentrations series were from 1 µM to 125 nM. PNKs were isolated and pre-stimulated as described in Figure 28. 96 hours after seeding MCTSs were embedded together with $1x10^5$ PNKS (stained with CFSE) and $2x10^4$ HDFs (stained with cell tracer blue) per well. Fluorescence was determined using Perkin Elmer's EnVision. Analysis was performed in six replicates per condition.
X-Axis: Different treatment conditions. Y-Axis: Mean RFU (+ STD) indicating tumour cell viability. Mean RFU: Mean relative fluorescence units. Experiment was repeated three times with three different PNK donors. ns: not significant
$p > 0.5$: ns, $p < 0.05$: *, $p < 0.01$: **, $p < 0.001$: ***, $p < 0.0001$: ***

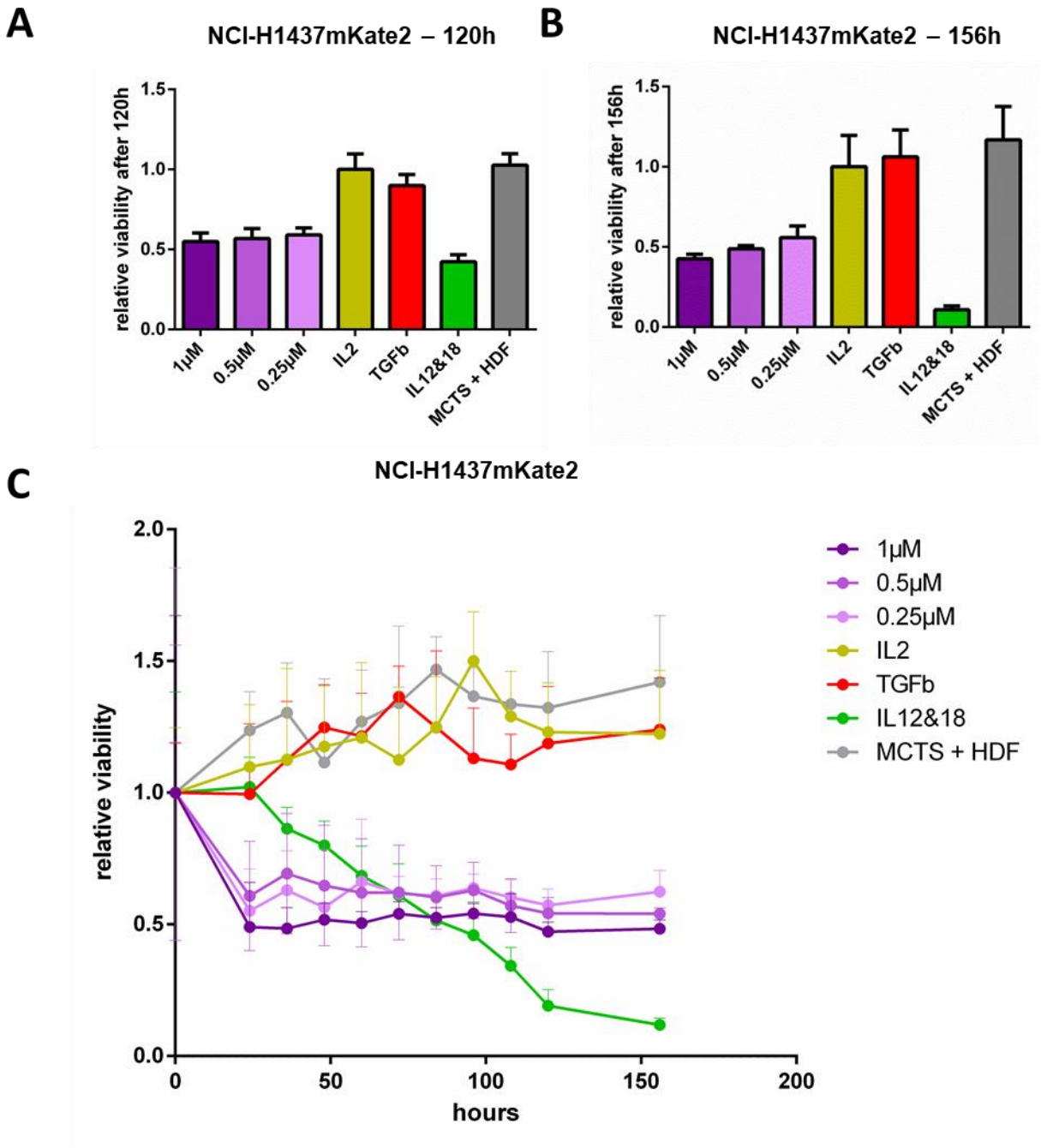

Figure 32: Relative tumour cell viability (NCI-H1437) in embedded triple cultures treated with BI90.

Relative MCTSs viability was determined 120 hours (A) and 156 hours (B) after embedding. (C) Presents a time course of relative MCTSs viability upon embedding.

Absolute data (measured mean RFU) presented in Figure 31 was normalized towards measured values of time zero (= directly after embedding). For the bar charts (A, B) relative viability normalized to IL2 control.

X-Axis: Different treatment conditions (A, B) or hours (C).
Y-Axis: Fold change in tumour cell viability.

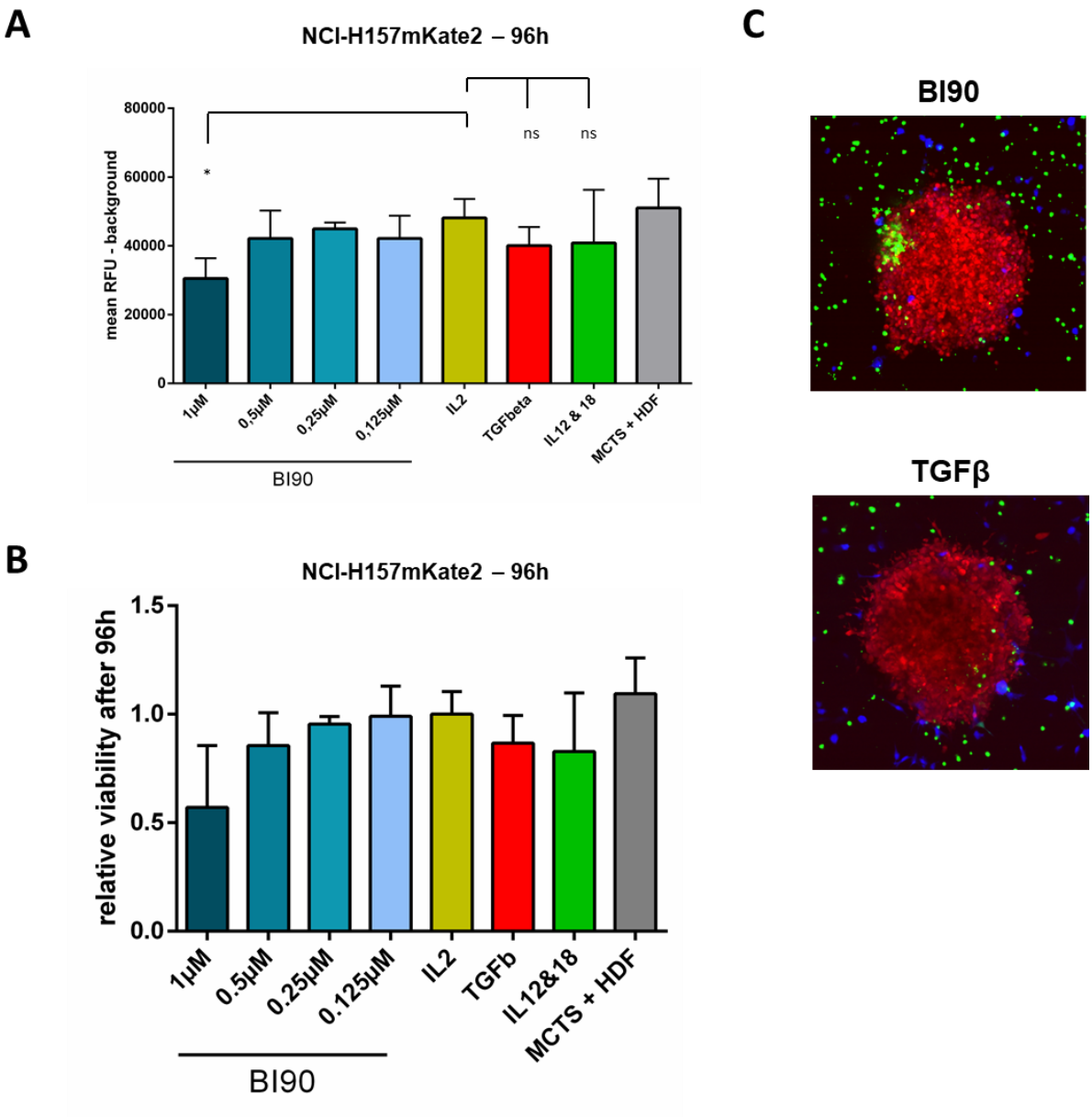

Figure 33: NCI-H157mKate2 were grown as spheroids and embedded with PNKs and human dermal fibroblasts (HDFs). MCTSs viability was determined 96 hours after embedding.

Mean Fluorescence (A) and relative viability (B) are presented. (C) Maximum intensity projections of z-stacks from triple-culture with PNKs and HDFs. BI90: 1 µM; TGFß: 1 ng/mL; IL2: 10 ng/mL; IL12: 5 ng/mL; IL18: 50 ng/mL. MCTSs: red (mKate2), PNKs: green (CFSE) and HDFs: blue (cell tracer blue).

For assay details see Figure 31 ($5x10^3$ NCI-H157 were seeded instead of $1x10^4$).
X-Axis: Different treatment conditions. Y-Axis: Mean RFU (+ STD) indicating tumour cell viability (A) or fold change in tumour cell viability (B). For relative tumour cell viability, absolute data (measured mean RFU) presented in (A) was normalized towards measured values of time zero (= directly after embedding). For the bar charts (A, B) relative viability normalized to IL2 control.
Assay was redone three times with three different PNK donors.
$p > 0.5$: ns, $p < 0.05$: *

In 3D embedded co-culture models, dose-dependent reduction in viability of BI90 treated MCTSs was observed for both cell lines. In general, effects were smaller compared to 3D floater co-cultures. In the floater model, treatment with BI90 (2 µM – 0.25 µM) induced virtually complete MCTSs destruction for both cell lines whereas in the embedded system reduction in NCI-H1437mKate2 viability was around 50 % compared to DMSO & IL2 control (**Figure 31**, **Figure 32**). For NCI-H157 a reduction of about 50 % compared to DMSO & IL2 was only observed in presence of 1 µM BI90, while the other concentrations (0.5 µM – 0.125 µM) did not cause significant reduction in MCTS's viability (**Figure 33**).

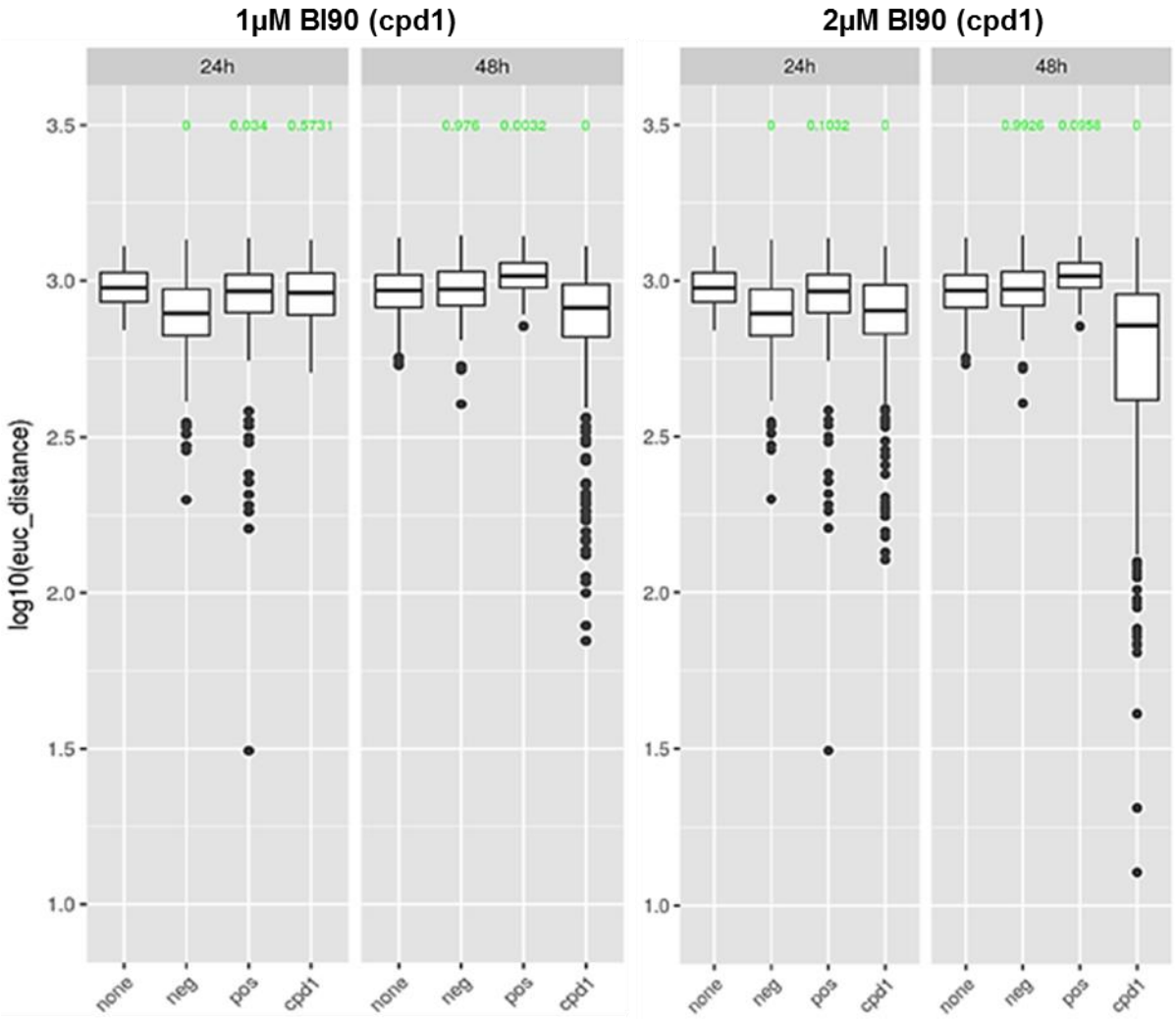

Figure 34: Euclidian distance-based algorithm to analyse infiltration rates of PNKs co-cultivated with NCI-H1437dTomato and HDFs in an embedded 3D culture.

Distance (euc_distance; Y-Axis) was plotted against different time points (24 hours and 48 hours) for each treatment (1 µM BI90 and 2 µM BI90) (X-Axis). euc_distance (in pixel) represents distance of NK cells towards MCTSs mass center. Y-Axis is logarithmic to show outliers better. Outliers represent NK cells, which rapidly infiltrated tumour spheroids.

None: IL2 (10 ng/mL), neg: TGFβ (1 ng/mL) & IL2 (10 ng/mL), pos: IL12 (5 ng/mL) & IL18 (50 ng/mL) & IL2 (10 ng/mL), cpd1: BI90 & IL2 (10 ng/mL).

For all conditions DMSO levels were kept equal at 0.1 %.
For details of generation of 3D embedded culture see Figure 31.

Increased infiltration was observed in presence of BI90 compared to controls. In contrast to BI90 concentration at 1 µM, infiltration was already detectable after 24 hours at 2 µM BI90 and was further increased after 48 hours. Outliers (with a low euc_distance value) represent

NK cells which rapidly infiltrated tumour spheroids. Thus, a small euc_distance indicates high infiltration. Note: The algorithm was co-developed with University Turku/Finland (collaborators: Nees Matthias, Hannu-Pekka Schukov and Malin Åkerfelt; Manuscript is in preparation).

5.3. *HPSE* Transcript Levels after BI90 Treatment

A previous study showed that shRNA-mediated *BPTF* knock down leads to reduced *HPSE* (heparanse) expression. Thereby removal of heparan sulfates – known to function as NCR co-ligands – by *HPSE* is prevented. As a consequence, NK cells recognise tumour cells more efficiently and can attack them [42, 68]. Therefore, we next analysed *HPSE* transcript levels by qPCR in NSCLC tumor cell lines upon treatment with BI90 (**Figure 35**).

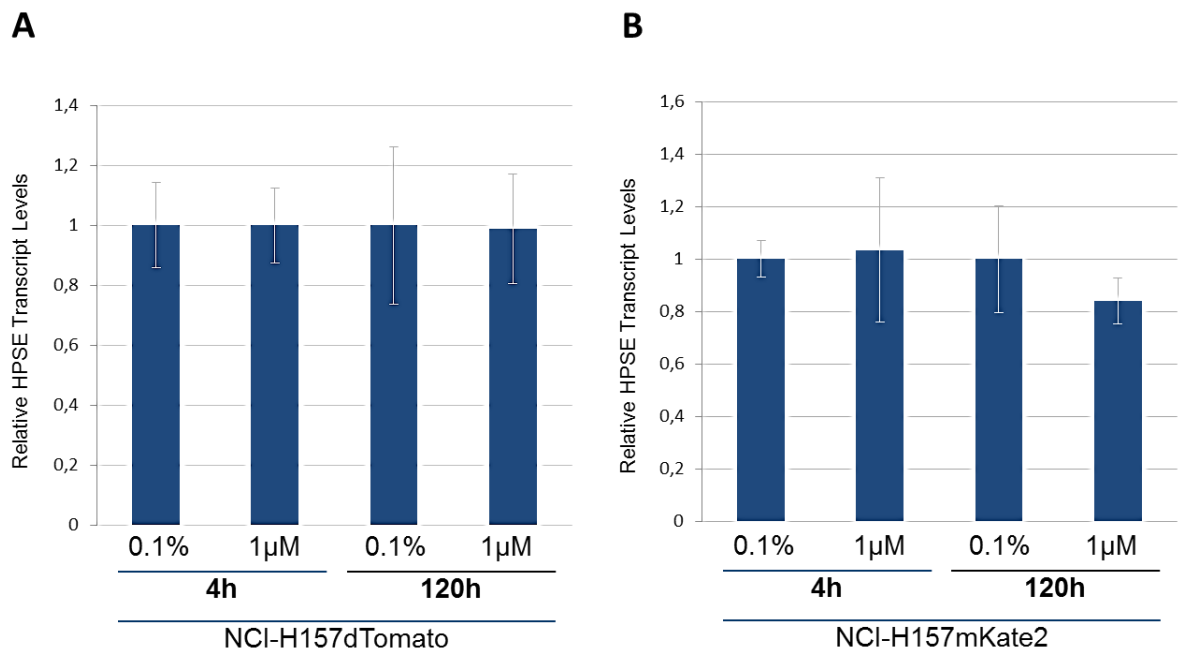

Figure 35: Relative *HPSE* transcript levels in (A) NCI-H157dTomato and (B) NCI-H157mKate2 after treatment with BI90.

$0.75x10^6$ cells were seeded in 2 mL medium. 24 hours after seeding cells were washed and fresh medium containing 1 µM BI90 was added.
Samples were taken after 4 hours and 120 hours. RNA was isolated and cDNA was generated. qPCR was performed in four replicates per condition. 18S rRNA served as housekeeping gene. Relative transcript levels were calculated by normalizing to 18S rRNA transcript levels and *HPSE* levels in 0.1 % DMSO control.
X-Axis: Time points and treatment modalities.
Y-Axis: Relative transcript levels.

No significant reduction of *HPSE* transcript levels was detected - neither after short time exposure (4 hours) to BI90 nor after long term treatment (120 hours).

5.4. Genetic Perturbation of *BPTF* in NSCLC cell lines NCI-H157 and NCI-H1437

CRISPR technology allows specific destruction of genes with high specificity. Knock out (KO) caused by CRISPR is stable in contrast to siRNA-mediated knock down (KD) [95, 96]. As a consequence, KO leads to more severe effects than transient KD, stable shRNA-mediated KD or pharmacological target inhibition.

5.4.1. siRNA-mediated *BPTF* Knock Down in NCI-H157

To compare effects caused by pharmacological inhibition of *BPTF* with effects generated by genetic approaches, transient siRNA-mediated *BPTF* KD was performed. This was of particular importance, as the overall transduction efficiency for NCI-H157 was too little, to sort for *BPTF* KO cells during the CRISPR assay (**Figure 38**, **Figure 39**). Therefore, siRNA-mediated KD was used as an alternative. Deconvoluted siRNAs against *BPTF* were used to knock down its expression in NCI-H157. As for KO experiments, it is necessary in KD studies to confirm that proteins of interest are actually targeted. For small chemical entities target specificity cannot be tested easily and one has to rely on *in vitro* specificity assays.

3.3.2. Confirmation of *BPTF* KD

The first step was to confirm *BPTF* KD. For this, protein lysates were generated after transfection (see Material and Methods: siRNA Mediated Knock Down (KD) Studies) and analysed by WES (**Figure 36**).

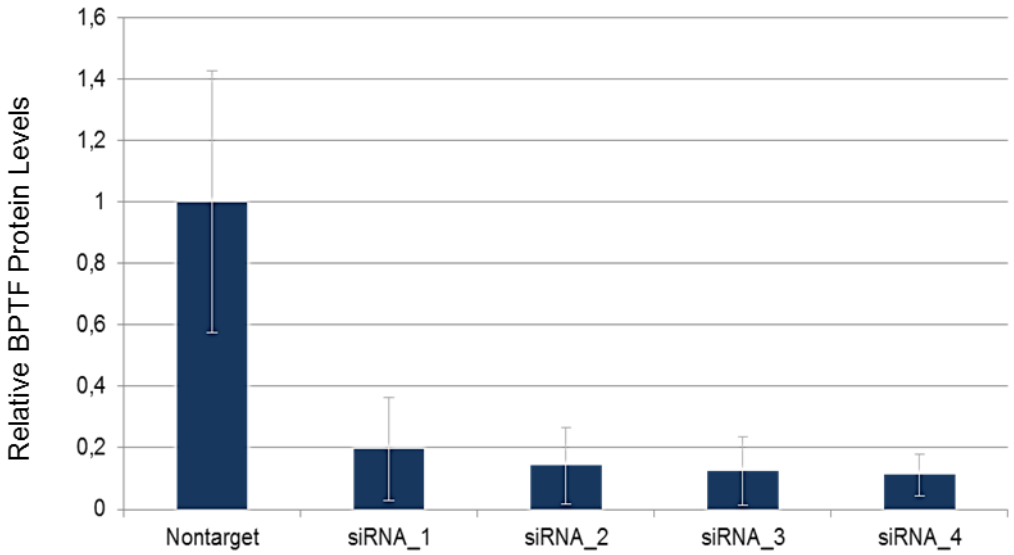

Figure 36: Relative *BPTF* protein levels in NCI-H157 48 hours after siRNA transfection.

Revers transfection was performed. $0.375x10^6$ cells were seeded. siRNA 1 to 4 target *BPTF*. Cells were incubated 48 hours post transfection before generating protein lysates (0.2 µg/µL). *BPTF* abundance was quantified by WES protein simple analysis in technical triplicates.
Antibodies against *BPTF* (1:25) and vinculin (1:500) were used. *BPTF* levels were normalized to vinculin and nontarget control.
X-Axis: Different treatment modalities.
Y-Axis: Relative *BPTF* expression.

All four used deconvoluted siRNAs reduced *BPTF* expression substantially compared to nontarget siRNA. As reduction was efficient with all four tested siRNAs, all four were selected for further co-culture studies.

5.4.2. PNK-mediated Killing of *BPTF* KD Tumour Cells

siRNA-mediated *BPTF* KD cells were used in 2D co-culture assays (**Figure 37**). 2D cultivation was chosen because siRNA-mediated effects are transient [95] and 3D cultivation requires a longer lead time before starting the actual experiment. Therefore, it cannot be ruled out that normal expression levels might have been restored by the time tumour cells would have formed spheroids.

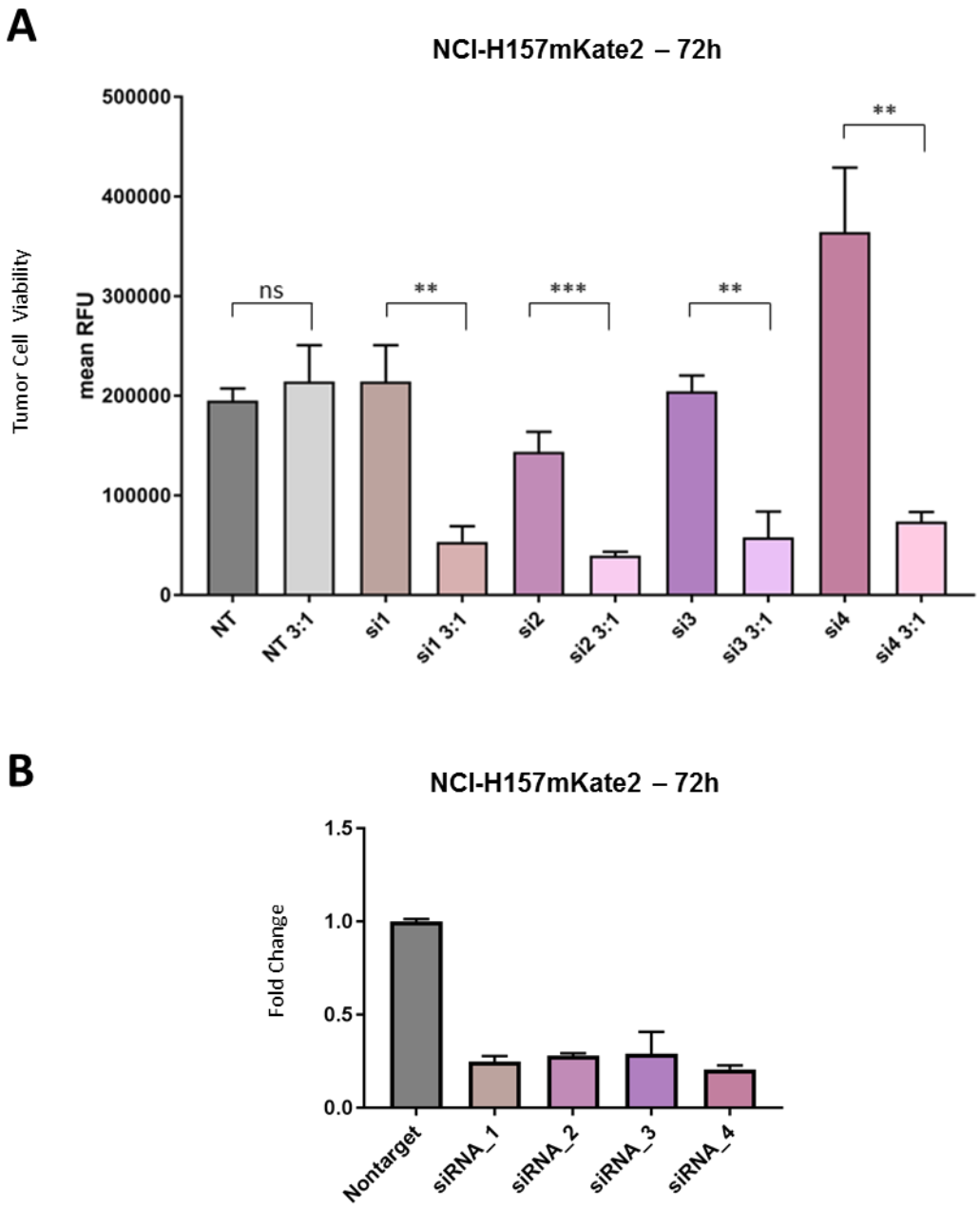

Figure 37: Viability of NCI-H157 BPTF KD 72 hours after adding PNKs (A) and the corresponding fold change of viability in the presence of PNKs (B).

Revers transfection was performed. $1x10^4$ cells were seeded per 96-well. siRNAs 1 to 4 (si1 – si4) target *BPTF*. Cells were incubated 24 hours before adding PNKs.
$3x10^4$ PNKs were added per well. Tumour cell viability was measured by Presto Blue assay 72 hours after adding PNKs.
Results from viability assay were used to calculate fold changes for each siRNA compared to the nontarget control.

$p > 0.5$: ns, $p < 0.05$: *, $p < 0.01$: **, $p < 0.001$: ***

BPTF KD in NCI-H157 led to a highly significant reduced viability in co-cultures compared to mono-cultures. In contrast, no differences in viability of NCI-H157 mono- and co-cultures transfected with nontarget control were detectable. Although - due to technical reasons - a *BPTF* KO was not feasible in NCI-H157, transient *BPTF* KD strongly increases NK cell-mediated tumour cell killing in this cell line. This indicates that even a transient *BPTF* KD has the potential to increase the immunogenicity of tumour cells.

5.4.3. CRISPR/Cas9 Depletion Assay

First it was determined whether BPTF KO does influence tumour cells viability (**Figure 38**, **Figure 39**). Nine different small guide RNAs (sgRNAs) targeting different domains of *BPTF* were designed and used in a depletion assay. The plasmid encoding for the sgRNAs additionally encodes for GFP which makes it possible to detect transduced cells easily and to follow the percentage of GFP-positive cells over time (enrichment or depletion). If an essential gene is destroyed, the amount of GFP positive cells will decrease rapidly.

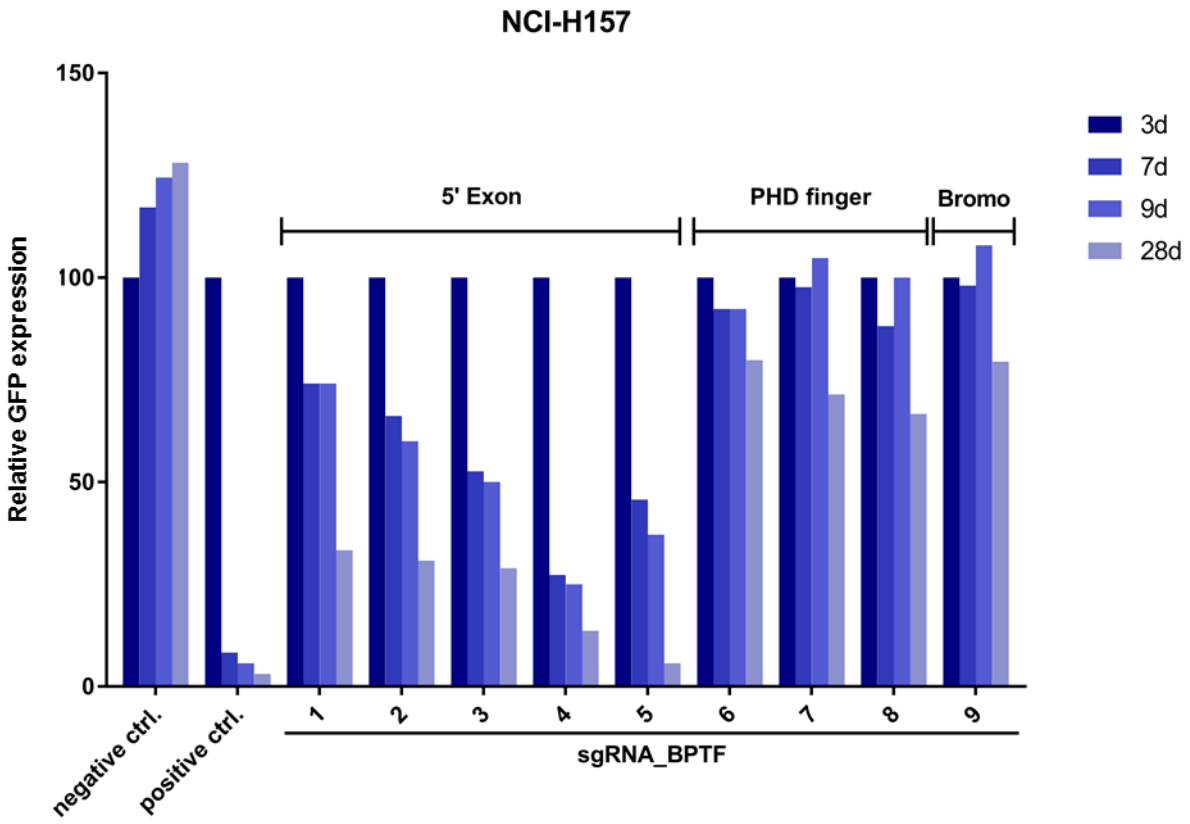

Figure 38: NCI-H157: GFP depletion indicates domain-specific effects of *BPTF* KO on cells viability.

$2x10^5$ cells were seeded in 2.5 mL medium and pre-treated with 8 µg/mL polybrene for 24 hours. Cells were washed and 1mL of medium and 400 µL of virus were added per well. Starting from day three post transduction, cells were analysed by flow cytometry to track number of GFP positive cells.
X-Axis: Different sgRNAs used and different time point of analysis.
Y-Axis: Relative percentage of GFP positive cells. Signal obtained at first analysis on day 3 was set as 100 % and values obtained from later measurements were normalized towards it.

Positive control: sgRNA targeting *POLR2A* which encodes for RNA polymerase II subunit A. Negative control: sgRNA targeting a sequence not present in the human genome.

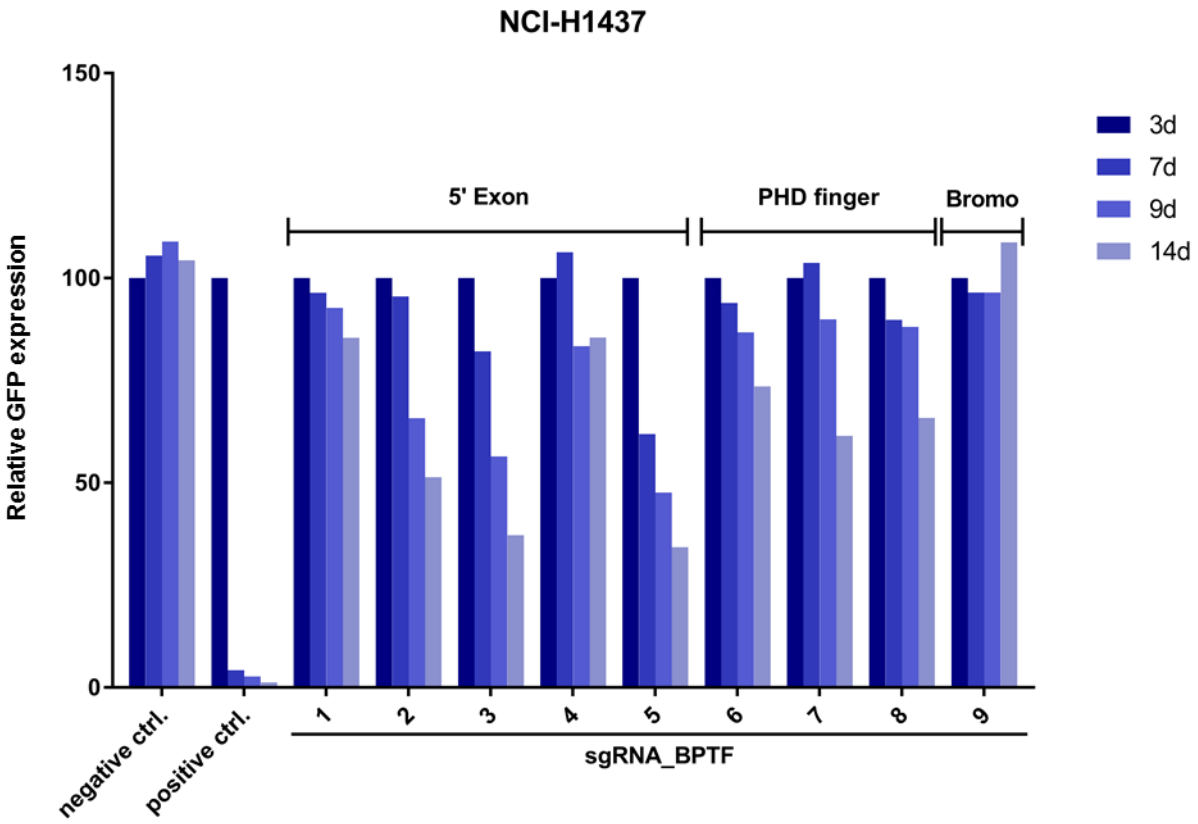

Figure 39: NCI-H1437: GFP depletion indicates domain-specific effects of *BPTF* KO on cells viability.

For details see Figure 38.

As shown in **Figure 38** and **Figure 39** the positive control proofed depletion efficacy, the negative one does not affect viability of GFP positive cells at all. Interestingly, *BPTF* KO influence cells viability in both - NCI-H157 and NCI-H1437 - in a domain-specific manner. Strongest effects were observed with sgRNA *BPTF* 1 - 5 targeting the 5' exon. sgRNAs targeting PHD finger domain (sgRNA *BPTF* 5 – 7) show less effects. sgRNA *BPTF* 9 (Bromodomain) does not reduce cell's viability. Overall stronger effects were observed in NCI-H157 compared to NCI-H1437.

Next, cell populations of NCI-H1437 transfected with sgRNA *BPTF* 1, 6, 8 and 9 were sorted including the nontarget control. By this at least one sgRNA targeting the 5' exon, PHD domain or bromodomain were selected. It was possible to enrich for GFP expressing NCI-H1437 populations. Unfortunately, low transduction efficacy in NCI-H157 prevented FACS

sorting. Therefore, all further experiments were only performed in NSCLC cell line NCI-H1437.

5.4.4. Confirmation of *BPTF* KO in Cell Pools

To analyse whether GFP enriched populations exhibit indeed reduced *BPTF* expression levels, WES analysis of the respective sgRNA pool cultures was performed (**Figure 40**).

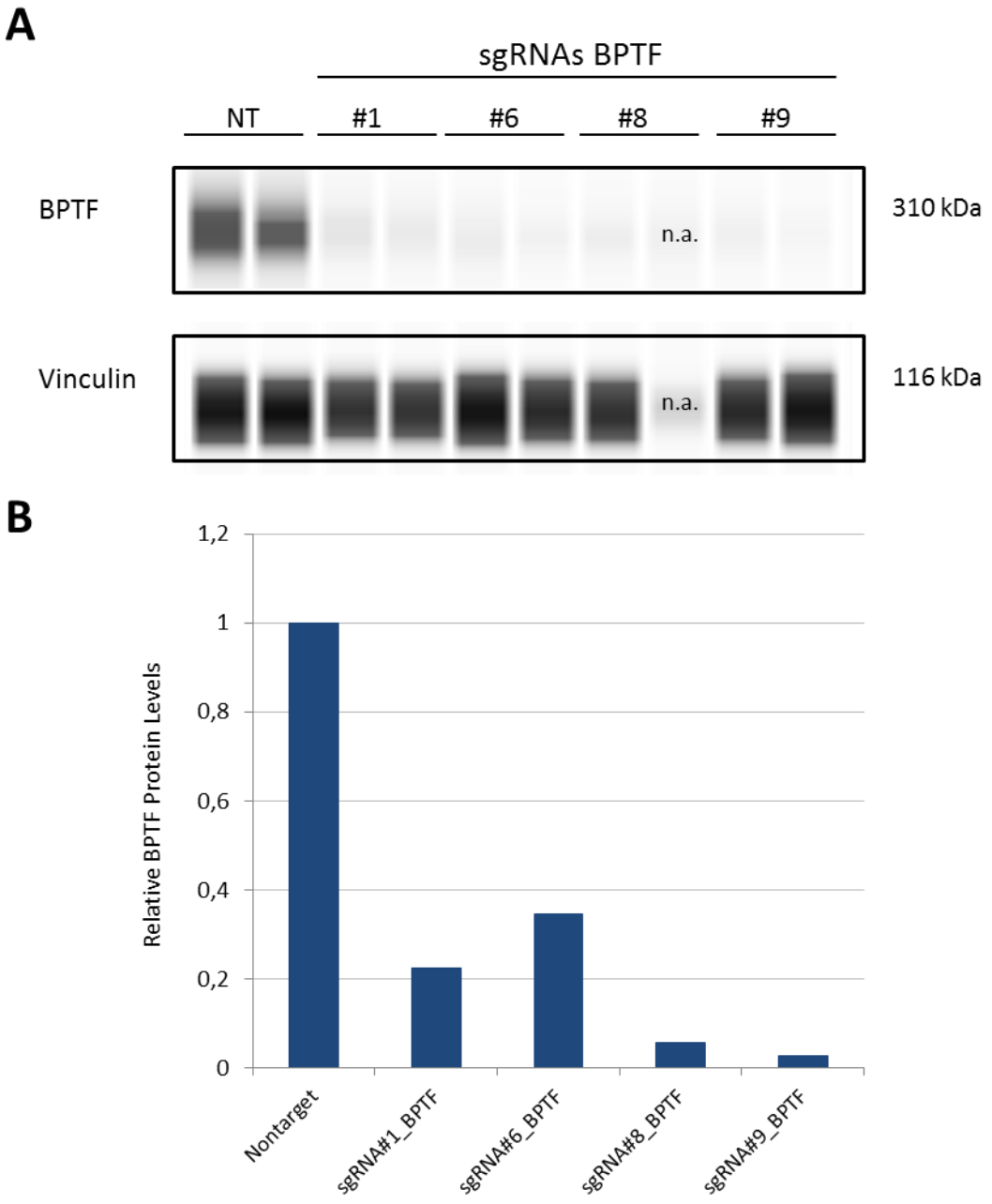

Figure 40: WES protein simple assay (A) and deduced relative *BPTF* expression levels in different pools of NCI-H1437 populations (B).

Protein lysates were generated (0.2 µg/µl) for WES analysis. Antibodies against *BPTF* (1:25) and vinculin (1:500) were used. *BPTF* levels were compared to vinculin and normalized to the *BPTF* levels in nontarget control samples (set to 1).
X-Axis: Different used cell lines (pools).
Y-Axis: Relative protein levels.

5.4.5. *HPSE* and *NDST1* Transcript Levels in *BPTF* KO Cells

As shown in **Figure 35**, pharmacologic target inhibition via BI90 did not lead to reduced *HPSE* expression levels. To determine whether *BPTF* KO is able to reduce *HPSE* and/or *NDST1* expression qPCR was performed of NCI-H1437 cell pools (**Figure 41**). Apart from *HPSE*, *NDST1* is another gene claimed to be (de)regulated by *BPTF* [68]. GFP^+ cells transduced with either nontarget control or sgRNA *BPTF* 1, 6, 8, 9 were used for analysis.

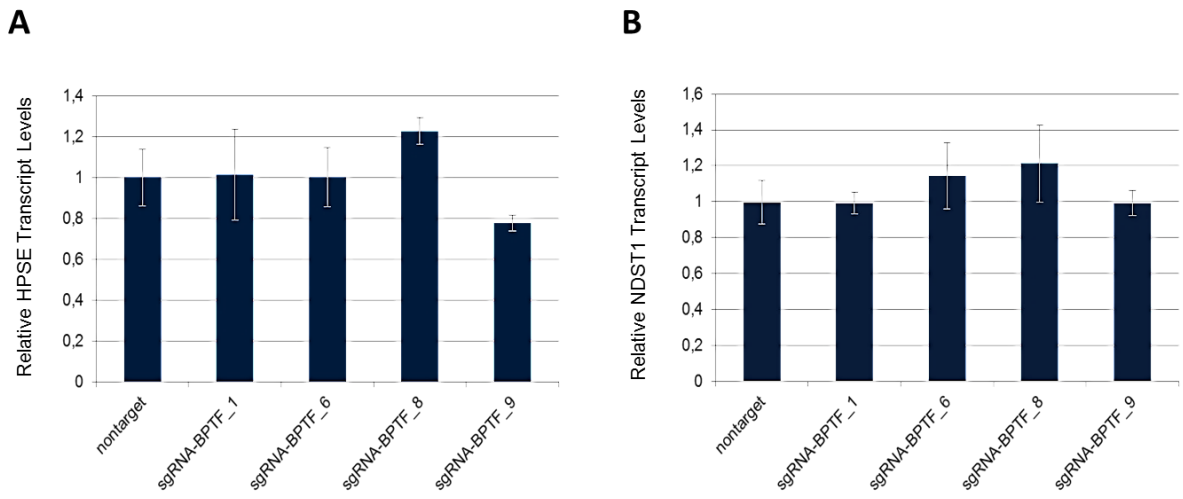

Figure 41: Relative *HPSE* transcript levels (A) and relative *NDST1* transcript levels (B) after long term cultivation of *BPTF* KO populations.

RNA from $1x10^7$cells was isolated and cDNA generated. qPCR was performed in four replicates per condition. 18S rRNA served as housekeeping gene. Relative transcript levels were calculated by normalizing to 18S rRNA transcript levels and *HPSE*/*NDST1* levels in nontarget control.
X-Axis: Different used cell lines.
Y-Axis: Relative transcript levels.

As seen in **Figure 41**, *BPTF* KO does not cause reduction in *HPSE* or *NDST1* expression. This is in contrast to Mayes and colleagues who described a significant reduction in *HPSE* and *NDST1* upon shRNA-mediated KD of *BPTF* (FC *HPSE*: -3.3 for 67NR and -1.4 in 66cl4; FC *NDST1*: -1.5 in 66cl4) [68].

5.4.6. PNK-mediated Tumour Cell Killing of *BPTF* KO Tumour Cell Pools of NCI-H1437

As *BPTF* KO was confirmed by WES analysis, PNK-mediated tumour cell killing was performed (**Figure 42**).

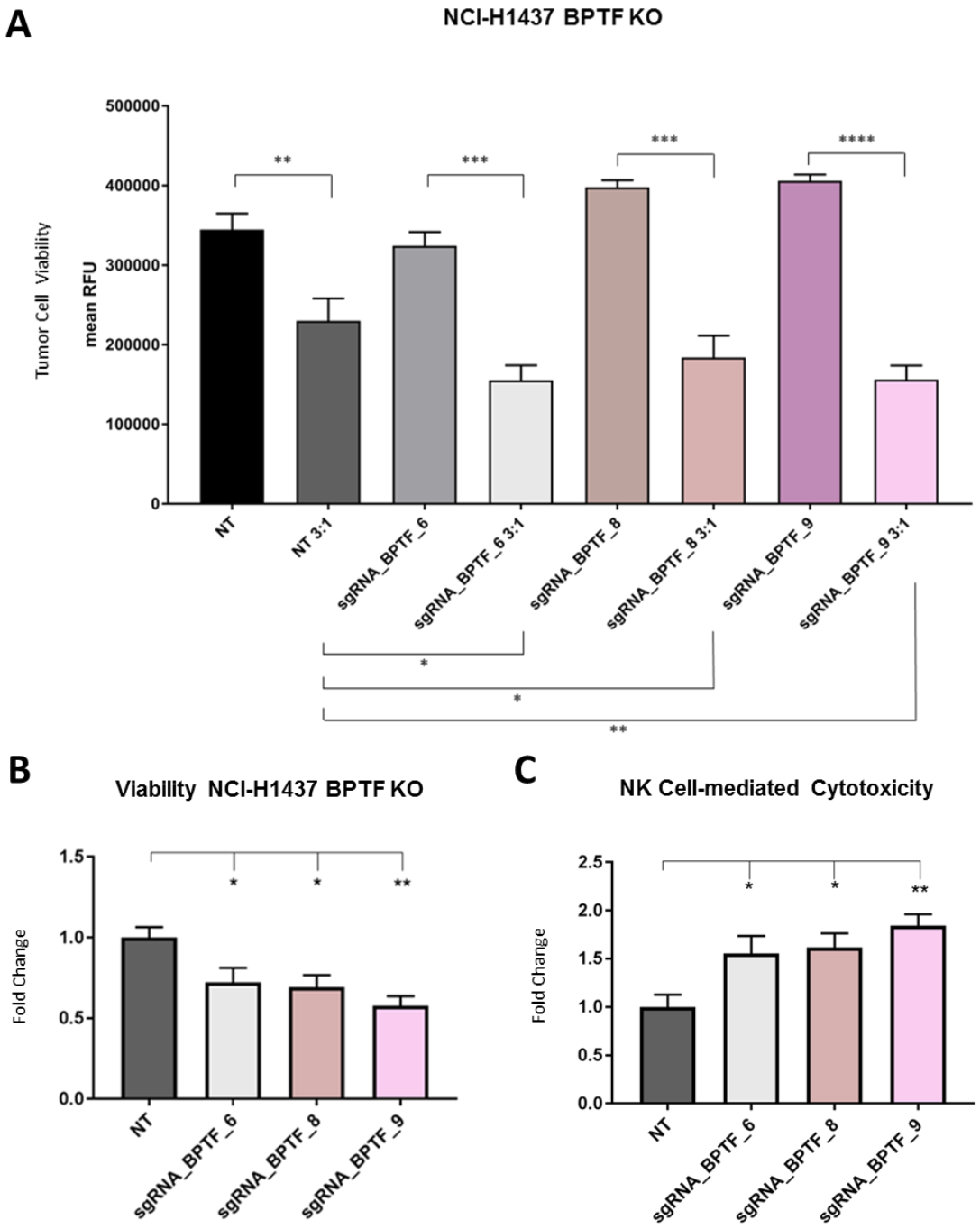

Figure 42: Tumour cell viability and PNK-mediated cytotoxicity in various *BPTF* sgRNA cell pools of NCI-H1437.

(A) Comparison of tumour cell viability (NCI-H1437 *BPTF* KO) in 2D mono- and co-cultures with PNKs. (B) Fold change of tumour cell viability in presence of PNKs and (C) fold changes of NK cell-mediated cytotoxicity.

Cells were incubated 24 hours before adding PNKs. Tumour cell viability was measured by Presto Blue assay 48 hours after adding PNKs. Analysis was performed in triplicates per condition. Results from viability assay were used to calculate fold changes of tumour cells viability and PNK-mediated cytotoxicity compared to nontarget control.
$p > 0.5$: ns, $p < 0.05$: *, $p < 0.01$: **

Presence of PNKs led to reduction of tumour cell viability in all used NCI-H1437 populations compared to corresponding mono-culture. However, significant stronger reduction was observed in NCI-H1437 *BPTF* KO than in nontarget control cells.

5.4.7. Characterisation of *BPTF* KO Single Cell Clones

As seen in **Figure 40** cell pools do still express small amounts of *BPTF* or exhibiting a genetic background leading to a diametrically opposed effect of *BPTF* KO, genetically uniform populations (single cell clones) from *BPTF* KO (sgRNA BPTF 1) NCI-H1437 were generated.

5.4.7.1. *BPTF* Expression Level Determination in NCI-H1437 *BPTF* (sgRNA 1) KO Single Cell Clones

BPTF protein levels were determined by WES protein simple (**Figure 43**).

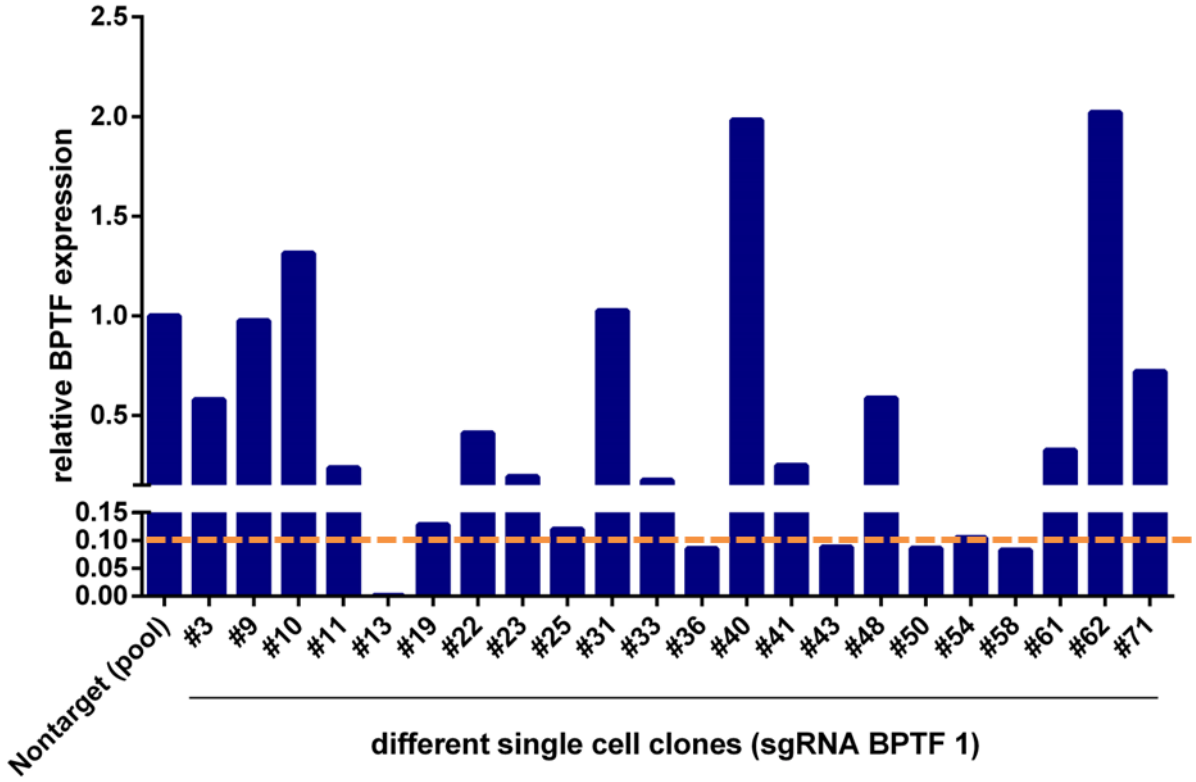

Figure 43: Relative *BPTF* expression levels in different single cell clones generated from NCI-H1437 *BPTF* KO (sgRNA BPTF 1).

Protein lysates (0.2 µg/µL) were generated for WES analysis. Antibodies against *BPTF* (1:25) and vinculin (1:500) were used. *BPTF* levels were compared to vinculin and normalized to nontarget control. Orange dotted line indicates unspecific background limit (noise) (data not shown).
X-Axis: Different used cell lines.
Y-Axis: Relative protein levels.

Most of the cell pools exhibited reduced levels, while few showed even elevated expression (#40, #61). Least levels of *BPTF* were found in cell pool #13, #36, #43, #50, #54 and 58, respectively. These single cell clones were selected for further analysis.

5.4.7.2. Two-dimensional Co-cultures of *BPTF* KO Single Cell Clones and PNKs from Different Donors.

Due to appropriate growth behaviour the following single cell clones #50, #54 and #58 were selected for further analysis in co-cultivation assays utilizing different donors for PNKs (**Figure 44**, **Figure 45** and **Figure 46**).

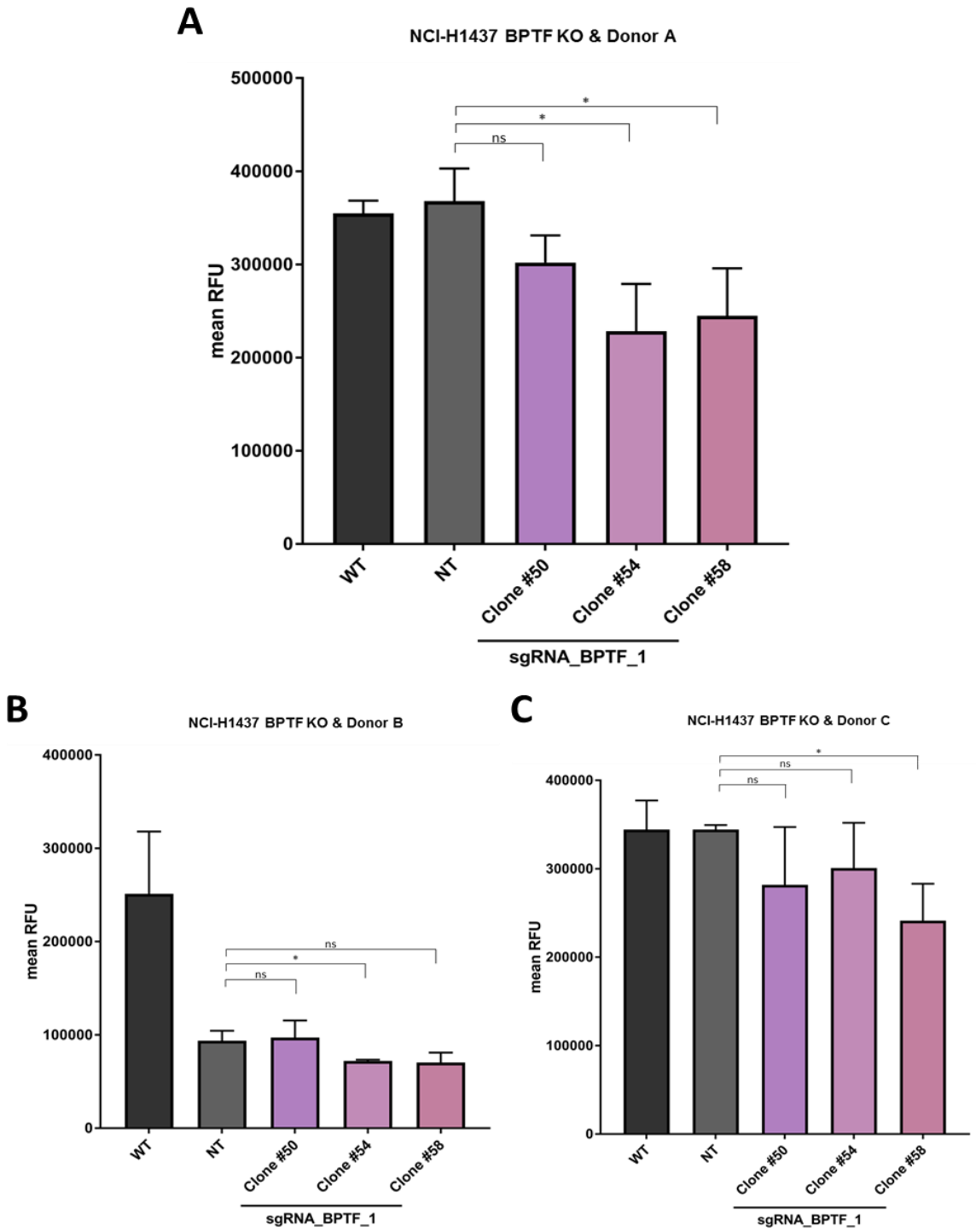

Figure 44: Tumour cell viability in 2D co-cultures of NCI-H1437 *BPTF* KO (sgRNA_*BPTF*_1) single cell clones (#50, #54, #58) and PNKs from three different donors - Donor A (A), Donor B (B) and Donor C (C).

For assay details see Figure 42. Co-cultures were cultivated for 72 hours.
X-Axis: Different used cell lines. Y-Axis: Mean RFU indicating tumour cell viability.
Mean RFU: Mean fluorescence intensity.
$p > 0.5$: ns, $p < 0.05$: *

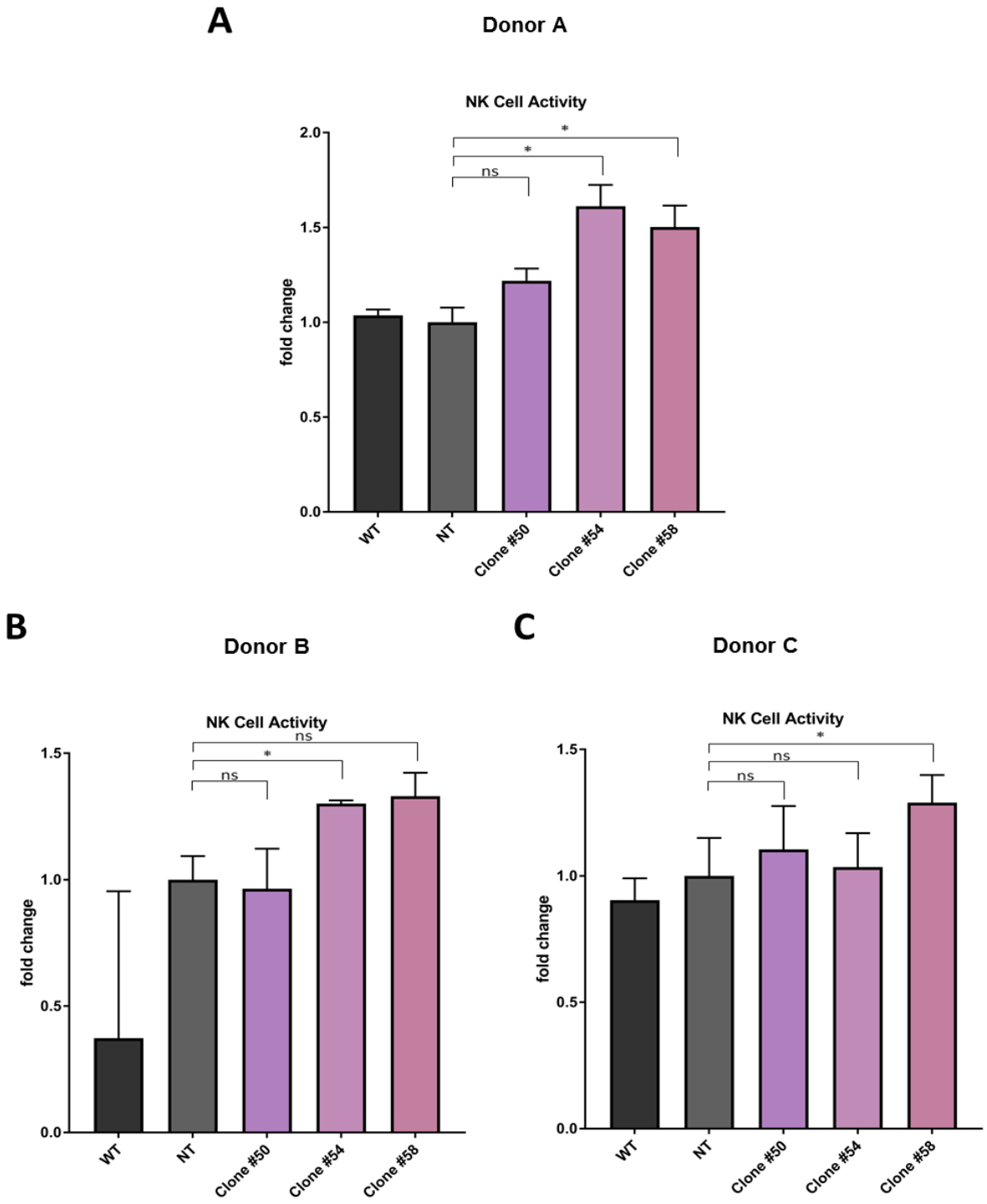

Figure 45: PNK activity in 2D co-cultures of NCI-H1437 *BPTF* KO (sgRNA_*BPTF*_1) single cell clones (#50, #54, #58) and PNKs from three different Donors - Donor A (A), Donor B (B) and Donor C (C).

For assay details see Figure 42. Co-cultures were cultivated for 72 hours.
X-Axis: Different used cell lines. Y-Axis: Fold change in PNK-mediated cytotoxicity.
$p > 0.5$: ns, $p < 0.05$: *

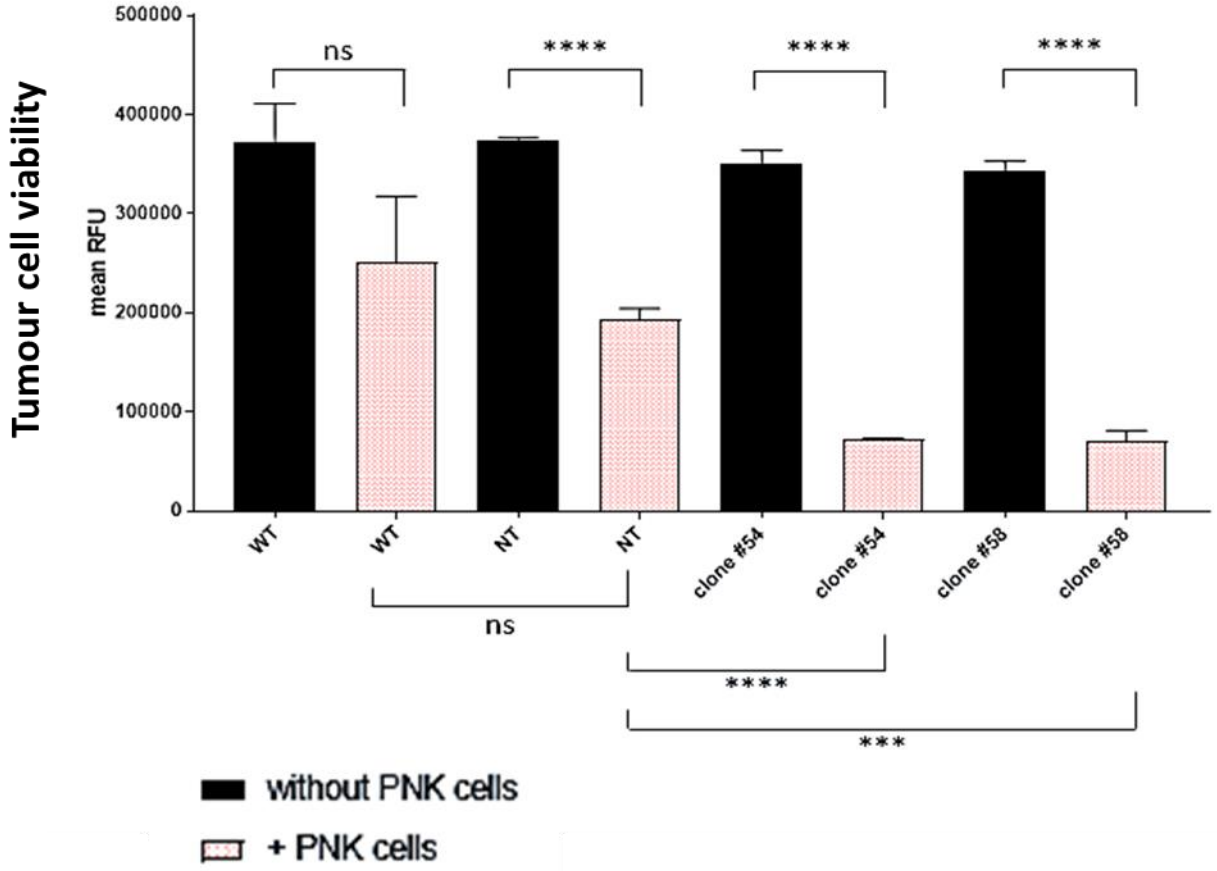

Figure 46: Tumour cell viability in 2D co-cultures of NCI-H1437 *BPTF* KO (sgRNA_*BPTF*_1) single cell clones (#54, #58) and PNKs (Donor D).

For assay details see Figure 42. Co-cultures were cultivated for 72 hours.
X-Axis: Different used cell lines.
Y-Axis: Mean RFU (+ STD) indicating tumour cell viability.
Mean RFU: Mean fluorescence intensity. ns: not significant
$p > 0.5$: ns, $p < 0.05$: *, $p < 0.01$: **, $p < 0.001$: ***, $p < 0.0001$: ****

Except for donor B, no significant differences in viability between NCI-H1437 wildtype (WT) and nontarget (NT) were detectable in co-cultures with PNKs. In general, single cell clones #54 and #58 exhibit both a drop of viability and an increase in PNK activity. As expected, different donors led to different levels of PNK activation. For instance, donor A can induce tumour cell killing in both single cell clones, whereas donor B and C exhibited an opposite activity profile; donor B active on #54, donor C on #58. Induction of PNK activity always goes hand in hand with an increase in tumour cell killing (see summary in **Table 9**)

Single Cell Clone	Viability of Tumour Cells				Activity of PNKs			Normalized to
	Donor A	Donor B	Donor C	Donor D	Donor A	Donor B	Donor C	
NT	no	yes	no	no	no	no	no	WT
#50	no	no	no	na.	no	no	no	NT
#54	yes	yes	no	yes	yes	yes	no	NT
#58	yes	no	yes	yes	yes	no	yes	NT

Table 9: Overview – Effect of BPTF KO in single cell clones on PNK activity and tumour cell killing.

It summarizes Figures 44 - 46. na: not administered; NT: nontarget

5.4.7.3. Three-dimensional Growth Behaviour of NCI-H1437 *BPTF* KO

Next the influence of *BPTF* KO on the 3D growth potential was determined (**Figure 47**).

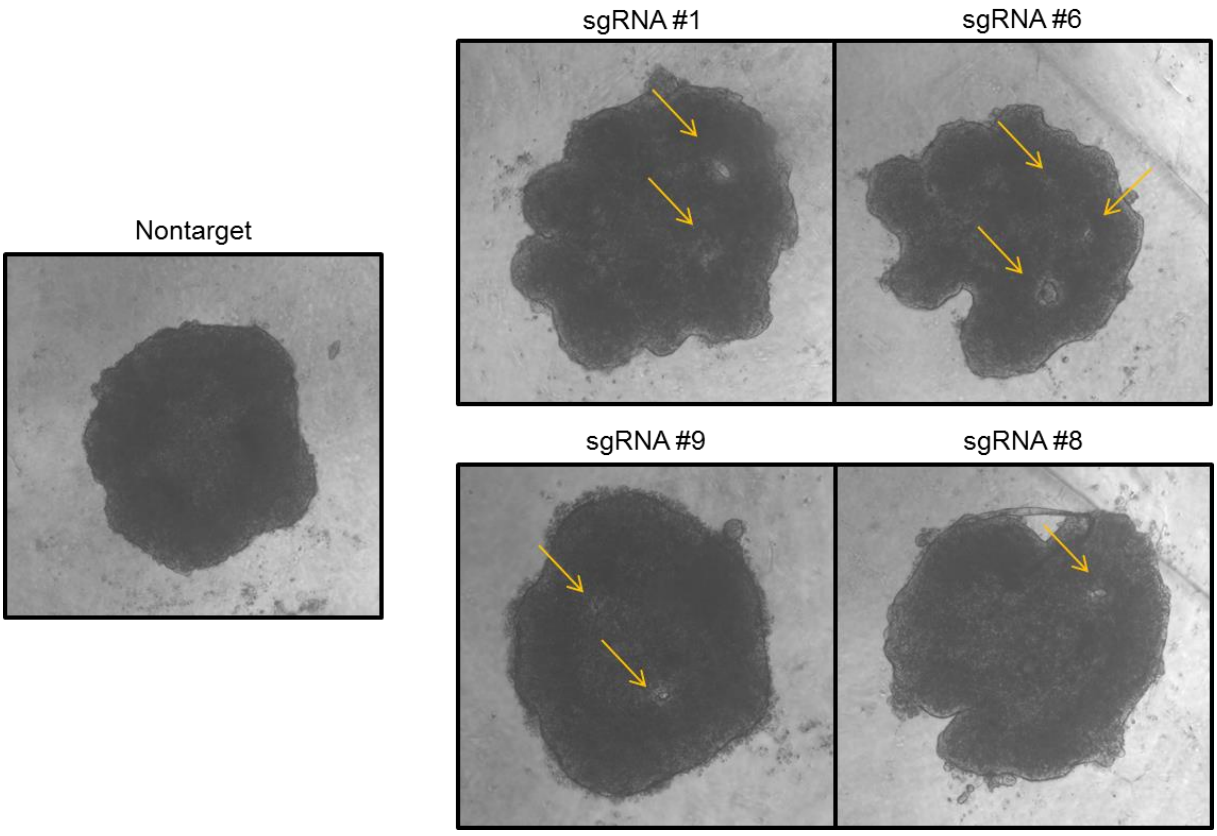

Figure 47: Three-dimensional growth of NCI-H1437 *BPTF* KO cell pools and nontarget control populations.

MCTSs were grown as floaters for 96 hours and embedded in a collagen/Matrigel mixture. Images were taken 72 hours after embedding using a Leica brightfield microscope (4X objective).
Arrows indicate holes in the tumour spheroids.

The influence of *BPTF* KO on the proliferation rate in 2D was negligible. However, although *BPTF* KO cell pools have the ability to form three-dimensional spheroids, they grow differently compared to the nontarget control. *BPTF* KO MCTSs from *BPTF* KO cell pools contain little “holes”, indicating that loss of *BPTF* somehow interferes with NCI-H1437’s potential to form homogenous spheroids. The reason for this phenotype remains to be determined.

5.5. Gene Expression Profiling of *BPTF* KO Single Cell Clone Cultures and BI90 Treated Tumour Cells

In order to receive a basic understanding how many and which genes and protein networks are affected indeed by *BPTF* KO, a time-resolved DNA microarray profiling was performed (**Figure 48**, **Figure 49**). Single cell clones #13, #36, #43, #50 and #54 were used for a detailed transcriptional analysis. Identifying genes that are commonly up- or down-regulated in all or at least in most of the selected clones is essential for a better understanding of the pleiotropic effects that are induced in tumour cells upon modulation of *BPTF* expression. The thereby obtained information is a powerful tool to uncover the biological mechanisms altering the tumour cell´s immunogenicity in a *BPTF*-dependent manner. The same holds true for a pharmacologic inhibition by *BPTF* inhibitor BI90. The central question to be addressed will be whether an overlapping deregulated transcription profile can be detected by comparing transcriptomes from genetically modified (*BPTF* KO) with those from pharmacologically treated (BI90; *BPTF* inhibitor) tumour cells.

5.5.1. Gene Expression Profiling of *BPTF* KO Single Cell Clone Cultures

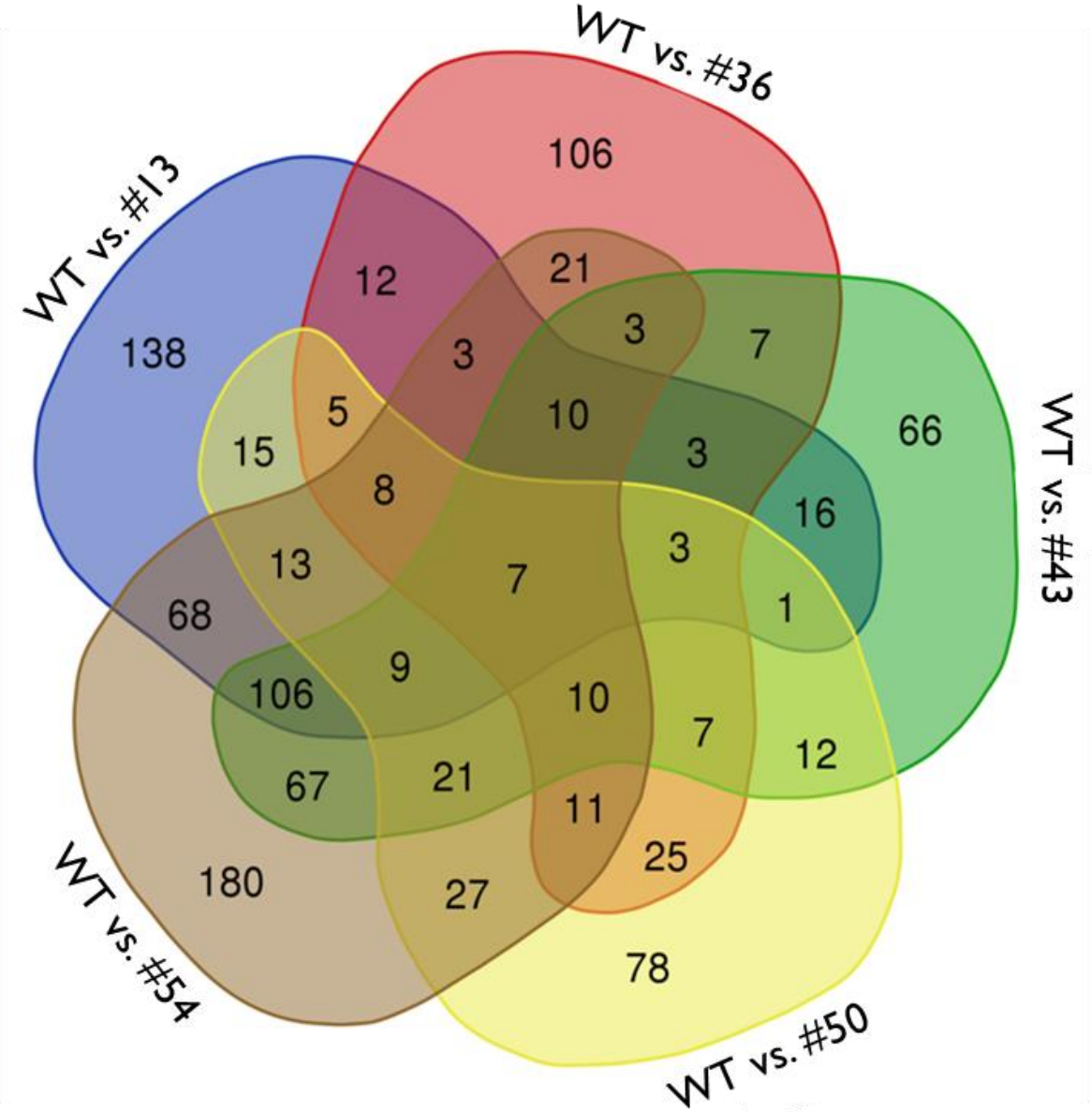

Figure 48: Venn diagram showing the number of genes jointly down-regulated in different single cell clones.

Data set is based on DNA microarray analysis. After long term (5 weeks) cultivation of *BPTF* KO clones in 2D, RNA was isolated (details see Material and Methods) and sent to ATLAS Biolabs GmbH for gene expression profiling on utilizing Affymetrix Gene Chips (Affymetrix EXP). For generation of Venn diagrams a FC of $\geq$ 1.8 and a p-value of $\leq$ 0.01 was chosen.

The seven genes found to be jointly down-regulated in all five NCI-H1437 *BPTF* KO single cell clones are: *CCL22*, *ABCA1*, *CGA*, *CLEC3A*, *SERPINB4*, *AKAP12* and *CLIC6*, respectively.

CCL22 (C-C Motif Chemokine Ligand 22) is involved in chemotactic movement of immune cells[14]. *ABCA1* (ATP-binding membrane cassette transporter A1) was described to essentially contribute to the cholesterol efflux and immune response during the chronic inflammation response in atherosclerosis patients [98, 99]. *ABCA1* has also been discussed as the possible link between inflammation and reverse cholesterol transport [100]. *CGA* (Glycoprotein hormones alpha chain) represents the shared alpha chain of the active heterodimeric glycoprotein hormones TSH, LH, FSH and CG. These hormones bind specific receptors on target cells that in turn activate downstream signalling pathways. It was detected together with *PD-L1* expression and TILs (tumour infiltrating lymphocytes) in hot spots of primary and liver metastases in prostate cancer with neuroendocrine differentiation [101]. *CLEC3A* (C-type lectin domain family 3 member A) is found on tumour cells surface and serves as a substrate for MMPs [102]. *CLEC3A* autoantibodies are detected in osteoarthritis patients [103]. *SERPINB4*, an inhibitor of serine and cysteine proteinases [104], was shown to inhibit granzyme M-induced cell death [105] and serves as a biomarker for skin inflammatory diseases [106]. *AKAP12* (A-kinase anchoring protein 12) expressing cells in the fibrotic scar may restrict excessive inflammation during the CNS repair process [107]. *CLIC6*, a member of the intracellular chloride channel family, was originally shown to interact with dopamine D (2)-like receptors [108]. *CLIC6* was recently identified in a proteomic landscape signature linked with molecular predisposition of regions to ophthalmic diseases such as age-related macular degeneration [109].

[14] https://www.genecards.org/cgi-bin/carddisp.pl?gene=CCL22, 19.04.2019

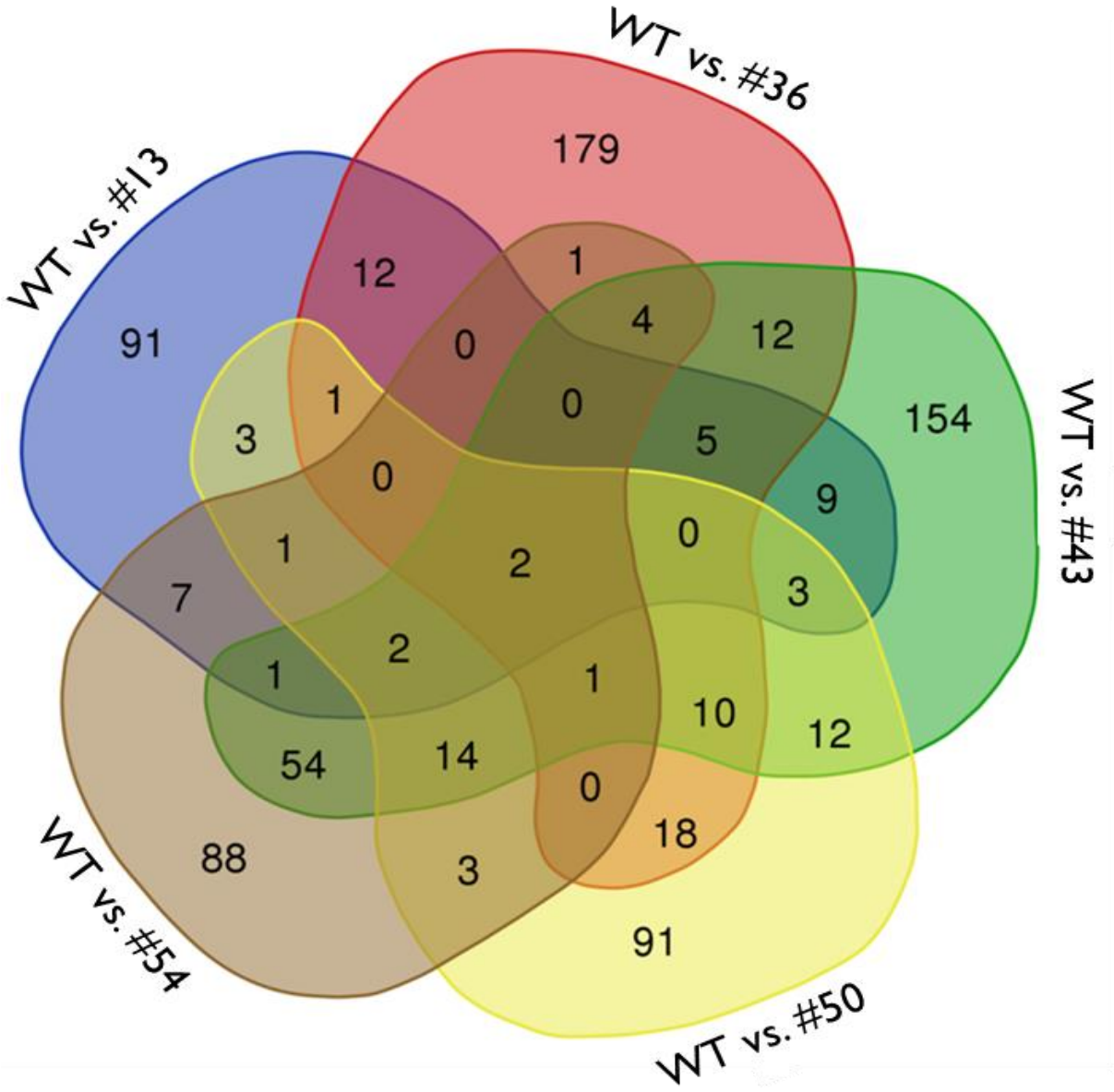

Figure 49: Venn diagram showing the number of genes jointly up-regulated in different clones.

For assay details see Figure 48**.**

Two genes were found up-regulated in all five single cell clones analysed, *OVGP1* and *CALCOCO1*.

OVGP1 (oviduct-specific glycoprotein) is a large, epithelial glycoprotein. It plays a role during late follicular development through early cleavage-stage embryonic development. *OVGP1* is secreted from non-ciliated oviductal epithelial cells and is also detected in the mouse ovary, testis and epididymis suggesting its roles beyond fertilization. It is required for maintaining

the receptivity phenotype and trophoblast adhesion and *OVGP1* mRNA levels are reduced in endometrium of women with recurrent implantation failure [110-112]. During inflammation, *OVGP1* levels were shown to be reduced [113].

CALCOCO1 is a calcium binding and coiled-coil domain 1 protein which functions as a steroid hormone (glucocorticoid) receptor co-regulator gene [114]. It has been suggested to play a role in mediating transcriptional activation by *CTNNB1* (beta-catenin) [115]. It functions as a secondary co-activator in *LEF1*-mediated transcriptional activation via its interaction with *CTNNB1* [116].

These analyses clearly show that genes are commonly more down than up-regulated in *BPTF* KO cells. At the moment it is not clear which of those deregulated genes are the most relevant ones for increasing tumour cell´s immunogenicity. Via the Search Tool for the Retrieval of Interacting Genes/Proteins ("STRING") database [117], interactions between genes of interest were identified. For this, all deregulated genes at least showing up in 3/5 single cell clones where included for a detailed analysis in "STRING". The majority of deregulated genes involve in the cell cycle (**Figure 50**). A more detailed analysis identified additional specific cellular processes including small GTPase mediated signalling, G1/S transition of mitotic cycle, DNA replication, DNA metabolic process (**Figure 51**) and establishment of organelle localization to name but a few.

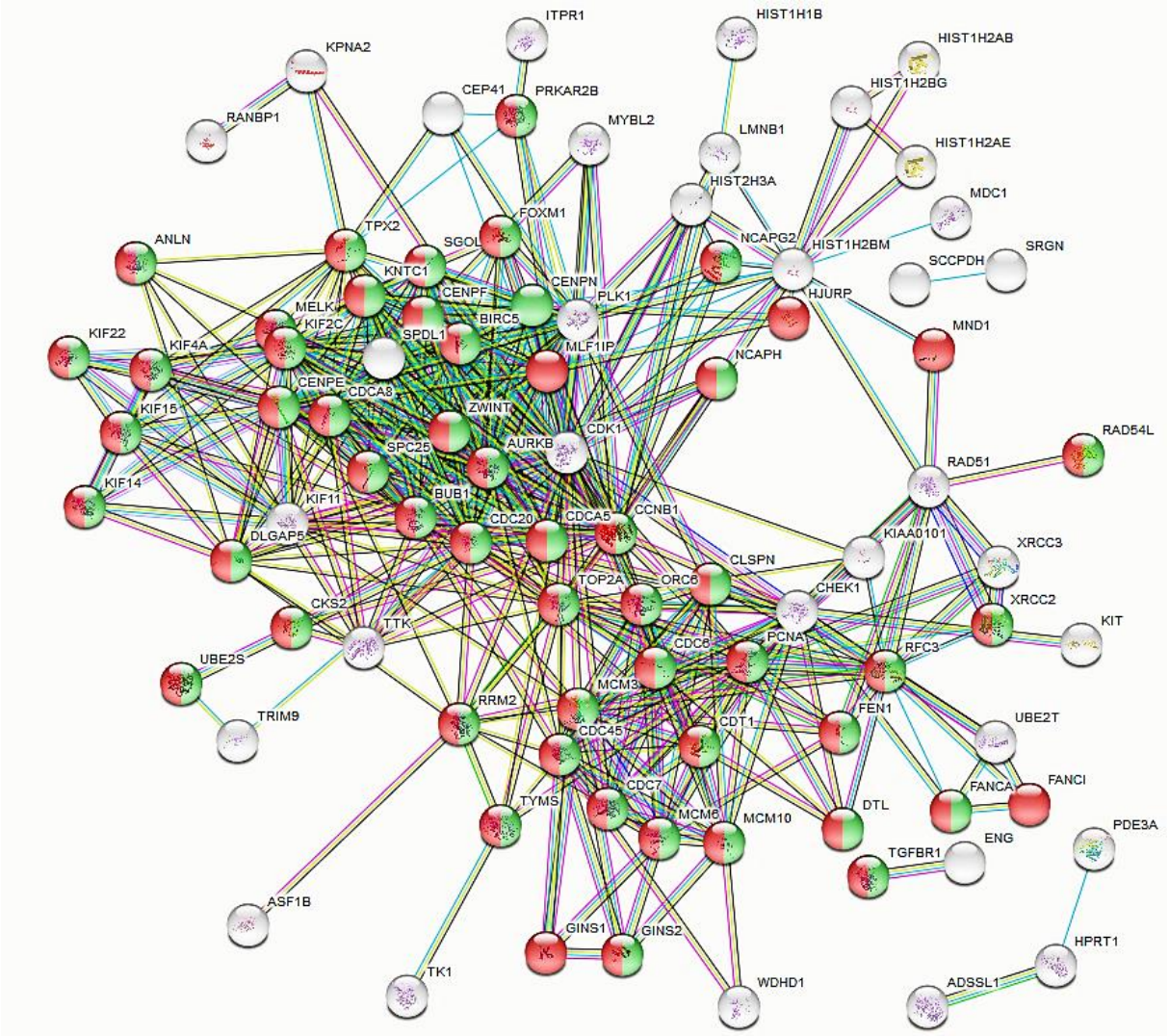

Figure 50: Interaction-network 1 composed of down-regulated genes after *BPTF* KO.

Proteins involved in cell cycle or cell cycle process are shown in red or green.

Deregulated genes from the five single cell clones (#13, #36, #43, #50 and #54) (at least commonly down-regulated in three of five single cell clones) were used for analysis (FC: ≥ log1.8, p-value: ≤ 0.01). Networks were generated using STRING database. Highest confidence level (0.9) was chosen and pathways were identified via GO terms.

Stand-alone genes are not shown.

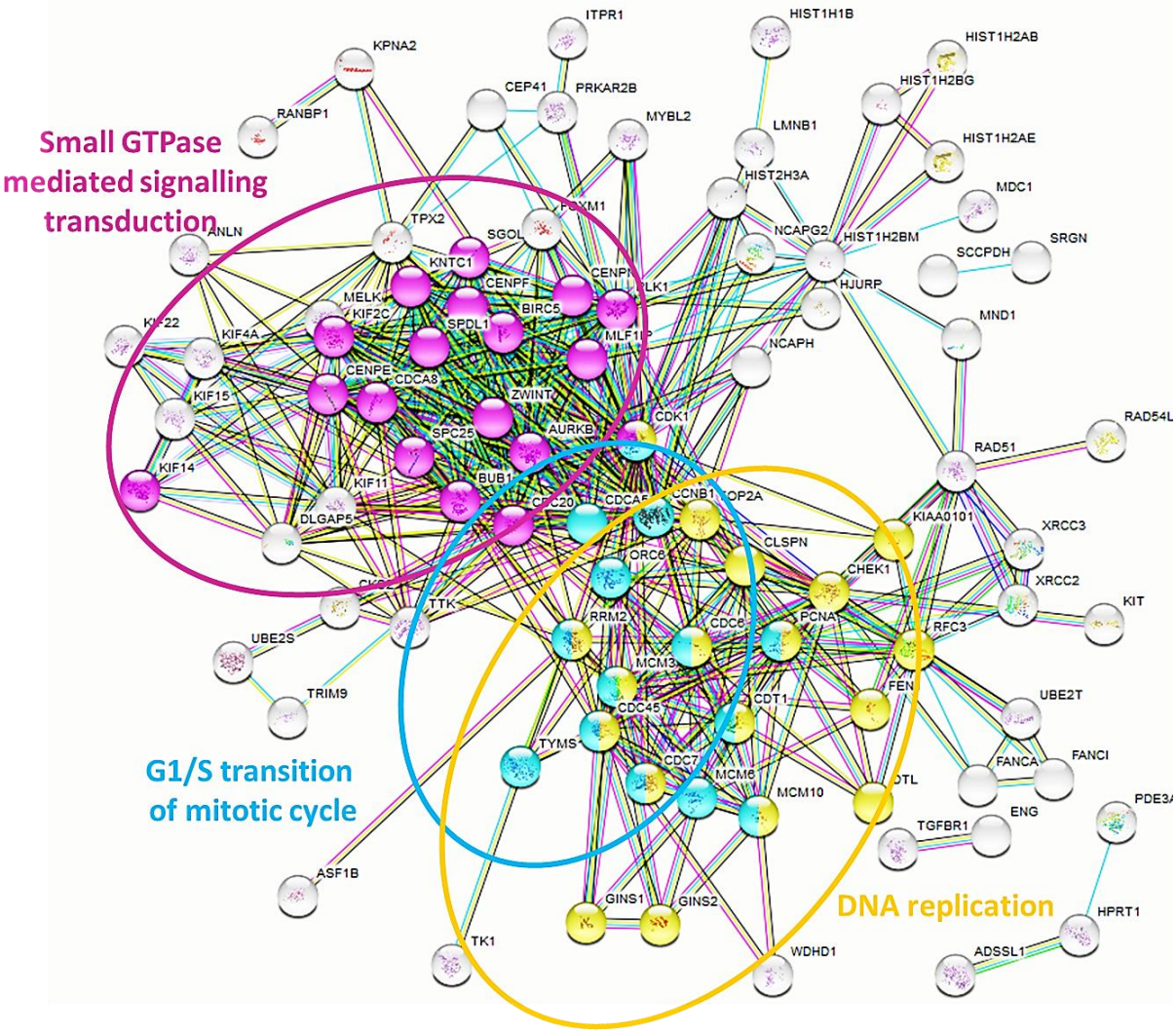

Figure 51: Interaction-network 2 composed of down-regulated genes after *BPTF* KO.

Proteins involved in small GTPase mediated signalling (purple), G1/S transition (light blue), core histones (dark blue) and DNA replication (yellow) are highlighted.

Deregulated genes (at least commonly down-regulated in three of five single cell clones) from the five single cell clones (#13, #36, #43, #50 and #54) were used for analysis (FC: ≥ log1.8, p-value: ≤ 0.01). Networks were generated using STRING database. Highest confidence level (0.9) was chosen and pathways were identified via GO terms.

Stand-alone genes are not shown.

STRING database analysis revealed reproducibility of the results. The same pathways could be identified independently regardless whether deregulated genes from all five sequenced *BPTF* KO clones were used for analysis or only overlapping deregulated genes from clone #13, #43 and #54, respectively.

Interestingly, identification of pathways with up-regulated genes (after *BPTF* KO) involves only fewer genes (**Figure 52**).

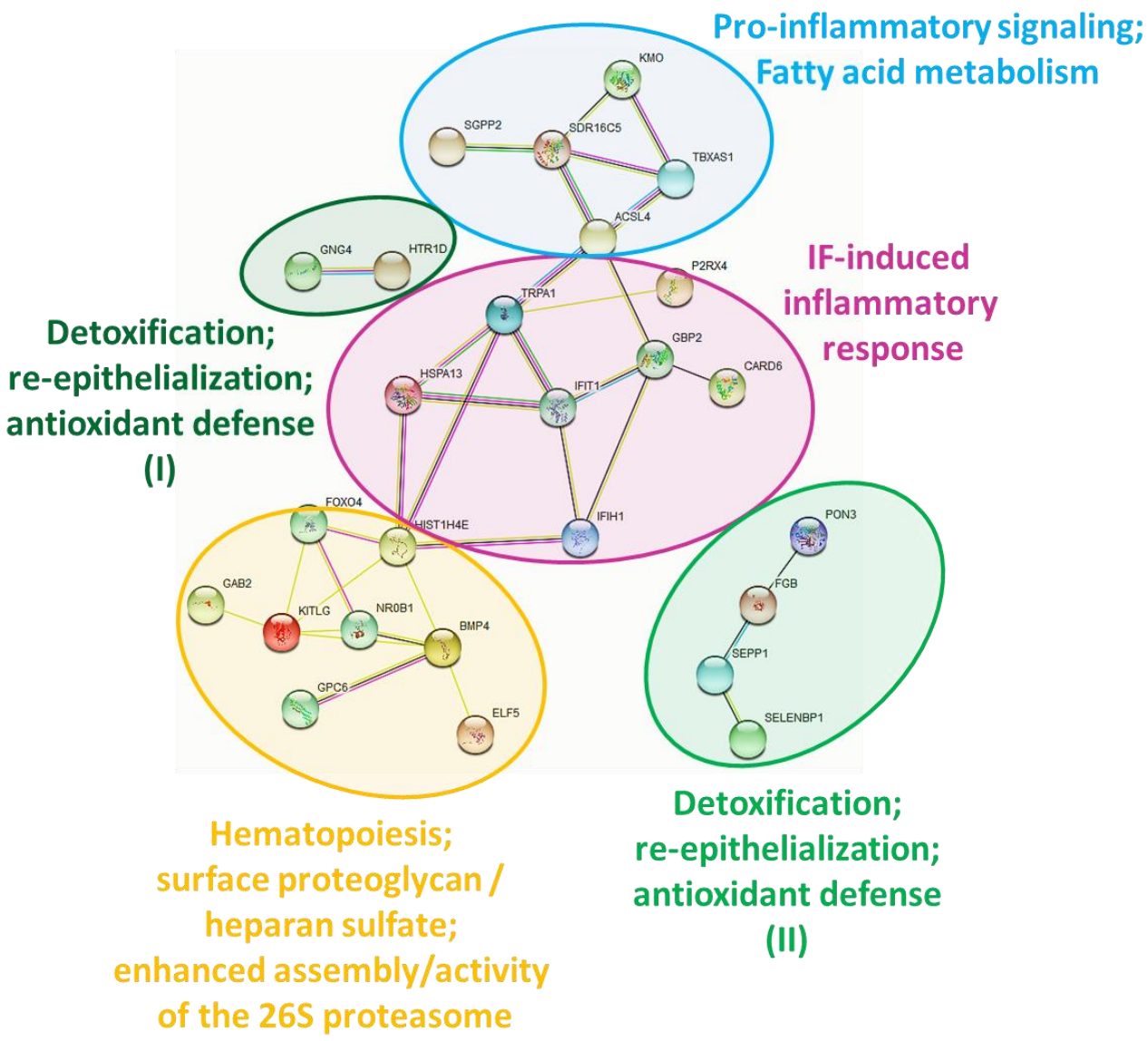

Figure 52: Interaction-network 3 composed of up-regulated genes after *BPTF* KO.

Proteins involved in pro-inflammatory signalling and fatty acid metabolism (light blue), interferon (IF)–induced inflammatory response (purple), detoxification/re-epithelialization/antioxidant defense I and II (dark green and light green) and hematopoiesis/surface proteoglycan or heparan sulfate/enhanced assembly or activity of the 26S proteasome (yellow) are highlighted.

Overlapping deregulated genes from three single cell clones (#13, #43 and #54) were used for analysis (FC: ≥ log1.8, p-value: ≤ 0.01). Networks were generated using STRING database. Lowest confidence level (0.15) was chosen and pathways / biological functions were assigned manually.

Stand-alone genes are not shown.

5.5.2. Change in the Transcription Profile upon Treatment with BI90

Additionally to identifying genes deregulated after *BPTF* KO, also deregulations in BI90 treated NCI-H157's and NCI-H1437's transcriptomes were identified. In order to receive a more detailed understanding what genes are deregulated by BI90, a time course was performed. RNA samples for DNA Microarray analysis were generated two hours, four hours, eight hours, 24 hours, 48 hours, 72 hours, 96 hours and 120 hours after treatment with BI90 and DMSO control (0.1 %). To identify genes jointly up-or down-regulated in NCI-H1437 and NCI-H157, Venn diagrams were established (**Figure 53**).

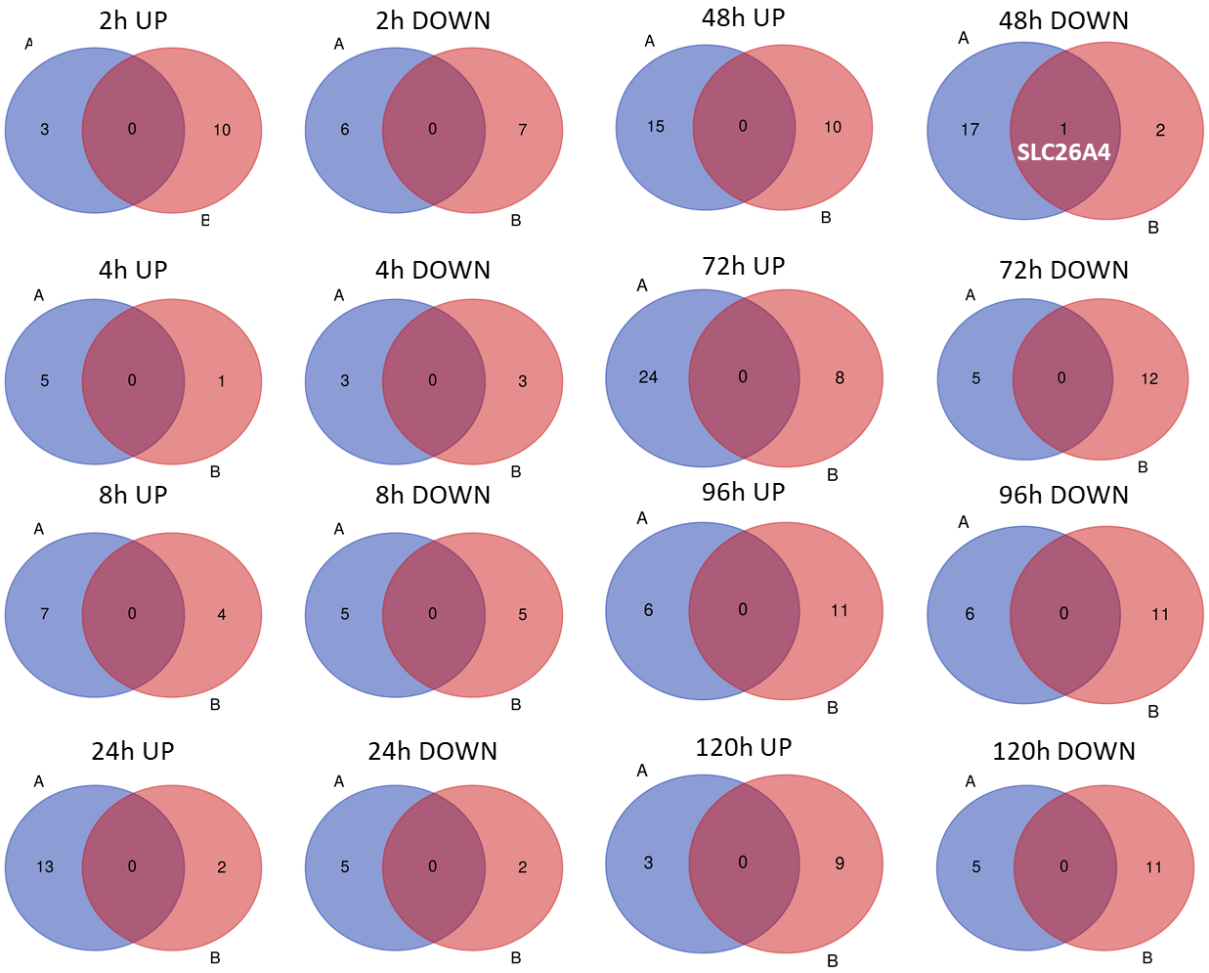

Figure 53: Venn diagram of BI90-treated tumour cell lines NCI-H157 vs. NCI-H1437 at different time points.

$2.5x10^5$ cells were seeded in 1.9 mL media. 24 hours after seeding 100 µL of 20 µM BI90 solution were added into each well (final BI90 concentration: 1 µM). RNA was isolated after 2 hours, 4 hours, 8 hours, 24 hours, 48 hours, 72 hours and 120 hours. For details see material and methods. RNA was sent to ATLAS Biolabs GmbH for gene expression profiling utilizing Affymetrix Gene Chips (Affymetrix EXP). For generation of Venn diagrams FC $\geq$ 1.8, p-value $\leq$ 0.01 were chosen.
A: NCI-H157
B: NCI-H1437
UP: Up-regulated
DOWN: Down-regulated

Except for time point 48 hours (DOWN), no overlap in deregulated transcripts could be identified in NCI-H157 and NCI-H1437 after treatment with BI90. Only the *SLC26A4* (Pendrin) transcript was shown to be down-regulated in both cell lines.

5.5.3. Transcripts modulated in NCI-H1437 KO single cell clones and in BI90 tumour treated cell lines NCI-157 and NCI-H1437.

Next, we analysed whether there is an overlap between deregulated genes after BI90 treatment and *BPTF* KO (**Figure 54**).

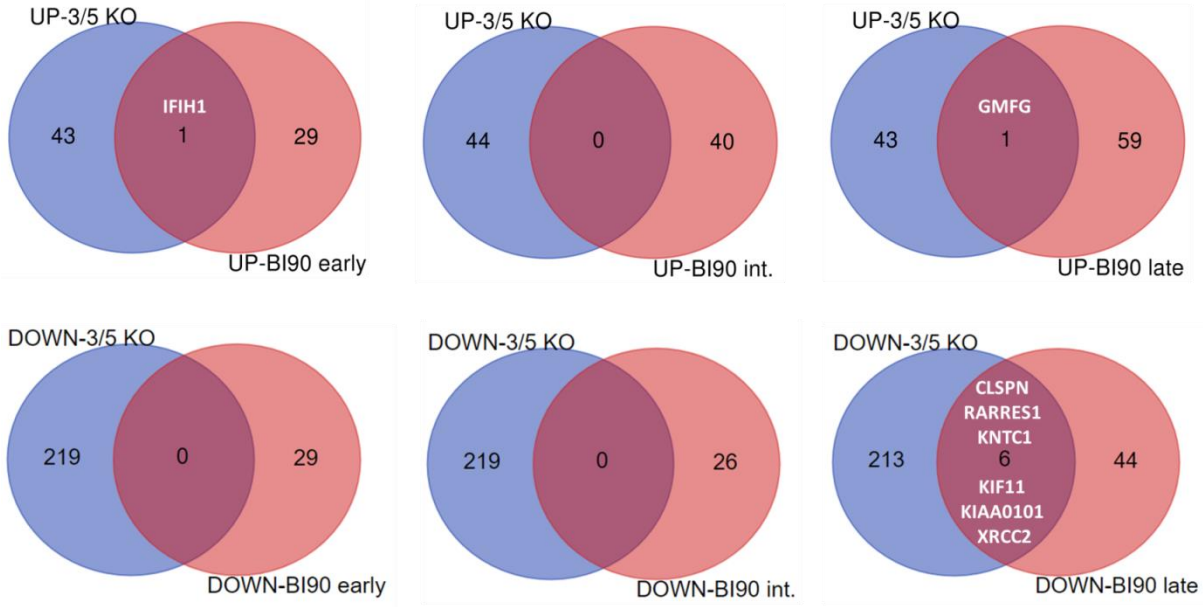

Figure 54: Venn diagrams of expression profiles (transcriptomes) from long-term cultivated NCI-H1437 single cell clones and from BI90-treated tumour cells (NCI-H1437 and NCI-H157) at different time points.

BPTF KO single cell clones from NCI-H1437 were cultivated for five weeks. Only those transcripts from NCI-H1437 KO single cell clones were taken into account exhibiting a FC of >1.8 in at least three out of five clones (p-value: < 0.01). Cell lysates of BI90-treated NCI-H157 and NCI-H1437 tumour cells were generated after 2 hours, 4 hours, 8 hours, 24 hours, 48 hours, 71 hours, 96 hours, 120 hours and 170 hours of incubation with BI90. Reference samples (control): Untreated samples taken at the same time points containing 0.1 w/v % DMSO only. As only a few genes were found to be modulated per time point in both cell lines and to facilitate a more comprehensive analysis, transcripts from both cell lines were pooled and subcategorized in early, intermediate and late transcripts. For a detailed description of cell lysates see Table 9. Venn diagrams were generated according to the algorithm at http://bioinformatics.psb.ugent.be/webtools/Venn/.

UP-3/5 KO: Up-regulated transcripts from three out of five single cell clones from NCI-H1437 *BPTF*.

KO DOWN-3/5 KO: Down-regulated transcripts from three out of five single cell clones from NCI-H1437 *BPTF*.

KO UP-BI90 early, int. (intermediate) and late: Up-regulated transcripts from a pool of samples taken at time point 2 hours + 4 hours + 8 hours (early), 24 hours + 48 hours (int.; intermediate) and 71 hours + 96 hours + 120 hours (late) from both NCI-H157 and NCI-H1437 BI90 -treated cells.

DOWN-BI90 early, int. (intermediate) and late: Down-regulated transcripts from a pool of samples taken at time points 2 hours + 4 hours + 8 hours (early), 24 hours + 48 hours (int.; intermediate) and 71 hours + 96 hours + 120 hours (late) from both NCI-H157 and NCI-H1437 BI90 treated cells.

Of note, comparison of transcripts being up- or down-regulated in at least three out of five *BPTF* KO single cell clones with the transcriptome of BI90-treated tumour cells revealed a different set of modulated genes (**Figure 54**)**.** For this comparison the transcriptome of BI90-treated tumour cells was analysed at different treatment time points (early, intermediate and late. Only two transcripts were found jointly up-regulated upon treatment with BI90 and compared to NCI-H1437 *BPTF* clones (#13, #43 and #54): At an early time point the transcript of *IFIH1* and at late one *GMFG*. The intermediate time point did not show any significant changes in the compared transcriptomes. In contrast to up-regulation, down-regulation of transcripts has only been observed at the late time point where six transcripts were shown significantly down-regulated: *CLSPN*, *RARRES1*, *KNTC1*, *KIF11*, *KIAA0101*, and *XRCC2*.

CLSPN (claspin), a ring-shaped DNA-binding protein with high affinity to branched DNA structures [118], functions as a regulator of *CHEK1* in DNA replication stress pathway [119] and its down-regulation inhibits *CHEK1* activation in response to replication stress [120]. *CLSPN* promotes normal replication fork rates in human cells [121]. It is involved in DNA repair and radio-resistance of lung cancer brain metastasis [122] and has been recently suggested to function as a tumour suppressor [123].

Expression of *RARRES1* (retinoic acid receptor responder 1) is significantly related to tumour differentiation and staging in colorectal adenocarcinoma [124]. *RARRES1* functions as a tumour suppressor and its hypermethylation [125] has been shown in several tumour types including EBV-positive nasopharyngeal carcinoma [126], gastric cancer [125, 127], malignant melanoma [128], prostate cancer [129]. *RARRES1* also plays a role in regulation of autophagy as a survival mechanism in tumour cells [130, 131].

Very little is known about the function of *KNTC1* (kinetochore-associated protein 1). shRNA-mediated KD of *KNTC1* suppresses cell viability and induces apoptosis in esophageal squamous cell carcinoma (SCC) whereas overexpression was associated with increases in the mitotic spindle and hypoxia pathways, and decreases in the DNA repair and mismatch repair pathways [132].

KIF11 (kinesin-5 or Eg5) belongs to the family of kinesin motor proteins, an ATPase superfamily tightly linked to the microtubules. *KIF11* is a plus-end-directed motor localized

to interpolar spindle microtubules and to the spindle poles. Its function primarily is to slide anti-parallel microtubules apart from one another [133].

The *PCNA*-associated factor *KIAA0101* (*p15(PAF)*, *OEATC-1*) binds the potential tumor suppressor product p33ING1b. Overexpression was found to protect cells from UV-induced cell death suggesting that *KIAA0101* acts as a putative tumour suppressor gene. *KIAA0101* forms part of a larger protein complex potentially involved in the regulation of DNA repair, apoptosis and cell cycle progression [134].
Most interestingly, the mean expression of ten proliferation-associated genes including *KIAA0101* was recently identified as a marker of response to immune checkpoint inhibitors in NSCLC patients, in particular in *PD-L1* negative tumours [135]. Similarly, in ovarian cancer *KIAA0101* was shown to be part of a network module related to DNA repair, replication, immune and cytokine mediated signalling pathways. In addition, *KIAA0101* was found associated with poor prognosis [136].

XRCC2 (X-Ray Repair Cross Complementing 2) belongs to the *RAD51* family of genes, including *RAD51* and the five *RAD51*-like genes (*XRCC2*, *XRCC3*, *RAD51L1*, *RAD51L2*, *RAD51L3*). It is involved in non-homologous end joining (NHEJ) repair mechanism and its deregulation/mutation has been linked with specific forms of cancer [137-139].

6. Basic Considerations

Carcinomas are highly complex structures composed of genetically altered tumour cells and tumour stem cells, together with both normal-activated (NAF) and cancer associated fibroblasts (CAFs), other present cells including endothelial cells and inflammatory cells embedded the extracellular matrix (ECM) [85]. The present cellular heterogeneity influences the way tumour cells migrate, proliferate, and survive during tumour progression [8, 85, 140-142]. The cross-talk between cancer cells and their tumour microenvironment (TME) influences the tumour's "immunologic behaviour" finally leading to evasion of immune destruction by those malignant cells that disrupt anticancer response pathways [85, 143-146]. The term "cancer immunoediting" describes the fact that the immune system plays a kind of Dr. Jekyll and Mr. Hyde dual role in the complex interactions between tumours and the host immune system [85, 143-145, 147-149]. The consequence of the cross-talk between tumour and stromal cells is a "reshaped" immunogenic tumour environment [28, 85] e.g. represented by NF-κB-dependent, tumour-promoting inflammation [16, 85, 150, 151]. This results in negative regulation of T cells via checkpoint receptors such as *PD-1*, *CTLA4*, *LAG3* or *TIM3* [85, 152] and to the inactivation of the innate immune response in particular inactivation of NK cells [153-158]. Immune checkpoint inhibition is an effective treatment strategy in multiple tumour types, including non-small cell lung cancer (NSCLC) and melanoma especially in combinations with targeted therapeutic concepts [85, 159, 160]. Unfortunately, only subpopulations of patients - in particular in advanced stages of disease - respond to the anti-immune checkpoint treatment [85, 160-164]. The molecular reasons causing resistance to immune checkpoint blockade are – if at all – only partially understood [85, 164-169]. To elucidate the underlying molecular mechanisms/cross-talks contributing to activation or inactivation of infiltrating immune cells, novel three-dimensional (3D) culture models are urgently needed [85]. Cells grown in 3D floaters or as 3D aggregates (multicellular organotypic spheroids) embedded in an extracellular matrix much better recapitulate the *in vivo* situation [85, 170-180].

Currently, these culture models are already used in drug discovery, drug delivery, drug resistance and drug repositioning research [85, 179, 181-185] but they may also be useful in addressing questions such as the transcriptional requirements for infiltrating T and NK cells,

the role of macrophages in immune modulation in tumours, the induction of immunogenic cell death and drug screening for activation of T_{regs} or NK cells to name but a few [85, 186, 187].

To capture tumour complexity *in vitro*, we recently have compared 2D and 3D tumour models (including slice-based tumour models) for drug discovery, clearly demonstrating that end points differ according to cell type, stromal co-culture, and culture format [83, 85, 188, 189]. Utilizing our 3D co-culture models we could show that human NSCLC cell lines with a high EMT-score (including NCI-H157) dictate an NF-κB-dependent expression of cytokines and chemokines in fibroblasts [16, 85]. This led us to establishment of 3D triple cultures (3D-3) with an increased complexity either based on embedding tumour spheroids and fibroblasts together with immune cells in a collagen/Matrigel matrix or on alginate microencapsulation and stirred culture systems [85, 190]. Monocytes can be differentiated into tumour-associated macrophages (TAMs with an M2-like phenotype) – without addition of exogenous cytokines – due to the present cross-talk between ECM and the various cell types in microencapsulated 3D-3-cultures [85, 190].

There is emerging evidence that epigenetic events associated with tumourigenesis such as aberrant histone acetylation, might strongly inhibit the immunogenic potential of cancer cells [191, 192]. On the other hand, histone deacetylase inhibitors have been proven to promote immune responses against tumours by increasing the expression of components of the antigen processing machinery such as *TAP-1*, *TAP-2* and *LMP-2* [193]. In contrast to the targets of anti-*PD-1* or anti-*CTLA4* approaches, the druggable molecular target is expressed in the tumour cell itself. For instance, (re-)expression of cancer-testis-antigens (CTAs) has been demonstrated in human cancers sometimes leading to a humoral and/or cellular immune response in cancer patients. CTAs, therefore, represent appropriate targets for anticancer drug discovery in particular for identifying novel immunotherapeutic concepts [194]. The central future question for establishing novel therapeutics in immune-oncology will be: “The modulation of which target genes can transform a “cold” into a “hot” tumour?”

Recently, *BPTF* (Bromodomain PHD Finger Transcription Factor), an epigenetic reader protein, was claimed to play an important role in immune suppression. Mayes and colleagues have shown in a murine model that *BPTF* depletion enhances both T cell- and NK

cell-mediated antitumor immunity. Their results suggested that *BPTF* activates heparanase expression, which subsequently reduces cell surface HSPGs and NCR co-ligands, thereby inhibiting NK cell activity [68]. For T cells, mechanistic investigations revealed that *BPTF*, as part of the NURF complex, directly regulated the expression of genes encoding immunoproteasome subunits Psmb8 and Psmb9 and the antigen transporter genes *TAP1* and *TAP2* leading to a strong reduction in the tumour antigenicity. *BPTF* depletion led to an increase in antigen processing, $CD8^+$ T cell cytotoxicity and anti-tumour activity in murine models [73]. However, mice and men differ quite substantially in the regulation of the immune system [195]. Therefore, we wanted to study the contribution of *BPTF* on the immune modulation in a human setting by making use of our complex 3D organoid-like human models.

7. Discussion

In the course of my Master Thesis not only genetic BPTF perturbations (siRNA, shRNA, CRISPR/Cas9) but – due to the availability of a highly specific, proprietary BPTF inhibitor (BI-90) – also pharmacologic inhibition of *BPTF* could be performed. For this, we chose two human NSCLC cell lines exhibiting a low (NCI-H1437) or a high EMT score (NCI-H157). We recently have shown that the two cell lines differ substantially in their potency to induce cytokines in co-cultures with fibroblasts [16, 188]. Both cell lines can successfully be grown in three-dimensional cultures – either as floating spheroids or as embedded organoids [16, 85, 196, 197].

In preliminary studies the 3D cultures proofed as suitable for studying immune cell activity. Applying compounds in 3D co-cultures consisting of tumour, stromal (CAFs or NAFs) and immune cells it is of great importance to first test the compound´s activity on each cell type alone. This is necessary in order to exclude any inhibitory or activating effect of the compound on a cell type *per se*. The addition of BI90 to each cell-type specific monoculture neither interfered with the viability of NSCLC cell lines (**Figure 23**) nor with fibroblasts (data not shown). The same holds true for donor-derived primary NK cells (PNKs); exposure of PNKs to BI90 neither reduced their viability (**Figure 26**) nor influenced their cytotoxic potential (**Figure 27**). Fortunately, also BI90 did not interfere with the formation of MCTS or the 3D growth behaviour *per se* (**Figure 24**, **Figure 25**). Thus, BI90 could be applied for pharmacological *BPTF* inhibition in NSCLC cell lines without generating any effect in the respective monocultures. In addition, pretreatment of tumour cells alone and subsequent washing out of the BI90 could generate a similar stimulating/activating effect on PNKs (data not shown) supporting the hypothesis that BI90 triggers a program exclusively in tumour cells making them susceptible to NK cell attack.

As sometimes also strong effects of the solvent DMSO on the growth rate have been reported for cultivated cells [198, 199] we analyzed the impact of DMSO as well. DMSO at concentrations up to 0.5 % in the tissue culture medium did not influence the viability of tumour cells (**Figure 23**). The viability and activity of PNKs stayed untouched up to 0.1 % DMSO (**Figure 19**, **Figure 20**, **Figure 26**). In order to rule out any inhibitory effect of DMSO *per se* all experiments including negative controls were performed at 0.1% DMSO.

Treatment of floater co-cultures with BI90 led to a strong and dose-dependent increase in the PNK-mediated killing of MCTSs (**Figure 28, Figure 29**). The increased cytotoxic potential of PNKs towards BI90 treated MCTSs was confirmed by an increase in *GZMB* and *IFNG* in supernatants of floater co-cultures (**Figure 30**). NCI-H157, a NSCLC cell line with a high EMT score, was killed more efficiently by NK cells than NCI-H1437 (low EMT score). Our finding is in agreement with the reported fact that (in contrast to T cells) the metastatic process can be limited by NK cell-mediated cytotoxicity by targeting up-regulated NKG2D ligands on tumour cells undergoing EMT [200].

Next, we performed similar studies in a more *in vivo*-like environment. Embedded 3D cultures recapitulate the *in vivo* situation much better than floater models [74, 85]. The presence of a matrix and HDFs allows additional interactions between stroma, tumour and immune cells building up the tumour microenvironment that "shapes" the immune response [74, 150, 201]. A prerequisite for tumour cell killing by immune cells is their active migration and invasion into MCTSs [202]. It is an advantage of embedded 3D co-cultures to allow both, the monitoring of migration and tumour cell killing by activated immune cells. In our model the reduction in red fluorescence is equivalent to tumour cell death (tumour cells constitutively express the recombinant fluorescent mKate2 protein). The migratory potential of infiltrating immune cells was monitored via green fluorescence (immune cells are labelled with cell tracer CFSE prior to analysis). The major difference in embedded models is that PNKs need to actively migrate towards the MCTSs [85, 202], while in floater models PNKs are brought in direct contact with MCTSs by gravity [85]. The potential of NK cells to move through the matrix (and to infiltrate the MCTSs) was shown by generation of z-stack images (plus the corresponding maximum intensity projections) and the subsequent infiltration analysis by a novel algorithm based on Euclidean distance measurements (**Figure 31C**, **Figure 33C**, **Figure 34**). In general, similar dose-dependent effects were seen in 3D embedded cultures, but with a stronger killing effect in cultures with NCI-H1437 than with NCI-H157 clearly supporting our hypothesis that the EMT (score) status of a tumour cell strongly impacts on the outcome of the treatment (**Figure 3**) [85, 200]. In contrast to the floater cultures without fibroblasts, embedded 3D systems allow the intensive cross-talk with stroma cells and the tumour microenvironment leading in the case of NCI-H157 to a more immune-suppressive environment. The induction of such an immune modulating cross-talk

was previously described by our lab [16, 190] and may explain why observed immunogenic effects in 3D embedded systems are smaller compared to 3D floaters. Embedded co-cultures of HDFs and EMT-high NCI-H157 cells led to enhanced production of immunosuppressive interleukins and cytokines including *CFS2* [16]. Except for *CFS2*, expression of other immunosuppressive molecules such as IL1B, IL6 and IL8 was also increased in co-cultures of NCI-H1437 (low EMT score) and HDFs [16]. *CFS2* is associated with differentiation of hematopoietic stem cells and stimulation of immune cell activity but exhibit tumour-promoting functions as well [203, 204]. High expression of *CFS2* correlates with bad prognosis in urothelial carcinoma patients [204]. IL6 is an important interleukin linked to tumour cells immune evasion [205]. Long-lasting exposure of NK cells to IL6 reduces their cytotoxic potential, as production of *GZMB* and perforins is reduced in those NK cells [92, 206].

Besides the generation of an immunesuppressive environment it should also be considered that the bioavailability of novel chemical entities (NCEs) and novel biological entities (NBEs) in 3D embedded co-cultures is generally inferior to 3D floaters. Unspecific interactions with the ECM, uptake by FBs, enzymatic degradation, metabolization, a low distribution coefficient and the induction of molecular resistance/escape mechanisms in tumour and adjacent cells negatively interfere with an appropriate bioavailability and finally with the efficacy of the respective drug [207]. Again, the application of the more in vivo-like embedded model might also contribute to a better understanding of parameters influencing the bioavailability of compounds and biological therapeutics.

Even in an immunosuppressive environment as present in embedded cultures, BI90 has the potential to induce tumour cell killing by NK cells. Obviously, BI90 can compensate the immunosuppressive crosstalk between non-invasive tumour cells (e.g. NCI-H1437) and the TME (represented by HDFs). However, this effect is almost abolished in co-cultures exhibiting a higher immunosuppressive crosstalk exemplified by the co-culture of NCI-H157 cells (EMT high) and HDFs. Potentially an increase in tumour cell killing might be triggered, if BI90 would be re-added to the co-cultures after a couple of days.

Mayes and colleagues reported that *BPTF* KD reduced *HPSE* expression [68]. Heparan sulfates (HSs) are known NCR co-ligands [42]. According to their published work, reduction in

HSs prevents the interaction of NK cells with tumour cells (**Figure 12**) [68]. In contrast to their findings, we were not able at all to identify reduced *HPSE* mRNA levels in BI90-treated tumour cells (**Figure 35**). However, Mayes *et al.* performed shRNA-mediated *BPTF* KD whereas we first made use of BI90 to pharmacologically inhibit *BPTF*. In contrast to a pharmacological inhibition of a distinct protein function, a KD completely abolishes all integrated functions of a gene product. Particularly, in the case of *BPTF* a pharmacologic inhibition might differ substantially from a KD as *BPTF* harbours many different functional domains (**Figure 8**) such as a high mobility group box A (HMGA) binding site, a DNA-binding homeodomain, different transcription factors domain (DDT), a plant-homeodomain (PhD) finger domain 1 and 2, a bromodomain (BROMO; BRD), a Q-rich domain etc. Inhibiting only one functional part (BI90 is only targeting the BROMO domain) clearly leads to a complete different inhibitory profile than a KD as it has recently been shown for the pharmacological and genetic inhibition of heme oxygenase-1 [208]. Therefore, we decided to perform a genetic *BPTF* KD via siRNA and a protein domain-specific CRISPR-mediated *BPTF* KO. Applying those methods in parallel allows the discrimination and characterization of different functional parts of a given gene/protein. The CRISPR technology, for instance, enables both the analysis of a complete loss of a protein(function) as well as the identification of essential functional parts of a protein [97]. In contrast, KD generates a more gene dose-like effect whereas pharmacologic inhibition by small NCEs targets selectively a distinct function of a protein such as an enzymatic function. Taken together, temporary removal of certain proteins via siRNA-mediated KD may cause stronger effects on cells than constitutive pharmacological target inhibition and weaker effects than a complete KO.

BPTF is a large protein, containing multiple domains with specialized (and partially still unknown) functions [66, 67]. Thus, sgRNAs (single guide RNAs) targeting different domains of *BPTF* were designed. Indeed, domain-specific effects were observed, with larger outcome in NCI-H157 than in NCI-H1437 (**Figure 38**, **Figure 39**). Strongest effects were observed with sgRNAs targeting the N-terminal domain, while those recognizing more C-terminal domains (PHD-finger, BRD) showed weaker or no effects. However, more sgRNAs were designed against the 5’ exon than against the other domains (5’ exon: 5, PHD: 3, BRD: 1) and for a final judgement a more comprehensive study with at least 10 sgRNAs per domain will be required.

Nevertheless, we were able to generate stable transduced NCI-H1437 cell pools via FACS sorting for at least one sgRNA per domain (5' exon: sgRNA1; PHD: sgRNA6, sgRNA8; BRD: sgRNA9). All pools exhibited a reduced *BPTF* expression on the protein level (**Figure 40**). Of particular importance, NCI-H1437 *BPTF* KO cells (pool) were significantly better killed in 2D co-cultures with PNKs compared to the nontarget control (**Figure 42**). The same holds true for NCI-H157 *BPTF* KD and the nontarget control when co-cultivated with PNKs (**Figure 37**). Again, no significant changes in abundance of *HPSE* and *NDST1* mRNA levels were detected in FACS-sorted pools from NCI-H1437 *BPTF* KO cells (**Figure 41**). These results are in line with our finding that pharmacological *BPTF* inhibition does also not affect *HPSE* expression. Yet *HPSE* transcript levels in NCI-H157 *BPTF* KD remain to be determined. Interestingly, NCI-H1437 *BPTF* KO (pool) cells exhibited differences in their 3D growth compared to the nontarget control (**Figure 47**). As discussed above, a complete KO of the multifunctional BPTF protein leads to a different inhibitory profile than a specific pharmacologic targeting by BI90. This is in line with previously published data that tumours formed by murine *BPTF* KD breast cancer cell lines grew flat compared to the nontarget control [66].

One reason for the discrepancy between the data from Mayes and colleagues and our results may be the species-specific effect of BPTF inhibition. In contrast to Mayes *et al*. [68, 73] we used the human NSCLC cell lines NCI-H157 and NCI-H1437, respectively, which we previously had extensively characterized [85, 188]. It is easily conceivable that the human NSCLC cell lines may use a completely different immune escape/modulatory mechanism than the mouse breast cancer cell lines 67NR and 66cl used by Mayes and colleagues. Human and murine immune systems differ substantially [209], thus it is possible that the *HPSE*-triggered mechanism is species-specific. Interestingly, Mayes *et al*. showed that the highly cytotoxic human lymphoma NK cell line (NK-92) has the potential to kill murine and human *BPTF* KD cells more efficiently than the control cell lines [68]. Interestingly, we and others have shown that the human NK cell line NK-92 lacks most of the killer inhibitory receptors (KIRs) [210] and we therefore had excluded this cell line from our studies. According to Mayes *et al*. all three used human breast cancer cell lines exhibited reduced *HPSE* expression after shRNA-mediated *BPTF* KD [68]. Two of the three used human cell lines are derived from breast cancer (T47D, MDA-MB-436) and *BPTF* expression can be linked with poor prognosis. However, the third cell line is a neuroblastoma cell line (SH-SY5Y). No

information is presented by Mayes *et al*., why this cell line was selected and whether there is a correlation between *BPTF* and *HPSE* expression in this indication [68]. In general, one could question how meaningful cross-species experiments are addressing immunologic questions.

Even though Mayes *et al*. worked with human cell lines as well, microarray analysis was only done for the murine cell lines [68]. Thus, it remains unclear whether their observations with human cell lines are due to reduced *HPSE* expression or not. Their argument for an inter-species conserved mechanism is that only blocking of NKp30 in NK-92 could rescue tumour cells from NK-92-mediated killing whereas blocking of NKp46 had no influence on the cytotoxic potential of NK-92 towards *BPTF* KD and control cells. Importantly, the human ortholog of murine NCR1 is NKp46 not NKp30 [211]. Thus, it is not possible to prove the given hypothesis with this blocking experiment.

To ensure working with fully functional NK cell populations, we decided to use donor-derived primary NK cells (PNKs) instead of relying on the aberrant NK cell-specific phenotype of NK-92 [210]. As a consequence, we had to cope with donor variability (**Figure 44**) [212]. However, working with PNKs allowed us to rule out any artificial observations due to the altered behaviour of NK cell-derived cell lines like NK-92.

Only few natural cytotoxicity receptor (NCR) ligands are identified so far [42]. This and the discovery that at least NKp44 contains a functional immunoreceptor tyrosine-based inhibitory motif (ITIM) with a corresponding ligand *PCNA* (proliferating cell nuclear antigen) [42], makes it challenging to identify biological mechanism(s) underlying *BPTF*-mediated immune escape. It does not only dependent on the tumour cell (e.g. their genetic background), but also on the molecular repertoire of NK cells and possibly on other cell types present in the TME. Potentially more than one tumour immune escape mechanism utilizes *BPTF*.

Mayes *et al.* publish a second paper discussing another hypothesis how *BPTF* KD increases immune cell-mediated tumour cell killing in mice models: *BPTF*-dependent NURF activity prevents expression of *PSMB8*, *PSMB9, TAP1* and *TAP2* [73]. Presence of these proteins would increase immunoproteasome activity (**Figure 13**) finally leading to enhanced T cell-mediated tumour cell killing [73]. Interestingly, depletion experiments (via monoclonal antibodies (mAb) treatment) for NK cells (anti-asialo-GM1 mAb), $CD4^+$ T cells (anti-CD4 mAb)

or $CD8^+$ T cells (anti-CD8 mAb) in mice did either identify NK cells [68] or T cells [73] as the executing cell type.

To gain a more detailed biological understanding, gene expression profiling of five different *BPTF* KO single cell clone cultures (#13, #36, #43, #50, #54) was performed (**Figure 48**, **Figure 49**). Two genes were found up-regulated in all five single cell clones analysed (*OVGP1* and *CALCOCO1*) and seven genes were found to be jointly down-regulated in all five NCI-H1437 *BPTF* KO single cell clones (*CCL22*, *ABCA1*, *CGA*, *CLEC3A*, *SERPINB4*, *AKAP12* and *CLIC6*).

OVGP1, the oviduct-specific glycoprotein is a large, carbohydrate-rich, epithelial glycoprotein with numerous O-glycosylation sites located within threonine, serine, and proline-rich tandem repeats. It plays a role during trophoblast implantation [110-112] and was shown to be decreased during inflammation [113]. *CALCOCO1* is a calcium binding and coiled-coil domain 1 protein which functions as a steroid hormone (glucocorticoid) receptor coregulator gene [114]. It enhances *GATA1*- and *MED1*-mediated transcriptional activation from the gamma-globin promoter during erythroid differentiation of K562 erythroleukemia cells [116]. Whether and how these two genes might contribute to the increase in immune cell infiltration upon *BPTF* KO remains to be determined.

Interestingly, all down-regulated genes exhibit a link to immune regulatory functions or inflammatory responses and their following degenerative molecular events (for detailed description of all identified genes see *5.5. Gene Expression Profiling of BPTF KO Single Cell Clone Cultures and BI90 Treated Tumour Cells*). For instance, *CCL22* was shown to be involved in promoting regulatory T cell communication with dendritic cells in lymph nodes [213] and in the establishment of an immunosuppressive tumour microenvironment [214]. C-type lectin domain family 3 member A (*CLEC3A*) is a tumour cell membrane-bound substrate of *MMP-7* (matrilysin). Cleavage of *CLEC3A* modulates cell adhesion activity [102]. A-kinase anchoring protein 12 (*AKAP12*) drives M2 macrophages during inflammation recovery, promoting an M2 polarization of macrophages [215].

"STRING" (Search Tool for the Retrieval of Interacting Genes/Proteins) database analysis revealed that many genes deregulated in at least 3 out of 5 single cell clones were found to be involved in cell cycle regulation (**Figure 50**). It was previously shown that inhibitors targeting cell cycle regulators (e.g. *CDK4* and *CDK5*), not only arrest cells but also increase

their immunogenicity [216]. Among various other proteins involved in cell cycle regulation, *PLK1* expression was found down-regulated upon *BPTF* KO. The gene encodes for Polo-like kinase 1, a serine/threonine kinase[15]. *PLK1* is essential for cell cycle progression and it is highly expressed in many tumours. Therefore, research focused on development of *PLK1* inhibitors aiming at reduction of cancer cell proliferation[16]. A recent study revealed a correlation between *PLK1* inactivation and increased immunogenicity of different cancer cell lines [217]. Inhibition of *PLK1* by BI2536, a PLK1-specific inhibitor leads to an increase in expression of HLA proteins and – most interestingly – of *TAP1* [217]. Increased *TAP1* abundance was also described by Mayes and colleagues upon shRNA-mediated *BPTF* KD [73] and was identified as a cause of elevated immunoproteasome activity [73]. Additionally, we identified genes up-regulated involved in interferon-induced anti-viral defence (e.g. *IFIT1*, *IFIH1*) [216]. Whether the expression of these genes leads indeed to an altered interferon secretion in *BPTF* KO tumour cells remains to be elucidated.

Furthermore, *FOXO4* (Forkhead box protein O4) and *GPC6* (glypican 6) were identified as up-regulated. *FOXO4* is a transcription factor involved in assembly and/or activity of the 26S proteasome, as it activates *PSMD11* (Proteasome 26S Subunit, Non-ATPase 11) expression - at least in embryonic stem cells[17][18]. Members of the *PSMD* family (*PSMB8*, *PSMB9*) were described by Mayes *et al*. to alter tumour cells immunogenicity towards T cells in a *BPTF*-dependent manner [73]. *GPC6* belongs to the family of glycosylphosphatidylinositol (GPI)-anchored heparan sulfate proteoglycans. They function as co-receptors for ECM proteins, growth factors and proteases[19] [218]. *GPC6* is also involved in regulating cell cycle and cell division[20]. A higher HSPG surface abundance may increase the immunogenic “visibility” of *BPTF* KO tumour cells towards PNKs in a *HPSE*-independent manner.

In contrast to down-regulated genes, the “STRING” data base analysis of up-regulated genes (upon *BPTF* KO) is based on a low confidence level. To draw statistically more robust conclusions, additional data sets need to be generated. For instance, gene expression

[15] https://www.ncbi.nlm.nih.gov /gene/5347, 12.02.2019
[16] https://www.ncbi.nlm.nih.gov /gene/5347, 12.02.2019
[17] https://www.genecards.org/cgi-bin/carddisp.pl?gene=FOXO4, 12.02.2019
[18] https://www.genecards.org/cgi-bin/carddisp.pl?gene=PSMD11, 12.02.2019
[19] https://www.genecards.org/cgi-bin/carddisp.pl?gene=GPC6 &keywords=GPC6, 12.02.2019
[20] https://www.genecards.org/cgi-bin/carddisp.pl?gene=GPC6 &keywords=GPC6, 12.02.2019

profiling of additional *BPTF* KO single cell clones ideally generated from additional sgRNAs should be performed including more than one tumour cell model.

Comparison of transcripts being up- or down-regulated in at least three out of five *BPTF* KO single cell clones with the transcriptome of BI90-treated tumor cells revealed a different set of modulated genes (**Figure 54, Figure 58**). For this comparison the transcriptome of BI90-treated tumor cells was analysed at different treatment time points; early, intermediate and late (for details see Figure 54, Figure 58 and Table 10). Only two transcripts were found up-regulated upon treatment with BI90; at an early time point the transcript of *IFIH1* and at late one *GMFG*. The intermediate time point did not show any significant changes in the compared transcriptomes.

IFIH1, also known as *MDA5* (Melanoma Differentiation-Associated protein 5) is a RIG-I-like receptor dsRNA helicase enzyme belonging to the DEAD box protein family. It is up-regulated in response to treatment with beta-interferon (IFNB). *IFIH1* is part of the RIG-I-like receptor (RLR) family and functions as a pattern recognition receptor (recognizing dsRNA) that is a sensor for viral infection [219-221]. Recent studies found that cancer cells can mimic a viral infection to activate RNA sensing pattern recognition receptors (PRRs) and interferon response pathway [222-224]. This in turn stimulates cytotoxic immune cells such as NK cells and $CD8^+$ T cells, which kill infected cells via induced cell lysis and apoptosis [225]. *GMFG* (glia maturation factor gamma) is a cytokine-responsive protein mediating pluripotentiality and lineage commitment of human hematopoietic stem cells. It gets induced by *GCSF* (granulocyte-colony stimulating factor) and *EPO* (erythropoietin) [226] and it mediates neutrophil chemotaxis [227]. High expression of *GMFG* has recently been linked with poor prognosis in epithelial ovarian and colorectal cancer promoting cell migration and invasion [228, 229]. In addition, *GMFG* is also involved in polarization of macrophages toward an anti-inflammatory M2 phenotype [230].

In our project, both settings of gene expression profiling (specific *BPTF* inhibition via BI90 and *BPTF* KO), showed up-regulation of *IFIH1*. *BPTF* is an essential and unique subunit of the ISWI family chromatin remodeling complex NURF [66], which has the ability to modify cell's epigenome. Impaired NURF function, due to *BPTF* inhibition/KO, may induce cellular stress and expression of endogenous retroviral dsRNA. Increase in immunogenicity of *BPTF*

inhibited/KO cells may be induced via *IFIH1*-dependet type 1 interferon response. Thus, analyzing the abundance of dsRNA in the used tumour cell lines will an essential aim for future experiments.

To conclude, we were able to generate and apply complex 3D *in vivo*-like co-culture models which were successfully used to study the contribution of BPTF expression in tumour cells on the infiltration and activation of PNKs. Both, genetic and pharmacologic inhibition in tumour cells, clearly demonstrated the essential contribution of *BPTF* to the tumor cell´s immunogenic visibility. The differences observed between 3D floater and 3D embedded co-culture models nicely showed that increasing complexity influences the outcome of experiments. The differences in the immunogenicity of tumour cells is most likely due to the induction of an anti-inflammatory microenvironment driven by the cross-talk with stromal cells in the more complex models. Thus, our 3D models proved as powerful tools, to study complex immune-response related biological questions in more *in vivo*-like settings.

It remains to be elucidated how *BPTF*-mediated immune escape works on the molecular level and whether it is a commonly utilized mechanism by cancer cells. Although, both the genetic as well as the pharmacologic inhibition of BPTF led to an increase in infiltration and activation of NK cells, it remains challenging as expression profiling of BI90-treated NCI-H157 and NCI-H1437 as well as NCI-H1437 *BPTF* KO single cell clones exhibited only little overlap. Gain- and loss-of-function analysis of the identified putative driver genes may lead already to a better understanding of *BPTF*´s contribution to the immunogenicity of cancer cells. However, it cannot be ruled out that pharmacologic inhibition and genetic *BPTF* KO may lead to different transcriptional perturbations. These differences need to be dissected in future experiments, for example, via usage of additional sgRNAs to identify the essential active regions or by a more detailed time-resolved transcriptional profiling upon BI90 treatment in more than one tumour cell line. The diverse outcome might also be due to the large heterogeneity of tumour cells *per se* e.g. caused by genomic instability, mutational load and EMT status. To receive a more comprehensive insight, detailed time course kinetics with additional single cell clones via deep sequencing/RNA-Seq or even single cell sequencing should be performed. Our preliminary transcriptional profiling experiments on DNA microarrays are certainly inferior to NGS-based analyses [231-233]. In addition, identification of altered post-translational phosphorylation events upon *BPTF* inhibition or *BPTF* KO via

phosphoproteomics [234, 235] should be considered. The same holds true for a detailed time-resolved cytokine profiling approach. As *BPTF* is a subunit of a chromatin remodelling complex, a genome-wide ChIPSeq analysis [236] would be the ultimate goal to identify those chromatin regions that are occupied and regulated by *BPTF*. Last but not least, it should be analysed whether *BPTF* depletion/inhibition does also increase human primary T cell immune response as previously shown by Mayes *et al*. in a murine model [73].

Apart from of many open questions in the context of the underlying molecular mechanisms of *BPTF*´s contribution to tumour immunogenicity, *BPTF* can be regarded as a highly promising target in the immunological approach of combating human cancer.

8. Supplementary

8.1. *BPTF* and *HPSE* Expression in NCI-H1437 and NCI-H157

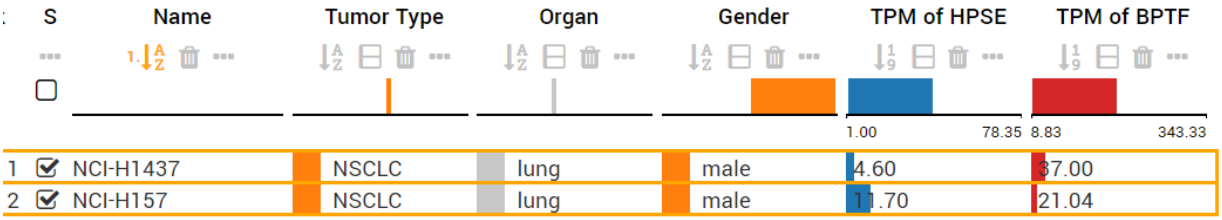

Figure 55: *BPTF* (red) and *HPSE* (blue) expression in NSCLC cell lines NCI-H1437 and NCI-H157.

TPM: Transcripts per million

8.2. Plasmid cards

8.2.1. NucLight Red expression vector

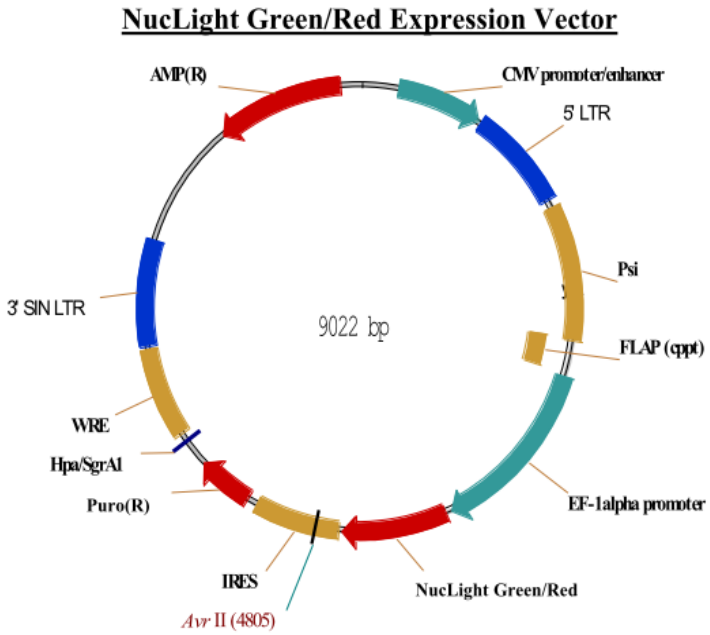

LentiEF1a NucLight Puro			
Feature	Start	End	Description
CMV Enhancer	245	821	Promoter/Enhancer
Psi	1570	2454	Packaging Sequence
FLAP (cppT)	2432	2665	Integration Sequence
CMV Promoter	3231	3810	Promoter
NucLight Red/Green	3834	4550	Coding Sequence
WPRE	4664	5251	Regulatory Element
3'SIN-LTR	5270	5959	Long Terminal Repeat
AmpR	6783	7640	Resistance Gene

Figure 56: LucLight Green / Ref Expression vector.

LucLight Green/Ref Expression vector was used to stably transduce NCI-H1347 and NCI-H157 to stably express mKate2 fluorescence protein.

8.2.2. pRSF91.dTomato-Blasti-controltargets

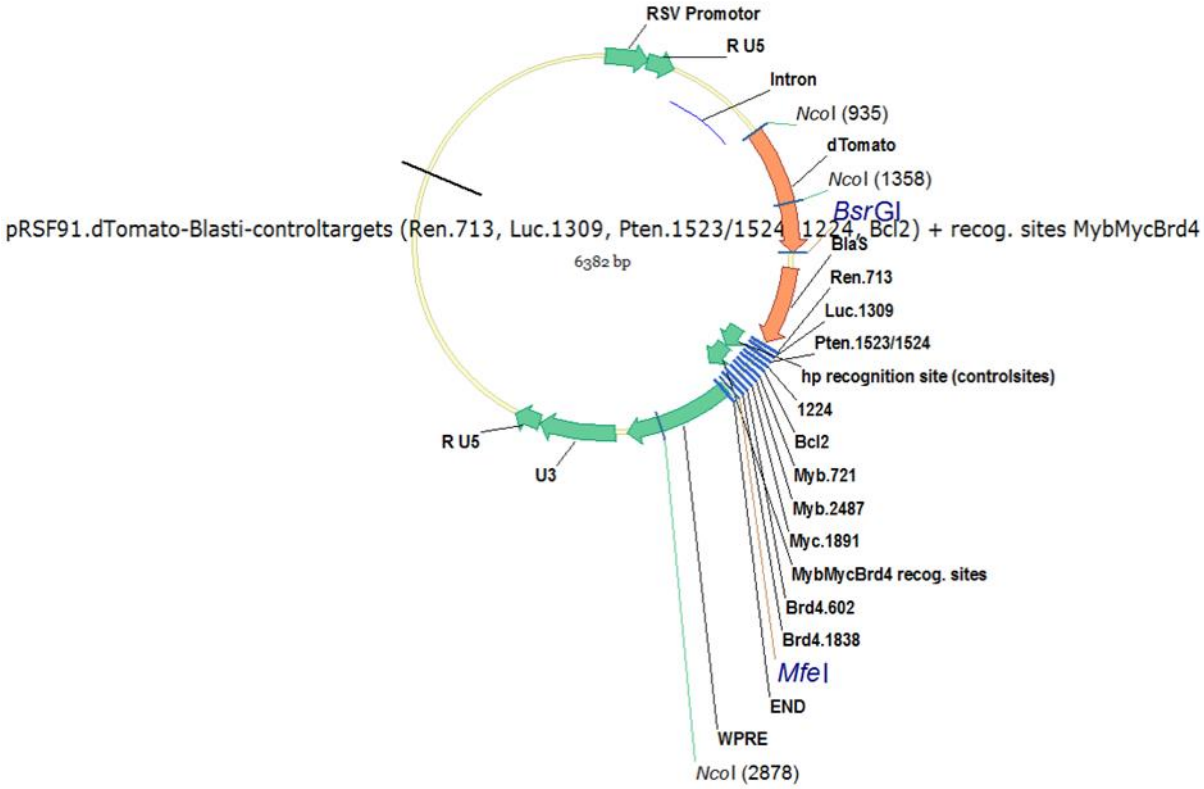

Figure 57: pRSF91.dTomato-Blasti-controltargets plasmid

pRSF91.dTomato-Blasti-controltargets plasmid was used stably express dTomato in NCI-H1437 and NCI-H157.

8.3. Genotype One Shot™ Stbl3™ Chemically Competent E. coli strain

F^- mcrB mrr hsdS20(r_{B-}, m_{B-}) recA13supE44 ara-14 galK2 LacY1 proA2 rpsL20(Str^R) xyl-5 λ^- leu mtl-1

One Shot™ Stbl3™ Chemically Competent E. coli were purchased from Invitrogen (#C737303).

3.4 Supplementary Gene Expression Profiling

Sample #	Sample ID	Conc. [ng/µl]	Volume [µl]	OD 260/280	OD 260/230	Background Information	Comparison	
1	5	482,1	45	1,98	1,8	NCI-H157 untreated		
2	6	140,9	45	2,04	1,71	NCI-H1437 untreated		
3	7	601,6	45	1,96	1,13	157 2h 1µM cpd	7 & 8	5 & 7
4	8	390,8	45	2,01	1,76	157 2h 0,1% DMSO		5 & 8
5	9	532,9	45	1,95	1,88	1437 2h 1µM	9 & 10	6 & 9
6	10	440,2	45	2	1,27	1437 2h 0,1%		6 & 10
7	11	794,9	45	2,04	1,81	157 4h 1µM	11 & 12	5 & 11
8	12	236,7	45	2,03	1,42	157 4h 0,1%		5 & 12
9	13	262,6	45	2,03	1,49	1437 4h 1µM	13 & 14	6 & 13
10	14	877,2	45	2,03	1,66	1437 4h 0,1%		6 & 14
11	15	604,8	45	2,04	1,2	157 8h 1µM	15 & 16	5 & 15
12	16	171,9	45	2,03	1,76	157 8h 0,1%		5 & 16
13	17	140,3	45	2,04	1,69	1437 8h 1µM	17 & 18	6 & 17
14	18	551,1	45	2	2,44	1437 8h 0,1%		6 & 18
15	19	1141	45	2,01	1,83	157 24h 1µM	19 & 20	5 & 19
16	20	870,1	45	2,05	1,99	157 24h 0,1%		5 & 20
17	21	392,1	45	2,08	1,5	1437 24h 1µM	21 & 22	6 & 21
18	22	567,4	45	2,04	2,37	1437 24h 0,1%		6 & 22
19	23	366,8	45	2,05	1,74	157 48h 1µM	23 & 24	5 & 23
20	24	734,3	45	2,04	2,06	157 48h 0,1%		5 & 24
21	25	408,1	45	2,06	1,07	1437 48h 1µM	25 & 26	6 & 25
22	26	593	45	2,11	0,89	1437 48h 0,1%		6 & 26
23	27	382,2	45	2,05	1,96	157 71h 1µM	27 & 28	5 & 27
24	28	690,3	45	2,08	1,43	157 71h 0,1%		5 & 28
25	29	732,8	45	2,06	1,97	1437 71h 1µM	29 & 30	6 & 29
26	30	536,2	45	2,02	1,67	1437 71h 0,1%		6 & 30
27	31	886,5	45	2,02	2,03	157 96h 1µM	31 & 32	5 & 31
28	32	1102	45	2	2,11	157 96h 0,1%		5 & 32
29	33	992,6	45	2,02	1,7	1437 96h 1µM	33 & 34	6 & 33
30	34	543,4	45	2,02	1,3	1437 96h 0,1%		6 & 34
31	35	678,9	45	1,99	1,87	157 120h 1µM	35 & 36	5 & 35
32	36	460,5	45	1,99	2	157 120h 0,1%		5 & 36
33	37	328,7	45	2,03	1,74	1437 120h 1µM	37 & 38	6 & 37
34	38	450,2	45	1,98	1,83	1437 120h 0,1%		6 & 38
35	39	900,5	45	2,05	2,33	157 170h 1µM	39 & 40	5 & 39
36	40	818,3	45	2,06	2,13	157 170h 0,1%		5 & 40

Table 10: Overview on cell lysate samples prepared from BI90-treated NSCLC cell lines NCI-H157 and NCI-H1437 for expression profiling on Affymetrix Gene Chips (Affymetrix EXP).

Samples derived from NCI-H157 are highlighted in yellow; those from NCI-H1437 are shown in blue. For comparison of expression profiles (transcriptomes) at a given time point, cells were left

untreated for the respective time in a medium containing an equal concentration of DMSO (0.1 w/v %) as applied in the culture medium of treated cells. The column “Comparison” indicates how the comparison was performed for each time point (for the corresponding heatmaps see Figure 58). As the time point 170 hours for NCI-H1437 did not reveal any informative data set, this time point was excluded from further analyses. Cell lysates were prepared in biological triplicates for each time point.

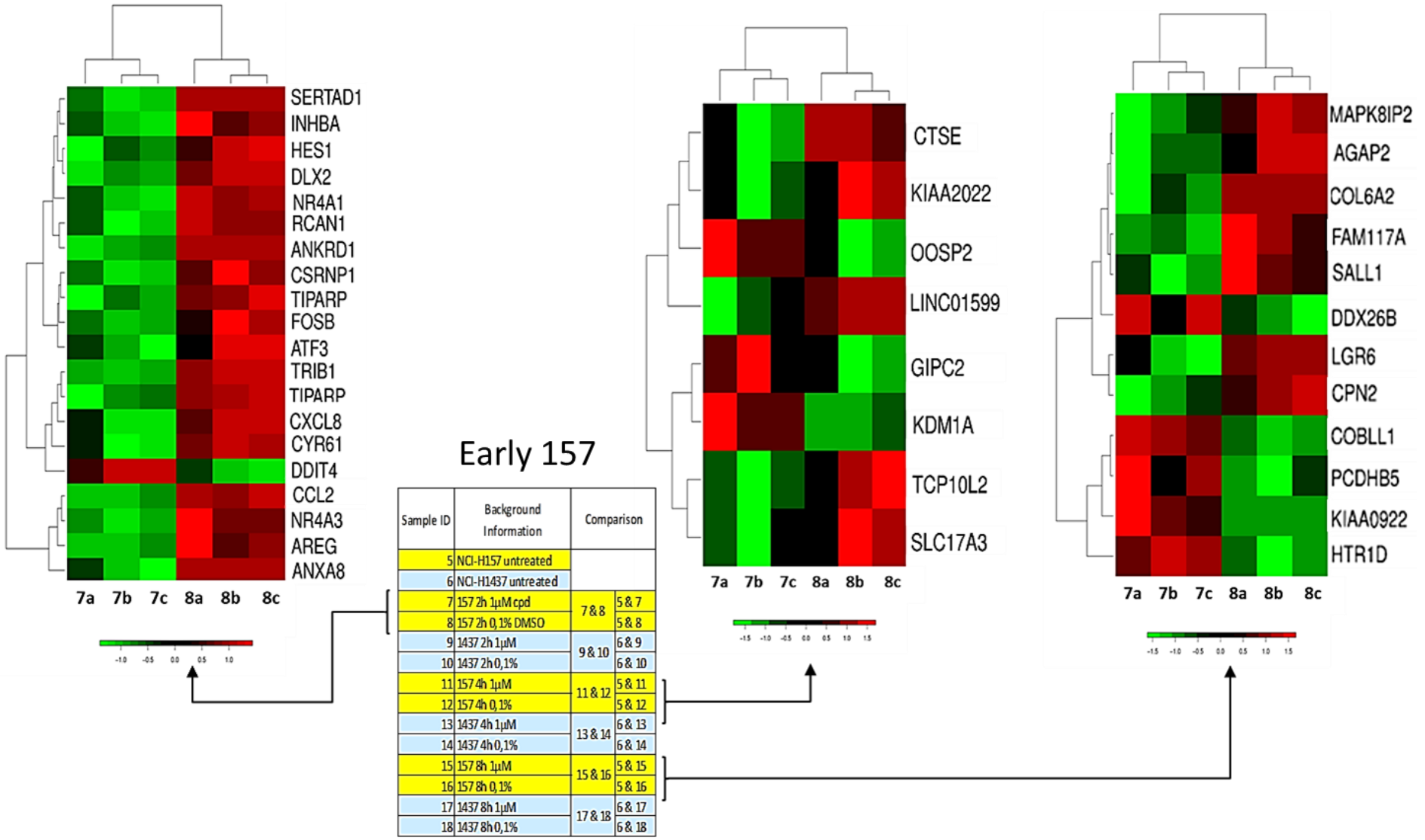

Sample ID	Background Information	Comparison	
5	NCI-H157 untreated		
6	NCI-H1437 untreated		
7	157 2h 1µM cpd	7 & 8	5 & 7
8	157 2h 0,1% DMSO		5 & 8
9	1437 2h 1µM	9 & 10	6 & 9
10	1437 2h 0,1%		6 & 10
11	157 4h 1µM	11 & 12	5 & 11
12	157 4h 0,1%		5 & 12
13	1437 4h 1µM	13 & 14	6 & 13
14	1437 4h 0,1%		6 & 14
15	157 8h 1µM	15 & 16	5 & 15
16	157 8h 0,1%		5 & 16
17	1437 8h 1µM	17 & 18	6 & 17
18	1437 8h 0,1%		6 & 18

Figure 58A)

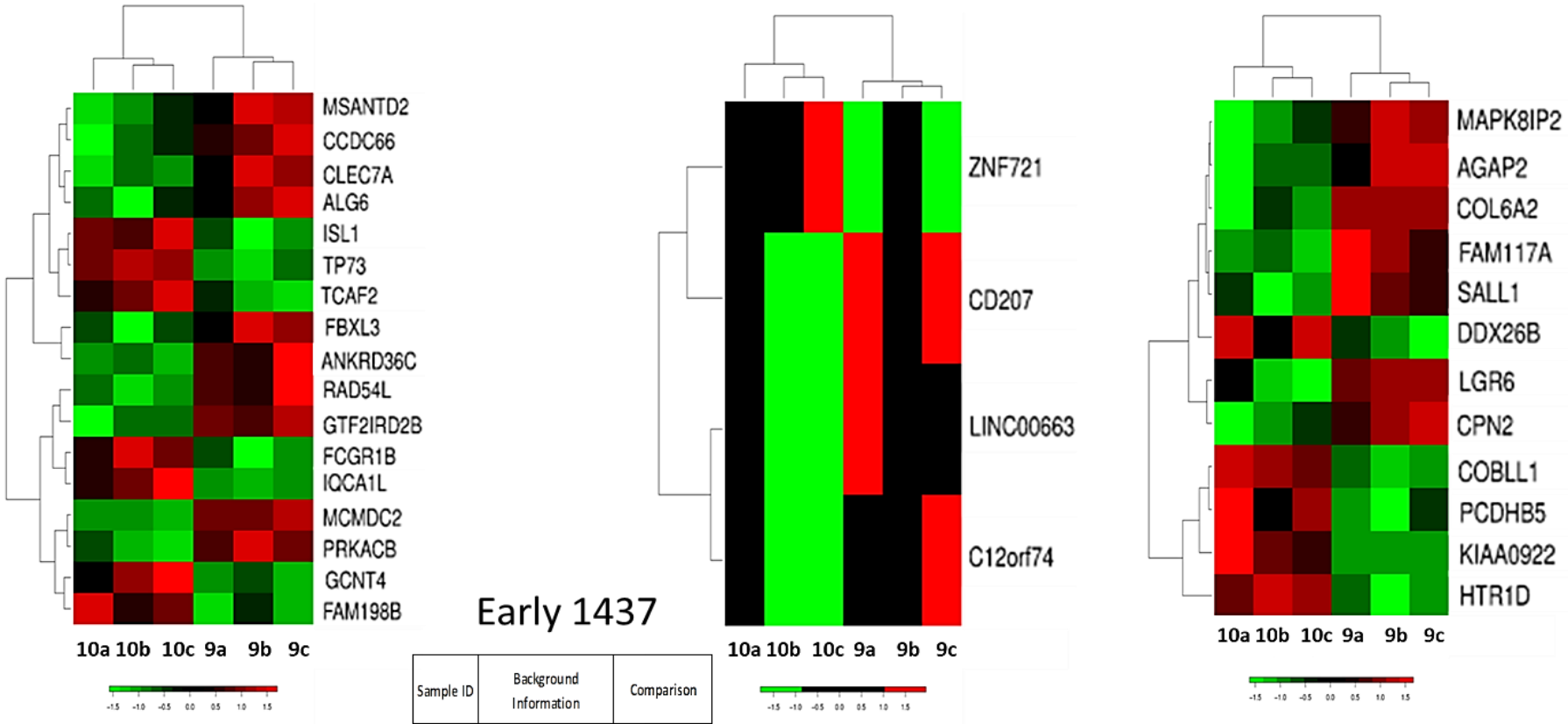

Early 1437

Sample ID	Background Information	Comparison	
5	NCI-H157 untreated		
6	NCI-H1437 untreated		
7	157 2h 1µM cpd	7 & 8	5 & 7
8	157 2h 0,1% DMSO		5 & 8
9	1437 2h 1µM	9 & 10	6 & 9
10	1437 2h 0,1%		6 & 10
11	157 4h 1µM	11 & 12	5 & 11
12	157 4h 0,1%		5 & 12
13	1437 4h 1µM	13 & 14	6 & 13
14	1437 4h 0,1%		6 & 14
15	157 8h 1µM	15 & 16	5 & 15
16	157 8h 0,1%		5 & 16
17	1437 8h 1µM	17 & 18	6 & 17
18	1437 8h 0,1%		6 & 18

Figure 58B)

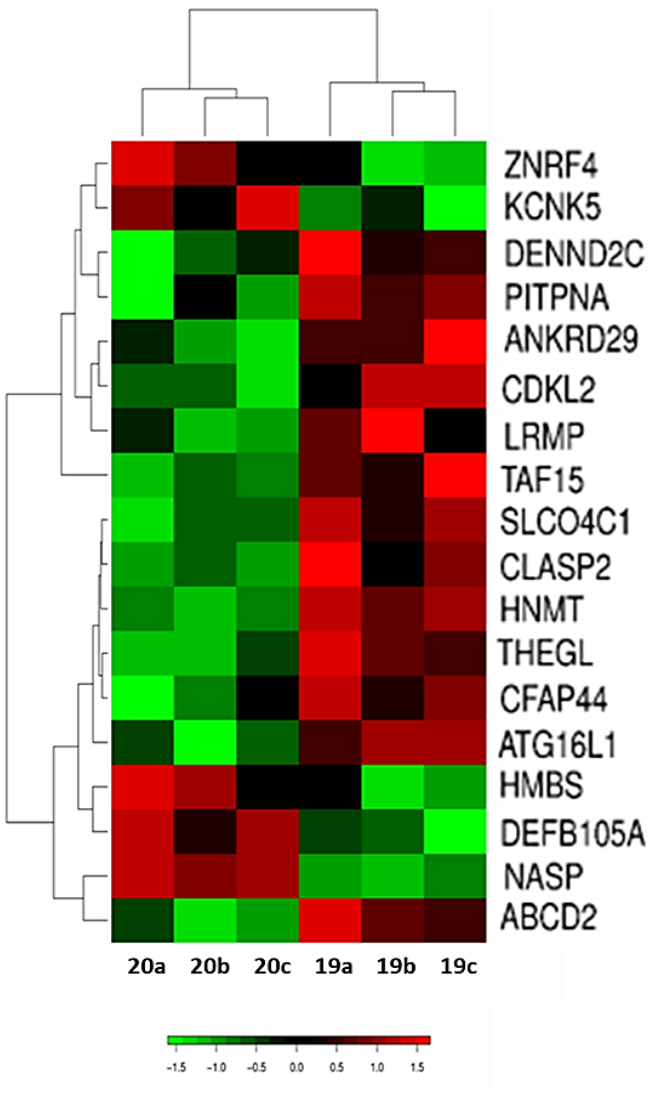

Intermediate 157

Sample ID	Background Information	Comparison	
5	NCI-H157 untreated		
6	NCI-H1437 untreated		
19	157 24h 1µM	19 & 20	5 & 19
20	157 24h 0,1%		5 & 20
21	1437 24h 1µM	21 & 22	6 & 21
22	1437 24h 0,1%		6 & 22
23	157 48h 1µM	23 & 24	5 & 23
24	157 48h 0,1%		5 & 24
25	1437 48h 1µM	25 & 26	6 & 25
26	1437 48h 0,1%		6 & 26

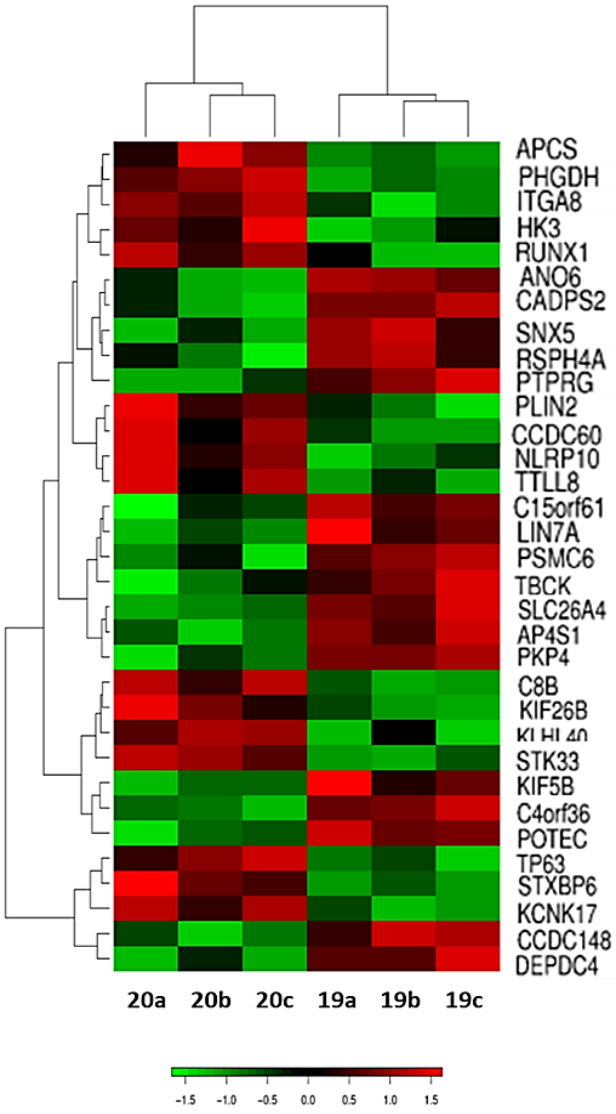

Figure 58C)

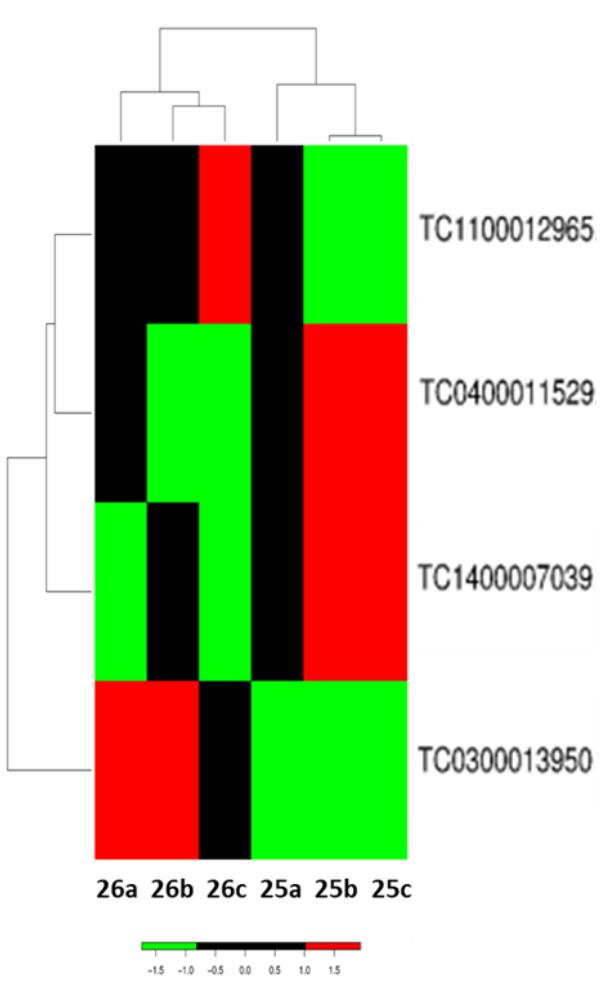

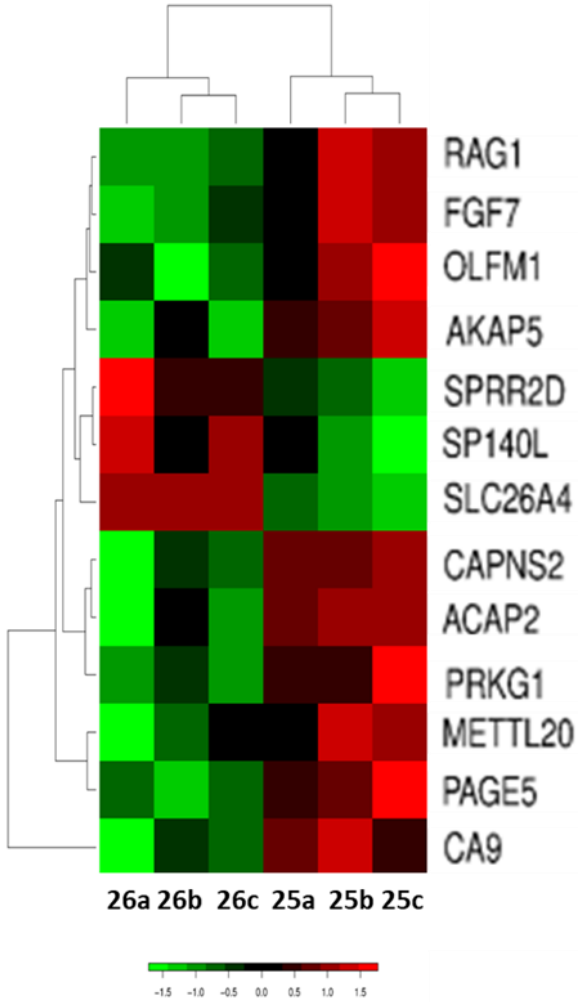

Intermediate 1437

Sample ID	Background Information	Comparison	
5	NCI-H157 untreated		
6	NCI-H1437 untreated		
19	157 24h 1µM	19 & 20	5 & 19
20	157 24h 0,1%		5 & 20
21	1437 24h 1µM	21 & 22	6 & 21
22	1437 24h 0,1%		6 & 22
23	157 48h 1µM	23 & 24	5 & 23
24	157 48h 0,1%		5 & 24
25	1437 48h 1µM	25 & 26	6 & 25
26	1437 48h 0,1%		6 & 26

Figure 58D)

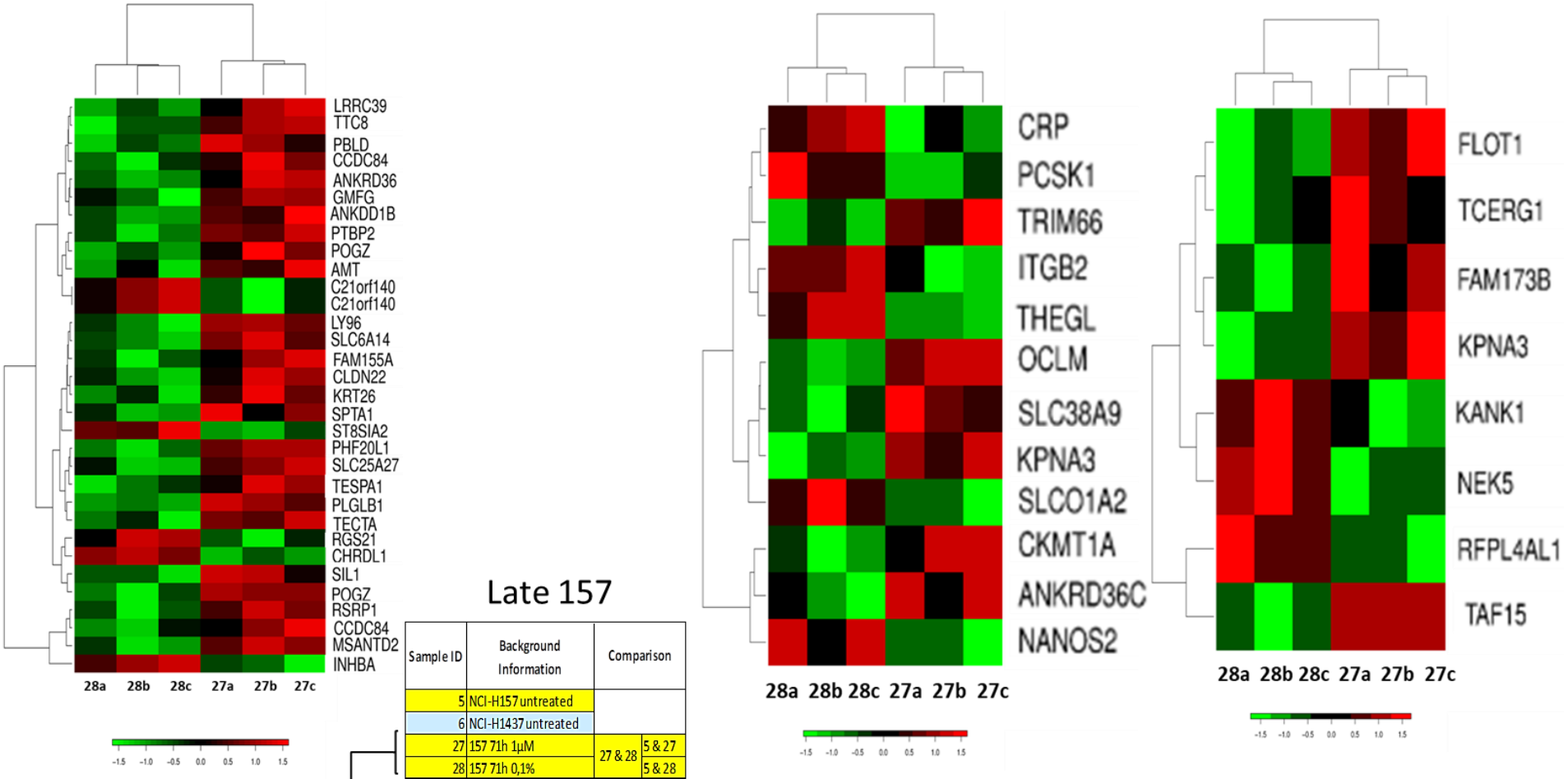

Late 157

Sample ID	Background Information	Comparison	
5	NCI-H157 untreated		
6	NCI-H1437 untreated		
27	157 71h 1µM	27 & 28	5 & 27
28	157 71h 0,1%		5 & 28
29	1437 71h 1µM	29 & 30	6 & 29
30	1437 71h 0,1%		6 & 30
31	157 96h 1µM	31 & 32	5 & 31
32	157 96h 0,1%		5 & 32
33	1437 96h 1µM	33 & 34	6 & 33
34	1437 96h 0,1%		6 & 34
35	157 120h 1µM	35 & 36	5 & 35
36	157 120h 0,1%		5 & 36
37	1437 120h 1µM	37 & 38	6 & 37
38	1437 120h 0,1%		6 & 38

Figure 58E)

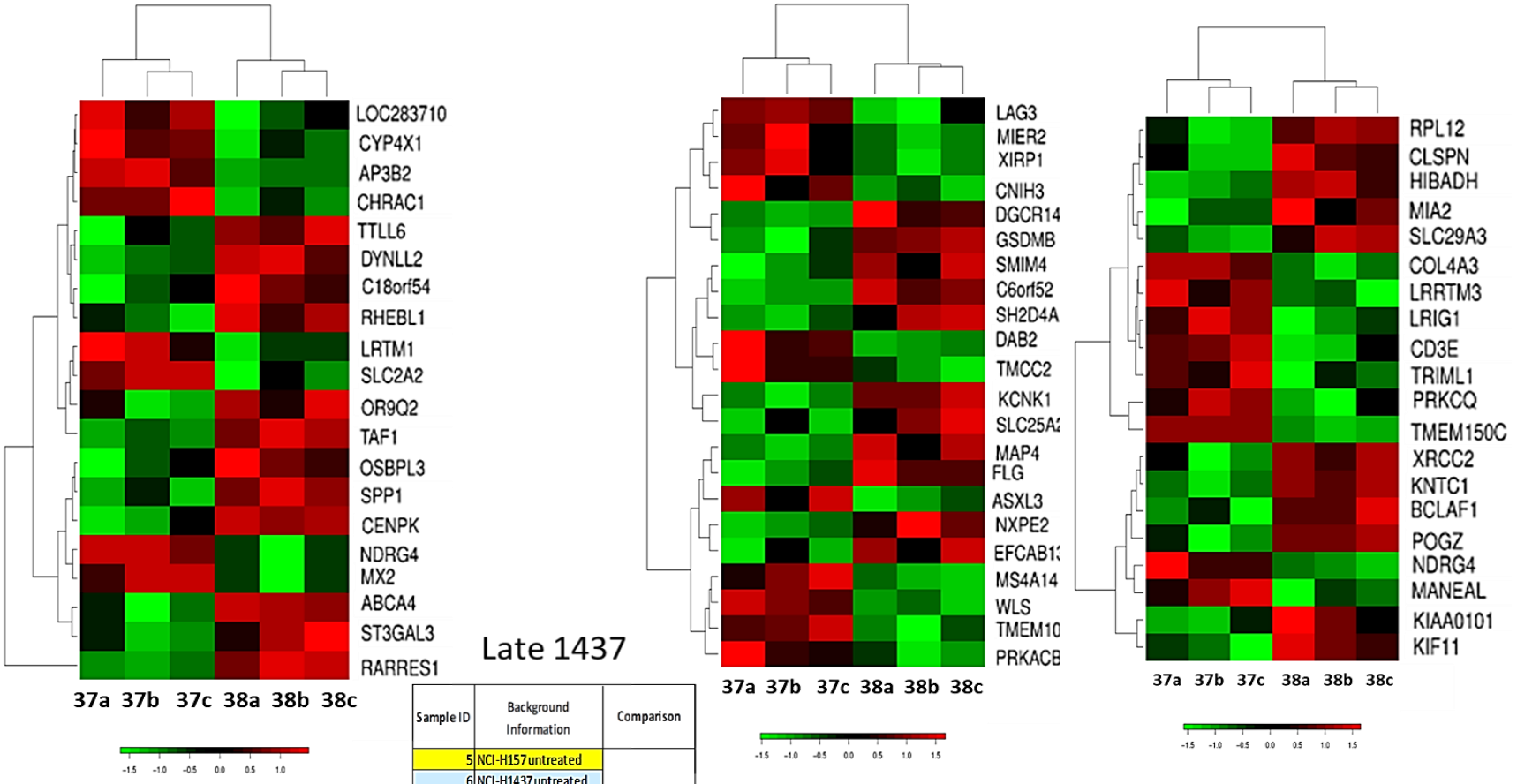

Sample ID	Background Information	Comparison	
5	NCI-H157 untreated		
6	NCI-H1437 untreated		
27	157 71h 1µM	27 & 28	5 & 27
28	157 71h 0,1%		5 & 28
29	1437 71h 1µM	29 & 30	6 & 29
30	1437 71h 0,1%		6 & 30
31	157 96h 1µM	31 & 32	5 & 31
32	157 96h 0,1%		5 & 32
33	1437 96h 1µM	33 & 34	6 & 33
34	1437 96h 0,1%		6 & 34
35	157 120h 1µM	35 & 36	5 & 35
36	157 120h 0,1%		5 & 36
37	1437 120h 1µM	37 & 38	6 & 37
38	1437 120h 0,1%		6 & 38

Figure 58F)

Figure 58: Time-resolved heatmaps of significantly deregulated genes in NCI-H157 and NCI-H1437 upon treatment with BI90.

Heatmaps are shown from different time points after treatment of NCI-H157 or NCI-H1437 with BI90. The numbers of the respective columns refer to a certain time point (indicated in the table). Small letters indicate the three biologic triplicates. For instance, 7a – c refers to time point 2 hours treatment of NCI-H157 with BI90, whereas 8a – c refers to the corresponding control (0.1 w/v % DMSO only). The colour code (green/down-regulation – red/up-regulation) below each heatmap indicates the level of deregulation for each of the genes shown at the right side of each heatmap.

Early time points comprise 2 hours + 4 hours + 8 hours, intermediate 24 hours + 48 hours and late ones 71 hours + 96 hours + 120 hours, respectively. Heatmaps are shown in:

A) early treatment time points for NCI-H157
B) early treatment time points for NCI-H1437
C) intermediate treatment time points for NCI-H157
D) intermediate treatment time points for NCI-H1437
E) late treatment time points for NCI-H157
F) late treatment time points for NCI-H1437

Expression profiling was performed at *atlas biolabs* utilizing Affymetrix Gene Chips (Affymetrix EXP).

9. Abbreviations

#

2D	two-dimensional
3D	three-dimensional

A

ABCA1	ATP-binding membrane cassette transporter A1
ac	acetylated
ADCC	antibody dependent cellular cytotoxicity
AKAP12	A-kinase anchoring protein 12
αSMA	alpha smooth muscle actin
AT-hooks	DNA-binding motif (binds adenine/thymine-rich DNA sequenes in minor groove)

B

BAG6/BAT3	BCL2 associated athanogene 6
BALB/c	immunocompetent laboratory-bred mouse strain
bHLH	basic helix-loop-helix
BM	basement membrane
BM	basement membrane
BPTF	bromodomain PHD finger transcription factor
BRD	bromodomain

C

CAFs	cancer-associated fibroblasts
CALCOCO1	calcium binding and coiled-coil domain 1
Cas9	CRISPR-associate 9

CCAR1	cell division cycle and apoptosis regulator 1
CCL22	C-C Motif Chemokine Ligand 22
CCL5	C C motif chemokine ligand 5, also: RANTES
CD16	cluster of differentiation 16, also: Fc fragment of IgG receptor IIIa
CD27	cluster of differentiation 27, also: TNF receptor superfamily member 7 (TNFRSM7)
CD56	cluster of differentiation 56, also: neural cell adhesion molecule 1 (NCAM1)
CD70	cluster of differentiation 70, also: TNF (Ligand) superfamily, member 7 or CD27 ligand
CDH1	E-cadherin
CDH2	N-cadherin
cDNA	complementary DNA
CFS2	colony stimulating factor 2
CFSE	carboxyfluorescein succinimidyl ester
CGA	Glycoprotein hormones alpha chain
CHEK1	checkpoint kinase 1
CLEC3A	C-type lectin domain family 3 member A
CLIC6	chloride intracellular channel 6
CLSPN	claspin
CMAC	7-amino-4-chloromethylcoumarin
CRISPR	clustered regularly interspaced short palindromic repeats
CTAs	cancer-testis-antigens
CTGF	connective tissue growth factor
CTLA4	cytotoxic T lymphocyte-associated Protein 4, also: cluster of differentiation 152 (CD152)
CTNNB1	beta-catenin
CXCL	C X C motif chemokine ligand
CYP	cytochrome P450

D

DDT-domain	DNA-binding homeobox- containing proteins and the different transcription and chromatin remodelling factors in which it is found, (protein domain)
DMEM	Dulbecco's Modified Eagle Medium
DMSO	dimethyl sulfoxide
D-PBS	Dulbecco's phosphate-buffered saline
dsRNA	double-stranded RNA
DTT	dithiothreitol

E

E:T ratio	effector to target ratio
EBV	Epstein-Barr virus
EC	endothelial cell
ECM	extracellular matrix
EGF	epidermal growth factor
EMT	epithelial-mesenchymal transition
EPO	erythropoietin
ER	endoplasmatic reticulum
ER	endoplasmatic reticulum

F

F/Phe	phenylalanine
FAP	fibroblast activation protein
FAS	Fas Cell Surface Death Receptor, also: cluster of differentiation 95 (CD95)
FBs	fibroblasts
FBS/FCS	fetal bovine serum
FC	fold change

FGF	fibroblast growth factor
FGF2	fibroblast growth factor 2
FOXO4	forkhead box protein O4
FSH	follicle-stimulating hormone

G

GATA1	GATA Binding Protein 1
GCSF	granulocyte-colony stimulating factor
GF	growth factor
GFP	green fluorescence protein
GMFG	glia maturation factor gamma
GPC6	glypican 6
GSC	homeobox protein Goosecoid
GZMB	granzyme B

H

H3K4me3	histone 3 trimethylated lysins at position 4
H4	histone 4
H4K12	lysine at position 12 in histone 4
H4K12ac	histone 4 acetylated lysine at position 12
H4K16	lysine at position 16 in histone 4
H4K16ac	histone 4 acetylated lysine at position 16
H4K20	lysine at position 20 in histone 4
HDF	human dermal fibroblasts
HEPES	4-(2-hydroxyethyl)-1-piperazineethanesulfonic acid
HGF	hepatocyte growth factor
HIF1A	Hypoxia induced factor 1 alpha

HLA-1	human leukocyte antigen class 1
HMGA	high mobility group box A (protein domain)
HPSE	heparanase
HS	heparan sulphate
HSPG2	heparan sulfate proteoglycan 2 / perlecan
HSPGs	heparan sulphate proteoglycans (glycoproteins)

I

ICAM1	intercellular adhesion molecule 1
IFIH1	interferon induced with helicase C domain 1, also: melanoma differentiation-associated protein 5 (MDA5)
IFNG/IFNγ	interferon γ
IgG	immunoglobulin G
IL	interleukin
IL10	interleukin 10
IL15	interleukin 15
IL18	interleukin 18
IL2	interleukin 2
IL6	interleukin 6
IL8	interleukin 8
IFN	interferon
IFNG	interferon gamma/interferon γ
IFNGR	interferon gamma receptor
ITAM	immunoreceptor tyrosine-based activation motifs
ITIM	immunoreceptor tyrosine-based inhibitory motifs

K

K/Lys	lysine
KD	knock down
KIAA0101	PCNA-associated factor (p15(PAF), OEATC-1)
KIF11	kinesin-5 / Eg5
KIRs	killer cell immunoglobulin-like receptors
KLRs	killer cell lectin-like receptors
KNTC1	kinetochore-associated protein 1
KO	knock out

L

LAG3	lymphocyte activation gene 3
LH	luteinizing hormone
Ly49C	murine killer cell lectin-like receptor, subfamily A, member 3 (Klra3)
Ly49I	murine killer cell lectin-like receptor subfamily A, member 9 (Klra9)

M

mAb	monoclonal antibody
MCTSs	multicellular tumour spheroids
MDR	multidrug resistance
MDSC	myeloid-derived suppressor cell
MED1	mediator complex subunit 1
MEZ	mezerein, a protein kinase C-activating compound
MHC	major histocompatibility complex
MMP-7	matrix metalloproteinase 7 / matrilysin
MMPs	matrix metalloproteinases

MOI	multiplicity of infection
MOPS	(3-N-morpholino)-propansulfonic acid, a running buffer

N

NAF	normal activated fibroblasts
NBEs	novel biological entities
NCAM1	neural cell adhesion molecule 1, also: cluster of differentiation 56 (CD56)
NCEs	novel chemical entities
NCR1	murine
NCRs	natural cytotoxicity receptors
NDST1	N-Deacetylase And N-Sulfotransferase 1
NEAA	non-essential amino acids
NF-κB	Nuclear Factor Kappa B
NHEJ	non-homologous end joining
NK cells	natural killer cells
NKARs	natural killer cell activating receptors
NKG2A	Killer Cell Lectin Like Receptor C1
NKG2C	Killer Cell Lectin Like Receptor C2
NKIRs	natural killer cell inhibiting receptors
NKp30	natural cytotoxicity triggering receptor 3 (*NCR3*)
NKp44	natural cytotoxicity triggering receptor 2 (*NCR2*)
NKp46	natural cytotoxicity triggering receptor 1 (*NCR1*)
NOD	non-obese diabetic
NOD/SCID (NSG)	immune-deficient laboratory-bred mouse strain
NSCLC	non-small cell lung cancer
NURF	nucleosome remodelling factor

O

OVGP1	oviduct-specific glycoprotein

P

PBMCs	peripheral blood mononuclear cells
PBS	phosphate-buffered saline
PCNA	proliferating cell nuclear antigen
PCR	polymerase chain reaction
PD-1	programmed cell death protein 1
PDGF	platelet-derived growth factor
PD-L1	programmed cell death protein 1 ligand, also: cluster of differentiation 274 (CD274)
Pen/Strep	Penicillin-Streptomycin
PGE2	prostaglandin E2
PGs	proteoglycans
PHD finger	plant homeodomain fingers
PLK1	polo-like kinase 1
PNKs	primary NK cells (human)
POLR2A	RNA polymerase II subunit A
PSMB8	proteasome subunit beta 8
PSMB9	proteasome subunit beta 9
PSMD11	proteasome 26S subunit, non-ATPase 11

Q

qPCR	quantitative polymerase chain reaction
Q-rich	glutamate-rich

R

R/Arg	arginine
RAD51	RAD51 recombinase
RARRES1	retinoic acid receptor responder 1
RBBP4	retinoblastoma-binding protein p48 a WD-repeat domain protein
RBBP7	retinoblastoma-binding protein p46 a WD-repeat domain protein
RFU	relative fluorescence units
ROS	reactive oxygen species
RPMI 1640	Roswell Park Memorial Institute 1640 medium
rRNA	ribosomal RNA
RT	room temperature

S

SCID	severe combined immunodeficiency
SERPINB4	serpin family B member 4
sgRNA	small guide RNAs
shRNA	short hairpin RNA
siRNA	small interfering RNA
SLC26A4	solute carrier family 26 member 4 / pendrin
SLUG	Zinc finger protein SNAI2
SMARCA1	nucleosome remodeling factor subunit SNF2L
SNAIL	Zinc finger protein SNAI1
SSC	squamous cell carcinoma
STD	standard deviation
STRING	search tool for the retrieval of interacting genes/proteins

T

T/Thr	threonine
TAMs	tumour-associated macrophages
TAP1	transporter 1, ATP binding cassette subfamily B member
TAP2	transporter 2, ATP binding cassette subfamily B member
TBS-T	Tris-buffered Saline, 0.1% Tween 20
TCR	T cell receptor
TFs	transcription factors
TGFβ1	transforming growth factor β1
TGP1	tight junction protein 1
TIM3	T cell membrane protein 3
TIMPs	tissue inhibitors of metalloproteinases
TME	tumour microenvironment
TNFα	tumour necrosis factor alpha
TNFαR	tumour necrosis factor alpha receptor
TRAIL	TNF-related apoptosis inducing ligand
TRAILR1/2	TNF receptor superfamily, member 10a / TRAIL receptor
Tregs	regulatory T cells
TSH	thyroid-stimulating hormone
TWIST(1)	Twist-related protein (1); basic helix-loop-helix protein 38 (bHLHa38)

V

VBM	vascular basement membrane
VEGF	vascular-endothelial growth factor
VSV-G	vesicular stomatitis virus glycoprotein

W

W/Trp	tryptophan
WD-repeat	tryptophan-aspartic acid repeat
WT	wildtype

X

XRCC2	X-ray repair cross complementing 2

Y

Y/Tyr	tyrosine

Z

ZO-1	Zonula Occludens; synonym for tight junction protein 1

10. References:

1. Kalluri, R., *The biology and function of fibroblasts in cancer.* Nat Rev Cancer, 2016. **16**(9): p. 582-98.
2. Lee, E., N.B. Pandey, and A.S. Popel, *Crosstalk between cancer cells and blood endothelial and lymphatic endothelial cells in tumour and organ microenvironment.* Expert Rev Mol Med, 2015. **17**: p. e3.
3. Catalano, V., et al., *Tumor and its microenvironment: a synergistic interplay.* Semin Cancer Biol, 2013. **23**(6 Pt B): p. 522-32.
4. Liotta, L.A. and E.C. Kohn, *The microenvironment of the tumour-host interface.* Nature, 2001. **411**(6835): p. 375-9.
5. Frantz, C., K.M. Stewart, and V.M. Weaver, *The extracellular matrix at a glance.* J Cell Sci, 2010. **123**(24): p. 4195-200.
6. Harburger, D.S. and D.A. Calderwood, *Integrin signalling at a glance.* J Cell Sci, 2009. **122**(Pt 2): p. 159-63.
7. Simi, A.K., M.F. Pang, and C.M. Nelson, *Extracellular Matrix Stiffness Exists in a Feedback Loop that Drives Tumor Progression.* Adv Exp Med Biol, 2018. **1092**: p. 57-67.
8. Hanahan, D. and R.A. Weinberg, *The hallmarks of cancer.* Cell, 2000. **100**(1): p. 57-70.
9. Medina, S.H., et al., *Identification of a mechanogenetic link between substrate stiffness and chemotherapeutic response in breast cancer.* Biomaterials, 2019. **202**: p. 1-11.
10. Das, V., et al., *The basics of epithelial-mesenchymal transition (EMT): A study from a structure, dynamics, and functional perspective.* J Cell Physiol, 2019.
11. Diepenbruck, M. and G. Christofori, *Epithelial-mesenchymal transition (EMT) and metastasis: yes, no, maybe?* Curr Opin Cell Biol, 2016. **43**: p. 7-13.
12. Kalluri, R. and R.A. Weinberg, *The basics of epithelial-mesenchymal transition.* J Clin Invest, 2009. **119**(6): p. 1420-8.
13. Taube, J.H., et al., *Core epithelial-to-mesenchymal transition interactome gene-expression signature is associated with claudin-low and metaplastic breast cancer subtypes.* Proc Natl Acad Sci U S A, 2010. **107**(35): p. 15449-54.
14. Tiwari, N., et al., *EMT as the ultimate survival mechanism of cancer cells.* Semin Cancer Biol, 2012. **22**(3): p. 194-207.
15. Maeda, M., K.R. Johnson, and M.J. Wheelock, *Cadherin switching: essential for behavioral but not morphological changes during an epithelium-to-mesenchyme transition.* J Cell Sci, 2005. **118**(Pt 5): p. 873-87.
16. Rudisch, A., et al., *High EMT Signature Score of Invasive Non-Small Cell Lung Cancer (NSCLC) Cells Correlates with NFkappaB Driven Colony-Stimulating Factor 2 (CSF2/GM-CSF) Secretion by Neighboring Stromal Fibroblasts.* PLoS One, 2015. **10**(4): p. e0124283.
17. Kwa, M.Q., K.M. Herum, and C. Brakebusch, *Cancer-associated fibroblasts: how do they contribute to metastasis?* Clin Exp Metastasis, 2019.
18. Ghesquiere, B., et al., *Metabolism of stromal and immune cells in health and disease.* Nature, 2014. **511**(7508): p. 167-76.
19. Dvorak, H.F., *Tumors: wounds that do not heal-redux.* Cancer Immunol Res, 2015. **3**(1): p. 1-11.
20. Valin, A. and J.L. Pablos, *The Role of the Transcriptional Regulation of Stromal Cells in Chronic Inflammation.* Biomolecules, 2015. **5**(4): p. 2723-57.
21. Tao, L., et al., *Cancer associated fibroblasts: An essential role in the tumor microenvironment.* Oncol Lett, 2017. **14**(3): p. 2611-2620.

22. Ronca, R., J.A. Van Ginderachter, and A. Turtoi, *Paracrine interactions of cancer-associated fibroblasts, macrophages and endothelial cells: tumor allies and foes.* Curr Opin Oncol, 2018. **30**(1): p. 45-53.
23. Santi, A., F.G. Kugeratski, and S. Zanivan, *Cancer Associated Fibroblasts: The Architects of Stroma Remodeling.* Proteomics, 2018. **18**(5-6): p. e1700167.
24. Ge, S., et al., *Comparative proteomic analysis of secreted proteins from nasopharyngeal carcinoma-associated stromal fibroblasts and normal fibroblasts.* Exp Ther Med, 2012. **3**(5): p. 857-860.
25. Bagordakis, E., et al., *Secretome profiling of oral squamous cell carcinoma-associated fibroblasts reveals organization and disassembly of extracellular matrix and collagen metabolic process signatures.* Tumour Biol, 2016. **37**(7): p. 9045-57.
26. Liberato, T., et al., *Signatures of protein expression revealed by secretome analyses of cancer associated fibroblasts and melanoma cell lines.* J Proteomics, 2018. **174**: p. 1-8.
27. Alvarez-Teijeiro, S., et al., *Factors Secreted by Cancer-Associated Fibroblasts that Sustain Cancer Stem Properties in Head and Neck Squamous Carcinoma Cells as Potential Therapeutic Targets.* Cancers (Basel), 2018. **10**(9).
28. Ziani, L., S. Chouaib, and J. Thiery, *Alteration of the Antitumor Immune Response by Cancer-Associated Fibroblasts.* Front Immunol, 2018. **9**: p. 414.
29. Stabile, H., et al., *Role of Distinct Natural Killer Cell Subsets in Anticancer Response.* Front Immunol, 2017. **8**: p. 293.
30. Gras Navarro, A., A.T. Bjorklund, and M. Chekenya, *Therapeutic potential and challenges of natural killer cells in treatment of solid tumors.* Front Immunol, 2015. **6**: p. 202.
31. Chester, C., K. Fritsch, and H.E. Kohrt, *Natural Killer Cell Immunomodulation: Targeting Activating, Inhibitory, and Co-stimulatory Receptor Signaling for Cancer Immunotherapy.* Front Immunol, 2015. **6**: p. 601.
32. Karre, K., *NK cells, MHC class I molecules and the missing self.* Scand J Immunol, 2002. **55**(3): p. 221-8.
33. Shifrin, N., D.H. Raulet, and M. Ardolino, *NK cell self tolerance, responsiveness and missing self recognition.* Semin Immunol, 2014. **26**(2): p. 138-44.
34. Cruz-Munoz, M.E., et al., *From the "missing self" hypothesis to adaptive NK cells: Insights of NK cell-mediated effector functions in immune surveillance.* J Leukoc Biol, 2019.
35. Capietto, A.H., S. Jhunjhunwala, and L. Delamarre, *Characterizing neoantigens for personalized cancer immunotherapy.* Curr Opin Immunol, 2017. **46**: p. 58-65.
36. Karre, K., *Natural killer cell recognition of missing self.* Nat Immunol, 2008. **9**(5): p. 477-80.
37. Hanke, T., et al., *Direct assessment of MHC class I binding by seven Ly49 inhibitory NK cell receptors.* Immunity, 1999. **11**(1): p. 67-77.
38. Vance, R.E., et al., *Mouse CD94/NKG2A is a natural killer cell receptor for the nonclassical major histocompatibility complex (MHC) class I molecule Qa-1(b).* J Exp Med, 1998. **188**(10): p. 1841-8.
39. Fernandez, N.C., et al., *A subset of natural killer cells achieves self-tolerance without expressing inhibitory receptors specific for self-MHC molecules.* Blood, 2005. **105**(11): p. 4416-23.
40. Jonsson, A.H. and W.M. Yokoyama, *Natural killer cell tolerance licensing and other mechanisms.* Adv Immunol, 2009. **101**: p. 27-79.
41. Lopez-Soto, A., et al., *Control of Metastasis by NK Cells.* Cancer Cell, 2017. **32**(2): p. 135-154.
42. Horton, N.C. and P.A. Mathew, *NKp44 and Natural Cytotoxicity Receptors as Damage-Associated Molecular Pattern Recognition Receptors.* Front Immunol, 2015. **6**: p. 31.
43. Hudspeth, K., B. Silva-Santos, and D. Mavilio, *Natural cytotoxicity receptors: broader expression patterns and functions in innate and adaptive immune cells.* Front Immunol, 2013. **4**: p. 69.

44. Kumar, S., *Natural killer cell cytotoxicity and its regulation by inhibitory receptors.* Immunology, 2018. **154**(3): p. 383-393.
45. Burshtyn, D.N. and E.O. Long, *Regulation through inhibitory receptors: Lessons from natural killer cells.* Trends Cell Biol, 1997. **7**(12): p. 473-9.
46. Vivier, E., J.A. Nunes, and F. Vely, *Natural killer cell signaling pathways.* Science, 2004. **306**(5701): p. 1517-9.
47. Sheppard, S., et al., *The Murine Natural Cytotoxic Receptor NKp46/NCR1 Controls TRAIL Protein Expression in NK Cells and ILC1s.* Cell Rep, 2018. **22**(13): p. 3385-3392.
48. Biassoni, R., et al., *The murine homologue of the human NKp46, a triggering receptor involved in the induction of natural cytotoxicity.* Eur J Immunol, 1999. **29**(3): p. 1014-20.
49. Sivori, S., et al., *Human NK cells: surface receptors, inhibitory checkpoints, and translational applications.* Cell Mol Immunol, 2019.
50. Biassoni, R. and M.S. Malnati, *Human Natural Killer Receptors, Co-Receptors, and Their Ligands.* Curr Protoc Immunol, 2018. **121**(1): p. e47.
51. Iozzo, R.V. and L. Schaefer, *Proteoglycan form and function: A comprehensive nomenclature of proteoglycans.* Matrix Biol, 2015. **42**: p. 11-55.
52. Kwon, H.J., N. Kim, and H.S. Kim, *Molecular checkpoints controlling natural killer cell activation and their modulation for cancer immunotherapy.* Exp Mol Med, 2017. **49**(3): p. e311.
53. Cerwenka, A. and L.L. Lanier, *Natural killer cell memory in infection, inflammation and cancer.* Nat Rev Immunol, 2016. **16**(2): p. 112-23.
54. Armeanu, S., et al., *Natural killer cell-mediated lysis of hepatoma cells via specific induction of NKG2D ligands by the histone deacetylase inhibitor sodium valproate.* Cancer Res, 2005. **65**(14): p. 6321-9.
55. Carosella, E.D., et al., *HLA-G: An Immune Checkpoint Molecule.* Adv Immunol, 2015. **127**: p. 33-144.
56. Maecker, H.L., et al., *Epigenetic changes in tumor Fas levels determine immune escape and response to therapy.* Cancer Cell, 2002. **2**(2): p. 139-48.
57. Zhang, X.H., et al., *Latent bone metastasis in breast cancer tied to Src-dependent survival signals.* Cancer Cell, 2009. **16**(1): p. 67-78.
58. Schlecker, E., et al., *Metalloprotease-mediated tumor cell shedding of B7-H6, the ligand of the natural killer cell-activating receptor NKp30.* Cancer Res, 2014. **74**(13): p. 3429-40.
59. Bidwell, B.N., et al., *Silencing of Irf7 pathways in breast cancer cells promotes bone metastasis through immune escape.* Nat Med, 2012. **18**(8): p. 1224-31.
60. Mlecnik, B., et al., *Functional network pipeline reveals genetic determinants associated with in situ lymphocyte proliferation and survival of cancer patients.* Sci Transl Med, 2014. **6**(228): p. 228ra37.
61. Pedroza-Pacheco, I., A. Madrigal, and A. Saudemont, *Interaction between natural killer cells and regulatory T cells: perspectives for immunotherapy.* Cell Mol Immunol, 2013. **10**(3): p. 222-9.
62. Palumbo, J.S., et al., *Platelets and fibrin(ogen) increase metastatic potential by impeding natural killer cell-mediated elimination of tumor cells.* Blood, 2005. **105**(1): p. 178-85.
63. Kopp, H.G., T. Placke, and H.R. Salih, *Platelet-derived transforming growth factor-beta down-regulates NKG2D thereby inhibiting natural killer cell antitumor reactivity.* Cancer Res, 2009. **69**(19): p. 7775-83.
64. Placke, T., et al., *Platelet-derived MHC class I confers a pseudonormal phenotype to cancer cells that subverts the antitumor reactivity of natural killer immune cells.* Cancer Res, 2012. **72**(2): p. 440-8.
65. Young, A., et al., *Targeting cancer-derived adenosine: new therapeutic approaches.* Cancer Discov, 2014. **4**(8): p. 879-88.

66. Li, H., et al., *Molecular basis for site-specific read-out of histone H3K4me3 by the BPTF PHD finger of NURF.* Nature, 2006. **442**(7098): p. 91-5.
67. Ruthenburg, A.J., et al., *Recognition of a mononucleosomal histone modification pattern by BPTF via multivalent interactions.* Cell, 2011. **145**(5): p. 692-706.
68. Mayes, K., et al., *BPTF inhibits NK cell activity and the abundance of natural cytotoxicity receptor co-ligands.* Oncotarget, 2017. **8**(38): p. 64344-64357.
69. Alkhatib, S.G. and J.W. Landry, *The nucleosome remodeling factor.* FEBS Lett, 2011. **585**(20): p. 3197-207.
70. Barak, O., et al., *Isolation of human NURF: a regulator of Engrailed gene expression.* EMBO J, 2003. **22**(22): p. 6089-100.
71. Doerks, T., R. Copley, and P. Bork, *DDT -- a novel domain in different transcription and chromosome remodeling factors.* Trends Biochem Sci, 2001. **26**(3): p. 145-6.
72. Sims, R.J., 3rd, et al., *Recognition of trimethylated histone H3 lysine 4 facilitates the recruitment of transcription postinitiation factors and pre-mRNA splicing.* Mol Cell, 2007. **28**(4): p. 665-76.
73. Mayes, K., et al., *BPTF Depletion Enhances T-cell-Mediated Antitumor Immunity.* Cancer Res, 2016. **76**(21): p. 6183-6192.
74. Nyga, A., U. Cheema, and M. Loizidou, *3D tumour models: novel in vitro approaches to cancer studies.* J Cell Commun Signal, 2011. **5**(3): p. 239-48.
75. Takahashi, Y., et al., *3D spheroid cultures improve the metabolic gene expression profiles of HepaRG cells.* Biosci Rep, 2015. **35**(3).
76. Ding, Y., et al., *Three-dimensional tissue culture model of human breast cancer for the evaluation of multidrug resistance.* J Tissue Eng Regen Med, 2018. **12**(9): p. 1959-1971.
77. Movia, D., et al., *Multilayered Cultures of NSCLC cells grown at the Air-Liquid Interface allow the efficacy testing of inhaled anti-cancer drugs.* Sci Rep, 2018. **8**(1): p. 12920.
78. Weiss, M.S., et al., *Dynamic, large-scale profiling of transcription factor activity from live cells in 3D culture.* PLoS One, 2010. **5**(11): p. e14026.
79. Xu, X., M.C. Farach-Carson, and X. Jia, *Three-dimensional in vitro tumor models for cancer research and drug evaluation.* Biotechnol Adv, 2014. **32**(7): p. 1256-1268.
80. Yang, Z., et al., *Transcriptome Profiling of Panc-1 Spheroid Cells with Pancreatic Cancer Stem Cells Properties Cultured by a Novel 3D Semi-Solid System.* Cell Physiol Biochem, 2018. **47**(5): p. 2109-2125.
81. Fitzgerald, K.A., et al., *Life in 3D is never flat: 3D models to optimise drug delivery.* J Control Release, 2015. **215**: p. 39-54.
82. Vidic, S., et al., *PREDECT Protocols for Complex 2D/3D Cultures.* Methods Mol Biol, 2019. **1888**: p. 1-20.
83. de Hoogt, R., et al., *Protocols and characterization data for 2D, 3D, and slice-based tumor models from the PREDECT project.* Sci Data, 2017. **4**: p. 170170.
84. Hickman, J.A., et al., *Three-dimensional models of cancer for pharmacology and cancer cell biology: capturing tumor complexity in vitro/ex vivo.* Biotechnol J, 2014. **9**(9): p. 1115-28.
85. Osswald, A., V. Hedrich, and W. Sommergruber, *3D-3 Tumor Models in Drug Discovery for Analysis of Immune Cell Infiltration.* Methods Mol Biol, 2019. **1953**: p. 151-162.
86. Sherman, H., H.J. Gitschier, and A.E. Rossi, *A Novel Three-Dimensional Immune Oncology Model for High-Throughput Testing of Tumoricidal Activity.* Front Immunol, 2018. **9**: p. 857.
87. Wang, S., et al., *Near-physiological microenvironment simulation on chip to evaluate drug resistance of different loci in tumour mass.* Talanta, 2019. **191**: p. 67-73.
88. Bueno, C., et al., *The excited-state interaction of resazurin and resorufin with amines in aqueous solutions. Photophysics and photochemical reactions.* Photochem Photobiol, 2002. **76**(4): p. 385-90.

89. Xu, M., D.J. McCanna, and J.G. Sivak, *Use of the viability reagent PrestoBlue in comparison with alamarBlue and MTT to assess the viability of human corneal epithelial cells.* J Pharmacol Toxicol Methods, 2015. **71**: p. 1-7.
90. Kang, S.J., et al., *Regulation of hierarchical clustering and activation of innate immune cells by dendritic cells.* Immunity, 2008. **29**(5): p. 819-33.
91. Pasley, S., C. Zylberberg, and S. Matosevic, *Natural killer-92 cells maintain cytotoxic activity after long-term cryopreservation in novel DMSO-free media.* Immunol Lett, 2017. **192**: p. 35-41.
92. Kang, Y.J., et al., *An increased level of IL-6 suppresses NK cell activity in peritoneal fluid of patients with endometriosis via regulation of SHP-2 expression.* Hum Reprod, 2014. **29**(10): p. 2176-89.
93. Mirjacic Martinovic, K., et al., *Favorable in vitro effects of combined IL-12 and IL-18 treatment on NK cell cytotoxicity and CD25 receptor expression in metastatic melanoma patients.* J Transl Med, 2015. **13**: p. 120.
94. Kehrl, J.H., *Transforming growth factor-beta: an important mediator of immunoregulation.* Int J Cell Cloning, 1991. **9**(5): p. 438-50.
95. Agrawal, N., et al., *RNA interference: biology, mechanism, and applications.* Microbiol Mol Biol Rev, 2003. **67**(4): p. 657-85.
96. Komor, A.C., A.H. Badran, and D.R. Liu, *CRISPR-Based Technologies for the Manipulation of Eukaryotic Genomes.* Cell, 2017. **169**(3): p. 559.
97. Shi, J., et al., *Discovery of cancer drug targets by CRISPR-Cas9 screening of protein domains.* Nat Biotechnol, 2015. **33**(6): p. 661-7.
98. Yvan-Charvet, L., N. Wang, and A.R. Tall, *Role of HDL, ABCA1, and ABCG1 transporters in cholesterol efflux and immune responses.* Arterioscler Thromb Vasc Biol, 2010. **30**(2): p. 139-43.
99. Fitzgerald, M.L., Z. Mujawar, and N. Tamehiro, *ABC transporters, atherosclerosis and inflammation.* Atherosclerosis, 2010. **211**(2): p. 361-70.
100. Yin, K., D.F. Liao, and C.K. Tang, *ATP-binding membrane cassette transporter A1 (ABCA1): a possible link between inflammation and reverse cholesterol transport.* Mol Med, 2010. **16**(9-10): p. 438-49.
101. von Hardenberg, J., et al., *Programmed Death Ligand 1 (PD-L1) Status and Tumor-Infiltrating Lymphocytes in Hot Spots of Primary and Liver Metastases in Prostate Cancer With Neuroendocrine Differentiation.* Clin Genitourin Cancer, 2018.
102. Tsunezumi, J., S. Higashi, and K. Miyazaki, *Matrilysin (MMP-7) cleaves C-type lectin domain family 3 member A (CLEC3A) on tumor cell surface and modulates its cell adhesion activity.* J Cell Biochem, 2009. **106**(4): p. 693-702.
103. Ruthard, J., et al., *Identification of antibodies against extracellular matrix proteins in human osteoarthritis.* Biochem Biophys Res Commun, 2018. **503**(3): p. 1273-1277.
104. Al-Khunaizi, M., et al., *The serpin SQN-5 is a dual mechanistic-class inhibitor of serine and cysteine proteinases.* Biochemistry, 2002. **41**(9): p. 3189-99.
105. de Koning, P.J., et al., *Intracellular serine protease inhibitor SERPINB4 inhibits granzyme M-induced cell death.* PLoS One, 2011. **6**(8): p. e22645.
106. Izuhara, K., et al., *Squamous Cell Carcinoma Antigen 2 (SCCA2, SERPINB4): An Emerging Biomarker for Skin Inflammatory Diseases.* Int J Mol Sci, 2018. **19**(4).
107. Cha, J.H., et al., *AKAP12 mediates barrier functions of fibrotic scars during CNS repair.* PLoS One, 2014. **9**(4): p. e94695.
108. Griffon, N., et al., *CLIC6, a member of the intracellular chloride channel family, interacts with dopamine D(2)-like receptors.* Brain Res Mol Brain Res, 2003. **117**(1): p. 47-57.
109. Skeie, J.M. and V.B. Mahajan, *Proteomic landscape of the human choroid-retinal pigment epithelial complex.* JAMA Ophthalmol, 2014. **132**(11): p. 1271-81.

110. Laheri, S., D. Modi, and P. Bhatt, *Extra-oviductal expression of oviductal glycoprotein 1 in mouse: Detection in testis, epididymis and ovary.* J Biosci, 2017. **42**(1): p. 69-80.
111. Lok, I.H., et al., *Variable expression of oviductin mRNA at different stages of human reproductive cycle.* J Assist Reprod Genet, 2002. **19**(12): p. 569-76.
112. Moros-Nicolas, C., et al., *Genes Encoding Mammalian Oviductal Proteins Involved in Fertilization are Subjected to Gene Death and Positive Selection.* J Mol Evol, 2018. **86**(9): p. 655-667.
113. Ibrahim, S., et al., *Expression pattern of inflammatory response genes and their regulatory micrornas in bovine oviductal cells in response to lipopolysaccharide: implication for early embryonic development.* PLoS One, 2015. **10**(3): p. e0119388.
114. Wu, D.Y., et al., *Distinct, genome-wide, gene-specific selectivity patterns of four glucocorticoid receptor coregulators.* Nucl Recept Signal, 2014. **12**: p. e002.
115. Yang, C.K., J.H. Kim, and M.R. Stallcup, *Role of the N-terminal activation domain of the coiled-coil coactivator in mediating transcriptional activation by beta-catenin.* Mol Endocrinol, 2006. **20**(12): p. 3251-62.
116. Mizuta, S., et al., *CCAR1/CoCoA pair-mediated recruitment of the Mediator defines a novel pathway for GATA1 function.* Genes Cells, 2014. **19**(1): p. 28-51.
117. Szklarczyk, D., et al., *The STRING database in 2017: quality-controlled protein-protein association networks, made broadly accessible.* Nucleic Acids Res, 2017. **45**(D1): p. D362-D368.
118. Sar, F., et al., *Human claspin is a ring-shaped DNA-binding protein with high affinity to branched DNA structures.* J Biol Chem, 2004. **279**(38): p. 39289-95.
119. Chini, C.C. and J. Chen, *Claspin, a regulator of Chk1 in DNA replication stress pathway.* DNA Repair (Amst), 2004. **3**(8-9): p. 1033-7.
120. Chini, C.C. and J. Chen, *Human claspin is required for replication checkpoint control.* J Biol Chem, 2003. **278**(32): p. 30057-62.
121. Petermann, E., T. Helleday, and K.W. Caldecott, *Claspin promotes normal replication fork rates in human cells.* Mol Biol Cell, 2008. **19**(6): p. 2373-8.
122. Choi, S.H., et al., *TopBP1 and Claspin contribute to the radioresistance of lung cancer brain metastases.* Mol Cancer, 2014. **13**: p. 211.
123. Azenha, D., M.C. Lopes, and T.C. Martins, *Claspin functions in cell homeostasis-A link to cancer?* DNA Repair (Amst), 2017. **59**: p. 27-33.
124. Wu, C.C., et al., *RARRES1 expression is significantly related to tumour differentiation and staging in colorectal adenocarcinoma.* Eur J Cancer, 2006. **42**(4): p. 557-65.
125. Qu, Y., S. Dang, and P. Hou, *Gene methylation in gastric cancer.* Clin Chim Acta, 2013. **424**: p. 53-65.
126. Kwok, W.K., et al., *Role of the RARRES1 gene in nasopharyngeal carcinoma.* Cancer Genet Cytogenet, 2009. **194**(1): p. 58-64.
127. Son, M.S., et al., *Expression and mutation analysis of TIG1 (tazarotene-induced gene 1) in human gastric cancer.* Oncol Res, 2009. **17**(11-12): p. 571-80.
128. Mithani, S.K., I.M. Smith, and J.A. Califano, *Use of integrative epigenetic and cytogenetic analyses to identify novel tumor-suppressor genes in malignant melanoma.* Melanoma Res, 2011. **21**(4): p. 298-307.
129. Kloth, M., et al., *The SNP rs6441224 influences transcriptional activity and prognostically relevant hypermethylation of RARRES1 in prostate cancer.* Int J Cancer, 2012. **131**(6): p. E897-904.
130. Maimouni, S., et al., *Tumor suppressor RARRES1 links tubulin deglutamylation to mitochondrial metabolism and cell survival.* Oncotarget, 2019. **10**(17): p. 1606-1624.
131. Jamali, L., et al., *Potential Prognostic Role for SPOP, DAXX, RARRES1, and LAMP2 as an Autophagy Related Genes in Prostate Cancer.* Urol J, 2019.

132. Liu, C.T., et al., *shRNAmediated knockdown of KNTC1 suppresses cell viability and induces apoptosis in esophageal squamous cell carcinoma.* Int J Oncol, 2019. **54**(3): p. 1053-1060.
133. Wojcik, E.J., et al., *Kinesin-5: cross-bridging mechanism to targeted clinical therapy.* Gene, 2013. **531**(2): p. 133-49.
134. Simpson, F., et al., *The PCNA-associated factor KIAA0101/p15(PAF) binds the potential tumor suppressor product p33ING1b.* Exp Cell Res, 2006. **312**(1): p. 73-85.
135. Pabla, S., et al., *Proliferative potential and resistance to immune checkpoint blockade in lung cancer patients.* J Immunother Cancer, 2019. **7**(1): p. 27.
136. Wang, X., et al., *A network-pathway based module identification for predicting the prognosis of ovarian cancer patients.* J Ovarian Res, 2016. **9**(1): p. 73.
137. Thacker, J., *The RAD51 gene family, genetic instability and cancer.* Cancer Lett, 2005. **219**(2): p. 125-35.
138. Thacker, J. and M.Z. Zdzienicka, *The XRCC genes: expanding roles in DNA double-strand break repair.* DNA Repair (Amst), 2004. **3**(8-9): p. 1081-90.
139. Sullivan, M.R. and K.A. Bernstein, *RAD-ical New Insights into RAD51 Regulation.* Genes (Basel), 2018. **9**(12).
140. Fouad, Y.A. and C. Aanei, *Revisiting the hallmarks of cancer.* Am J Cancer Res, 2017. **7**(5): p. 1016-1036.
141. Lazebnik, Y., *What are the hallmarks of cancer?* Nat Rev Cancer, 2010. **10**(4): p. 232-3.
142. Hanahan, D. and R.A. Weinberg, *Hallmarks of cancer: the next generation.* Cell, 2011. **144**(5): p. 646-74.
143. Dunn, G.P., L.J. Old, and R.D. Schreiber, *The three Es of cancer immunoediting.* Annu Rev Immunol, 2004. **22**: p. 329-60.
144. Sukari, A., et al., *Cancer Immunology and Immunotherapy.* Anticancer Res, 2016. **36**(11): p. 5593-5606.
145. Swann, J.B. and M.J. Smyth, *Immune surveillance of tumors.* J Clin Invest, 2007. **117**(5): p. 1137-46.
146. Teng, M.W., et al., *From mice to humans: developments in cancer immunoediting.* J Clin Invest, 2015. **125**(9): p. 3338-46.
147. Qu, X., Y. Tang, and S. Hua, *Immunological Approaches Towards Cancer and Inflammation: A Cross Talk.* Front Immunol, 2018. **9**: p. 563.
148. Neagu, M., et al., *Inflammation: A key process in skin tumorigenesis.* Oncol Lett, 2019. **17**(5): p. 4068-4084.
149. Vahidian, F., et al., *Interactions between cancer stem cells, immune system and some environmental components: Friends or foes?* Immunol Lett, 2019. **208**: p. 19-29.
150. Erez, N., et al., *Cancer-Associated Fibroblasts Are Activated in Incipient Neoplasia to Orchestrate Tumor-Promoting Inflammation in an NF-kappaB-Dependent Manner.* Cancer Cell, 2010. **17**(2): p. 135-47.
151. Erez, N., et al., *Cancer associated fibroblasts express pro-inflammatory factors in human breast and ovarian tumors.* Biochem Biophys Res Commun, 2013. **437**(3): p. 397-402.
152. Pardoll, D.M., *The blockade of immune checkpoints in cancer immunotherapy.* Nat Rev Cancer, 2012. **12**(4): p. 252-64.
153. Jewett, A. and H.C. Tseng, *Tumor induced inactivation of natural killer cell cytotoxic function; implication in growth, expansion and differentiation of cancer stem cells.* J Cancer, 2011. **2**: p. 443-57.
154. Krasnova, Y., et al., *Bench to bedside: NK cells and control of metastasis.* Clin Immunol, 2017. **177**: p. 50-59.
155. Vesely, M.D., et al., *Natural innate and adaptive immunity to cancer.* Annu Rev Immunol, 2011. **29**: p. 235-71.
156. Guillerey, C. and M.J. Smyth, *NK Cells and Cancer Immunoediting.* Curr Top Microbiol Immunol, 2016. **395**: p. 115-45.

157. Guillerey, C., N.D. Huntington, and M.J. Smyth, *Targeting natural killer cells in cancer immunotherapy.* Nat Immunol, 2016. **17**(9): p. 1025-36.
158. Bald, T., et al., *Hide and seek: Plasticity of innate lymphoid cells in cancer.* Semin Immunol, 2019.
159. Bianco, A., et al., *Targeting immune checkpoints in non small cell lung cancer.* Curr Opin Pharmacol, 2018. **40**: p. 46-50.
160. Furue, M., et al., *Melanoma and Immune Checkpoint Inhibitors.* Curr Oncol Rep, 2018. **20**(3): p. 29.
161. Remon, J., N. Vilarino, and N. Reguart, *Immune checkpoint inhibitors in non-small cell lung cancer (NSCLC): Approaches on special subgroups and unresolved burning questions.* Cancer Treat Rev, 2018. **64**: p. 21-29.
162. Kazaz, S.N. and I. Oztop, *Immune Checkpoint Inhibitors in Advanced-Stage Non-small Cell Lung Cancer.* Turk Thorac J, 2017. **18**(4): p. 101-107.
163. Lugowska, I., P. Teterycz, and P. Rutkowski, *Immunotherapy of melanoma.* Contemp Oncol (Pozn), 2018. **22**(1A): p. 61-67.
164. Rausch, M.P. and K.T. Hastings, *Immune Checkpoint Inhibitors in the Treatment of Melanoma: From Basic Science to Clinical Application*, in *Cutaneous Melanoma: Etiology and Therapy*, W.H. Ward and J.M. Farma, Editors. 2017: Brisbane (AU).
165. Ribas, A., *Adaptive Immune Resistance: How Cancer Protects from Immune Attack.* Cancer Discov, 2015. **5**(9): p. 915-9.
166. Pitt, J.M., et al., *Resistance Mechanisms to Immune-Checkpoint Blockade in Cancer: Tumor-Intrinsic and -Extrinsic Factors.* Immunity, 2016. **44**(6): p. 1255-69.
167. Berraondo, P., et al., *Innate immune mediators in cancer: between defense and resistance.* Immunol Rev, 2016. **274**(1): p. 290-306.
168. Schito, L., *Bridging angiogenesis and immune evasion in the hypoxic tumor microenvironment.* Am J Physiol Regul Integr Comp Physiol, 2018. **315**(6): p. R1072-R1084.
169. Wu, Q., et al., *JNK signaling in cancer cell survival.* Med Res Rev, 2019.
170. Gudjonsson, T., et al., *Normal and tumor-derived myoepithelial cells differ in their ability to interact with luminal breast epithelial cells for polarity and basement membrane deposition.* J Cell Sci, 2002. **115**(Pt 1): p. 39-50.
171. Pupovac, A., et al., *Toward Immunocompetent 3D Skin Models.* Adv Healthc Mater, 2018. **7**(12): p. e1701405.
172. Zhuang, P., et al., *3D neural tissue models: From spheroids to bioprinting.* Biomaterials, 2018. **154**: p. 113-133.
173. Zscheppang, K., et al., *Human Pulmonary 3D Models For Translational Research.* Biotechnol J, 2018. **13**(1).
174. Jackson, E.L. and H. Lu, *Three-dimensional models for studying development and disease: moving on from organisms to organs-on-a-chip and organoids.* Integr Biol (Camb), 2016. **8**(6): p. 672-83.
175. Sreepadmanabh, M. and B.J. Toley, *Investigations into the cancer stem cell niche using in-vitro 3-D tumor models and microfluidics.* Biotechnol Adv, 2018. **36**(4): p. 1094-1110.
176. Moreira, L., et al., *Pancreas 3D Organoids: Current and Future Aspects as a Research Platform for Personalized Medicine in Pancreatic Cancer.* Cell Mol Gastroenterol Hepatol, 2018. **5**(3): p. 289-298.
177. Rodenhizer, D., et al., *The Current Landscape of 3D In Vitro Tumor Models: What Cancer Hallmarks Are Accessible for Drug Discovery?* Adv Healthc Mater, 2018. **7**(8): p. e1701174.
178. Hoarau-Vechot, J., et al., *Halfway between 2D and Animal Models: Are 3D Cultures the Ideal Tool to Study Cancer-Microenvironment Interactions?* Int J Mol Sci, 2018. **19**(1).
179. Caballero, D., et al., *Tumour-vessel-on-a-chip models for drug delivery.* Lab Chip, 2017. **17**(22): p. 3760-3771.

180. Weeber, F., et al., *Tumor Organoids as a Pre-clinical Cancer Model for Drug Discovery.* Cell Chem Biol, 2017. **24**(9): p. 1092-1100.
181. Langhans, S.A., *Three-Dimensional in Vitro Cell Culture Models in Drug Discovery and Drug Repositioning.* Front Pharmacol, 2018. **9**: p. 6.
182. Vanderburgh, J., J.A. Sterling, and S.A. Guelcher, *3D Printing of Tissue Engineered Constructs for In Vitro Modeling of Disease Progression and Drug Screening.* Ann Biomed Eng, 2017. **45**(1): p. 164-179.
183. Jacobi, N., et al., *Organotypic three-dimensional cancer cell cultures mirror drug responses in vivo: lessons learned from the inhibition of EGFR signaling.* Oncotarget, 2017. **8**(64): p. 107423-107440.
184. Fang, Y. and R.M. Eglen, *Three-Dimensional Cell Cultures in Drug Discovery and Development.* SLAS Discov, 2017. **22**(5): p. 456-472.
185. Osswald, A., et al., *Three-dimensional tumor spheroids for in vitro analysis of bacteria as gene delivery vectors in tumor therapy.* Microb Cell Fact, 2015. **14**: p. 199.
186. Wernitznig, D., et al., *First-in-class ruthenium anticancer drug (KP1339/IT-139) induces an immunogenic cell death signature in colorectal spheroids in vitro.* Metallomics, 2019.
187. Giannattasio, A., et al., *Cytotoxicity and infiltration of human NK cells in in vivo-like tumor spheroids.* BMC Cancer, 2015. **15**: p. 351.
188. Stock, K., et al., *Capturing tumor complexity in vitro: Comparative analysis of 2D and 3D tumor models for drug discovery.* Sci Rep, 2016. **6**: p. 28951.
189. Davies, E.J., et al., *Capturing complex tumour biology in vitro: histological and molecular characterisation of precision cut slices.* Sci Rep, 2015. **5**: p. 17187.
190. Rebelo, S.P., et al., *3D-3-culture: A tool to unveil macrophage plasticity in the tumour microenvironment.* Biomaterials, 2018. **163**: p. 185-197.
191. Maio, M., et al., *Epigenetic targets for immune intervention in human malignancies.* Oncogene, 2003. **22**(42): p. 6484-8.
192. Smyth, M.J., G.P. Dunn, and R.D. Schreiber, *Cancer immunosurveillance and immunoediting: the roles of immunity in suppressing tumor development and shaping tumor immunogenicity.* Adv Immunol, 2006. **90**: p. 1-50.
193. Setiadi, A.F., et al., *Epigenetic enhancement of antigen processing and presentation promotes immune recognition of tumors.* Cancer Res, 2008. **68**(23): p. 9601-7.
194. Salmaninejad, A., et al., *Cancer/Testis Antigens: Expression, Regulation, Tumor Invasion, and Use in Immunotherapy of Cancers.* Immunol Invest, 2016. **45**(7): p. 619-40.
195. Masopust, D., C.P. Sivula, and S.C. Jameson, *Of Mice, Dirty Mice, and Men: Using Mice To Understand Human Immunology.* J Immunol, 2017. **199**(2): p. 383-388.
196. Jacobi, *Organotypic three-dimensional cancer cell cultures mirror drug responses in vivo: lessons learned from the inhibition of EGFR signaling.* 2017.
197. Stock, *Capturing tumor complexity in vitro: Comparative analysis of 2D and 3D tumor models for drug discovery.* 2016.
198. Hammoudeh, S.M., A.M. Hammoudeh, and R. Hamoudi, *High-throughput quantification of the effect of DMSO on the viability of lung and breast cancer cells using an easy-to-use spectrophotometric trypan blue-based assay.* Histochem Cell Biol, 2019.
199. Jiang, Z., et al., *Altered Hepa1-6 cells by dimethyl sulfoxide (DMSO)-treatment induce anti-tumor immunity in vivo.* Oncotarget, 2016. **7**(8): p. 9340-52.
200. Chockley, P.J. and V.G. Keshamouni, *Immunological Consequences of Epithelial-Mesenchymal Transition in Tumor Progression.* J Immunol, 2016. **197**(3): p. 691-8.
201. Tommelein, J., et al., *Cancer-associated fibroblasts connect metastasis-promoting communication in colorectal cancer.* Front Oncol, 2015. **5**: p. 63.
202. Vu, L.T., et al., *Cell migration on planar and three-dimensional matrices: a hydrogel-based perspective.* Tissue Eng Part B Rev, 2015. **21**(1): p. 67-74.

203. Hong, *Stimulatory versus suppressive effects of GM-CSF on tumor progression in multiple cancer types*. 2016.
204. Lee, *CSF2 Overexpression Is Associated with STAT5 Phosphorylation and Poor Prognosis in Patients with Urothelial Carcinoma*. 2016.
205. Fisher, *The two faces of IL-6 in the tumor microenvironment*. 2014.
206. Cifaldi, *Inhibition of natural killer cell cytotoxicity by interleukin-6: implications for the pathogenesis of macrophage activation syndrome.* 2015.
207. Dittmer, J. and B. Leyh, *The impact of tumor stroma on drug response in breast cancer.* Semin Cancer Biol, 2015. **31**: p. 3-15.
208. Mucha, O., et al., *Pharmacological versus genetic inhibition of heme oxygenase-1 - the comparison of metalloporphyrins, shRNA and CRISPR/Cas9 system.* Acta Biochim Pol, 2018. **65**(2): p. 277-286.
209. Mestas, *Of Mice and Not Men: Differences between Mouse and Human Immunology*. 2004.
210. Maki, G., et al., *Factors regulating the cytotoxic activity of the human natural killer cell line, NK-92.* J Hematother Stem Cell Res, 2001. **10**(3): p. 369-83.
211. Sheppard, *The Murine Natural Cytotoxic Receptor NKp46/NCR1 Controls TRAIL Protein Expression in NK Cells and ILC1s*. 2018.
212. Brodin, P. and M.M. Davis, *Human immune system variation.* Nat Rev Immunol, 2017. **17**(1): p. 21-29.
213. Rapp, M., et al., *CCL22 controls immunity by promoting regulatory T cell communication with dendritic cells in lymph nodes.* J Exp Med, 2019.
214. Wang, D., et al., *Macrophage-derived CCL22 promotes an immunosuppressive tumor microenvironment via IL-8 in malignant pleural effusion.* Cancer Lett, 2019. **452**: p. 244-253.
215. Yang, J.M., et al., *Structural environment built by AKAP12+ colon mesenchymal cells drives M2 macrophages during inflammation recovery.* Sci Rep, 2017. **7**: p. 42723.
216. Goel, S., et al., *CDK4/6 inhibition triggers anti-tumour immunity.* Nature, 2017. **548**(7668): p. 471-475.
217. Li, M., Z. Liu, and X. Wang, *Exploration of the Combination of PLK1 Inhibition with Immunotherapy in Cancer Treatment.* J Oncol, 2018. **2018**: p. 3979527.
218. Iozzo, R.V. and L. Schaefer, *Proteoglycans in health and disease: novel regulatory signaling mechanisms evoked by the small leucine-rich proteoglycans.* FEBS J, 2010. **277**(19): p. 3864-75.
219. Kato, H., et al., *Length-dependent recognition of double-stranded ribonucleic acids by retinoic acid-inducible gene-I and melanoma differentiation-associated gene 5.* J Exp Med, 2008. **205**(7): p. 1601-10.
220. Satoh, T., et al., *LGP2 is a positive regulator of RIG-I- and MDA5-mediated antiviral responses.* Proc Natl Acad Sci U S A, 2010. **107**(4): p. 1512-7.
221. Takeuchi, O. and S. Akira, *MDA5/RIG-I and virus recognition.* Curr Opin Immunol, 2008. **20**(1): p. 17-22.
222. Roulois, D., et al., *DNA-Demethylating Agents Target Colorectal Cancer Cells by Inducing Viral Mimicry by Endogenous Transcripts.* Cell, 2015. **162**(5): p. 961-73.
223. Chiappinelli, K.B., et al., *Inhibiting DNA Methylation Causes an Interferon Response in Cancer via dsRNA Including Endogenous Retroviruses.* Cell, 2015. **162**(5): p. 974-86.
224. Chiappinelli, K.B., et al., *Inhibiting DNA Methylation Causes an Interferon Response in Cancer via dsRNA Including Endogenous Retroviruses.* Cell, 2017. **169**(2): p. 361.
225. Besch, R., et al., *Proapoptotic signaling induced by RIG-I and MDA-5 results in type I interferon-independent apoptosis in human melanoma cells.* J Clin Invest, 2009. **119**(8): p. 2399-411.
226. Shi, Y., et al., *Glia maturation factor gamma (GMFG): a cytokine-responsive protein during hematopoietic lineage development and its functional genomics analysis.* Genomics Proteomics Bioinformatics, 2006. **4**(3): p. 145-55.

227. Aerbajinai, W., et al., *Glia maturation factor-gamma mediates neutrophil chemotaxis.* J Leukoc Biol, 2011. **90**(3): p. 529-38.
228. Zuo, P., et al., *High GMFG expression correlates with poor prognosis and promotes cell migration and invasion in epithelial ovarian cancer.* Gynecol Oncol, 2014. **132**(3): p. 745-51.
229. Wang, H., et al., *Expression of glia maturation factor gamma is associated with colorectal cancer metastasis and its downregulation suppresses colorectal cancer cell migration and invasion in vitro.* Oncol Rep, 2017. **37**(2): p. 929-936.
230. Aerbajinai, W., et al., *Glia maturation factor-gamma regulates murine macrophage iron metabolism and M2 polarization through mitochondrial ROS.* Blood Adv, 2019. **3**(8): p. 1211-1225.
231. Chen, L., et al., *Correlation between RNA-Seq and microarrays results using TCGA data.* Gene, 2017. **628**: p. 200-204.
232. Rai, M.F., et al., *Advantages of RNA-seq compared to RNA microarrays for transcriptome profiling of anterior cruciate ligament tears.* J Orthop Res, 2018. **36**(1): p. 484-497.
233. Castillo, D., et al., *Integration of RNA-Seq data with heterogeneous microarray data for breast cancer profiling.* BMC Bioinformatics, 2017. **18**(1): p. 506.
234. Mayya, V. and D.K. Han, *Phosphoproteomics by mass spectrometry: insights, implications, applications and limitations.* Expert Rev Proteomics, 2009. **6**(6): p. 605-18.
235. Ardito, F., et al., *The crucial role of protein phosphorylation in cell signaling and its use as targeted therapy (Review).* Int J Mol Med, 2017. **40**(2): p. 271-280.
236. Raha, D., M. Hong, and M. Snyder, *ChIP-Seq: a method for global identification of regulatory elements in the genome.* Curr Protoc Mol Biol, 2010. **Chapter 21**: p. Unit 21 19 1-14.

11. Figures

12. Tables